Fault Zone Structure and Rupture Behavior with Fiber-Optic Sensing and Second Moments

Thesis by
James Atterholt

In Partial Fulfillment of the Requirements for the
Degree of
Doctor of Philosophy

CALIFORNIA INSTITUTE OF TECHNOLOGY
Pasadena, California

2025
Defended July 18, 2024

ACKNOWLEDGEMENTS

I will begin by thanking my two advisors, Zhongwen Zhan and Zach Ross. These two shaped me into a scientist. Regardless of the problem, Zhongwen manages to spontaneously conjure the right questions and find the interesting path forward. It has been a great pleasure to observe and learn from his approach to science during my time here. Zach gave me the space to figure things out for myself and corrected my course when I got lost. When I arrived he gifted me a hardcover copy of Aki and Richards and made sure I corrected a sign error in the middle of the book. The rest is history.

I am also deeply grateful to the members of my committee: Rob Clayton and Jennifer Jackson. Rob is an immensely supportive person and a deep well of knowledge on seismic imaging and earth structure. Jennifer gave me whatever meager background I have on the deep earth and has been an encouraging voice throughout my time here. I would also like to thank Mike Gurnis and Joann Stock. Mike and Joann have both been supportive of my work and have provided me with many useful suggestions over the years. I would also like to thank the Seismolab staff for their endless help and good friendship, particularly Donna Mireles, Kim Baker-Gatchalian, and Priscilla McLean. I am very glad to have worked with Lucy Jones and Ariel Raymond and all of the Earthquake Fellows; this program gave me far more than I put in.

I would also like to thank my former advisors. To Gary Pavlis, at Indiana, I owe my career in seismology and my time at Caltech. If it were not for him, I have no idea what I would be doing. I would also like to thank Kaj Johnson, who was a second mentor to me and was immensely helpful during my time at Indiana. I would like to thank Ting Chen at Los Alamos for her patience and guidance during my IRIS internship and for suggesting I apply to Caltech. And I would like to thank Bill Stephenson and Alena Leeds at the USGS, for advising me well and sending me around the country on seismic surveys.

Being a student at the Seismolab would be woefully incomplete without all the other students and postdocs that generate a fun and supportive community. Celeste, Ethan, Tobi, and Chenxi made the SM358 office a second home. Thank you to the graduate students that came before me and provided me with unending advice and aid, Valere, Zhichao, Zhe, Jack, Erin, Jorge, Voon, Ollie, Olivia, Yida, and Pond. My cohort, Ben, Ojashvi, Yan, and Kai were important keepers of my sanity during our first year and persist in being good friends. Thanks too to students that came after me in Zach and Zhongwen's groups, Jack, Valeria, Caifeng, Rajani, Jiaqi, Auden, and Eli; and all the postdocs, Ettore, Jiaxuan, Thea, Zefeng, Xin, Xiaozhuo, Jonny, Bing, Hongyu, Zhiang, Erik, Shane, Qiushi, Meichen, Jiuxun, Alba, Weiqiang, and too many others to name. Thanks too to the non-Seismolab friends I have made along the way, Alec, Abe, Max, Paulette, Hannah, Rachel, Maria, Henry, and Emily. A special thanks to Tori Moore, honest and good and geologist to the end. I am grateful to have known her.

I would also like to thank my family for their encouragement prior to and throughout my PhD. Yes, my mother's flash card training gave me an early leg up in arithmetic. Yes, my father insisted that I know the full Spell Bowl word list by heart. Yes, my brothers, Jack and Joe, shuttled me to any and every academic extracurricular in high school. There are many more examples, but perhaps the greatest unearned advantage is to be born into a stable home full of people that love you. There is no one luckier than me. I also thank my toy poodle, Bentinho, who is as of yet illiterate and so unfortunately cannot read this, but his habit of attaching himself to me when I am anxious is a saving grace.

I feel the need to thank my library, which is a fountain of wisdom and joy that I can always return to when I most need it. Certain members of it feel like old friends. A select few in chronological order. Cicero for his courage. Adams for his example. Machado de Assis for his feeling. Conan Doyle for his comfort. Borges for his magic. Caro for his world.

The most important thanks I have is for my wife, Hannah. To try to put it all into words would be to trivialize it. I will say, coming home every day to our shared life shrank every problem and negated every failure. Or, at the beginning of my life, the world had an enormous capacity to wound me; upon meeting you, the world is benign and my life is full.

ABSTRACT

The structure of fault zones and the behavior of ruptures are indivisible. Fault structure is molded by the continued overprinting of slip events, and rupture propagation is highly sensitive to fault zone parameters. Observational constraints on both fault zone characteristics and the behavioral response of ruptures to fault variability are thus needed to understand earthquakes. Fault zones are narrow structures that are difficult to image in detail, particularly at depth. This means that fault structure is often oversimplified in rupture models and inversions. Earthquake source descriptions are frequently high dimensional. Fault slip distributions are often complicated and nonunique and seismicity catalogs can contain hundreds of thousands of events. This complexity can be difficult to reduce for the purpose of making clear conclusions on earthquake phenomenology. In this sense, observations of fault structure may benefit from a dimensionality expansion and observations of earthquakes may benefit from a dimensionality reduction. In Chapters 2-5 of this thesis I address the former problem. I show how an emergent technology, distributed acoustic sensing (DAS), that transforms fiber optic cables into dense arrays of strainmeters can be used to resolve fault zone characteristics with astonishing detail. This applies to small and large faults at shallow and deep depths. I define a framework for partitioning the seismic wavefield and show that scattered phases in earthquake wavefields encode information on the location and dimensions of small faults. I then investigate the Garlock Fault with an intersecting DAS array and uncover structural variability across the fault at shallow and seismogenic depths. I also use this array to investigate Moho topography, and find that the Garlock Fault offsets and, by extension, penetrates the mantle over a narrow width. In Chapters 6-8 of this thesis I address the latter problem. I show that second moments, both of source and seismicity distributions, can improve the clarity of observations and make drawing meaningful conclusions about rupture behavior possible. I first develop a framework to probabilistically invert for the second moments of source distributions and use it to investigate all large strike-slip events of the past three decades. These solutions show several patterns between faults and rupture behavior. I also create a seismicity catalog for the Ridgecrest earthquake sequence and use a second moment measure to constrain the evolution of fault orientation and the stress state.

PUBLISHED CONTENT AND CONTRIBUTIONS

Atterholt, J., Wilding, J. D., and Ross, Z. E. (In Prep). The evolution of fault orientation in the 2019 Ridgecrest Earthquake Sequence with a new long-term catalog of seismicity and moment tensors. (Chapter 8).
J.A. conceptualized the project, analyzed the data, developed the methodology, designed the figures, and wrote the manuscript. J.D.W. applied certain methodologies toward developing the moment tensor catalog. Z.E.R. contributed to conceptualization, assisted in the application of the methodology, and supervised the project.

Atterholt, J. and Zhan, Z. (In Review). Fine scale Southern California Moho structure uncovered with distributed acoustic sensing. (Chapter 5).
J.A. conceptualized the project, analyzed the data, developed the methodology, designed the figures, and wrote the manuscript. Z.Z. contributed to conceptualization, collected the data, and supervised the project.

Atterholt, J., Zhan, Z., Yang, Y., and Zhu, W. (2024). Imaging the Garlock Fault Zone with a fiber: a limited damage zone and hidden bimaterial contrast. *Journal of Geophysical Research: Solid Earth* 129. DOI: `10.1029/2024JB028900`. e2024JB028900 (Chapter 4).
J.A. conceptualized the project, collected and analyzed the data, developed the methodology, designed the figures, and wrote the manuscript. Z.Z. contributed to conceptualization, collected the data, and supervised the project., Y.Y. and W.Z. helped apply existing methodologies to the data.

Atterholt, J. and Ross, Z. E. (2023). Finite source properties of large strike-slip earthquakes. *Geophysical Journal International* 236. DOI: `10.1093/gji/ggad459`. 889–903 (Chapter 7).
J.A. conceptualized the project, analyzed the data and further developed the methodology, designed the figures, and wrote the manuscript. Z.E.R. contributed to conceptualization, assisted in method development, and supervised the project.

– (2022). Bayesian framework for inversion of second-order stress glut moments: application to the 2019 Ridgecrest Sequence mainshock. *Journal of Geophysical Research: Solid Earth* 127. DOI: `10.1029/2021JB023780`. e2021JB023780 (Chapter 6).
J.A. conceptualized the project, analyzed the data, developed the methodology, designed the figures, and wrote the manuscript. Z.E.R. contributed to conceptualization, assisted in method development, and supervised the project.

Atterholt, J., Zhan, Z., and Yang, Y. (2022). Fault zone imaging with distributed acoustic sensing: body-to-surface wave scattering. *Journal of Geophysical Research: Solid Earth* 127. DOI: `10.1029/2022JB025052`. e2022JB025052 (Chapter 3).
J.A. conceptualized the project, analyzed the data, developed the methodology,

designed the figures, and wrote the manuscript. Z.Z. contributed to conceptualization, collected the data, and supervised the project., Y.Y. helped verify the results and helped develop the methodology.

Atterholt, J., Zhan, Z., Shen, Z., and Li, Z. (2021). A unified wavefield partitioning approach to distributed acoustic sensing. *Geophysical Journal International* 228. DOI: `10.1093/gji/ggab407`. 1410–1418 (Chapter 2).
J.A. conceptualized the project, developed the partitioning methodology, applied the method to the data, designed the figures, and wrote the manuscript. Z.Z. contributed to conceptualization, collected the data, and supervised the project. Z.S. and Z.L. performed the template matching workflow.

TABLE OF CONTENTS

Acknowledgements iii
Abstract v
Published Content and Contributions vi
Table of Contents vii
List of Illustrations x
List of Tables xxxii
Chapter I: Introduction 1
Chapter II: Partitioning and Denoising the DAS Wavefield 7
  2.1 Introduction 7
  2.2 Methodology 10
  2.3 Application 17
  2.4 Discussion 20
  2.5 Conclusions 23
Chapter III: Finding Small Faults with Scattered Waves Recorded by DAS . . 27
  3.1 Introduction 27
  3.2 Data 31
  3.3 Mapping Faults Using Local Backprojection 31
  3.4 Modeling Scatterers as Fault Zones 37
  3.5 Constraining Fault Geometry 39
  3.6 Discussion 42
  3.7 Conclusions 46
Chapter IV: Imaging the Garlock Fault with a DAS Array 50
  4.1 Introduction 50
  4.2 A Heterogeneous Shallow Subsurface 53
  4.3 An Upper Limit on Damage Zone Size 58
  4.4 A Hidden Bimaterial Contrast at Seismogenic Depth 61
  4.5 Discussion and Conclusions 65
Chapter V: Mapping Fine-Scale Moho Topography with DAS Wavefields . . 78
  5.1 Introduction 78
  5.2 Autocorrelation for Secondary Phase Retrieval 80
  5.3 Fine-Scale Crustal Thickness Variability from Dense Moho Depth Profiles 83
  5.4 Sharp Moho Changes Across the Garlock Fault and Coso Volcanic Field 88
  5.5 Discussion of Ambiguity and Uncertainty 90
  5.6 Materials and Methods 96
Chapter VI: Computing Earthquake Second Moments in a Bayesian Framework 107
  6.1 Introduction 107
  6.2 Preliminaries 109

- 6.3 Methods 111
- 6.4 Results 118
- 6.5 Discussion 124
- 6.6 Conclusions 128

Chapter VII: Comparing Second Moments of Large Strike-Slip Earthquakes . 131
- 7.1 Introduction 132
- 7.2 Preliminaries 134
- 7.3 Methods 138
- 7.4 Results and Discussion 141
- 7.5 Conclusions 156

Chapter VIII: Measuring Fault Orientation Evolution using Seismicity 168
- 8.1 Introduction 168
- 8.2 Constructing a Seismicity and Moment Tensor Catalog 171
- 8.3 Computing Fault Orientations with Focal Mechanisms 174
- 8.4 Measuring Seismicity Anisotropy with Cylindrical K-Functions . . . 180
- 8.5 Comparison of Results and Discussion 185
- 8.6 Conclusions 192

Chapter IX: Conclusions 202

Bibliography 205

LIST OF ILLUSTRATIONS

Number *Page*

2.1 Geographic setting and waveform examples. A. Map showing the geographic setting for the data segments in this figure. The yellow star indicates the location of the M_l 1.79 earthquake recorded by the Ridgecrest array and the LRL station at distances of 44 km (specifically the station highlighted in panel C) and 62 km respectively. The blue line indicates the location of the DAS array that recorded the time series shown in the middle image of this figure. The white box indicates the approximate location of the DAS station whose individual station data is shown in this figure. The orange triangle shows the location of the broadband station (LRL) whose station data is shown in this figure. The black and gray lines delineate faults and roads respectively. The light-red dots indicate the locations of aftershocks used as templates in this study. The inset gives regional context. B. Full DAS record section at the time of a regional earthquake, the location of which is shown in the map in A. The black arrow marks the location of the DAS channel given as an example in C (channel 899). C. Comparison of station data from a single DAS station (top) with the east-west component of station data from the nearby LRL broadband station (bottom). The DAS stations in panels B and C and the broadband station in panel C are band-pass filtered from 2-8 Hz using a Butterworth filter. 9

2.2 Curvelet polar tiling framework. A. Schematic illustration of the polar tiling used to construct curvelet coefficients. The wedges delineate the compartmentalization of the frequency-wavenumber domain. B. Plot of select curvelets in both the frequency-wavenumber domain. C. Plot of the same curvelets as in B in the spatiotemporal domain. Colors of arrows correspond to equivalent curvelets between B and C. 11

2.3 Illustration of stochastic denoising using soft-thresholding in the curvelet domain. Thresholds for this example were determined empirically using a window with little coherent signal from the same data set. A. Unfiltered record sections for the entire DAS array. B. Curvelet filtered record sections for the entire DAS array. C. The individual DAS station data from the record sections in A (black) and B (red) for the DAS station marked by the gray (channel 422) arrows. D. The individual DAS station data from the record sections in A (black) and B (red) for the DAS station marked by the black (channel 780) arrows. 15

2.4 Illustration of coherent denoising using the polar-tiling framework of the curvelet construction. A. Pseudo-synthetic noisy window made by superimposing a record section with high cultural noise onto a record section with an earthquake. B. Time series in which velocities in the range 0-1000 m/s were removed using an untapered FK-filter. C. Time series in which velocities in the range 0-1000 m/s were removed using our curvelet windowing technique. The black arrows point to a region of prominent filter-generated artifacts. 16

2.5 Hourly (PST) event counts of the catalogs created using template matching. A 3-hour moving average filter was applied to each of the time series. The yellow line shows the hourly counts for the catalog of templates made using the SCSN catalog. The red line shows the hourly counts for the catalog created using template matching (TM) on the unfiltered data. The blue line shows the hourly counts for the catalog created using template matching (TM) on the curvelet filtered data. 20

2.S1 Hourly (PST) event counts of the catalogs created using template matching. A 3-hour moving average filter was applied to each of the time series. The yellow line shows the hourly counts for the catalog of templates made using the SCSN catalog. The red line shows the hourly counts for the catalog created using the unfiltered data. The green line shows the hourly counts for the catalog created using data filtered using only the coherent noise filter. The purple line shows the hourly counts for the catalog created using data filtered using only the stochastic noise filter. The blue line shows the hourly counts for the catalog created using data filtered with both the coherent noise and stochastic noise filters. 25

2.S2 Hourly (PST) measure of the percentage of events from the catalog produced using unfiltered data retained in the catalog produced using data filtered for both stochastic and coherent noise. Events are considered retained if there exists a corresponding event in the catalog produced using filtered data that has an origin time within 2.5 seconds of the event. A 3-hour moving average filter was applied to this time series. 26

2.S3 Example of a detection made in the original catalog but not made in the new catalog. A. Template event taken from the unfiltered data. B. Wavefield of the detection made using the template in A. C. Same template as in A but taken from the filtered data. D. Same wavefield as in B but taken from the filtered data. Black arrows point to the earthquake-generated body waves of the template event. 26

3.1 Geographic setting and illustration of scattered phases. Top: The geographic setting of the data used in this study. Blue line corresponds to the DAS array. Red dots correspond to the epicenters of the events used in this study. Yellow star corresponds to the epicenter of the event shown below (depth 5.6 km). Green lines correspond to the USGS-mapped Quaternary faults in the area. Bottom: Example of the DAS-measured wavefield of the onset of an event used in this study. Black dotted lines correspond to the locations of the chevron-like features that are mapped in Figure 3.3. 32

3.2 Schematic illustration of the phenomena observed in the earthquake wavefields used in this study. Top: Record section corresponding to the processes illustrated below. Bottom: Illustration of the phenomena resulting in the generation of the chevron-like features shown in Figure 3.1. Colors represent the same phenomena in both top and bottom. Green corresponds to incident body wave. Gray features indicate a fault zone. Purple corresponds to the scattered surface waves resulting from the body waves impinging on the fault zone. Orange line and triangles indicate the fiber optic cable and stations, respectively. Blue box represents the DAS interrogator unit. 33

3.3 Backprojection of scattered phase results. Left: Backprojection profiles made using 50 events recorded by the DAS array in Ridgecrest, CA. Light blue lines correspond to profiles made using a single event. Dark blue lines correspond to the mean profile. Orange lines correspond to the topographic prominence of the mean energy profile. Top and bottom plots correspond to profiles generated with 4 and 7 Hz center frequencies, respectively. Black arrows point to referenced peaks α, β, γ, and ϕ. Right: Prominence profiles to the left, convolved with Gaussian kernel to widen peaks for representation, plotted on the DAS array geometry shown in Figure 3.1. Color corresponds to prominence amplitude. Green lines correspond to fault locations. Solid lines are moderately or well constrained fault locations, and dotted lines are inferred fault locations. Faults are labeled according to associated peaks indicated in the profiles to the left. Curved black arrows indicate the proposed relocation of the fault associated with peak α. 37

3.4 Synthetic tests of shallow scatterers. Left: Example of velocity model modified from Yang, Atterholt, et al. (2022) and Small et al. (2017) with two fault zone-approximating velocity perturbations emplaced in the model. Green line corresponds to array of strainmeters. Black arrows point to incident wave direction and fault locations. Note the large vertical exaggeration. Right: Record section generated from scenario illustrated to the left. 39

3.5 Comparison of modeled and observed spectra. A. Pseudocolor plot of mean backprojection amplitude plotted against center frequency and distance along array. Dotted green and dotted blue lines correspond to cross sections of this plot, associated with peaks α and β, respectively. B. Plots of backprojection amplitude versus center frequency for the cross-sections shown in A. Light green and light blue lines are the frequency-amplitude curves determined for a single event for peaks α and β, respectively. Dark green and dark blue lines are the mean frequency amplitude curves for peaks α and β, respectively. Dotted black lines correspond to the frequency-amplitude curves for our preferred fault zone model for each peak. Dotted colored lines are frequency amplitude curves for fault zone models with variant parameters to illustrate the constraints of this methodology. The parameters used for each model are given in Table 3.S1. The asterisk in the legend indicates that, for visualization purposes, the corresponding model is normalized by the maximum height of the data curve rather than the integrated sum. 41
3.S1 Examples of the wavefield partitioning, described in Atterholt et al. (2021), applied for separating the direct waves from the surface waves. The left column shows the total wavefield for 3 separate events used in this study. The middle column shows the separated direct waves of the events. The right column shows the separated scattered waves of the events. 47
3.S2 Dispersion curve generated using the backprojection framework to perform a grid search at velocities in narrow frequency bands on the earthquake wavefield shown in Figure 1. Black dotted line is the 1D average of the velocity model from Yang, Atterholt, et al. (2022) . . . 48
3.S3 Dispersion curve generated using the backprojection framework to perform a grid search at velocities in narrow frequency bands on a synthetic shot gather with an emplaced fault model. Black dotted line is the 1D average of the velocity model from Yang, Atterholt, et al. (2022) 48

3.S4 Peak decay functions of peaks α and β for ensemble of profiles shown in Figure 3. Light green and light blue lines are decay functions of individual profiles for peaks α and β, respectively. Dark green and dark blue lines are mean peak decay functions for peaks α and β, respectively. Dotted lines are peak decay functions for synthetics generated using different attenuation regimes defined using constant of proportionality c. 49

4.1 Study setting and dataset examples. a. Map summarizing the data used in this study. Blue, yellow, and purple curves represent the entire DAS array, the segment used for the ambient noise experiment, and the segment used for the active source experiment, respectively. Gray and green points show the earthquakes used to construct the profiles in Figs. 4.2 and 4.4. The gray star indicates the earthquake shown in c. The diamond shaped points indicate the earthquakes shown in Fig. 4.S8. Red points show earthquakes that were also used in the inversion in for the bimaterial contrast. Locations of the San Andreas Fault (SAF) and Death Valley (DV) are indicated on the inset. b. Example shot gathers located approximately on the mapped fault trace from the active source (top) and ambient noise experiments (bottom). Active source and ambient noise shot gathers are bandpass filtered between 2-10 and 1-5 Hz, respectively. c. Example of the waveforms from an on-fault earthquake. Olive dotted lines mark the P and S wave picks. Earthquake wavefield is filtered between 1-10 Hz. For b and c, zero distance is the location of the intersection between the central strand of the Garlock Fault and the DAS array. . . 54

4.2 Dispersion curves from the active source experiment (a) and ambient noise cross-correlations (b) along the purple segment of the array in Fig. 4.1. Black dotted lines show locations of mapped strands of the Garlock Fault where they cross the velocity profile. 55

4.3 Shallow shear wave velocity model and corresponding model-travel-time perturbation comparison along the purple segment of the array shown in Fig. 4.1. a. Profile taken from the shallow velocity model around 100 meters depth (averaged from 80-120 m and smoothed over 200 m laterally) that clearly shows the discontinuity across the fault. b. Shear wave velocity model from the joint inversion of the active source and ambient noise data. Black dotted lines mark the locations of the array-crossing mapped traces of the Garlock Fault. c. Travel-time perturbations from the cluster of earthquakes on the fault in Fig. 4.1 and the expected perturbations from the shallow model. Shallow model perturbations are modified by applying a moving average filter corresponding to the gauge length of the fiber recording the earthquake for comparability. 57

4.4 Cluster comparison and inversion results from differential travel-time measurements computed along the yellow segment in Fig. 4.1. a. Travel-time perturbations from on-fault (gray) and off-fault (green) clusters of earthquakes, shown in Fig. 4.1. b. difference between the two sets of perturbations (purple) plotted against the model fit from the inversion ensembles. c, d. Ensemble results using differential travel-times to invert for the necessary travel-time adjustments for the shallow (c) and deep (d) earth structure to the north and south of the fault. Joint distributions are shown in Fig. 4.5. 62

4.5 Joint probability distributions for ensembles of parameters from the differential travel-time inversion. Diagonal plots show the marginal distributions (also shown in Fig. 4.4), and the off-diagonal plots show the joint distribution for the row-column pairs. The values in these plots are unitless and correspond to the ratio between the time spent in each quadrant necessary to fit the arrival time data and the expected travel-time spent in each region computed using the initial velocity model. 64

4.6 Results from the broadband seismic analysis. a. Station map showing the stations used in this analysis. Each off-fault station (orange) was cross-correlated with the on-fault station (purple) to produce the corresponding models. b. The dispersion curves from each of the cross-correlation measurements and c. the corresponding inverted shear wave velocity profiles. 65

4.7 Schematic model summarizing the findings of this study. 67

4.S1 Geologic map of the study region with units defined in the Geologic Map of California (Jennings et al., 1977). The dimensions of this map are the same as those in Fig. 4.1. Black lines are faults. Gr = Mesozoic granitic rocks | Ns = Plio-Pleistocene and Pliocene loosely consolidated deposits | Tv = Tertiary volcanic flow rocks | Q = Quaternary alluvium | Sc = schist of various types | Mv = Paleozoic metavolcanic rocks | Pc = Precambrian rocks | Ms = Paleozoic marine rocks. 69

4.S2 Extended shallow imaging experiment phase (top) and shear wave velocity (bottom) models. 69

4.S3 Comparison of the near-fault velocity model recovered from the joint inversion (Fig. 4.3) and the inversion using only ambient noise data (Fig. 4.S2). 70

4.S4 1D velocity model and approximate ray paths. Left: velocity profile used to isolate travel-time perturbations from 3D structure. Right: approximate ray-paths between near-fault event cluster and DAS channel collocated with the mapped trace of the Garlock Fault. 70

4.S5 Normalized power spectra of the earthquake wavefields of events in the cluster of earthquakes on the Garlock Fault. 71

4.S6 Parametric evaluation of the sensitivity of our array to different velocity features at depth and comparison to velocity feature from Cochran et al. (2009). In this plot we vary depth of damage zone (d), velocity perturbation at depths greater than 0.2 km (dV_{sd}) and the width of the damage zone at depths greater than 0.2 km (W_d). 72

4.S7 Travel-time perturbations from the gray cluster of earthquakes shown in Fig. 4.1 at different distances from the Garlock fault for illustration. Near surface perturbations are computed using the model in Fig. 4.2. Seismogenic zone perturbations are computed using the model in Fig. 4.4. Shallow crust perturbations are computed as the difference between the total perturbations and the combined perturbations of the near surface and seismogenic zone. Black dotted line indicates location of Garlock fault in the USGS Quaternary Fault Database. . . 73

4.S8 Examples of earthquake wavefields from clusters of earthquakes on and off the Garlock Fault. Locations of these earthquakes are indicated by the diamond markers on the map in Fig. 4.1. Olive-colored dotted lines indicate the P and S phase picks made by PhasenetDAS. . 74
4.S9 Map of events used in the inversion for the bimaterial contrast across the fault. Green segment of the array indicates the channels from which travel-times were used. 75
4.S10 The SCEC Community Velocity Model along a path collocated with the DAS array used in this study. Note the high velocity anomaly at depth on the south side of the model. 76
4.S11 Setting and phase velocity picks for the low-frequency broadband cross-correlation measurements. Top left plot shows station locations used in this analysis. The Christmas Canyon station (CCC) was a member of each cross-correlation pair. Other plots show measurements and error estimates of phase velocity dispersion measurements. 77
5.1 Experiment setting and data. The DAS array geometry (blue curve) plotted against the kept (green) and discarded (red) M2.5+ events recorded by the array. Also plotted are the fault traces included in the USGS Quaternary Fault Database (2018) and locations of relevant tectonic provinces and features (GV = Great Valley | SN = Sierra Nevada | BR = Basin and Range | MD = Mojave Desert | CVF = Coso Volcanic Field | GF = Garlock Fault | SGM = San Gabriel Mountains | SBM = Santa Barbara Mountains). 81
5.2 Important phases and relative arrival times. (A) Ray paths for the three phases of interest in this study for a fixed source-receiver distance and representative velocity model: the direct phase (Pg), the Moho head wave (Pn), and the Moho reflected wave (PmP) (S not pictured for simplicity). (B) Reduced (8.1 km/s) arrival times of phases plotted against source-receiver distance. (C) Differential times of phases relative to the first arriving P-phase plotted against source-receiver distance. 82

5.3 Example of autocorrelation for phase retrieval. (A) Earthquake wavefield with representative data quality. Included are the PhaseNet DAS picks and computed P and PmP times for the representative velocity model used in this study with a Moho depth of 32 km. Green bars are a reference for the channel bounds within which differential time picks were made. (B) Autocorrelation image created for the corresponding earthquake wavefield using the framework outlined in the text. Included are the computed P-PmP differential times and the picks made on the positive correlation peak associated with the PmP arrival. Location of this event is indicated as a green star in Fig. 5.1 . 83
5.4 All PmP picks made in this study. Plotted are the autocorrelation correlograms for each channel for which estimates of P-PmP differential time could be made. Black dotted lines correspond to pick times, and correlograms are organized by decreasing pick times when following Pg and increasing pick times when following Pn. Gray dotted line marks the transition from Pg to Pn as first arrival. 84
5.5 Summary of resolved Moho depth variability. (A) Moho depth inversion results along corresponding bounce-point locations for all events included in this study. Included as squares are Moho depth estimates reported in Yan and Clayton (2007). Purple dotted line marks the DAS array location. (B) Cross-sections of Moho depth corresponding the profiles mapped in (A). Included are all estimates of Moho depth within 10 km of the profile reported in this study (black dots) and all estimates of Moho depth within 20 km of the profile reported in Yan and Clayton (2007) (orange squares). Lettering indicates different structural features where they cross the profiles (GF=Garlock Fault | LLFZ=Little Lake Fault Zone | CVF=Coso Volcanic Field | TRF=Tunnel Ridge Fault | NFT=North Frontal Thrust). The CVF location marks the approximate southern extent of the mid-crustal low velocity zone reported in (Zhang and Lin, 2014). Lateral dotted line corresponds to smoothed Moho depth estimates from the Community Moho Model (Tape et al., 2012). (C) Schematic diagrams of the cross-sections in (B). 86

5.6 Synthetic tests. (A) Velocity models and source-array geometry used in these synthetic tests. Double-sided arrows correspond to the approximate extent and locations of bounce-points in these tests. Solid black line marks the Moho and dotted black lines outline velocity anomalies. (B) Differential times from autocorrelation wavefields for each synthetic test. Shown are reference relative arrival times of PmP for a flat Moho at 25 and 30 km depth. 87

5.7 Auto-correlograms across Garlock Fault. (A) and (B) are correlograms for long and short bounce-point profiles across the Garlock fault, respectively. Plotted are reference curves of expected P-PmP differential times for different Moho depths. Also plotted are the estimates of the width of uncertain Moho depths on either side of which we can confidently identify distinct PmP peaks. Locations of these profiles are indicated as α and β in Figure 5.5. 90

5.8 Auto-correlograms near Coso Volcanic Field. (A) and (B) are correlograms for bounce-point profiles on and just south of the shallow Moho depth anomaly near Coso, respectively. Plotted are reference curves of expected P-PmP differential times for different Moho depths. Also identified is a correlogram peak that we speculate is the diffracted phase off nearby shallow Moho anomaly. Locations of these profiles are indicated as γ and δ in Figure 5.5. 91

5.9 Correlogram envelope summation results. (A) and (B) show profiles that summarize the amplitude of the summation of the envelopes of the correlogram profiles shown in Figures 5.7 and 5.8 along expected P-PmP differential times for different Moho depths. (A) shows the results of this operation performed along the spatial windows to the north and south of the expected step location for profile shown in Figure 5.7. (B) shows the results of this operation performed on profiles (on anomaly) and (off anomaly). Both (A) and (B) suggest the data between profiles are consistent with variant crustal thickness values. 93

5.S1 1D crustal model and average upper mantle velocity inversion. Left: Ensemble of crustal models drawn from the Community Velocity Model. Light blue lines are each a profile included in the ensemble. Black dotted line is the representative model used throughout this study. Right: Global Moho depth and upper mantle velocity loss distribution described in the main text. Red and blue indicate higher and lower loss, respectively. Yellow star indicates best fitting solution. 100
5.S2 Histogram of differences between nearby Moho depth estimates made in this study and those of Yan and Clayton (2007). Different colors correspond to different maximum distances between measurement points used as prerequisites for inclusion in the histogram. Measurements from Yan and Clayton (2007) are included only once using the nearest measurement from this study. 101
5.S3 Synthetic wavefield generated using the same parameters as the flat Moho model in Figure 5.6, but with an extended measuring array. . . 102
5.S4 Full stack of all cross-correlation wavelets associated with PmP used in this study. Alignment is performed using the peak picks shown in Figure 5.4. Black dotted lines encompass 1.5 wavelengths. 103
5.S5 Phase-P differential times for a diversity of source depth, Moho depth, and source-to-receiver distance combinations. 103
5.S6 Example of an SmS observation made using one of the earthquakes in this study. Earthquake location is indicated with a diamond marker in Figure 5.1. Vertical green lines mark the bounds over which PmP is observable. 104
5.S7 Comparison of several parameters with the proportion of station-channel pairs for which PmP was observable in this study. 104
5.S8 Moho depth distributions computed using modified velocity model parameters and shifted source depths. 105
5.S9 Distribution of differences between Moho depth values determined using the perturbations shown in Figure S8 and those of the preferred model shown in Figure 5.5. 106
5.S10 Distribution of depths for the SCSN catalog and the Hauksson et al. (2012) waveform cross-correlation relocation catalog for events used in the study and the distribution of depth differences between catalogs. 106

6.1 Geographic setting and data coverage. Left: Geographic setting of the 2019 Ridgecrest Sequence. Focal mechanism is the gCMT solution for the sequence mainshock. Yellow star indicates the gCMT solution centroid position. Green and red lines indicate USGS mapped quaternary faults (USGS and CGS, 2022) and faults that were activated during the Ridgecrest Earthquake sequence (Ross, Idini, et al., 2019). The strike, dip, and rake of the true nodal plane as given by the gCMT solution are 321°, 81°, and 180°, respectively. Map coloring is reflective of elevation. Right: Global distribution of stations from which waveforms were used in this study. 112

6.2 Marginal and joint probability density plots for the 10 independent parameters inverted for the synthetic test in this study. Off-diagonal plots are 2-dimensional histogram plots representing the joint probability distribution for each pair of independent parameters. On-diagonal plots are kernel density estimate plots for the marginal distributions of the adjacent joint probability distributions. Black dotted lines indicated the anticipated solution for each parameter in the inversion. 119

6.3 Waveform fits for a large subset of the windowed waveforms for the synthetic test conducted in this study. Waveforms are labeled according to the GSN station at which they were generated. Black waveforms are synthetic observations. Gray waveforms are generated using a single solution from the ensemble of solutions from our inversion. Waveforms from each solution in the ensemble are plotted. Red waveforms are generated using the mean solution of the ensemble of solutions from our inversion. Blue waveforms are generated using only the gCMT solution and exclude any consideration of the second moments of the stress glut. 120

6.4 Physically motivated representations of the ensembles of second moment solutions for the synthetic test. A. characteristic length (L^c), B. characteristic length strike (θ^{L^c}), C. characteristic length plunge (ϕ^{L^c}), D. characteristic duration (t^c), E. instantaneous centroid velocity magnitude ($|\mathbf{v_0}|$), F. instantaneous centroid velocity strike ($\theta^{\mathbf{v_0}}$), G. instantaneous centroid velocity plunge ($\phi^{\mathbf{v_0}}$), H. average velocity upper bound (v^u). Histogram shows density of realizations in the ensemble. Red vertical line shows the mean realization. Blue line shows the anticipated realization. 121

6.5 Marginal and joint probability density plots for the 10 independent parameters inverted for in this study. Off-diagonal plots are 2-dimensional histogram plots representing the joint probability distribution for each pair of independent parameters. On-diagonal plots are kernel density estimate plots for the marginal distributions of the adjacent joint probability distributions. 122

6.6 Waveform fits for a subset of the windowed waveforms used in this study. Waveforms are labeled according to the GSN station at which they were recorded. Black waveforms are observations. Gray waveforms are generated using a single solution from the ensemble of solutions from our inversion. Waveforms from each solution in the ensemble are plotted. Red waveforms are generated using the mean solution of the ensemble of solutions from our inversion. Blue waveforms are generated using only the gCMT solution and exclude any consideration of the second moments of the stress glut. 123

6.7 Physically motivated representations of the ensembles of second moment solutions for the 2019 Ridgecrest mainshock. A. characteristic length (L^c), B. characteristic length strike (θ^{L^c}), C. characteristic length plunge (ϕ^{L^c}), D. characteristic duration (t^c), E. instantaneous centroid velocity magnitude ($|\mathbf{v_0}|$), F. instantaneous centroid velocity strike ($\theta^{\mathbf{v_0}}$), G. instantaneous centroid velocity plunge ($\phi^{\mathbf{v_0}}$), H. average velocity upper bound (v^u). Histogram shows density of realizations in the ensemble. Red vertical line shows the mean realization. Green, purple, and yellow vertical lines correspond to the fault-slip distribution results from prior studies, simplified into spatial second moments, from Ross, Idini, et al. (2019), Xu et al. (2020), and Jin and Fialko (2020), respectively. 124

6.8 Summary figure of the map-view spatial and directivity features of the 2019 Ridgecrest mainshock as derived from the second moment inversion. Left: Map-view projections of a 500-solution subset of the ensemble of second spatial moment ellipsoids solved for in this study. Ellipsoids are defined using $r_c(\hat{\mathbf{n}})$ in equation 6.3, and the largest principal semi-axis is L_c. Right: Map-view projections of a 500-solution subset of the ensemble of $\mathbf{v_0}$, as defined in equation 6.4, solved for in this study. Black lines represent the surface-rupture faults mapped after the Ridgecrest mainshock. Yellow star marks the location of the gCMT centroid of the Ridgecrest mainshock. Transparent blue lines represent a single solution from the ensemble of second moment solutions. Solid blue lines represent the mean solution from the ensemble second moment solutions. Green, purple, and yellow vertical lines correspond to the fault-slip distribution results from prior studies, simplified into spatial second moments, from Ross, Idini, et al. (2019), Xu et al. (2020), and Jin and Fialko (2020), respectively. 125

6.S1 Traces of stations submitted to manual quality control in this study. Station plots with black outlines indicate stations that were kept. Station plots with red outlines indicate stations that were not kept . . 129

6.S2 Kernel density estimate plots for multiple chains describing the distributions of independent components of the second moments of the stress glut for the 2019 Ridgecrest sequence mainshock. Different colors (blue, red, and green) represent different chains of the inversion. 130

6.S3 Distribution of hyperparameter σ determined in the inversion using real data and included in the inversion using synthetic data. 130

6.S4 Posterior distribution of the maximum off-fault distance derived using the ensemble of spatial covariance matrices and assuming a vertically dipping fault plane. Left plot is the ensemble for the synthetic test. Right plot is the ensemble for the test using observations. Red vertical lines delineate the mean of the ensemble. 130

7.1 Centroid locations and centroid depths of the earthquakes used in this study. White lines are fossil fracture zone locations from Seton et al. (2014) and Wessel et al. (2015). Green lines are plate boundaries from Bird (2003). 133

7.2 Examples of waveform fits for the 1999 $M_w 7.61$ Izmit earthquake. The waveforms in the top grouping are fits to the SH phase. The waveforms in the bottom grouping are fits to the R1 phase. Each waveform panel includes corresponding station name and back-azmith. The black and blue lines correspond to the observed waveforms and the point source theoretical Green's functions at each respective station. The red and gray lines correspond to the waveform fit of the mean solution and the distribution of fits for the ensemble of solutions, respectively. Waveforms are filtered between 7.5 and 12.3 mHz according to the described bandpass framework. 137

7.3 Summary of characteristic values. Left: Twice the characteristic temporal deviation ($\pm 2\sigma$ of moment rate function) for each event plotted against event moment magnitude. Black dotted line is the empirical magnitude-duration relationship used in (Ekström et al., 2012). Center: Characteristic spatial deviation plotted against centroid propagation length. Black dotted lines separate bilateral, mixed, and unilateral categories described in the text. Right: Twice the characteristic spatial deviation plotted against event moment magnitude; several scaling relationships from prior studies are plotted as dotted lines (Wells and Coppersmith, 1994; Mai and Beroza, 2000; Blaser et al., 2010; Thingbaijam et al., 2017; Scholz, 1982; Romanowicz, 1992). Green, red, and purple correspond to continental strike-slip, oceanic interplate, and oceanic intraplate, respectively. 142

7.4 Derived source quantities described in the text. Top row: Distributions of all event ensembles for each quantity. Second row from the top: Distributions of all ensembles within individual tectonic groups for each quantity. Green, red, and purple correspond to continental strike-slip, oceanic interplate, and oceanic intraplate, respectively. Bottom three rows: ensemble distributions for individual events within each tectonic category for each quantity. The relative heights of a few distributions of directivity ratios for individual sources were reduced for visualization purposes. 145

7.5 Depth extent of earthquakes plotted against lithospheric age. Isotherms generated using a half-space cooling model with an ambient mantle temperature of 1350°. Gray points are the gCMT centroid depths. Green violin plots are distributions of depth extents estimated by $\boldsymbol{\xi}^c(z) + \frac{1}{2}Z$. Yellow violin plots are depth extents estimated by $\boldsymbol{\xi}^c(z) + \frac{\sqrt{2}}{2}Z$. Left and right figures includes all interplate and intraplate events included in this study for which oceanic lithosphere age was obtainable respectively. Lithospheric age is obtained from Seton et al. (2020). 149

7.6 Evaluating source orientation against faults and crustal fabric. Left: Comparison of principal eigenvector strike ensembles with true nodal plane strikes for all continental strike-slip and interplate oceanic earthquakes. Right: Comparison of principal eigenvector strike ensembles with fracture zone strike estimation described in the main text for intraplate oceanic earthquakes near mapped fossil fracture zones. For both plots, black dotted lines correspond to differences of 45°. Green, red, and purple correspond to continental strike-slip, oceanic interplate, and oceanic intraplate, respectively. 151

7.7 Map view (top row) and vertical plane (bottom row) projections of median (dark blue) and individual ensemble members (light blue) of spatial second moment ellipsoids for several events considered in this study. Other colored ellipsoid projections come from geodetically-constrained fault slip distributions reduced to the second moment form. Orange, green, red, purple, pink, and olive colored ellipsoids correspond to solutions from Çakir et al. (2003), Delouis (2002), Reilinger et al. (2000), Asano (2005), and Socquet et al. (2019), respectively. 153

7.S1 Examples of waveform fits for the 2002 $M_w 7.88$ Denali earthquake. The waveforms in the top grouping are fits to the SH phase. The waveforms in the bottom grouping are fits to the R1 phase. The black and blue lines correspond to the observed waveforms and the point source theoretical Green's functions at each respective station. The red and gray lines correspond to the waveform fit of the mean solution and the distribution of fits for the ensemble of solutions respectively. . 158

7.S2 Examples of waveform fits for the 2018 M_w7.60 Palu earthquake. The waveforms in the top grouping are fits to the SH phase. The waveforms in the bottom grouping are fits to the R1 phase. The black and blue lines correspond to the observed waveforms and the point source theoretical Green's functions at each respective station. The red and gray lines correspond to the waveform fit of the mean solution and the distribution of fits for the ensemble of solutions, respectively. 159

7.S3 Station distribution for the three events plotted in Figure 3 of the main text in an azimuthal equidistant projection. Orange triangles represent Global Seismographic Network Stations and focal mechanisms are produced using the gCMT solution (Ekström et al., 2012). 160

7.S4 Ensembles of parameters defined in equations 4 and 5 of the main text for the oceanic interplate earthquakes considered in this study. . . 160

7.S5 Ensembles of parameters defined in equations 4 and 5 of the main text for the continental strike-slip earthquakes considered in this study. 161

7.S6 Ensembles of parameters defined in equations 4 and 5 of the main text for the oceanic intraplate earthquakes considered in this study. . . 162

7.S7 Evaluation of the significance of directivity ratio results. Left: Histogram comparing the combined ensembles of directivity ratios computed in this study (observed distribution) plotted against the expected distribution of directivity ratios given 1D rupture scenarios with random hypocenter locations on predefined faults with uniform slip (simulated distribution). Middle: Median values for many random draws of 25 directivity ratios from simulated distribution plotted against median values from random ensemble draws from the observed distribution. Right: Distribution of p-values for median for the observed distribution draws compared to the distribution of median computed from the simulated distribution. 163

7.S8 λ_2/λ_3 for the events shown in Figure 5. Left and right columns correspond to oceanic interplate and oceanic intraplate events, respectively. Top and bottom show the same plots but with different y-axis bounds. The event index corresponds to the relative lithospheric age (youngest to oldest) plotted in Figure 5. 163

7.S9 Map-view comparison of deviation ellipsoids between the second moment solutions produced in this study and those computed from peer-reviewed fault slip distributions in the SRCMOD database (Mai and Thingbaijam, 2014). Additional solutions for Palu earthquake from Socquet et al. (2019) and Hayes (2012), which is not peer reviewed but includes multiple faults, are included as well. 164

7.S10 Comparisons of vertical deviations between the second moment solutions produced in this study and those computed from peer-reviewed fault slip distributions in the SRCMOD database (Mai and Thingbaijam, 2014). Additional solutions for Palu earthquake from Socquet et al. (2019) and Hayes (2012), which is not peer reviewed but includes multiple faults, are included as well. 165

7.S11 The same plots as shown in Figure 7.S7, but produced with all slip patches with slip < 10% of the peak slip removed. 166

7.S12 The same plots as shown in Figure 7.S8, but produced with all slip patches with slip < 10% of the peak slip removed. 167

8.1 Plot of the seismicity (A) and focal mechanisms (B) resolved during the catalog creation step in this study. The regionalization used to measure faulting evolution over narrower spatial windows is shown in A. Also shown are the locations of the Mw 6.4 foreshock and Mw 7.1 mainshock centroid locations as the smaller and larger black star, respectively. 173

8.2 Direct comparison plot showing time evolution of faulting between methods applied in this study. The progression of the dip direction (black) measured using the peaks of the K_{cyl} plots is compared to the horizontal trend of σ_1 (blue) and the P-axis (red) by transforming the y-axis bounds using the measured dihedral angle. The direction of deviation in the dip from 90 degrees is chosen according to whether the dip is towards the corresponding dip direction (+) or away from the corresponding dip direction (-). In the foreshock zone, the pre-mainshock bin has two windows, one prior to the Mw6.4 foreshock (labelled P) and one between the Mw6.4 foreshock and the Mw7.1 mainshock (labelled F). K_{cyl} values of the aftershock sequence in the NW zone are plotted as light gray to highlight that these values do not show a stable progression of the primary fault orientation mode with time. 176

8.3 r_{CLVD} values and corresponding focal mechanism diagrams for the normalized summed potency tensor solutions for the spatial and temporal windows used in this study. The dotted line marks where r_{CLVD} is equal to zero. In the foreshock zone, the pre-mainshock bin has two windows, one prior to the M6.4 foreshock (labelled P) and one between the M6.4 foreshock and the M7.1 mainshock (labelled F). . . 178

8.4 K_{cyl} values for sweeps of dip direction (φ) and dip (θ) for the time-integrated seismicity for the regions defined in and the catalog produced in this study. The azimuth and the distance from the center define the dip direction and dip, respectively. Locations of the crosses in the full catalog plot correspond to the picked modes of anisotropy used to define the dihedral angle used for comparison in this study. . . 182

8.5 K_{cyl} plots, like those defined in Figure 8.2, for narrower temporal windows within each region. Pre-mainshock plots were made using hypocenter locations from the Hauksson et al. (2012) catalog. The time ranges correspond to the time of the first and last earthquake used for each K_{cyl} in years after the mainshock. The azimuth and the distance from the center define the dip direction and dip, respectively. White dotted lines denote dip values defined in Figure 8.4. 184

8.6 Comparison of difference between pre-mainshock stress axis and mainshock fault strike (θ) and the stress rotation ($\Delta\theta$) computed using the methods and assumptions necessary for transformation to stress used in this study. Gray contours correspond to different ratios between the stress drop and the deviatoric stress from the relationship defined by Hardebeck and Hauksson (2001). Purple and brown dashed boxes correspond to values drawn from the centroid and foreshock regions, respectively. 189

8.7 Synthetic test for possible biases in P-axis strike due to assumptions of fault alignment. Figure shows deviation of P-axis strike from the true maximum horizontal stress direction for variable proportion of misaligned faults (from the σ_1 axis). Focal mechanisms correspond to the source mechanism aligned with the stress field (labelled MF), misaligned from the stress field by a 30 degree counterclockwise rotation (labelled OF), and source mechanism aligned with the stress field but rupturing a conjugate fault (labelled CF). The x-axis refers to the relative proportion of MF and OF (with 1.0 being entirely MF sources). Different lines correspond to different proportions of the summed mechanisms that are of the CF class. The vertical black dotted line indicates the point at which there is an equal mix between OF and MF sources. The horizontal black line marks the point at which there is no difference between the P-axis strike and the true principal stress axis. The gray rectangle indicates the range possible differences between the P-axis strike and the dip direction in the foreshock zone at a point where the two values diverge substantially (0.05 years after the mainshock). 190

8.S1 The station distribution used for catalog creation in this study. Colors indicate the network code of the corresponding station. 196

8.S2 Evaluation of moment tensor uncertainties and non-double-couple components. Left column: an example extraction of strike, dip, and rake uncertainties from the posterior distribution of a single moment tensor. The posterior is shown in blue and the fitted Gaussian distribution is shown in orange. Middle column: distribution of strike, dip, and rake uncertainties for all 7,645 moment tensor solutions. We use a maximum threshold of 7.5° to identify well-constrained solutions. Right column: 2D histogram on the lune plot showing the results of moment tensor decompositions for all 4,892 well-constrained solutions. 197

8.S3 Number of earthquakes per day for the duration of the catalog produced in this study (blue) and that of Hauksson et al. (2012) (red). . . 198

8.S4 Plot of all the seismicity (A) and focal mechanisms (B) from Hauksson et al. (2012) and Yang et al. (2012) used for the pre-mainshock computations in this study. 199

8.S5 Equivalent of the plot shown in Figure 8.2 but produced using only the catalogs from Hauksson et al. (2012) and Yang et al. (2012) for both the pre-mainshock and the post-mainshock windows. 199
8.S6 Equivalent of the plot shown in Figure 8.3 but produced using only the catalogs from Yang et al. (2013) for both the pre-mainshock and the post-mainshock windows. 200
8.S7 Comparison of the pre-mainshock stress orientation analogs from the methods described in this study using both the entirety of the pre-mainshock seismicity from the Hauksson et al. (2012) seismicity catalog and the Yang et al. (2012) focal mechanism catalog. Dip direction values have been transformed to stress orientation using the dihedral angle measured in this study. 201

LIST OF TABLES

Number *Page*

3.S1 Model parameters for each of the models shown in Figure 5. Fault model is rectangular, where the burial depth is the depth of the top of the rectangle, the maximum depth is the depth of the bottom of the rectangle, the width is the lateral extent of the rectangle, and the velocity reduction is the applied velocity perturbation. All fault models are vertical. 47
7.1 Global strike-slip earthquakes considered in this study. The hypocenter locations and magnitudes are drawn from the gCMT catalog (Ekström et al., 2012). Categories of earthquakes are continental (C), oceanic interplate (E), and oceanic intraplate (A). 139
7.2 Ensembles of parameters defined in Equations 7.4-7.8 summarized for the events in this study. For each parameter, the median value and a credible interval (5th to 95th percentile) are given. 148
7.S1 Frequency bands used for the second moment inversion for each event. 157
7.S2 Summary of second moment parameter results from prior studies. . . 157
8.S1 Certain parameters and results from the normalized potency tensor summation for the spatiotemporal windows for the spatiotemporal windows of focal mechanisms described in this study. 194
8.S2 Certain parameters and results for the SATSI inversion for the spatiotemporal windows of focal mechanisms described in this study. . . 195

Chapter 1

INTRODUCTION

Earthquakes show substantial variability in rupture properties between events (Hayes, 2017; Yin et al., 2021; Bao et al., 2022). This variability is partially due to differences in the structure on and around faults. Fault zones are characterized by fault cores that localize strain and an encompassing volume of fractured rock termed a damage zone (Faulkner et al., 2010). Few generalizations beyond the existence of these key components are possible. Faults exist in varied geological settings and are modified by continued deformation due to a diversity of slip regimes. These differences map to a heterogeneity of characteristics and dimensions of fault zones. Observational studies of fault zones often employ the seismic wavefield to image subsurface fault zone structure (e.g., Share and Ben-Zion, 2018; Cochran et al., 2009; Qiu, Ben-Zion, et al., 2021). This works because fault zones perturb seismic wave propagation in a volume through fracture and the displacement of lithologies and lithological boundaries. In general, fault zone imaging techniques require observations near or on the fault zone. Because fault zones are narrow features, dense arrays are often necessary for measuring phase delays with sensitivity to fault zone structures and for identifying fault zone waves. Dense array deployments are limited in that they are often logistically challenging and temporary, meaning that datasets with sensitivity to fault zone structure for major faults are often unavailable or limited. Moreover, the logistical challenge of dense arrays means that they are often deployed with specific targets in mind, limiting available datasets for discovering unmapped low wavelength structure.

Distributed acoustic sensing (DAS) is a technique that uses phase interferometry of Rayleigh backscattered light to turn fiber optic cables into dense arrays of strainmeters (Zhan, 2020). This technique is powerful because it allows for the deployment of dense arrays over extensive distances and long time periods. This tool can also leverage existing fiber infrastructure, so-called dark fibers, which minimizes the logistical and financial costs of deployment. These dark fibers frequently cross faults. The extent of these fibers means that they span large distances of poorly studied regions that may contain unmapped but nonetheless important structural features. DAS thus has the potential to greatly increase the number of available datasets for studying known and unknown fault zones in detail. In the first part of this thesis I establish several frameworks for investigating fault structure with DAS, and I apply these frameworks to DAS arrays in the Eastern California Shear Zone to make several interesting observations on both major and minor faults.

In Chapter 2 (Atterholt et al., 2021), I introduce a framework for partitioning the seismic wavefield in DAS recordings. DAS data are noisier than traditional broadband seismic data both in terms of coherent noise and stochastic noise. Elevated coherent noise is due to the proximity of fiber to roads and elevated stochastic noise is in large part due to instrument-related effects and poor fiber-to-ground coupling. Care must be taken to partition the noise from the signal of interest. Moreover, this dense station spacing makes phases in the seismic wavefield observable that would otherwise be spatially aliased. Separating these phases from the rest of the wavefield is often necessary when using them to constrain earth structure. I use curvelets to partition the components of the seismic wavefield measured by DAS. Curvelets are an extension of directional wavelets that employs a parabolic scaling relationship that optimally represents images with discontinuities along curves. I show that these objects sparsify the DAS-measured wavefield which allows for efficient reductions in stochastic noise. I also show that the discretization of the frequency-wavenumber domain during curvelet construction is an excellent domain for separating coherent components of the wavefield from each other. I illustrate the efficacy of this framework by greatly improving a template matching catalog produced using DAS data by removing the stochastic noise and traffic noise signal from the data.

In Chapter 3 (Atterholt et al., 2022), I investigate scattered waves that are nearly ubiquitously observed in the body coda of DAS measured earthquake wavefields. These waves have been suspected to be the product of scattering by fault zones, but until this study, no work had confirmed or systematically investigated this phenomenon. Using the wavefield partitioning framework discussed in Chapter 3, I develop a backprojection framework with which the strength, location, and frequency content of these scattered waves recorded by a DAS array may be quantified. I apply this backprojection framework to a set of aftershocks from the 2019 Ridgecrest earthquake measured by a nearby DAS array and find exceptional spatial correlation between the locations of these scattered waves and the mapped faults in the area. I also observe distinct frequency contents of scattered waves associated with different faults. With synthetic modeling, I find that the frequency content of these scattered waves is related to the dimensionality of the faults that generate them, and I use this information to constrain the geometry of the faults observed near Ridgecrest. These results are consistent with a paired study that observes similar scattering behavior in ambient noise correlations.

In Chapter 4 (Atterholt et al., 2024), I use a DAS array that crosses the Garlock Fault, a major fault that bisects the Eastern California Shear Zone, to investigate its structure in unprecedented detail. The philosophy of this chapter is to investigate the fault in stages, first resolving the shallower structure and using that shallower structure as a correction term to better resolve the deeper structure. We determine a shallow velocity model across the fault zone jointly using both surface waves from an active source experiment across the fault and empirical Green's functions from ambient noise cross correlations. We find a collocated low velocity zone that is biased to the south of the mapped surface trace of the fault. We then compare this velocity model to depth integrated measurements of phase delay due to the low velocity zone from nearby earthquakes. We find that there is no phase delay signal that cannot be accounted for by the shallow velocity model, suggesting that the velocity perturbation due to the damage zone is only a shallow feature. Finally, using differential times from a variety of earthquakes, we resolve a sharp velocity contrast across the fault that may suggest preferred westward rupture directivity in the event of a future earthquake.

In Chapter 5 (Atterholt and Zhan, In Review), I use the same DAS array as in Chapter 4 to investigate Moho topography in Southern California. Investigating deep crustal structure with DAS is challenging because DAS has a high noise level at low frequencies. In this study I instead use the Moho reflected P-wave (PmP), a high frequency phase, to investigate crustal thickness. This phase has the added benefit of enabling us to make observations of crustal thickness far away from the fiber. I systematically investigate the seismic wavefields of all M2.5+ earthquakes recorded by this DAS array over the course of 2 years. I find that the large spatial extent of DAS makes PmP easily observable, because PmP can be verified using array-side moveout. I identify clear PmP arrivals for many earthquakes, and I develop a framework to pick the differential arrival time between the first arriving P wave and PmP using autocorrelation. I use these differential arrival times to invert for crustal thickness, and I make several interesting observations of low wavelength Moho topography. I find that there is a step in the Moho across the Garlock Fault, suggesting that this fault penetrates the mantle and maintains a narrow width at depth. I also observe a shallow Moho anomaly near the Coso Volcanic Field, suggesting an upper mantle source for the associated magma chamber.

The aforementioned observations provide important constraints on the structures that host earthquake ruptures, but in this thesis I also attempt to address the question of how these structures affect rupture phenomenology. To accomplish this, I search for measures of earthquake sources and associated transients that allow for the establishment of patterns in behavior. Earthquakes and earthquake locations can be characterized as distributions of slip and points in space. Distributions can be described by their moments, and lower order moments provide low dimensional approximations of the size and shape of a distribution. For the problem of earthquake slip the zeroth and first mathematical moments, corresponding to the seismic moment and the centroid position, are routinely computed (Ekström et al., 2012). The second moments describe the width and time-dependence of a slip distribution in 4 dimensions. A paradigm for computing second moments of the slip distribution has been established (Backus, 1977; McGuire et al., 2000), but is sporadically applied. This paradigm, however, is valuable because low dimensional estimates are useful quantities for establishing patterns in source distributions.

Thanks to advances in template matching (Ross, Trugman, et al., 2019), machine learning techniques (Ross, Yue, et al., 2019; Zhu and Beroza, 2018), and the increased use of cross-correlation-based relocation (Waldhauser and Ellsworth, 2000; Trugman and Shearer, 2017), seismicity catalogs are increasingly complete and precise. One challenge is using these catalogs to draw meaningful conclusions about the processes driving the distributions of events. Some help may be found from moment measures from point process theory, which can be used to described fundamental characteristics of distributions of points (Illian et al., 2007), with the second moment measure capturing how the intensity of these points varies in space (Ripley, 1976; Møller et al., 2016). In the second part of this thesis, I develop and apply frameworks for capturing the second moments of source distributions and seismicity catalogs, which offer reduced dimensionality compared to fault slip distributions and sets of hypocenter locations, to find patterns that inform a deeper understanding of what drives source behavior.

In Chapter 6 (Atterholt and Ross, 2022), I introduce a new framework for probabilistically inverting for second moments of the earthquake source distribution. The second moments of an earthquake source amount to a covariance matrix of the spatiotemporal source distribution, and thus yield estimates of the spatial extent, rupture propagation direction, and duration of the earthquake. The advance of this technique is that the inversion is Bayesian, allowing for an estimate of the posterior distribution of the second moments. This is important because determining whether earthquakes on different types of faults have parameters that are significantly different requires probabilistic estimates that accurately encode uncertainty. We solve for the second moments by fitting observed waveforms to synthetic Green's functions, and the inversion is performed using Hamiltonian Monte Carlo sampling and is constrained to produce a positive definite matrix using Cholesky decomposition. We validate this technique by inverting for second moment posteriors of a synthetic test and of the 2019 magnitude 7.1 Ridgecrest earthquake.

In Chapter 7 (Atterholt and Ross, 2023), I apply the framework developed in Chapter 6 to all large ($M_w \geq 7.5$) strike-slip earthquakes of the past 3 decades. This results in probabilistic estimates of fundamental source quantities like spatial extent, rupture directivity, and duration for 25 events from a diversity of tectonic environments. From these second moment estimates, I compute additional quantities like the source reclinearity, average moment density, and the vertical extent of the source. The intention of this study is to look for patterns that are either consistent between all events or events within particular tectonic regimes. As part of this analysis, I separate these events into groups for comparison: continental strike-slip, oceanic interplate, and oceanic intraplate (Table 7.1). I demonstrate that most events show at least some unilateral directivity, but many of the events show directivity patterns that have some mixture of unilateral and bilateral directivity. I also show that oceanic intraplate events commonly rupture depths with temperatures above the expected isothermal boundary for oceanic earthquakes, whereas oceanic interplate earthquakes do not. Finally, I show that a proposed mechanism for weakening in the oceanic crust, fossil fracture zones, are usually not aligned with large oceanic intraplate ruptures, suggesting alternative explanations for weakening in the oceanic crust are necessary to explain these events.

In Chapter 8 (Atterholt and Ross, In Prep), I investigate the evolution of fault orientations and the stress state throughout the 2019 Ridgecrest earthquake sequence. I start by developing a high resolution catalog of seismicity and moment tensors that encompasses the entire sequence. Active fault orientations are partially a function of the stress state, and evaluating how the orientations of active faults evolve may provide an observational constraint on the relationship between deformation and stress. I investigate fault orientations in narrow spatiotemporal windows using both seismicity and focal mechanisms to inform a fine scale understanding of the fault evolution throughout the sequence. Investigating fault orientations with focal mechanisms is common, but these techniques have particular biases that motivate the use of complementary measures. I use a particular second moment measure termed the cylindrical K-function to measure the modes of fault orientations throughout the earthquake sequence using the seismicity catalog. I find that this measure using seismicity informs a unique perspective on the stress state, and yields distinct estimates of the absolute differential stress and the progression of reloading due to postseismic deformation.

Chapter 2

PARTITIONING AND DENOISING THE DAS WAVEFIELD

Atterholt, J., Zhan, Z., Shen, Z., and Li, Z. (2021). A unified wavefield partitioning approach to distributed acoustic sensing. *Geophysical Journal International* 228. DOI: `10.1093/gji/ggab407`. Pp. 1410–1418.

Abstract

While Distributed Acoustic Sensing (DAS) has been demonstrated to have great potential in seismology, DAS data often have much higher levels of stochastic and coherent noise (e.g., instrument noise, traffic vibrations) than data collected by traditional seismometers. The linearly, densely spaced nature of DAS arrays presents a suite of opportunities for more innovative processing techniques that can be used to address this issue. One way to take advantage of DAS's array architecture is through the use of curvelets. Curvelets have a non-uniform scaling property that makes them an excellent tool for representing images with discontinuities along piecewise, twice continuously differentiable curves. This anisotropic scaling property makes curvelets an ideal processing tool for DAS data, for which the measured wavefield can be represented as an image composed of curved features. Here we use the curvelet frame as a tool for the manipulation of DAS signal, and we demonstrate how this manipulation can improve our ability to identify important features in DAS datasets. We use the curvelet representation to partition the measured wavefield using DAS data collected near Ridgecrest, CA following the 2019 $M_w 7.1$ Ridgecrest earthquake. Here we isolate the earthquake induced wavefield from coherent and stochastic noise using the curvelet frame in an effort to improve the results of template matching of the Ridgecrest aftershock sequence. We show that our wavefield partitioning technique facilitates the identification of over 30% more aftershocks and greatly reduces the magnitude of diurnal depressions in the aftershock catalog due to cultural noise.

2.1 Introduction

Distributed Acoustic Sensing (DAS) is a new tool in seismology that repurposes fiber optic cables as arrays of densely spaced strainmeters (see Hartog (2017) for a review). DAS employs a laser interrogator unit, which sends short laser pulses through optical fibers and performs interferometry to measure phase shifts in the

Rayleigh-backscattered light. These phase shifts are quasi-linearly proportional to strain or strain-rate in the fiber. This strain is averaged over a "gauge length" and sampled at discrete intervals along the fiber that constitute the so-called channels of the array. Laser pulses are sent at regular intervals to measure the temporal dependence of strain in the fiber.

DAS has the potential to transform seismology because of its dense spatial sampling and its capacity to transform in situ fibers into seismic arrays (see Zhan (2020) for a review). DAS functions as a large-N array of instruments, and because of this high spatial sampling, DAS may allow seismologists to probe the subsurface at resolutions that have historically been limited to expensive exploration experiments (Dou et al., 2017; Ajo-Franklin et al., 2019). Preexisting fiber optic cables in place for telecommunications can be easily re-purposed as DAS arrays. DAS's capacity to use pre-existing fiber allows seismologists to both deploy seismic arrays faster and extend seismology, particularly dense array seismology, to logistically challenging locations of immense societal and scientific interest (Lindsey et al., 2019; Sladen et al., 2019; Spica, Perton, et al., 2020; Lellouch et al., 2019; Booth et al., 2020).

But, DAS remains an emerging technology, and there still exist fundamental challenges in the acquisition and analysis of DAS data. One such challenge is noise, both stochastic and coherent. Stochastic noise in DAS signals is likely dominated by instrumental deficiencies like sampling error and phase noise and is bounded by the Crámer-Rao Lower Bound (Costa et al., 2019). Coherent noise can be defined as the coherent components of the DAS wavefield that are not interesting to the end user. In many cases, particularly for seismologists, traffic noise is a persistent source of coherent noise. Traffic noise is especially problematic for DAS, because pre-existing fiber optic cables are often placed along major roads. Both stochastic and coherent noise are problematic, because they can either mask or obscure relevant signal. This obfuscation is exemplified in Figure 2.1b, which shows a case in which cultural noise masks much of the signal generated by a local earthquake. Figure 2.1b also shows that even for a relatively quiet station along the DAS array, stochastic noise is much stronger in the DAS station than in a nearby broadband station. DAS stochastic noise is in large part instrument related, and the noise level in DAS will likely vary between generations and decrease as technology improves. But, since DAS signal degrades with distance, stochastic noise may persist as a challenge at the far end of the DAS array for many years to come.

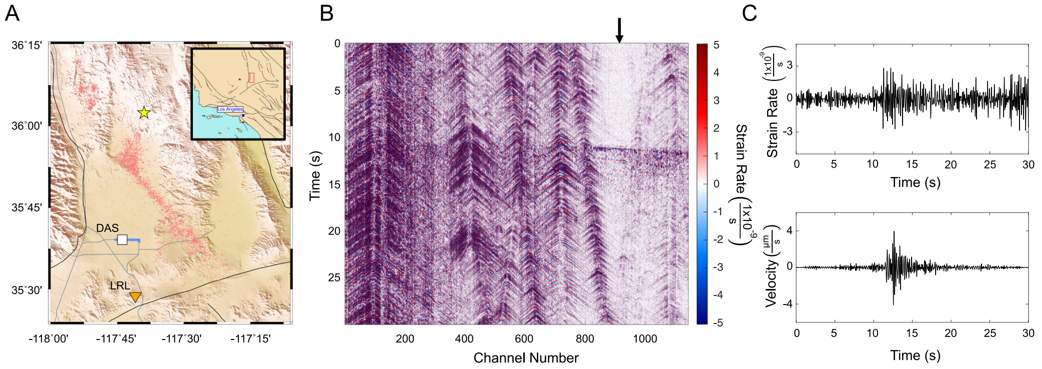

Figure 2.1: Geographic setting and waveform examples. A. Map showing the geographic setting for the data segments in this figure. The yellow star indicates the location of the M_l 1.79 earthquake recorded by the Ridgecrest array and the LRL station at distances of 44 km (specifically the station highlighted in panel C) and 62 km respectively. The blue line indicates the location of the DAS array that recorded the time series shown in the middle image of this figure. The white box indicates the approximate location of the DAS station whose individual station data is shown in this figure. The orange triangle shows the location of the broadband station (LRL) whose station data is shown in this figure. The black and gray lines delineate faults and roads respectively. The light-red dots indicate the locations of aftershocks used as templates in this study. The inset gives regional context. B. Full DAS record section at the time of a regional earthquake, the location of which is shown in the map in A. The black arrow marks the location of the DAS channel given as an example in C (channel 899). C. Comparison of station data from a single DAS station (top) with the east-west component of station data from the nearby LRL broadband station (bottom). The DAS stations in panels B and C and the broadband station in panel C are band-pass filtered from 2-8 Hz using a Butterworth filter.

Previous efforts to remove stochastic noise from DAS data have been varied and proposed both outside of and within seismology. Many of these efforts have successfully applied time-space analysis techniques from signal processing such as wavelet transforms (Qin et al., 2012), 2D edge detection (Zhu et al., 2013), 2D bilateral filters (He et al., 2017), empirical mode decomposition (Qin et al., 2017b), and principal component analysis (Ibrahim et al., 2020). In particular, Qin et al. (2017a) proposed an approach to remove random noise in the curvelet domain. They recognized that the curvelet domain, much like the wavelet domain, sparsely represents DAS data, and they perform thresholding of curvelet coefficients below a certain magnitude to remove random noise. We build on this approach in this study. More recently, Ende et al. (2021) proposed a deep learning approach for removing incoherent signal with a focus on DAS data.

There has been less discussion of removing coherent noise from DAS, partly because coherent noise is not well-defined. The difference between coherent noise and the signal of interest depends on how we define coherent noise and what the signal of interest is. Usually, signals of different types can be distinguished by one or more their physical characteristics. For the seismic wavefield, signals can be distinguished using the various velocity attributes of seismic waves. We can exploit this quality by transforming our DAS data from the spatiotemporal domain to the frequency-wavenumber domain, where our signals are localized by velocity. Williams et al. (2019) illustrates this point by localizing seismic waves from ocean waves recorded by a submarine DAS fiber using the frequency-wavenumber domain. It follows that if the coherent noise is localized by velocity, then muting the velocity range in the frequency-wavenumber domain associated with the coherent noise removes the coherent noise from the signal. This method of denoising has been used in exploration seismology for decades (Embree et al., 1963) and has been applied as a preprocessing step to DAS data (Fang et al., 2020). Though frequency-wavenumber domain filtering is commonly used, other tools, such as the continuous wavelet transform, have been used to diminish coherent noise in DAS data as well (Martin et al., 2018).

With DAS we encounter stochastic noise and coherent noise together. We argue that a simple, unified approach to noise reduction in DAS would be useful. Moreover, given the large volumes of DAS data which seismologists are prone to process, this filtering approach must be scalable such that it can be applied to terabytes of data in a reasonable amount of time. In this paper, we propose combining some of the principles described in this introduction into a unified approach to isolate a signal of interest in seismological data by wavefield partitioning entirely under the curvelet transform. We then illustrate the efficacy of this approach by applying it as a pre-processing step for template matching applied to a subset of DAS data recording the $M_w 7.1$ Ridgecrest earthquake aftershock sequence.

2.2 Methodology

Curvelets

Curvelets were described in a continuous setting (Candés and Donoho, 2004) as an almost optimal representation of images with discontinuities along twice continuously differentiable (C^2) curves. Candès et al. (2006) developed the Fast Discrete Curvelet Transform (FDCT), making curvelets easily applicable in image processing. This transform has since been used widely in a number of fields (see Ma

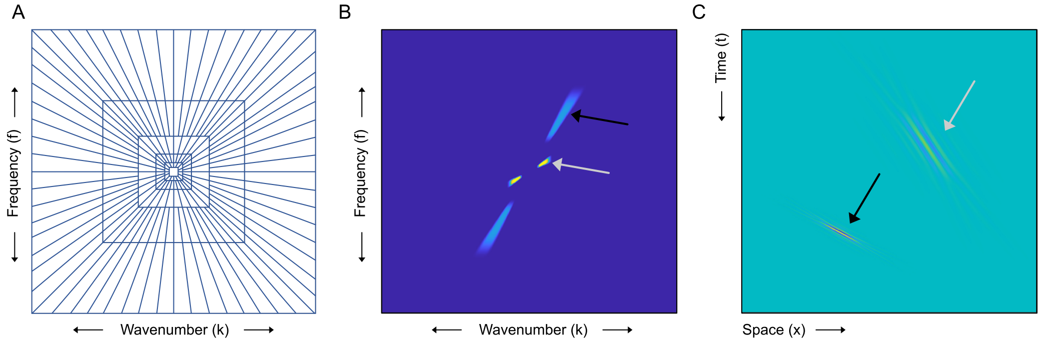

Figure 2.2: Curvelet polar tiling framework. A. Schematic illustration of the polar tiling used to construct curvelet coefficients. The wedges delineate the compartmentalization of the frequency-wavenumber domain. B. Plot of select curvelets in both the frequency-wavenumber domain. C. Plot of the same curvelets as in B in the spatiotemporal domain. Colors of arrows correspond to equivalent curvelets between B and C.

and Plonka (2010) for examples). Curvelets have been evaluated by how well they represent a 2D object, F, that has a discontinuity along a curve, but is otherwise smooth, using an m term approximation of the object, F_m. It has been shown that for such objects the mean squared error of the curvelet frame representation decays with $m^{-2}[log(m)]^3$ whereas the mean squared error of the wavelet representation decays with m^{-1} (Candés and Donoho, 2004). We claim that DAS data sections measuring the seismic wavefield can be approximated as smooth images with discontinuities along C^2 curves, because DAS data are marked by periods of quiescence (smoothness) interrupted by wavefronts (curvature). If this is a good approximation, the curvelet frame is the best available non-adaptive sparse representation of DAS data. In this study, we perform denoising of DAS data through applications of the FDCT on DAS record sections of finite length in time and space (e.g., Figure 2.1b).

Following closely after Candès et al. (2006), curvelets are constructed by first creating a polar tiling in the frequency-wavenumber domain. Specifically, we take the 2-dimensional Fourier Transform of our function and compartmentalize the resultant function using special tiling geometry. Letting (ω, k) be a coordinate in the frequency-wavenumber domain and letting $r = \sqrt{\omega^2 + k^2}$ and $\theta = arctan(\frac{\omega}{k})$, we can construct the polar tiling using windowing functions:

$$U_j(r,\theta) = 2^{-\frac{3j}{4}} W(2^{-j}r) V(\frac{2^{\lfloor \frac{j}{2} \rfloor}\theta}{2\pi}) \tag{2.1}$$

where $U_j(r,\theta)$ is a polar wedge corresponding to radius r, orientation θ, and scale integer j. Here, W is a window function along the radius and V is a window function along the orientation. Importantly, the scale, given by 2^{-j}, is inversely related to the scale integer term. Notice, then, that the radius is dilated by 2 for each jump in scale, and the number of wedges increases by a factor of 2 for every 2 jumps in scale. This prescribes a non-uniform scaling that results in curvelets becoming more needle-like with finer scales. The spacing of r and θ are thus dictated by the number of scales and the number of wedges at the coarsest scale. To be clear, tiles further away from the origin of the frequency-wavenumber domain correspond to smaller and more needle-like curvelets in the spatiotemporal domain. This relationship is illustrated in Figure 2.2b. The intuitive motivation for this non-uniform scaling rests in the observation that smooth curves appear more linear when viewed from up close, and thus needle-like objects can capture the sharp edges of smooth curves if the needles are sufficiently small.

Now, a so-called "mother" curvelet, $\phi_j(x,t)$, with scale integer j and coordinate (x,t) in the space-time domain, is defined by taking the inverse Fourier transform of the polar wedge:

$$\phi_j(x,t) = \mathcal{F}^{-1}[U_j(\omega,k)] \tag{2.2}$$

where $U_j(\omega,k)$ is the wedge described in Equation 2.1 in Cartesian coordinates in the frequency-wavenumber domain. This term, $\phi_j(x,t)$, is called the mother curvelet because all curvelets of scale 2^{-j} can be defined as some rotation and translation of $\phi_j(x,t)$. Indeed, with a sequence of rotation angles defined as $\theta_l = 2\pi \cdot 2^{\lfloor -\frac{j}{2} \rfloor} \cdot l$ where $l = 0,1,2,...$ satisfying $\theta_l \in [0,2\pi)$ and translation parameters defined as $k = (k_1,k_2)$, all curvelets can be defined as:

$$\phi_{j,l,k}(x,t) = \phi_j(x,t) \cdot R_{\theta_l} \cdot ((x,t) - (x_{k_1},t_{k_2})^{(j,l)}) \tag{2.3}$$

where R_{θ_l} is a standard rotation matrix and $(x_{k_1},t_{k_2})^{(j,l)}$ is the position prescribed by $R^{-1}_{\theta_l}(k_1 \cdot 2^{-j}, k_2 \cdot 2^{-j})$. Finally, the curvelet coefficients, the values of which we will use in the subsequent denoising procedure, are defined using the scalar product of the curvelets with an arbitrary function $f \in L^2(\mathbf{R^2})$:

$$\begin{aligned} c_{j,k,l} = \langle f, \phi_{j,k,l} \rangle &= \iint f(x,t) \cdot \overline{\phi_{j,k,l}(x,t)} dxdt \\ &= \frac{1}{(2\pi)^2} \iint f(\omega,k) \cdot \overline{\phi_{j,k,l}(\omega,k)} d\omega dk \end{aligned} \tag{2.4}$$

where $\overline{\phi_{j,k,l}}$ is the conjugate of $\phi_{j,k,l}$.

In words, these curvelets form a set of basis functions that, when weighted by curvelet coefficients, can represent an arbitrary smooth function like the seismic wavefield in space and time. But, the antecedent equations describe the curvelet construction for the continuous case, and seismic data are collected at discrete intervals. So, in practice, a few modifications to this methodology are necessary to make this continuous transformation applicable to discrete data. One modification is that the polar wedges, defined in Equation 2.1, are necessarily computed as so-called Cartesian shears. An illustration of the compartmentalization of the frequency-wavenumber domain into Cartesian shears is given in Figure 2.2a. The construction of these shears requires thoughtful considerations of geometry and windowing that are given a more complete treatment in Ma and Plonka (2010). In short, these windows are real, positive, smooth functions that localize the frequency-wavenumber domain into a tiling of trapezoidal shears and allow the resultant curvelets to form a tight frame. Additionally, these shears are not rectangular, and so the necessary inverse Fast Fourier Transform (FFT) for the discrete case is impossible to compute. To get around this problem, the FDCT employs a "wrapping" operation; that is, the curvelets are duplicated many times and situated adjacent to each other over the frequency-wavenumber domain. Then, the inverse FFT is taken on a rectangular section centered on the origin in this domain (see section 3.3 of Candés et al. (2006) for details). Curvelets of different scales and orientations for the discrete case are shown in both the frequency-wavenumber and spatiotemporal domain in Figure 2.2b. As mentioned previously, the spacing of r and θ are determined by the number of scales and the number of tiles at the coarsest scale. These parameters are user-defined in the FDCT according to the data matrix sampling and size.

Stochastic Noise Removal

The curvelet frame has previously been used to remove random noise from seismograms collected using traditional seismic arrays and has even been extended to nonuniformly sampled arrays (Hennenfent and Herrmann, 2006). Denoising with curvelets is often accomplished by producing white noise images with some assumed variance, performing FDCT transforms on these images to establish scale-dependent thresholds, and applying either hard or soft thresholding using these thresholds (Jean-Luc Starck et al., 2002). This method is imperfect because it requires an estimation of the variance and assumes that the noise is white.

With DAS seismic data, we benefit from having continuously recorded data over long periods of time. In these long time series, there are usually time windows in which there is minimal coherent signal. These time periods can be used as benchmarks for the level of incoherent noise throughout the time series. So, in this study, we chose wedge-dependent denoising thresholds using the distribution of curvelet coefficient amplitudes in quiet sections of the time series. Implicit in this selection of thresholds is the assumption that the stochastic noise levels are independent of time. That is, we assume that the noise in a quiet time segment will be representative of the noise throughout the data. This is not always true, as we expect the noise in DAS to fluctuate with time according to environmental factors like temperature variability. However, we still favor a uniform application of thresholding, because nonuniform applications are generally less stable and can produce artifacts like step discontinuities in the noise floor of denoised data. Because we intend to apply this technique to more data than can be visually scrutinized, we consider these potential issues to be unacceptable in this workflow. We also choose thresholds that are not dependent on translational parameter k. This means that we ignore any spatial and temporal variability of the noise floor *within* the quiet time segment. This is a reasonable assumption because we consider the noise floor to be largely reflective of the DAS interrogation unit, which is shared by all channels in the array, and because including a temporal variability within each time segment would suggest that the noise floor is periodic according to the arbitrarily chosen time segment duration.

When choosing a thresholding technique, one often chooses between hard thresholding and soft thresholding. Here, we chose soft thresholding, because it minimizes noise that barely exceeds the threshold and prevents the generation of artifacts that result from preserving high amplitude noise curvelet coefficients and zeroing their neighbors. Soft thresholding is defined as:

$$c_{j,k,l} = \begin{cases} 0 & \text{if } |c_{j,k,l}| < \tau_{j,l} \\ c_{j,k,l} - sign[c_{j,k,l}] \cdot \tau_{j,l} & \text{if } |c_{j,k,l}| > \tau_{j,l} \end{cases} \tag{2.5}$$

where $c_{j,k,l}$ is a given curvelet coefficient and $\tau_{j,l}$ is its associated threshold. We show an example of applying soft thresholding using empirical thresholds defined using a pure stochastic noise window in Figure 2.3. Soft thresholding systematically diminishes the observed amplitude of the seismic wavefield. This is acceptable in the coming example, but for amplitude dependent analyses, hard thresholding may be preferable.

Coherent Noise Removal

As described earlier, coherent noise can often be localized from interesting signal using velocity contrasts in the frequency-wavenumber domain. The curvelet frame, by construction, creates a polar tiling in the frequency-wavenumber domain that

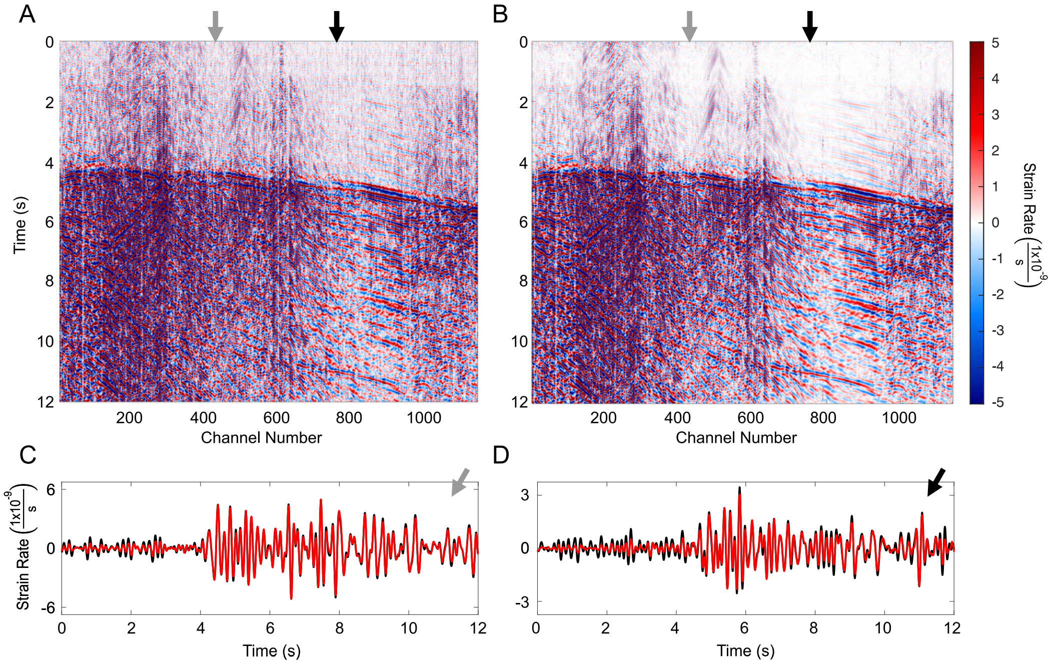

Figure 2.3: Illustration of stochastic denoising using soft-thresholding in the curvelet domain. Thresholds for this example were determined empirically using a window with little coherent signal from the same data set. A. Unfiltered record sections for the entire DAS array. B. Curvelet filtered record sections for the entire DAS array. C. The individual DAS station data from the record sections in A (black) and B (red) for the DAS station marked by the gray (channel 422) arrows. D. The individual DAS station data from the record sections in A (black) and B (red) for the DAS station marked by the black (channel 780) arrows.

finely compartmentalizes the wavefield by velocity and scale. Naturally, then, we can exploit this compartmentalization to filter out coherent noise under the curvelet transform. This can be done by simply muting the wedges under the curvelet transform that contain the part of the wavefield associated with the coherent noise. The curvelet transform has been used in array seismology for similar purposes in the past, namely to improve measurements of *SS* precursors by eliminating interfering phases (Yu et al., 2017) and to help isolate the scattered wavefield from teleseismic P waves (Zhang and Langston, 2020).

We can justify our decision to perform velocity filtering under the curvelet transform in a few ways. Firstly, it is convenient to perform coherent noise filtering under the same transform with which we perform stochastic noise filtering. Additionally, this filtering procedure is straightforward and useful for experimentation. The Cartesian shear framework provides a convenient basis with which to identify and remove wavefield components in velocity-scale space. Yet another reason is that the windowing functions used by the FDCT employ tapers that are effective at removing large artifacts produced by the creation of discontinuities in the frequency-wavenumber domain. We show this in Figure 2.4, where we evaluate the removal of coherent noise using real data. These tapers are also highly localized in the angular direction, yielding a precise separation of velocities.

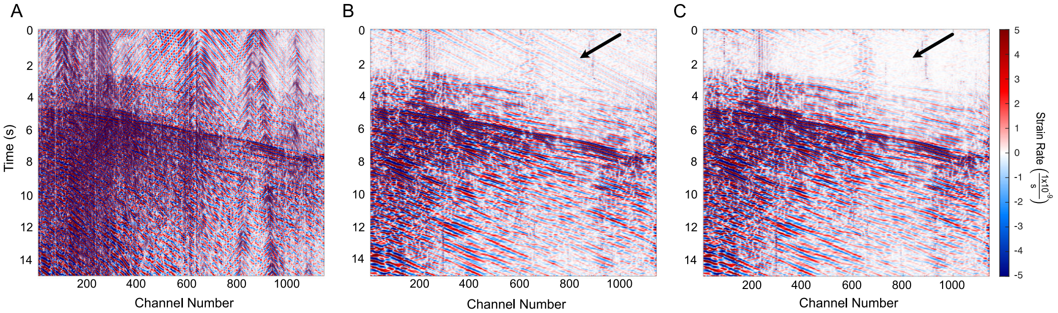

Figure 2.4: Illustration of coherent denoising using the polar-tiling framework of the curvelet construction. A. Pseudo-synthetic noisy window made by superimposing a record section with high cultural noise onto a record section with an earthquake. B. Time series in which velocities in the range 0-1000 m/s were removed using an untapered FK-filter. C. Time series in which velocities in the range 0-1000 m/s were removed using our curvelet windowing technique. The black arrows point to a region of prominent filter-generated artifacts.

Unified Approach

Since the methods described for removing stochastic noise and coherent noise are both performed under the same transform, we can remove both of these noise sources in the same step. This procedure simply involves transforming from the spatiotemporal domain to the curvelet domain under the FDCT, performing thresholding using thresholds determined by a noise window to remove stochastic noise, muting the curvelet wedges that are associated with unwanted signal, and finally performing the inverse FDCT to return to the spatiotemporal domain. If the threshold values are fixed, then the order of the second and third steps does not matter. Performing these procedures together simplifies preprocessing and lowers computational costs by avoiding additional transforms. The simplicity argument for this approach should not be undervalued. Rather than requiring a set of arbitrary signal processing decisions, our methodology effectively offers a "dial" to turn down stochastic noise and a "switch" to turn off coherent signal by velocity and scale. The computational cost reduction may vary, but if one were to perform stochastic noise filtering under the curvelet transform and coherent noise filtering under a second transform, the cost saved would amount to the cost of the forward and inverse computations of the second transform multiplied by the number of spatiotemporal windows being filtered.

2.3 Application

Data

Following the $M_w 7.1$ Ridgecrest earthquake on July 5, 2019, an OptaSense ODH3 interrogator unit was used to deploy a DAS array in the town of Ridgecrest, CA near the epicenter of the event. This array samples at 250 Hz and has 1250 channels with a channel spacing of 8 m for an overall cable length of 10 km. The array continuously recorded much of the aftershock sequence. We choose this array both because it has recorded many earthquakes, and because it is linear. The linearity of the array ensures that the apparent velocities of incoming waves are mostly constant across the entire array. A linear array geometry is not strictly necessary to perform the curvelet filtering approach outlined above, but the linear geometry ensures that the earthquake wavefield is more localized in the frequency-wavenumber domain. The location and aperture of the DAS array is shown in Figure 2.1a.

Template Matching

In order to demonstrate the efficacy of our filtering approach, we apply it to the DAS data prior to a template matching procedure to better illuminate small earthquakes masked by noise. Template matching is a technique that correlates known events, known as templates, with continuous time series to detect previously unknown events that are similar to the templates (Gibbons and Ringdal, 2006). Li and Zhan (2018) showed that template matching could be successfully applied to DAS data. This technique has been modified to perform template matching using the Ridgecrest DAS array to supplement the Southern California Seismic Network's (SCSN) catalog of Ridgecrest earthquake aftershocks (Li et al., 2021). Though this catalog is successful in improving the number of cataloged events, the template matching catalog contains diurnal depressions in the number of events due to cultural noise. Additionally, the completeness of this catalog may be limited by the noise floor of the Ridgecrest DAS array. We seek to show that these limitations can be mitigated by applying our unified curvelet filtering framework to Ridgecrest DAS array data.

Our filtering framework includes a few preprocessing steps. We first remove the stations of the array that are either coiled or too close to the interrogator unit. We then segment these array data into 60-second time windows recorded at the original sampling rate by the 1142 DAS stations that remain after the station removal step. The temporal and spatial sampling rates dictate the velocities associated with Cartesian shears under the curvelet domain. The number of samples along the time and space axes control the frequency and wavenumber resolution, respectively, which in turn dictates the precision of the velocity filtering. We segment these array data to ensure that each allocation of memory does not exceed a few gigabytes, but 60-second segments are long enough so as to ensure we have sufficient frequency resolution for velocity filtering. Segmenting these data also allows us to filter in parallel. We applied a Tukey window along the time axis to minimize artifacts due to discontinuities at the start and end of each segment. Time segments were staggered such that we could clip the tapered portions of the time segments when constructing the final time series. For each time segment, we applied a median filter to remove a source of optical noise, not handled by the curvelet filter, that results in random, high-strain spikes in the data (Bakku, 2015). Failure to remove these spikes before filtering results in the creation of star-like artifacts after filtering. Though median filtering mitigates this issue, these artifacts are often unavoidable. An adaptive spectrum screening algorithm can potentially help better separate earthquake signals from coherent noise, but for consistency with the original template matching framework, we band-pass filter each station between 2-8 Hz (Li et al., 2021).

For each time segment, we applied our unified curvelet filter procedure described above. For the stochastic noise removal, we used a representative noise window to establish thresholds for the entire time series. We opted to use a single representative noise window rather than multiple noise windows throughout the time series, because using multiple noise windows produces the undesirable side-effect of discontinuities in the noise floor. After applying these thresholds, we muted wedges associated with apparent velocities between 0-1000 m/s in both the east-going and west-going directions at scales corresponding to the seismic wavefield. We then took the inverse FDCT and removed the tapered portions of the time segment. We then placed the filtered time segment in its appropriate position in the final, filtered time series.

The templates used in the template matching algorithm were taken directly from the data. So, once we had filtered the data, we had also filtered the corresponding templates. We found template candidates using the SCSN catalog and determined which template candidates to keep using a criterion that requires at least a set number of stations to exceed a fixed signal-to-noise ratio (SNR). Because the curvelet denoising improves the SNR of the data, the curvelet filtered data produced many more templates that met our criteria. To be fair, we only used templates that the filtered and unfiltered data had in common. We then performed template matching on both our filtered and unfiltered time series. Processing 192 hours of DAS data (July 14-21, 2019) using our intentionally redundant methodology on 24 CPUs took just over 19 hours. Both the catalog produced before filtering and the catalog produced after filtering are plotted, by number of events per hour, in Figure 2.5. The template matching catalog corresponding to the unfiltered data contains 20,935 events while the template matching catalog corresponding to the filtered data contains 28,044 events. There exists a diurnal pattern in the difference between the filtered and unfiltered catalogs, with the difference reaching peaks during the daytime when traffic noise is highest. In particular, we see a 56% increase in number of events during the daytime (7 a.m. to 7 p.m.) and a 21% increase in number of events during the nighttime (7 p.m. to 7 a.m.).

To confidently identify the cause of this diurnal effect, we applied this template matching procedure to the same DAS data filtered using only the coherent noise filter and only the stochastic noise filter. These hourly catalogs are shown in Figure 2.S1. This diurnal pattern in the difference between the filtered and unfiltered catalogs is amplified when only the coherent noise is removed while this diurnal pattern is nonexistent when only the stochastic noise is filtered. This observation suggests that the improvement made by the coherent velocity filter is largely due to the removal of traffic-generated surface waves. Interestingly, performing only the stochastic noise filtering results in a catalog with slightly fewer events (19,826 events) than the catalog produced using unfiltered data (20,935 events); incongruously, performing the stochastic and coherent noise filtering together results in a catalog with many more events (28,044 events) than the catalog produced using data filtered using only the coherent noise filtering (25,731 events). This observation may be explained by noting that the stochastic noise filter will amplify both the earthquake waveforms and the coherent noise (e.g., traffic noise), and so the stochastic noise filtering in the presence of a large amount of coherent noise may be detrimental to the template matching procedure and stochastic noise filtering in the presence of little coherent noise is beneficial to the template matching procedure.

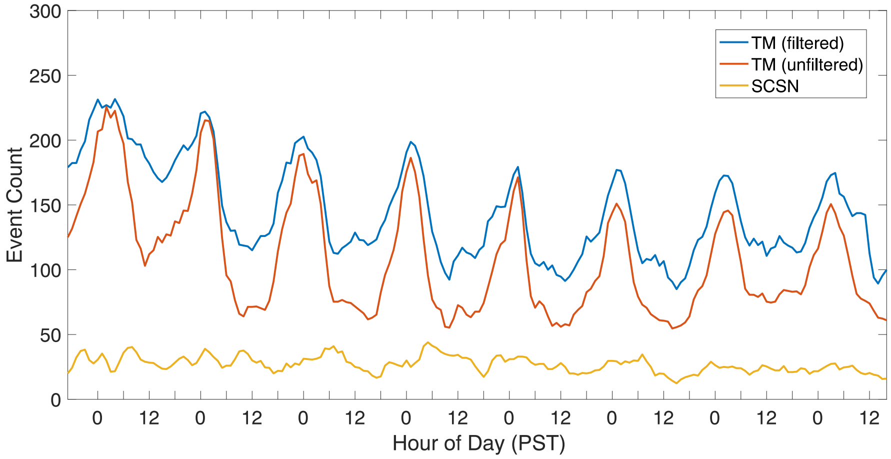

Figure 2.5: Hourly (PST) event counts of the catalogs created using template matching. A 3-hour moving average filter was applied to each of the time series. The yellow line shows the hourly counts for the catalog of templates made using the SCSN catalog. The red line shows the hourly counts for the catalog created using template matching (TM) on the unfiltered data. The blue line shows the hourly counts for the catalog created using template matching (TM) on the curvelet filtered data.

2.4 Discussion

Clearly, the curvelet filtering improved the performance of the template matching algorithm. One noteworthy feature of Figure 2.5 is the reduction in the magnitude of the diurnal depressions in the aftershock catalog. This is largely due to the removal of the cultural noise (mostly surface waves generated by vehicles), which is far more prevalent during the daytime, by the coherent noise filter. Because the apparent velocities of the earthquake-generated surface waves also often fall in our filtered velocity range, earthquake signals in our filtered time series are often degenerate. We argue this loss of information is well compensated by the remarkable illumination of the earthquake-generated body waves. As is clear in Figure 2.5, at no point did we see a decrease in the number of cataloged events due to filtering, suggesting that the information recovered by filtering outweighed the information lost. Given that DAS is more sensitive to the low velocity wavefield, earthquake-generated surface waves may prove useful in the detection of earthquakes in the future (Lior et al., 2021). However, traffic noise is also composed of largely low velocity surface waves and is thus especially prominent in DAS data, making the removal of this noise essential.

To evaluate the amount of overlap between catalogs, we compute the proportion of events in the original template matching catalog that were also detected in the new template matching catalog made using filtered data. Because the templates are altered in the filtering process, the same event may be matched with different templates between catalogs. This possibility adds significant uncertainty to any measure of overlap between catalogs. We choose to measure this overlap using the metric that if for any given event in the original catalog, there is a corresponding event in the new catalog with an origin time within 2.5 seconds of that of the given event, then the given event is represented in both catalogs. By this metric, 73% of the events in the original catalog were carried over to the new catalog. Indeed, this metric is conservative; if we extend the time window about the origin to 5 seconds, then we find that 83% of the events in the original catalog are represented in the new catalog. Additionally, the fact that some events are not represented in the new catalog does not necessarily represent a failure of the filtering methodology, but could be indicative of a success. Cultural noise is a consistent source of coherent signal that produces observables that are frequently almost replicated at different times. This noise can potentially produce false detections in the original catalog that will not be present in the new catalog, for which cultural noise has been largely removed. This removal of false detections is partially evidenced by the diurnal pattern shown in the plot of the percent of events retained between catalogs by hour shown in Figure 2.S2, which suggests that the percentage of events retained between catalogs is lowest during a large portion of the population's morning commute. Further evidence that the detections lost from the original catalog to the new catalog are false detections is given by the observation that most of these detections were made using noisy templates as opposed to quiet templates. These noisy templates thus provide a substantial coherent noise wavefield that can produce cross-correlation peaks with the coherent noise in the data. An example of one of these suspected false detections is shown in Figure 2.S3.

Our results summarized in Figures 2.5 and 2.S1 suggest that, in combination with the coherent noise filtering, the stochastic noise filtering produced a considerable improvement in the number of cataloged events. This improvement likely results from the fact that for a template matching algorithm to label a detection, the cross-correlation between the template and the time series must produce a peak that exceeds some significance threshold. It is easier, then, for an event's correlation to exceed a significance threshold when the baseline noise is lower. Additionally, in the absence of coherent noise filtering, the stochastic noise filtering produced a slight decrease in the number of cataloged events. This decrease may potentially be explained by the fact that the stochastic noise filtering increases the signal to noise ratio of all types of coherent signal, thus increasing the prominence of coherent noise in the data and making event detection more challenging. We suggest that this explanation for the loss of detections is more plausible than an explanation of simple over-filtering, because there exists a diurnal pattern in the loss of detections (we see a 9% decrease in the number of events between 7 a.m. and 7 p.m. and only a 3% decrease in detections between 7 p.m. and 7 a.m.). This pattern runs counter to our expectation for over-filtering; for which we would expect over-filtering to present more of a problem during the nighttime, because the detection threshold for template matching is much lower when coherent noise is lower.

Though this curvelet filtering methodology performs very well for this problem and is easily generalizable to other problems, it has some limitations. Many of these limitations are a result of the imperfect nature of DAS as a measuring instrument. Indeed, curvelets are exceptional at representing smooth discontinuities, but not rough discontinuities. In reality, DAS data exhibit many rough discontinuities such as random spikes of high strain that act as localized discontinuities. We also note that, for high strain events like earthquakes and large vehicles driving near the fiber, strain rates are so high they produce DAS phase errors that results in additional discontinuities. Optical fading, a spatially random effect that results from the destructive interference of scatterer-generated electric fields (Zhou et al., 2013), produces muted stations which, when near unmuted stations, act as discontinuities. A similar effect can be produced by variability in the degree of coupling between the DAS cable and the ground. These discontinuities are not well represented by curvelets and produce artifacts of varying severity under our filtering procedure.

We also note the importance of array geometry in the practicability of our methodology. The degree of localization of velocity dictates whether or not two signals can be separated on the basis of velocity. For example, a plane wave recorded by a complex DAS array geometry may be spread over a large range of velocities because of a high variability in the angle of incidence at different stations along the array. Traffic-generated surface waves are conducive to this technique, however, because DAS cables often run parallel to roads. In this case, most of the traffic-generated surface wave signal is recorded at near true velocity. This is the case in this study, but with a not-insignificant caveat. Because the cable and the road are separated by a small distance, for a short section of the array directly next to passing vehicles, traffic-generated surface waves are recorded with very high velocities. This results in systematic imperfections in the coherent noise removal in this study.

In this study, we apply stochastic and coherent noise removal together to illustrate a unified approach to noise removal that is convenient, scalable, and effective. However, there is no hinderence to applying either the stochastic or coherent noise filtering independently. Applying the stochastic noise filtering by itself is easily justifiable, because the curvelet representation is, to our knowledge, the best available, non-adaptive sparse representation of objects with smooth discontinuities. Applying the coherent noise filtering by itself is effective, but not more effective than traditional frequency-wavenumber filters with specialized tapers. The choice to perform only coherent noise filtering under the curvelet transform may be made out of convenience, but the flexibility of this filter is limited by the Cartesian coronae framework. Performing only coherent noise filtering using the curvelet domain can be made considerably faster by creating a frequency-wavenumber mask under the curvelet transform. Such a mask can be made by performing coherent noise filtering on a 2D delta function under the curvelet transform.

2.5 Conclusions

Here we proposed a unified wavefield partitioning approach for DAS data in a seismological context using curvelets. One component of our technique involves the application of thresholding to curvelet coefficients using data-specific thresholds under the curvelet transformation. Another component of our technique requires the implemention of scale dependent velocity filtering under the curvelet transform. By using these partitioning techniques together under the curvelet transform, we demonstrated that stochastic and coherent noise can be removed in a single step. We showed that this approach is effective and scalable by applying this filtering technique to 8 days of DAS data collected following the $M_w 7.1$ Ridgecrest earthquake. With a simple application of our filtering technique, we greatly improved a template matching-generated earthquake catalog, increasing the number of detected events by over 30 percent and reducing the magnitude of diurnal depressions in the catalog due to cultural noise.

With its high spatial sampling and logistical advantages, DAS presents numerous opportunities to advance the field of seismology. But, more so than for other seismic instrumentation, noise in DAS will persist in limiting how well we can seize these opportunities. In the coming years, we may expect improvements in DAS instrumentation to lower the instrument noise floor, but we should continue searching for preprocessing steps that help us get the most out of our data. Here we have outlined a methodology to remove noise sources from DAS data in a seismological context using a basis that we think is particularly well suited for DAS data. But our approach is non-adaptive, and we might expect to see significant improvements in coherent noise removal from adaptive techniques targeted to seismological applications. In particular, learning the structure of DAS data, using techniques like machine learning, will likely allow for more precise coherent noise removal. We see the framework of our methodology and the curvelet basis as potentially useful components of more effective adaptive filtering techniques that may be developed in the foreseeable future.

Supplementary Materials

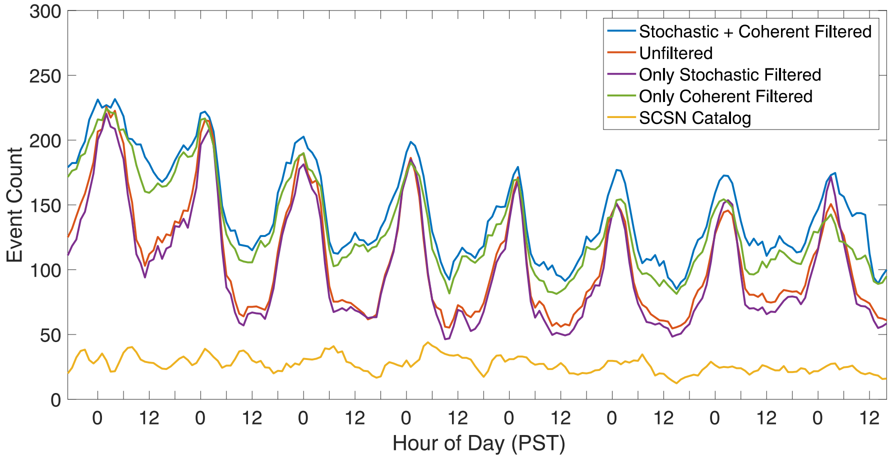

Figure 2.S1: Hourly (PST) event counts of the catalogs created using template matching. A 3-hour moving average filter was applied to each of the time series. The yellow line shows the hourly counts for the catalog of templates made using the SCSN catalog. The red line shows the hourly counts for the catalog created using the unfiltered data. The green line shows the hourly counts for the catalog created using data filtered using only the coherent noise filter. The purple line shows the hourly counts for the catalog created using data filtered using only the stochastic noise filter. The blue line shows the hourly counts for the catalog created using data filtered with both the coherent noise and stochastic noise filters.

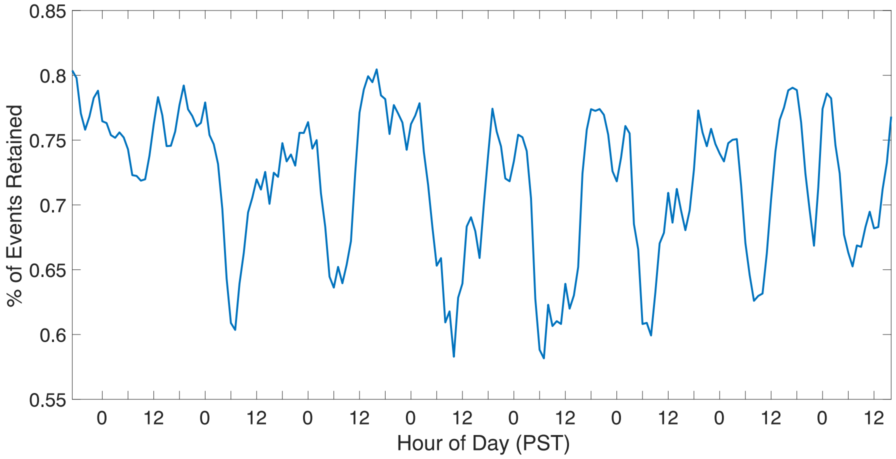

Figure 2.S2: Hourly (PST) measure of the percentage of events from the catalog produced using unfiltered data retained in the catalog produced using data filtered for both stochastic and coherent noise. Events are considered retained if there exists a corresponding event in the catalog produced using filtered data that has an origin time within 2.5 seconds of the event. A 3-hour moving average filter was applied to this time series.

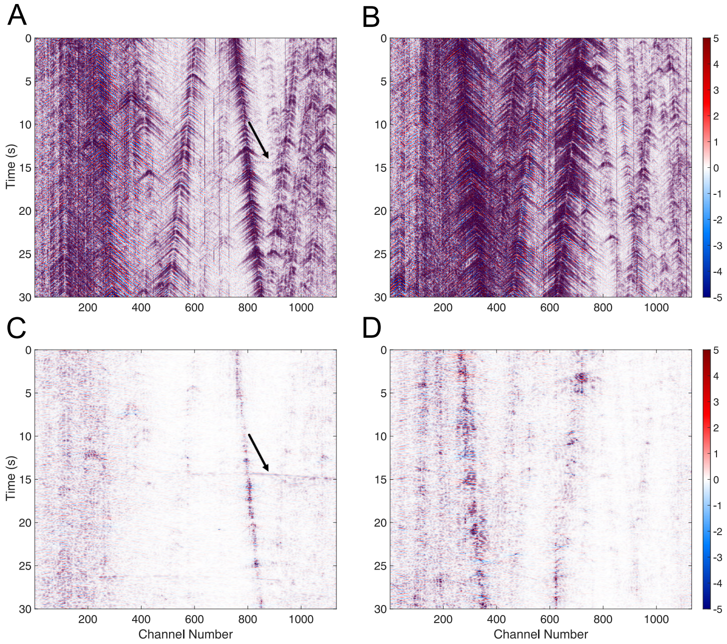

Figure 2.S3: Example of a detection made in the original catalog but not made in the new catalog. A. Template event taken from the unfiltered data. B. Wavefield of the detection made using the template in A. C. Same template as in A but taken from the filtered data. D. Same wavefield as in B but taken from the filtered data. Black arrows point to the earthquake-generated body waves of the template event.

Chapter 3

FINDING SMALL FAULTS WITH SCATTERED WAVES RECORDED BY DAS

Atterholt, J., Zhan, Z., and Yang, Y. (2022). Fault zone imaging with distributed acoustic sensing: body-to-surface wave scattering. *Journal of Geophysical Research: Solid Earth* 127. DOI: `10.1029/2022JB025052`. e2022JB025052.

Abstract

Fault zone structures at many scales largely dictate earthquake ruptures and are controlled by the geologic setting and slip history. Characterizations of these structures at diverse scales inform better understandings of earthquake hazards and earthquake phenomenology. However, characterizing fault zones at sub-kilometer scales has historically been challenging, and these challenges are exacerbated in urban areas, where locating and characterizing faults is critical for hazard assessment. We present a new procedure for characterizing fault zones at sub-kilometer scales using distributed acoustic sensing (DAS). This technique involves the backprojection of the DAS-measured scattered wavefield generated by natural earthquakes. This framework provides a measure of the strength of scattering along a DAS array and thus constrains the positions and properties of local scatterers. The high spatial sampling of DAS arrays makes possible the resolution of these scatterers at the scale of tens of meters over distances of kilometers. We test this methodology using a DAS array in Ridgecrest, CA which recorded much of the 2019 $M_w7.1$ Ridgecrest earthquake aftershock sequence. We show that peaks in scattering along the DAS array are spatially correlated with mapped faults in the region and that the strength of scattering is frequency-dependent. We present a model of these scatterers as shallow, low-velocity zones that is consistent with how we may expect faults to perturb the local velocity structure. We show that the fault zone geometry can be constrained by comparing our observations with synthetic tests.

3.1 Introduction

The Earth's crust is a geologically heterogeneous medium that hosts myriad sharp material contrasts at multiple scales. Among these heterogeneities are fault zones, features consisting of fault cores and surrounding zones of fracture that accommodate strain. Finding new ways to locate and characterize fault zones may potentially serve a variety of societally and scientifically important functions. Proximity to fault zones increases the likelihood of severe damage to infrastructure, both because fault zones host static deformation, and because fault zones may amplify ground motion (Kurzon et al., 2014). Additionally, the locations of faults control estimates of fault connectivity, which is an important parameter in some probabilistic hazard estimates (Field et al., 2014). Relatedly, relative fault positioning and fault geometry play a pivotal role in the propogation and termination of earthquakes (Harris and Day, 1993; Harris and Day, 1999; Wesnousky, 2008). Fault damage zone scaling is expected to play an influential role in earthquake nucleation (Ampuero et al., 2002), earthquake potency (Weng et al., 2016), and long-term earthquake sequence behavior (Thakur et al., 2020). Importantly, fault zones are multi-scale structures (Faulkner et al., 2010), and thus developing a more complete picture of fault zone structure at sub-kilometer scales contributes to these efforts to evaluate earthquake hazard and geological controls on earthquake phenomenology.

Considerable attention is given to major fault zones, those that are large and accommodate significant strain. But, minor and unmapped fault zones are an important consideration when evaluating the structural deformation and earthquake hazards in a region. Plate deformation is usually not accommodated by a single fault zone, but rather by a broad distribution of fault zones that extend sometimes hundreds of kilometers from the plate boundary, and minor fault zones play a key role in the accommodation of this strain (Scholtz, 2019). In the absence of high deformation rates, minor fault zones can develop a high risk potential if strain accumulates over a long time period, the stress state changes (Freed and Lin, 2001), or the stability of the fault is perturbed (Ellsworth, 2013). Relatedly, many significant earthquakes rupture within minor or unmapped fault zones. For example, the 2019 Ridgecrest earthquake sequence, which included the largest earthquake to take place in California in over two decades, ruptured mostly unmapped faults in the Little Lake and Airport Lake fault zones (Ross, Idini, et al., 2019), which only accommodated approximately 1 mm/y of slip (Amos et al., 2013).

For both major and minor fault zones, shallow fault zone structure is important. The shallowest few hundred meters of fault zones can exhibit sharp and localized velocity reductions (e.g., Zigone et al., 2019; Wang et al., 2019; Share et al., 2020) that can amplify ground motion, and shallow crustal faults play an important role in both facilitating and impeding the transport of groundwater and hydrocarbons (Bense et al., 2013). Shallow fault zone structure may also be used to infer the contribution of deep fault structure, which is very difficult to constrain, by correcting for shallow structure contributions in depth-integrated fault characterization approaches.

Previous efforts to locate and describe shallow fault zone structures at sub-kilometer scales have typically relied on geologic mapping, seismic surveying, and satellite imagery. Geologic mapping over decades has produced excellent records of Quaternary faults (e.g., USGS and CGS, 2022), but discerning faults using geologic mapping requires careful fieldwork and evidence of faulting at the surface. Seismic surveying produces detailed images of the subsurface, with which fault locations can be inferred e.g., Liberty et al., 2021; Lay et al., 2021, but surveys are often expensive and logistically challenging, particularly in urban settings. Satellite imagery is also used to map faults, often by identifying topographic anomalies in images (Joyce et al., 2009). More involved processing, such as producing phase gradient maps from InSAR interferograms (Xu et al., 2020), can also be used to identify fractures. These techniques are powerful, but they require surficial evidence of strain that can be imaged from above.

Other studies have used the earthquake wavefield to characterize the structure of major fault zones. For example, some studies have used fault zone head waves, head waves generated by refraction due to a bimaterial contrast across the fault, to image the fault interface and constrain the velocity contrast across the fault (e.g., McGuire and Ben-Zion, 2005; Allam et al., 2014; Share and Ben-Zion, 2018; Qin et al., 2020). Additionally, some studies have used travel-time anomalies from regional and teleseismic events to discern properties like the width of the damage zone and the velocity reduction within the damage zone (e.g., Cochran et al., 2009; Yang et al., 2020; Qiu, Ben-Zion, et al., 2021; Share et al., 2022). Moreover, low velocity structures can amplify ground motion, and some studies have used S-wave amplification caused by the reduced velocities in fault damage zones to delineate their structure (e.g., Qiu, Ben-Zion, et al., 2021; Song and Yang, 2022). Another approach is to use fault zone trapped waves, waves generated by constructive interference of critically reflected waves in the fault damage zone, which can be initiated by sources outside the fault zone (Fohrmann et al., 2004) and have been used to constrain the structure of fault damage zones (e.g., Ben-Zion et al., 2003; Catchings et al., 2016; Wang et al., 2019; Qiu, Ben-Zion, et al., 2021). In general, these techniques are highly effective tools for capturing geometric and internal properties of major fault zones. But, fault zones usually need to exhibit relatively large and spatially consistent elastic material contrasts for these techniques to be used. Hence, these techniques are typically applied to major fault zones using targeted deployments of dense networks of sensors. These factors make these methods ineffectual for the discovery and characterization of minor fault zones.

The weaknesses of these methods motivate the development of complimentary techniques for identifying and characterizing sub-kilometer scale fractures in the crust. To this end, we suggest an alternative method for identifying and characterizing fractures in the crust using distributed acoustic sensing (DAS) data. DAS is an emergent technology that repurposes fiber optic cables as dense arrays of strainmeters. DAS uses a laser interrogator unit to emit pulses of light that probe a fiber optic cable, and natural imperfections in the fiber send echoes back to the interrogator unit. Perturbations of the fiber change the travel times of these echoes, and these changes in travel time are quasi-linearly proportional to the strain induced by the perturbations. The high spatial frequency of DAS data allows for the resolution of high wavenumber phenomena that are incoherent in more sparsely measured data, which is useful for characterizing fault zones at high resolution (Jousset, 2019). One such phenomenon is the scattering of earthquake body waves to surface waves due to small-scale, local heterogeneities in the upper crust. We show an example of this scattering in Figure 3.1, and we subsequently refer to these features as chevrons, owing to their chevron-like shape in DAS data representations. These chevrons have been observed in other DAS datasets, and the scatterers generating these chevrons have been inferred to be faults (Lindsey et al., 2019; Spica, Nishida, Akuhara, Pétrélis, Shinohara, and Yamada, 2020). Moreover, these scattered surface waves are also visible in empirical Green's functions derived in DAS datasets that can be migrated to infer scatterer locations (Cheng et al., 2021; Yang, Zhan, et al., 2022a).

Our contributions in this paper are as follows. We suggest a local backprojection framework for the systematic location of the sources of these chevron-like features and find a strong spatial correlation between these locations and mapped faults. We suggest a model of these scatterers as rectangular perturbations in the velocity field, approximating a fault zone, and show that this model reproduces first-order features observed in the data. We then show that we can constrain key geometric features of the fault zone under this backprojection framework.

3.2 Data

In early July 2019, a large earthquake sequence initiated in the Eastern California Shear Zone. This sequence, which included a M_w6.4 foreshock and a M_w7.1 mainshock, produced thousands of aftershocks over the course of a few months. Shortly following the mainshock, a DAS array was deployed in Ridgecrest, CA using an Optasense ODH3 interrogator unit in an effort to record this aftershock sequence (Li et al., 2021). This DAS array began recording on July 10, 2019, and in this study we use recorded aftershocks that took place between the initiation of recording and October 4, 2019. The array is temporally sampled at 250 Hz and is spatially sampled at 8 m intervals over 1250 channels, with a total cable length of 10 km. The deployment of this DAS array ensured that numerous Ridgecrest sequence aftershocks were recorded nearby at a high spatial frequency.

For this study, we choose a subset of well-recorded, low-noise earthquakes on which we perform our subsequent analysis. We choose these earthquakes using straightforward quality control metrics to ensure that the earthquake wavefield has a high enough amplitude to be reliably analyzed and that the scattered surface waves are isolated from any cultural noise that may bias the analysis. As part of this quality control, we select from only events with $M_l \geq 2$ or $M_w \geq 2$ as determined by the Southern California Seismic Network catalog. We also restricted our selection to only events that occurred between 11 pm and 4 am local time, thus only keeping events with a low probability of being partially masked by cultural noise. We then manually inspected all of the remaining events and ensured that we only kept events with negligible cultural noise. After performing this processing, we are left with 50 events that meet our quality control criteria. These events are plotted in geographic context in Figure 3.1. These events are reasonably well clustered by distance and azimuth, minimizing variability due to the directional sensitivity of DAS.

3.3 Mapping Faults Using Local Backprojection

To quantify the magnitudes and locations of these scatterers, we employ a simple local backprojection technique to identify the locus points of the scattered waves in the body wave coda. This backprojection is based on the reasonable assumption that these chevron-like waves are surface waves generated by earthquake body waves impinging on a scatterer near the DAS array. We expect this phenomenon to be body-to-surface wave scattering because the scattered waves are dispersive, which we verify subsequently, and the onset of these waves occurs early in the body wave coda. We expect these scatterers to be local because the scattered waves attenuate

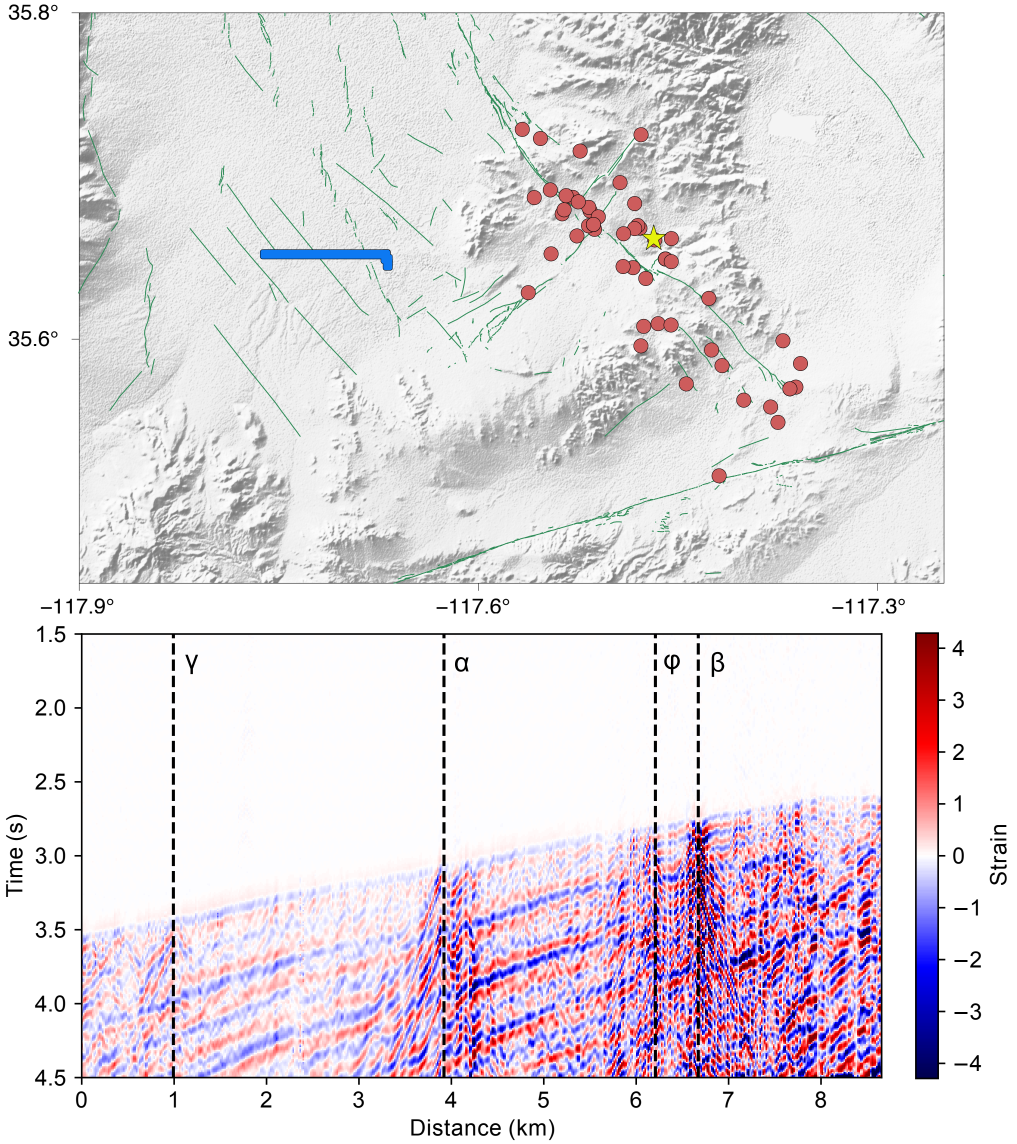

Figure 3.1: Geographic setting and illustration of scattered phases. Top: The geographic setting of the data used in this study. Blue line corresponds to the DAS array. Red dots correspond to the epicenters of the events used in this study. Yellow star corresponds to the epicenter of the event shown below (depth 5.6 km). Green lines correspond to the USGS-mapped Quaternary faults in the area. Bottom: Example of the DAS-measured wavefield of the onset of an event used in this study. Black dotted lines correspond to the locations of the chevron-like features that are mapped in Figure 3.3.

rapidly in space, as exemplified by the narrow width of these chevrons shown in Figure 3.1. Additionally, we exclude the possibility of fault resonance waves due to the fact that our resolution is approximately normal to the fault and that the chevron

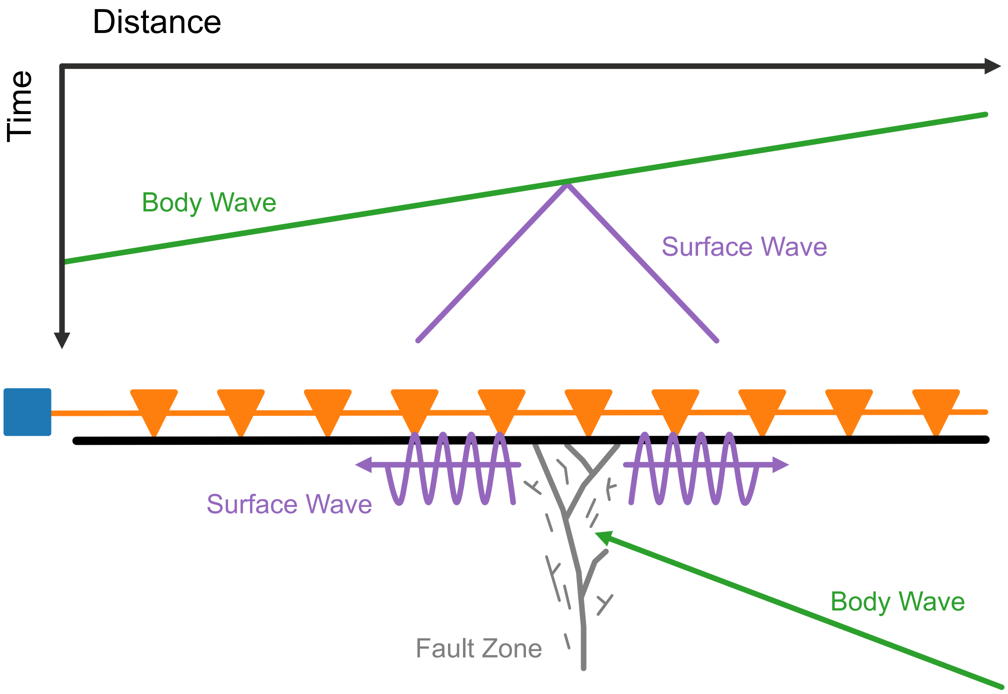

Figure 3.2: Schematic illustration of the phenomena observed in the earthquake wavefields used in this study. Top: Record section corresponding to the processes illustrated below. Bottom: Illustration of the phenomena resulting in the generation of the chevron-like features shown in Figure 3.1. Colors represent the same phenomena in both top and bottom. Green corresponds to incident body wave. Gray features indicate a fault zone. Purple corresponds to the scattered surface waves resulting from the body waves impinging on the fault zone. Orange line and triangles indicate the fiber optic cable and stations, respectively. Blue box represents the DAS interrogator unit.

width, though narrow, is wider than expected for fault resonance waves for minor faults. A schematic example of the generation of these scattered waves is shown in Figure 3.2. The driving principle of this methodology is the same for standard backprojection techniques used in seismology (Kiser and Ishii, 2017). In particular, for grid points near or above a scatterer, the backscattered energy resultant from the scatterer will align and sum coherently, producing a larger amplitude than that of a grid point far from any scatterers. In this case, we attempt to backproject locally scattered surface waves to image the scattering source, illustrated as a fault zone in Figure 3.2.

To accomplish this backprojection, we first bandpass our data to a narrow frequency band; this frequency band can vary depending on the desired dimensional sensitivity.

We select frequency bands with 1 Hz widths and center frequencies spanning 2-10 Hz at 0.5 Hz intervals. For each of these frequency bands, we partition the earthquake wavefield by velocity in the curvelet domain (Atterholt et al., 2021), using a curvelet basis to mute sections of the frequency-wavenumber domain and thus isolate desired wavefield components. This is equivalent to frequency-wavenumber filtering with specialized tapers that minimized velocity filtering artifacts. We use this wavefield-partitioning technique to separate the scattered wavefield and the direct waves into two separate windows. We classify velocities below 750 m/s to be the scattered wavefield and velocities above 1000 m/s to be the direct wavefield. We show examples of this wavefield partitioning in Figure 3.S1. Of the scattered wavefield, we select only the scattered waves from the early-onset body waves, because these early-onset scattered waves are typically more pronounced relative to the earthquake wavefield and are not superimposed by earthquake-generated surface waves, which can bias the final result. To isolate the early-onset scattered waves, we window the scattered wavefield over the time interval between 2 seconds prior to the onset of the P-wave and 5 seconds after the onset of the P-wave. Once we have isolated the scattered waves, we perform a local backprojection of surface wave energy according to a local velocity model across the array. For the local velocity model, we use a 1-dimensional velocity model made by taking averages of each period of the velocity model developed by Yang, Atterholt, et al. (2022). We perform this averaging to avoid biasing of the result due to lateral slopes in the model. We then define a grid of potential scattering sources along the array geometry, and we backproject the surface waves recorded by the surrounding channels, up to a fixed distance, according to their distance from the potential source. Our grid of potential source locations is spaced at 8 m along the array, which coincides with the station spacing. In this study, by inspecting the data, we fix the maximum distance to be 250 m based on the expected distance from the chevron center over which we can expect to get significant constructive interference by aligning the waveforms. We then stack the backprojected channels and sum the absolute value of the stack, giving us an amplitude for the grid point. We only define the grid at the surface along the array, because linear DAS array geometry poorly constrains backprojection images along orthogonal axes. But, the rapid attenuation of these surface waves suggests that most of the energy in the scattered wavefield is generated very close to the array, minimizing the consequence of this poor constraint. Furthermore, scattered waves from more distant scatterers will have higher apparent velocities, minimizing the impact of these scatterers in a backprojection framework that uses true velocity.

We can verify that these scattered waves are dispersive under this framework. That is, we apply this backprojection framework to the earthquake wavefield shown in Figure 3.1 over a range of velocities for each frequency, rather than using a single velocity model. We can then sum across each resultant profile to get a single value for each frequency and velocity pair. From this we can determine which velocities produce the largest sum at each frequency, which we expect to be correlated with the amount of constructive interference due to waveform alignment. In this way we can construct a dispersion curve using only the scattered wavefield. This is a similar approach to that taken by Spica et al. (2022), but because we sum across the entire profile, this produces a velocity spectrum that averages the contributions of the scattered waves produced across the array. A plot of this velocity spectrum is shown in Figure 3.S2. This spectrum shows a clear dispersion pattern that is well matched by the dispersive relationship for this setting computed in Yang, Atterholt, et al. (2022).

Since DAS measures longitudinal strain, which is distinct from conventional inertial seismometers, the sensitivity of DAS to these scattered waves is also distinct. For surface waves generated by scattering from a fault that runs orthogonal to the array, the recorded surface waves will propagate parallel to the fiber. Consequently, a significant component of the particle motion will be parallel to the fiber, motion to which DAS is most sensitive. For a fault that runs oblique to the array, the surface waves will not propagate exactly parallel to the fiber, and the apparent velocity will increase and the sensitivity of the DAS array to the waves will decrease. However, since these waves attenuate rapidly in space, the majority of the recorded energy will have been scattered very close to the array, minimizing variability due to obliquity. Additionally, because DAS is more sensitive to lower velocities, surface waves are amplified in DAS data relative to the other components of the earthquake wavefield. This potentially explains why these surface waves are such a common and well-recorded observation in DAS data (e.g., Lindsey et al., 2019; Spica, Nishida, Akuhara, Pétrélis, Shinohara, and Yamada, 2020; Ajo-Franklin et al., 2022). These factors suggest that the variability in scattered waves measured across the DAS array is largely due to variability in the strength and geometry of the scatterers near the array. Additionally, because we are using array seismology, we need to consider apparent velocity when performing velocity filtering and backprojecting these waves. But, since the recorded surface waves propagate approximately parallel to the fiber, the apparent velocity of locally scattered surfaces waves is very close to the true velocity. In particular, the apparent velocity follows $\mathrm{v_t}/\cos(\theta)$; where $\mathrm{v_t}$

is the true velocity and θ is the incident angle relative to the array geometry. In the case of surface waves scattered very close to the array, θ is close to zero.

We apply this backprojection technique to the 50 high quality events recorded by the DAS array in Ridgecrest, CA described in the preceding section. Backprojecting the scattered wavefields of these earthquakes results in an ensemble of profiles of scattering across the Ridgecrest DAS array. To ensure that the within-array and between-event amplitudes are comparable, we normalize the profile amplitudes by the sum of the absolute value of the body waves that occupy the same window used for each grid point in each profile. For this normalization, we account for the variability in azimuth and incident angle according to the directional sensitivity of strainmeters (Benioff, 1935). In particular, noting that the dominant body wave signal we use for this normalization is the P-wave, we divide the direct wavefield by $\cos^2(\theta)$. Although this normalization is imperfect, because some windows may include P-to-S conversions or S waves; we find it to be sufficient for our purposes. We smooth these profiles with a Gaussian kernel with a standard deviation of 5 channels to minimize any high-frequency, stochastic variability in these profiles. We show these ensembles of backprojection profiles computed at 4 and 7 Hz center frequencies in Figure 3.3. These profiles are generally "bumpy," and it can be difficult to determine to which of these peaks to assign significance. Additionally, some peaks are of low amplitude, but are noteworthy because they are positioned in areas with low noise floors. To help us determine which peaks are most likely associated with scatterers, we use the metric from mountaineering of topographic prominence, which is a measure of the height of a peak relative to its surroundings. We plot the prominence profiles alongside the backprojection amplitude profiles in Figure 3.3. Additionally, we superimpose these prominence profiles on the DAS array geometry in Figure 3.3. Indeed, there is a spatial correlation between peaks in the prominence profile and the locations of USGS-mapped Quaternary faults near the array. This spatial correlation partially evidences the argument that the nearly ubiquitous chevron-like features in the DAS measured wavefield are fault-zone scattered waves. In Figure 3.3, we make note of four peaks, which we term peaks α, β, γ, and ϕ. These are the most prominent peaks in both frequency bands, and by visual inspection we can associate these peaks with mapped faults nearby. In particular, peaks α and β are noteworthy in that they are prominent enough that we can analyze their behavior with space and frequency. We use peaks α and β to infer properties of the associated fault zones subsequently.

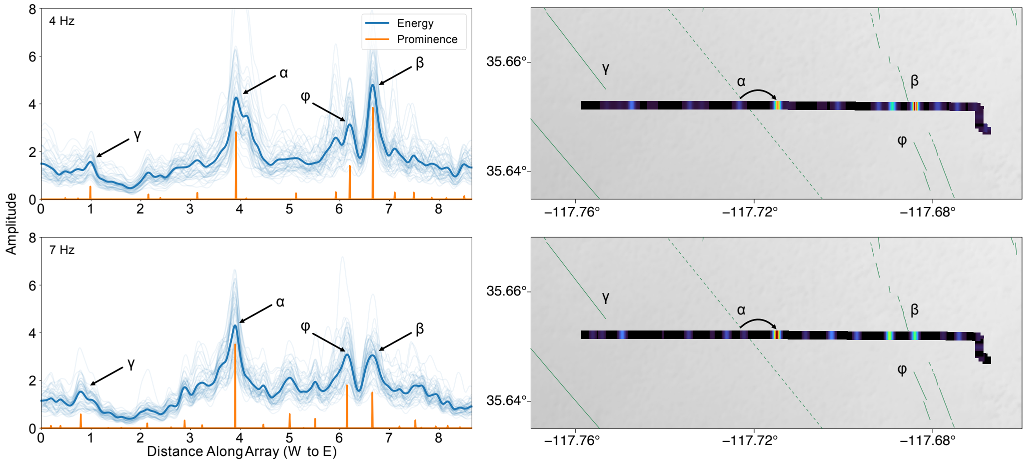

Figure 3.3: Backprojection of scattered phase results. Left: Backprojection profiles made using 50 events recorded by the DAS array in Ridgecrest, CA. Light blue lines correspond to profiles made using a single event. Dark blue lines correspond to the mean profile. Orange lines correspond to the topographic prominence of the mean energy profile. Top and bottom plots correspond to profiles generated with 4 and 7 Hz center frequencies, respectively. Black arrows point to referenced peaks α, β, γ, and ϕ. Right: Prominence profiles to the left, convolved with Gaussian kernel to widen peaks for representation, plotted on the DAS array geometry shown in Figure 3.1. Color corresponds to prominence amplitude. Green lines correspond to fault locations. Solid lines are moderately or well constrained fault locations, and dotted lines are inferred fault locations. Faults are labeled according to associated peaks indicated in the profiles to the left. Curved black arrows indicate the proposed relocation of the fault associated with peak α.

3.4 Modeling Scatterers as Fault Zones

To further investigate the nature of the sources of scattering evident in DAS data, we present a model for these scatterers as rectangular perturbations in the 2D velocity structure. Although natural faults are neither perfect rectangles nor uniform velocity perturbations, this simple parameterization allows us to capture first order structural properties of fault zones without including more complexity than we can feasibly resolve given our data. The few free parameters of this fault model are burial depth, maximum depth, width, and percent change in velocity. For a background velocity model, we use a combination of the aforementioned shear wave velocity model from Yang, Atterholt, et al. (2022) for the shallowest 150 m and a local 1D velocity profile taken from the SCEC Unified Community Velocity Model (Small et al., 2017) for depths deeper than 150 m; we combine these two models using a linear interpolation.

We then create a model fault zone by multiplying a section of the background model with an assigned rectangular geometry by a constant of proportionality.

We then use this model to perform synthetic tests that we can compare to our observations to assess the feasibility of this scatterer model. We generate these synthetics using Salvus (Afanasiev et al., 2019), a full waveform modeling software that simulates wave propagation using the spectral element method. We approximate the DAS array at Ridgecrest as a linear, 8 km array of strainmeters at the surface of our Earth model. We emplace a 2D double couple source with a 0.1 s half-duration Gaussian rate source time function 30 km east of the array at 10 km depth, a representative distance and depth for the earthquakes used in this study. We generate an adaptive mesh with which we can compute these synthetics up to 10.5 Hz with at least one element per wavelength. We use the same setup to perform tests of the fault geometry that we describe subsequently. We show an example of a simulation for a model with two faults with different geometries and velocity reductions in Figure 3.4. The faults in Figure 3.4 were parameterized using models for the faults associated with scatterers α and β that are proposed in the subsequent section. In particular, the fault on the left is parameterized as a 30% velocity reduction with a width of 20 m and a depth extent of 10 to 60 m. The fault on the right is parameterized as a 10% velocity reduction with a width of 50 m and a depth extent of 0 to 50 m. Both fault parameterizations are vertical. The resultant scattered waves in the synthetic wavefield match many of the first-order characteristics of the scattered waves in the observations of Figure 3.1. In particular, we have reproduced the observation of low-velocity scattered surface waves emanating from a narrow source. We can evaluate the similarities in the velocity content of the synthetic data and the observed data by computing the velocity spectrum of the scatterer component of the synthetic wavefield, as outlined in the preceding section. We show the velocity spectrum in Figure 3.S3. The dispersion of the scattered wavefield in the synthetic test is a close match to the dispersion for the real data in Figure 3.S2. Further, we see that secondary arrivals in the synthetics also produce scattered, dispersive waves. Secondary arrivals may thus explain why the scattered waves appear to reverberate in time. These simulations further confirm that these scatterers may be related to faults. As is clear in Figure 3.4, variations in the properties of the model fault zones create visually apparent differences in the strength of the scattered wavefield.

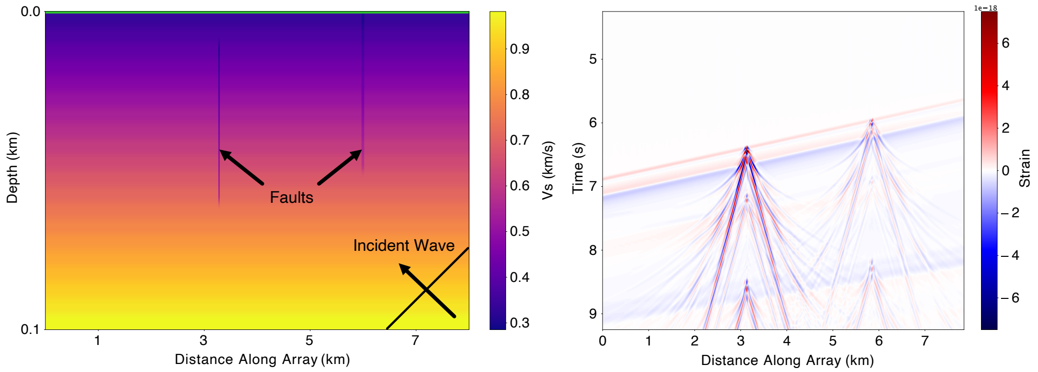

Figure 3.4: Synthetic tests of shallow scatterers. Left: Example of velocity model modified from Yang, Atterholt, et al. (2022) and Small et al. (2017) with two fault zone-approximating velocity perturbations emplaced in the model. Green line corresponds to array of strainmeters. Black arrows point to incident wave direction and fault locations. Note the large vertical exaggeration. Right: Record section generated from scenario illustrated to the left.

3.5 Constraining Fault Geometry

Now that we have a method of quantifying the degree of scattering in data and a means of simulating our observations using a reasonable model, we can constrain the properties of the sources of scattered waves by comparing features between the data and synthetics under this backprojection framework. As is evident in Figure 3.3, the peaks in these backprojection profiles have variant properties in space and frequency, and this variability may inform a better understanding of the faults that generate these peaks. Moreover, since we performed this backprojection for many events, we have an ensemble of profiles with which we can evaluate how well constrained the fault-zone properties that control these peak shapes are.

To generate our synthetics, we use the velocity model and source described in the preceding section. We also incorporate attenuation into our model. Since we do not have a priori estimates of the attenuation at this site, we parameterize the attenuation using the functional decay of the peaks from our backprojection profiles to obtain a rough estimate of the local attenuation structure. We assume an empirical relationship between shear wave velocity and attenuation structure, a common assumption when building an Earth model with heterogeneous attenuation structure (Graves and Pitarka, 2010), and may be denoted as $Q_\mu = cV_s$. To test the attenuation of surface waves away from a local scatterer, we define a fault zone according to the aforementioned simplified fault model with a width of 20 m, a depth extent of 0-100 m, and a 30% velocity reduction. We test several values for c and compare the spatial decay of the resultant synthetic peaks to those of peaks α and β at 4 Hz. We find that the data are best fit by a value of $c = 50$, a reasonable value for this relationship (Lin and Jordan, 2018; Lai et al., 2020). These peak comparisons are shown in Figure 3.S4. This empirical relationship between attenuation and velocity is imperfect, as other parameters such as temperature and fluid content also control attenuation (Brocher, 2008; Eberhart-Phillips et al., 2014), and other factors such as structural heterogeneity can control surface wave amplitude (Bowden and Tsai, 2017). But, since we are only trying to obtain a reasonable attenuation parameterization for our forward model, this approximation is sufficient for our purposes.

To constrain the local fault zone properties, we note that the backprojection profiles shown in Figure 3.3 are functions of the frequency band in which we filter the data, and that each peak behaves differently with frequency. We investigate this property by evaluating the backprojection profiles for all narrow frequency bands for which we computed profiles in this study, with center frequencies ranging from 2 to 10 Hz. By plotting the mean profiles at each center frequency together, we can better inform our understanding of the behavior of the frequency dependence of individual scattering features along the array. We plot these mean profiles against center frequency and distance as a pseudocolor plot in Figure 3.5. As is evident in Figure 3.5, there are peaks that are traceable across a range of center frequencies, and there is a high degree of variability in the behavior of these peaks with frequency.

We then focus on the two most prominent peaks in this image, peak α and peak β, both of which are spatially correlated with USGS-mapped faults (USGS and CGS, 2022). By taking cross sections of the center frequency versus distance along array plot, we can determine the frequency dependence of these specific scatterers along this profile. Clearly, these peaks have different frequency dependences, which likely reflects a variability in the depth and geometry of the scattering fault zone. To discern the properties of these faults, we test different fault zone geometries to match these frequency dependent trends. Because the amplitudes of DAS data are not well understood, we only attempt to match the shape of the synthetic profile with the shapes of the peak profiles, and we thus normalize the synthetic profile amplitude by the ratio of the integrated amplitude of the mean peak profile to the integrated amplitude of the synthetic peak profile. We attempted to reproduce these frequency-amplitude trends by performing synthetic simulations that included fault zones with varying free parameters. These simulations were too expensive to

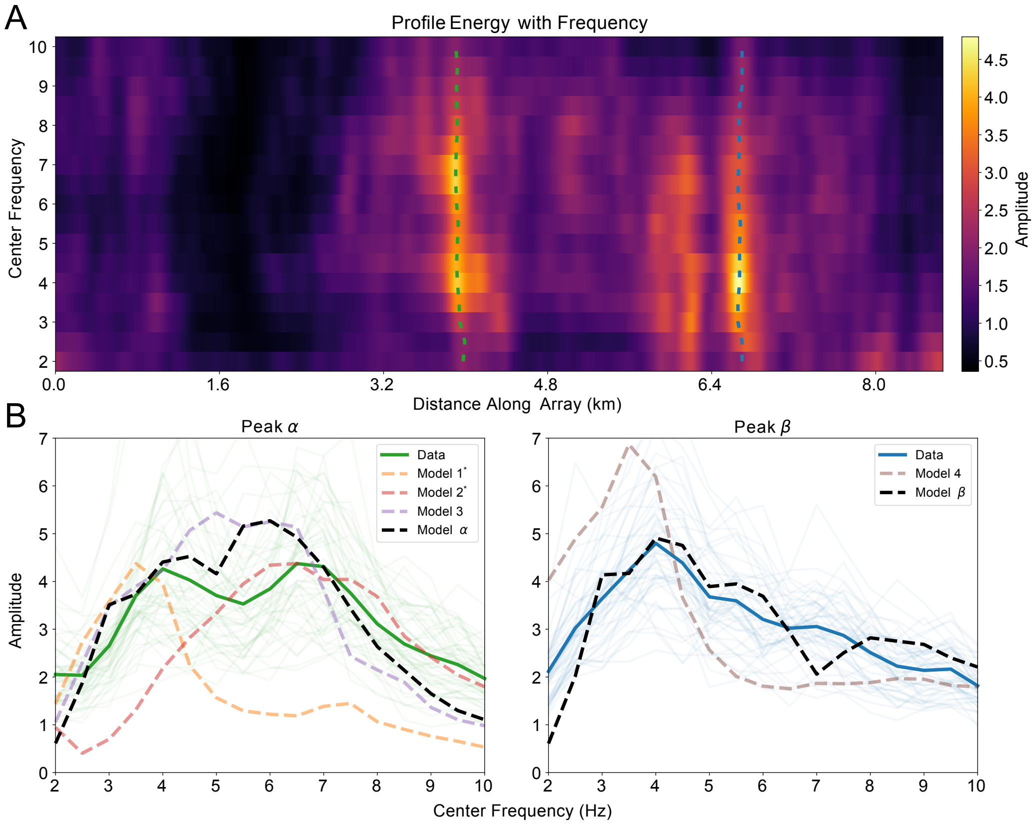

Figure 3.5: Comparison of modeled and observed spectra. A. Pseudocolor plot of mean backprojection amplitude plotted against center frequency and distance along array. Dotted green and dotted blue lines correspond to cross sections of this plot, associated with peaks α and β, respectively. B. Plots of backprojection amplitude versus center frequency for the cross-sections shown in A. Light green and light blue lines are the frequency-amplitude curves determined for a single event for peaks α and β, respectively. Dark green and dark blue lines are the mean frequency amplitude curves for peaks α and β, respectively. Dotted black lines correspond to the frequency-amplitude curves for our preferred fault zone model for each peak. Dotted colored lines are frequency amplitude curves for fault zone models with variant parameters to illustrate the constraints of this methodology. The parameters used for each model are given in Table 3.S1. The asterisk in the legend indicates that, for visualization purposes, the corresponding model is normalized by the maximum height of the data curve rather than the integrated sum.

perform a full grid search over all the fault model parameters, but by identifying patterns between fault zone parameterizations and subsequent simulated frequency-amplitude profiles, we were able to find fault zone models that produced good fits to the profile ensembles for both faults, as shown in Figure 3.5B. Indeed, reproducing the frequency-amplitude curves for the different peaks requires the use of variant fault zone parameterizations. Peak α is best fit by a 30% velocity reduction that is 20 m wide and spans 10 to 60 m depths. Peak β is best fit by a 10% velocity reduction that is 50 m wide and spans 0 to 50 m depths. The results for peak α suggest that we may be able to detect and constrain properties of small-scale buried faults.

3.6 Discussion

The spatial correlation between the locations of sources of scattering and the mapped faults near the Ridgecrest DAS array shown in Figure 3.3 suggests that the source of at least some of these scatterers are faults, and thus DAS arrays can detect measurable signatures of fault zones. An example of the potential utility of this technique is readily available in this dataset. In particular, peak α is located near, but is offset from, a mapped fault extending across the array. The Quaternary Fault Catalog (USGS and CGS, 2022) records this fault's location as inferred rather than directly observed; thus, we can use our backprojection profile to refine the location of this fault, treating peak α as a potential node of the fault trace. This node provides a stronger constraint on this fault's location near the town of Ridgecrest, CA, which has important implications for the location of possible static strain in the event of the activation of the Little Lake Fault Zone. This technique is generalizable to all DAS arrays that record seismicity, and may then be used elsewhere to systematically refine inferred fault locations and suggest the presence and locations of previously unmapped faults.

The profiles in Figure 3.3 bear a resemblance to results from distinct fault zone characterization methodologies, namely S-wave amplification analysis (e.g., Qiu, Ben-Zion, et al., 2021). Both techniques can be used to locate faults at small spatial scales using the peak locations, but these techniques otherwise provide complimentary information. For example, the shape of the peaks in S-wave amplification profiles can be interpreted as an estimate of the lateral characteristics of the fault damage zone, while the shape of the peaks in this study are largely reflective of the processing workflow and amplitude attenuation. But, the methodology presented in this study is more sensitive to small variations in the frequency of scattered waves that are reflective of characteristic dimensions of the fault zone, which includes constraints on the depth-dependence of the fault zone. Additionally, the methodology presented in this study is more readily applicable to DAS, both because DAS amplitudes are not well understood due to variability in coupling of the fiber and because DAS is particularly sensitive to low velocity surface waves.

The synthetic simulations in this study provide additional evidence that these chevron-like observations in DAS data are well-explained by fault zones. In particular, as shown in Figure 3.4, an approximation of a fault zone as a rectangular perturbation in velocity reproduces the first order features of these chevron-like observations. Additionally, the complexity in the frequency-amplitude curves shown in Figure 3.5 evidences a necessary variability in the finite properties of the scattering fault zones (Almuhaidib and Toksöz, 2014). But, importantly, this representation is non-unique, and the diversity of geologic heterogeneity in the upper crust suggests that features other than fault zones are likely responsible for at least some of the chevron-like observations we see in DAS data. Additionally, it is important to be careful when interpreting a backprojection image. Backprojection images are subject to spatial smearing due to constructive interference away from the true source location. Spatial smearing may bias frequency-amplitude curves by convolving contributions from multiple peaks. We minimize this form of biasing in this study by fitting only the most prominent peaks, which are spatially isolated from each other.

The geometric constraints we place on the faults in this study illustrate that, using DAS recorded earthquakes, we can constrain some aspects of the subsurface geometry of fault zones on the scale of tens of meters, potentially even for buried faults as is the case for peak α. Although these solutions are non-unique, they provide robust constraints on the approximate scaling of these subsurface structures. As stated prior, we were able to approach fault models that fit these data by identifying patterns in the relationship between fault zone geometry and the resultant synthetics. One interesting relationship, made clear in Figure 3.5, is related to the observation that peak β has a unimodal frequency-amplitude curve while peak α has a bimodal frequency-amplitude curve. The simulations suggest that two characteristic lengths produce distinct modes in these frequency-amplitude curves: the fault zone width and the fault zone depth extent. In particular, we obtain a unimodal frequency-amplitude curve when these lengths are the same (as with peak β) and a bimodal frequency-amplitude curve when these lengths are distinct (as with peak α), with the smaller characteristic dimension responsible for the highest frequency mode and vice versa. We demonstrate that variant characteristic dimensions can account for each frequency mode of peak α by running separate simulations for square-shaped buried faults, with velocity perturbations equivalent to the best fitting model for peak α, that extend up to 10 m depth with side lengths of 50 m and 20 m, lengths which match the depth extent and width, respectively, of the best fitting model for peak α. The amplitude-frequency curves of these simulations are plotted as Models 1 and 2 in Figure 3.5, respectively. Both of these models well approximate one of the individual modes of the bimodal data curve for peak α. Finally, although we normalize by amplitude, the magnitude of the velocity perturbation subtly changes the shape of the synthetic curves in our simulations in Figure 3.5; however, this is a weakly constrained parameter in this methodology.

Although this is not the first study to attempt to map fault zones using scattered waves in DAS data, a key contribution of this study is that it provides a framework to systematically locate the origins and discern the dimensions of these scatterers using the earthquake wavefield. Importantly, when using the earthquake wavefield, we are mostly looking at body-to-surface scattered waves, which have a different depth sensitivity than surface-to-surface scattered waves. In particular, body-to-surface wave scattering has a deeper depth sensitivity than surface-to-surface wave scattering because body waves can propagate at depth while surface waves have a frequency-limited depth extent (Barajas et al., 2022). But, body-to-surface wave scattering at a given frequency is still only sensitive to depths at which a scattering source can excite surface waves. Differences in sensitivity are important to consider when comparing this methodology to other scatterer characterization methods that use surface-to-surface wave scattering. Since we can only feasibly apply this technique between 2-10 Hz, this depth sensitivity constraint suggests that this methodology is only sensitive to the top few hundred meters. But, we suggest that the depth extents determined in this study are well-constrained by the data. To illustrate this, we perform a simulation for a fault with the same parameters as the best fitting model for peak β, but change the depth extent from 0-50 m to 0-100 m. The frequency-amplitude curve for this simulation is plotted as Model 4 in Figure 3.5. This curve shows that for a deeper fault, we would expect to observe a frequency-amplitude curve more depleted in higher frequencies and enriched in lower frequencies. Recent techniques (e.g., Touma et al., 2022) have shown promise in imaging even deeper scatterers at high resolution using targeted array deployments. For imaging major fault zones with deep structures, method integrated approaches may be useful for illuminating fault zone structures at all depths.

In Yang, Zhan, et al. (2022a), the authors discern properties of the fault zone associated with peak α in this study as a 30% velocity reduction that is 35 m wide and spans 0 to 90 m depths. While this geometry is very close to our result and provides a useful verification of our technique, the differences that arise are likely due to the different sensitivities of the measurements and the different frequencies used to fit the fault model. Namely, the geometry of the faults discerned in this study were partially constrained by measurements over 6 Hz, which were not used to constrain the geometry in Yang, Zhan, et al. (2022a). The higher frequency content used in this study likely explains why the characteristic dimensions discerned in this study are both smaller than those found in Yang, Zhan, et al. (2022a). The higher frequency content may account for our ability to resolve a shallow burial depth. This fault burial depth is largely constrained by subtle variations in the peak shape. To illustrate this, we generate synthetics for a fault model with the same parameters as the best fitting model for peak α, but use a depth extent of 0-50 m instead of 10-60 m. The frequency-amplitude curve for this synthetic test is plotted as Model 3 in Figure 3.5. This result shows, that for an unburied fault, we achieve a slightly different shape that does not capture any separation of the high and low frequency modes of the data curve for peak α.

Finally we note that, although this study focused on relatively minor faults, this methodology can be readily extended to major fault zones, and requires only an across-fault DAS array and earthquake observations. Indeed, since the interrogation length for DAS units is increasing, and since many in situ fibers cross major faults, we can expect the number of DAS arrays sensing structure over major fault zones to increase rapidly over time. The technique presented in this paper presents an opportunity to leverage these DAS arrays to measure the fracture density and characteristics within major fault zones. Moreover, this study only covers one method with which DAS can be used to characterize major fault zones. Many of the aforementioned techniques which have previously used densely deployed conventional seismometers can be performed with DAS. The key challenges in applying these techniques, however, are that DAS provides a different observation than traditional seismometers, single component strain, and that DAS amplitudes are not well understood due to variability in coupling. These differences make some traditional fault characterization techniques, such as detecting fault zone head waves using particle motion analysis or measuring S-wave amplification, more difficult to apply using only DAS data. But, including some conventional inertial seismometers along a DAS array has the potential to diminish some of the challenges of DAS data (e.g., Wang et al., 2018; Lindsey et al., 2020; Muir and Zhan, 2021a; Yang, Atterholt, et al., 2022). For the fault zone characterization case, including collocated 3-component seismic sensors allows for amplitude calibration of DAS data and provides local particle motion observations. In this way, we can leverage the high station density and extensive deployments of DAS data while minimizing its limitations.

3.7 Conclusions

In this study we present a framework for the systematic location and characterization of fault zones using the DAS measured earthquake wavefield. This framework, which relies on the simple backprojection of the scattered wavefield following an earthquake, yields profiles of the scattered wave energy across the array. We apply this framework to 50 earthquake record sections recorded by a DAS array in Ridgecrest, CA, yielding an ensemble of profiles of scattered wave energy across the array. With these profiles, we identify numerous scattering peaks that are spatially well-correlated with mapped faults in the area, suggesting that these observed scattered waves are faults. Using these backprojection profiles, we suggest a correction to the location of one of the mapped faults in the area. Moreover, we present a model for these scattering sources as rectangular perturbations in the velocity structure, which is a simple approximation of a fault zone, and through simulations we show that this model reproduces first order observations of the observed scattered waves. Using this backprojection technique and these simulations, we establish a framework for using the locally scattered wavefield to evaluate shallow attenuation structure and infer characteristic dimensions of fault zones. We then apply this framework to the profiles computed for the Ridgecrest DAS array and consequently make claims about the fault zone structure near the array. We use the frequency decay of the profile peaks and synthetic simulations to image local faults at the scale of tens of meters, and with these images we distinguish between a fault that is surface-breaching and a fault that is buried.

Supplementary Materials

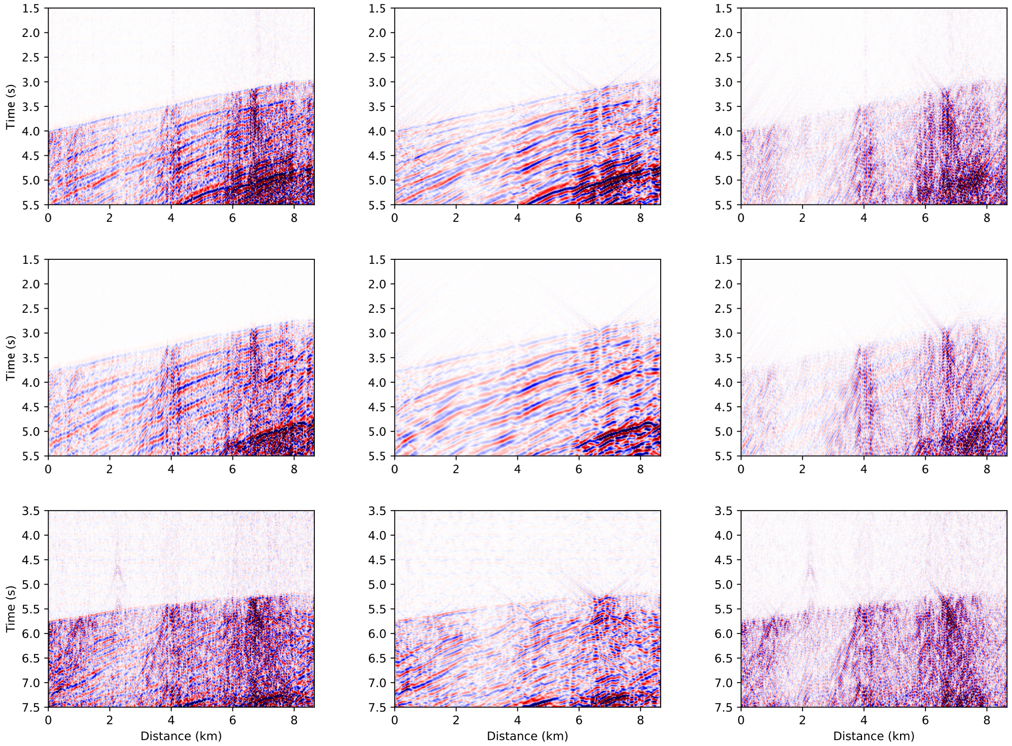

Figure 3.S1: Examples of the wavefield partitioning, described in Atterholt et al. (2021), applied for separating the direct waves from the surface waves. The left column shows the total wavefield for 3 separate events used in this study. The middle column shows the separated direct waves of the events. The right column shows the separated scattered waves of the events.

Model Parameters				
Model #	Burial Depth (m)	Maximum Depth (m)	Width (m)	Velocity Reduction (%)
Model 1	10	60	50	30
Model 2	10	30	20	30
Model 3	0	50	50	30
Model 4	0	100	50	10
Model α	10	60	20	30
Model β	0	50	50	10

Table 3.S1: Model parameters for each of the models shown in Figure 5. Fault model is rectangular, where the burial depth is the depth of the top of the rectangle, the maximum depth is the depth of the bottom of the rectangle, the width is the lateral extent of the rectangle, and the velocity reduction is the applied velocity perturbation. All fault models are vertical.

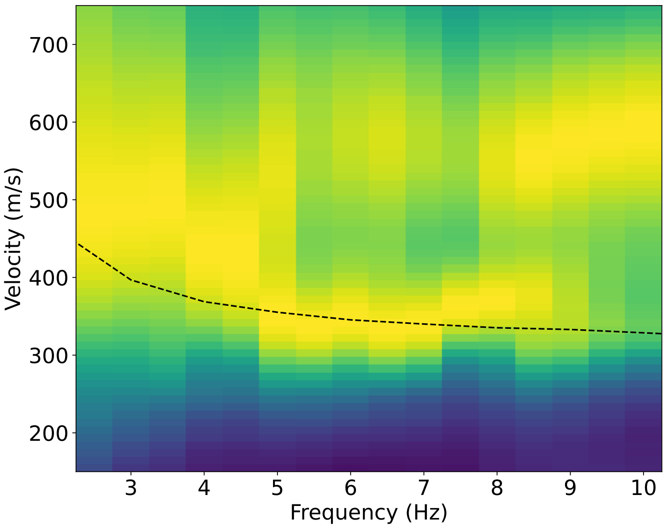

Figure 3.S2: Dispersion curve generated using the backprojection framework to perform a grid search at velocities in narrow frequency bands on the earthquake wavefield shown in Figure 1. Black dotted line is the 1D average of the velocity model from Yang, Atterholt, et al. (2022)

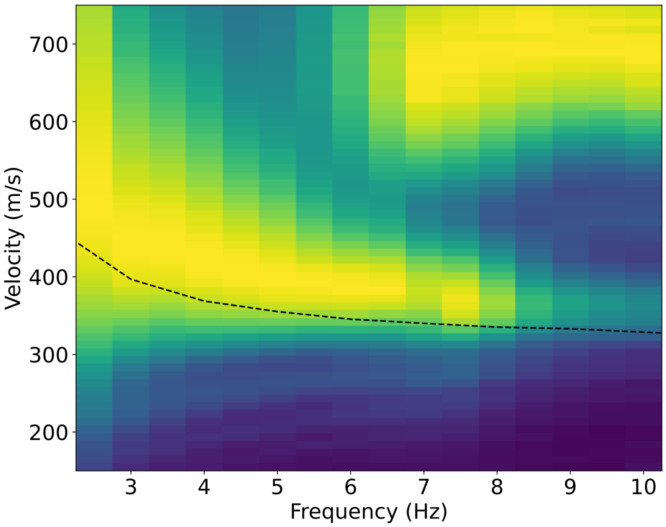

Figure 3.S3: Dispersion curve generated using the backprojection framework to perform a grid search at velocities in narrow frequency bands on a synthetic shot gather with an emplaced fault model. Black dotted line is the 1D average of the velocity model from Yang, Atterholt, et al. (2022)

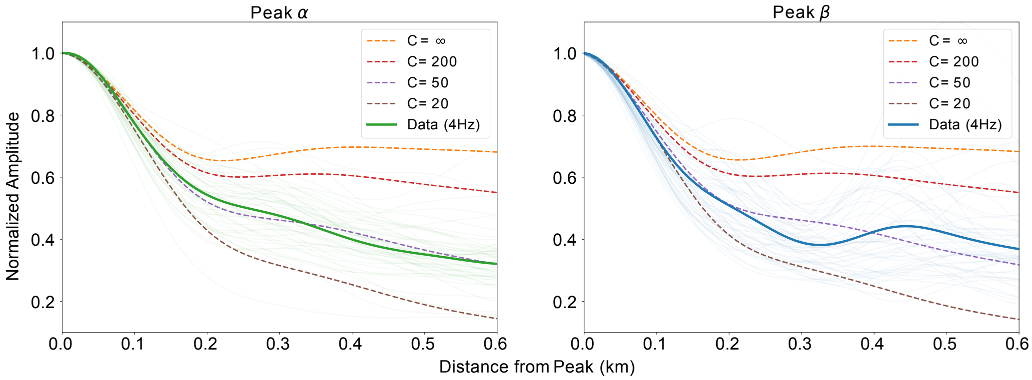

Figure 3.S4: Peak decay functions of peaks α and β for ensemble of profiles shown in Figure 3. Light green and light blue lines are decay functions of individual profiles for peaks α and β, respectively. Dark green and dark blue lines are mean peak decay functions for peaks α and β, respectively. Dotted lines are peak decay functions for synthetics generated using different attenuation regimes defined using constant of proportionality c.

Chapter 4

IMAGING THE GARLOCK FAULT WITH A DAS ARRAY

Atterholt, J., Zhan, Z., Yang, Y., and Zhu, W. (2024). Imaging the Garlock Fault Zone with a fiber: a limited damage zone and hidden bimaterial contrast. *Journal of Geophysical Research: Solid Earth* 129. DOI: `10.1029/2024JB028900`. e2024JB028900.

Abstract

The structure of fault zones and the ruptures they host are inextricably linked. Fault zones are narrow, which has made imaging their structure at seismogenic depths a persistent problem. Fiber-optic seismology allows for low-maintenance, long-term deployments of dense seismic arrays, which present new opportunities to address this problem. We use a fiber array that crosses the Garlock Fault to explore its structure. With a multifaceted imaging approach, we peel back the shallow structure around the fault to see how the fault changes with depth in the crust. We first generate a shallow velocity model across the fault with a joint inversion of active source and ambient noise data. Subsequently, we investigate the fault at deeper depths using travel-time observations from local earthquakes. By comparing the shallow velocity model and the earthquake travel-time observations, we find that the fault's low-velocity zone below the top few hundred meters is at most unexpectedly narrow, potentially indicating fault zone healing. Using differential travel-time measurements from earthquake pairs, we resolve a sharp bimaterial contrast at depth that suggests preferred westward rupture directivity.

4.1 Introduction

Fault zone structure plays an important role in the behavior of earthquake ruptures. Damage in the immediate vicinity of the fault alters the permeability and rheology of fault-adjacent rocks, potentially affecting the movement of fluids near the fault (Caine et al., 1996) and changing the dynamic properties of ruptures (Dunham et al., 2011; Thakur et al., 2020). Observational work has shown that large ruptures often propagate unilaterally (e.g., Atterholt and Ross, 2023; McGuire et al., 2002); simulations and experimental work suggest that a bimaterial contrast across the fault at seismogenic depths promotes asymmetric ruptures, but the consequences for future directivity of faults is unclear (Andrews and Ben-Zion, 1997; Anooshehpoor and Brune, 1999; Cochard and Rice, 2000; Harris and Day, 2005; Huang, 2018; Ranjith and Rice, 2001; Xia et al., 2005). Recent simulations suggest that, for sequences of earthquakes, bimaterial contrasts bias the nucleation sites towards asymmetric ruptures and a preferred rupture direction (Abdelmeguid and Elbanna, 2022; Erickson and Day, 2016). This consequent directivity can amplify ground motion in the path of the propagating rupture, which is an important consideration when evaluating rupture hazards and dynamic stress changes.

The Garlock Fault is a major left-lateral strike-slip fault that extends from the San Andreas to the southern tip of Death Valley and bisects the Eastern California Shear Zone. This fault has been quiet during the historical period but is known to have hosted several large earthquakes in the past few thousand years (Dawson et al., 2003; Madden Madugo et al., 2012; McGill and Rockwell, 1998). The most recent known event on the Garlock Fault took place several hundred years ago, and thus the fault is expectedly late in its interseismic period. Results from a well-studied site on the central segment of the Garlock Fault, which is of particular interest to this study, suggest the most recent earthquake to rupture the surface along the central segment of the fault took place between 1450 and 1610 AD (Dawson et al., 2003). The integrated displacement along the fault is approximately 50 km (Davis and Burchfiel, 1973; Monastero et al., 1997; Smith, 1962) and thus the Garlock is a mature fault with an expectedly well-developed damage zone. Based on empirical scaling relationships between fault displacement and damage zone width, the displacement on the Garlock would suggest a damage zone with a wide range of potential widths, but likely exceeding 100 m (Savage and Brodsky, 2011). Additionally, the large displacement along the fault could have potentially juxtaposed lithologies with distinct seismic velocities, creating a bimaterial contrast across the fault. But the juxtaposition observed at the surface is complicated (see Fig. 4.S1 for geologic map) and is not necessarily representative of the material contrast at depth. Recently, the 2019 Ridgecrest earthquake sequence triggered creep and an earthquake swarm on the Garlock Fault (Ross, Idini, et al., 2019). A rupture on the Garlock is of concern because of its proximity to several communities and because it would likely impose significant dynamic and static stress changes on the San Andreas (Toda and Stein, 2020) or could potentially be triggered to produce a large aftershock of a rupture on the San Andreas, as in the 2023 Kahramanmaras earthquake sequence (Jia et al., 2023).

Imaging fault zones is a challenging problem, particularly at depth, because fault zones are narrow structures, and the resolution of imaging techniques, such as travel-time tomography, typically degrade with depth. Fault structure at depth is important because large earthquakes typically nucleate at least several kilometers (5 km) below the surface (Hauksson et al., 2012), and the fault zone at these depths is thus important for understanding the physics of large ruptures. Hereafter, we refer to depths at which large earthquakes typically nucleate as seismogenic depths. Travel-times from individual earthquakes can sample structure near the fault (Ozakin et al., 2012), but these measurements are depth-integrated, and thus make drawing conclusions about the fault at seismogenic depths difficult. Fault zone trapped waves (e.g., Ben-Zion et al., 2003; Catchings et al., 2016; Qiu, Niu, et al., 2021) and fault zone head waves (e.g., Allam et al., 2014; McGuire and Ben-Zion, 2005) have been used to image fault damage zones and bimaterial contrasts, respectively, with great success. However, a recent study of the Garlock fault (Qiu et al., 2023) shows no fault zone trapped wave observations and some weak fault zone head wave observations, which are also depth-integrated, on the Garlock. This would suggest the damage zone is not an efficient trapping structure and that there is a material contrast across the fault; but the finer details and the depth-dependent behavior of these features are ambiguous. Imaging the depth-dependent properties of the fault damage zone and characterizing the properties of the fault interface at seismogenic depths thus present significant challenges.

Distributed acoustic sensing (DAS) is a technique that measures strain in a fiber optic cable using optical interferometry on backscattered light from laser pulses in the fiber. DAS arrays measure strain at high spatial and temporal frequency and can be deployed with minimal effort for long periods of time. In this study, we use a DAS array that crosses the Garlock to image the depth-dependent structure of the fault zone. To accomplish this, we apply a framework that uses multiple methods with complimentary depth sensitivities to recover the depth-dependent structure of the fault zone. This kind of approach has been successfully applied using dense arrays that cross fault zones in the past (Jiang et al., 2021; Zhang et al., 2022). We first resolve a high-resolution image of the shallow structure using a joint dataset of active source and ambient noise data. Subsequently, we measure the depth-integrated velocity structure on the fault zone using earthquake travel-times from a cluster of earthquakes near the fault. Using a broader set of earthquakes, we infer deeper fault structure using differential travel-times from earthquakes over a larger geographic area. These analyses are all performed using collocated measurements and each uniquely constrain different depth-dependent features of the fault zone.

4.2 A Heterogeneous Shallow Subsurface

The shallowest part of the fault zone has been shown to exhibit sharp, low-velocity anomalies that contribute to considerable ground motion amplification during earthquakes and may signify damage that facilitates fluid transport (Share et al., 2020; Wang et al., 2019; Zigone et al., 2019). The high heterogeneity imposed by the shallow subsurface may also significantly affect depth-integrated measurements which are used to infer the properties of fault zones at seismogenic depths. The shallowest fault zone structure is thus a natural starting point when seeking to understand the fault zone's full architecture, because this structure may subsequently be used to correct for its universal contribution to depth-integrated observations.

In August of 2021, a DAS array was deployed on a dark fiber traversing a path between Ridgecrest, CA and Barstow, CA. The array spans 100 kilometers with 10-meter channel spacing, amounting to 10,000 channels averaging strain over 50 or 100 meters, depending on the recording period (see Fig. 4.1). DAS is a powerful tool for characterizing the shallow subsurface (Atterholt et al., 2022; Cheng et al., 2021; Jousset et al., 2018; Spica, Nishida, Akuhara, Pétrélis, Shinohara, and Yamaha, 2020; Viens et al., 2022; Yang, Zhan, et al., 2022b), and we employ this array to solve for the heterogeneous structure in and around the Garlock Fault. We leverage data with complementary frequency sensitivity from an active source survey that used the in-situ DAS channels as receivers and ambient noise cross-correlations.

The active source experiment was performed using a Propelled Energy Generator (40 kg) source at 10 m intervals along a 1.4 km segment of the array centered on the mapped strand of the Garlock Fault (purple segment; Fig. 4.1a). At each shot location, we performed 10 shots for stacking. During the active source experiment, we reduced the channel spacing and gauge length of the array to 2 m and 16 m, respectively. To produce virtual shot gathers, we cross-correlate ambient noise for a week of continuous data with 10 m channel spacing and 50 m gauge length. Prior to performing the cross-correlations, we bandpass filter the data between 0.1 and 10 Hz and down-sample the data to 25 Hz. We apply absolute-average temporal normalization and spectral whitening to 1-hour segments of the data and subsequently apply cross-correlation and normalization in the frequency domain (Bensen et al., 2007). We then transform the cross-correlations to the time domain

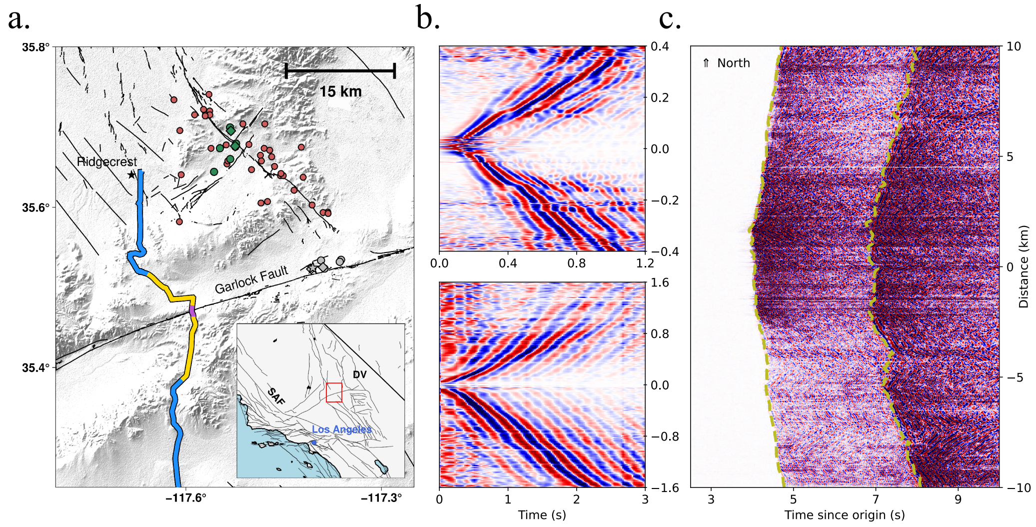

Figure 4.1: Study setting and dataset examples. a. Map summarizing the data used in this study. Blue, yellow, and purple curves represent the entire DAS array, the segment used for the ambient noise experiment, and the segment used for the active source experiment, respectively. Gray and green points show the earthquakes used to construct the profiles in Figs. 4.2 and 4.4. The gray star indicates the earthquake shown in c. The diamond shaped points indicate the earthquakes shown in Fig. 4.S8. Red points show earthquakes that were also used in the inversion in for the bimaterial contrast. Locations of the San Andreas Fault (SAF) and Death Valley (DV) are indicated on the inset. b. Example shot gathers located approximately on the mapped fault trace from the active source (top) and ambient noise experiments (bottom). Active source and ambient noise shot gathers are bandpass filtered between 2-10 and 1-5 Hz, respectively. c. Example of the waveforms from an on-fault earthquake. Olive dotted lines mark the P and S wave picks. Earthquake wavefield is filtered between 1-10 Hz. For b and c, zero distance is the location of the intersection between the central strand of the Garlock Fault and the DAS array.

and organize them into common shot gathers for each virtual source. Examples of both active source and virtual source shot gathers are shown in Fig. 4.1b.

To invert for dispersion curves for both sets of shot gathers, we employ a beamforming approach (Yang, Atterholt, et al., 2022). In short, this approach takes a window of stations around each station that recorded an individual shot gather and measures the local phase dispersion. The window used is set according to the approximate wavelength of the data. This technique resolves many dispersion curves at each channel location for each dataset. The resultant dispersion curves in the immediate vicinity around the fault are shown in Fig. 4.2, and the dispersion curves for an extended region computed using only the ambient noise data are shown in Fig. 4.S2.

We subsequently perform a joint inversion to infer the depth-dependent velocity structure around the fault shown in Fig. 4.3. To accomplish this, we use several key components of the level set tomography approach outlined in Muir and Tsai (2020) and Muir et al. (2022). We parameterize our model as a Gaussian random field that is regularized by a Whittle-Matérn covariance function. The covariance function incorporates a dominant length scale, set to 40 m in this study, and a roughness parameter, set to 2.5 in this study. We choose this length scale both because it conservatively exceeds the minimum gauge length and corresponds to the minimum wavelength in our dataset. Because of the dominant length scale, some of the high spatial frequency features in the data are not captured in the joint model. This is acceptable for our purposes. Setting the roughness parameter to 2.5 is equivalent to enforcing that each individual realization of the Gaussian random process is twice continuously differentiable. The inversion is solved using the Ensemble Kalman Sampler (Garbuno-Inigo et al., 2020). This solver initializes a set of particles and uses Langevin diffusion dynamics to iterate towards the posterior distribution. We incorporate both sets of data into this inversion by computing the model-data misfit for each dataset, weighted by the corresponding standard deviations, at each iteration. For the joint inversion, we up-sample the ambient noise dispersion curve profile so that the dimensions of the two datasets are the same.

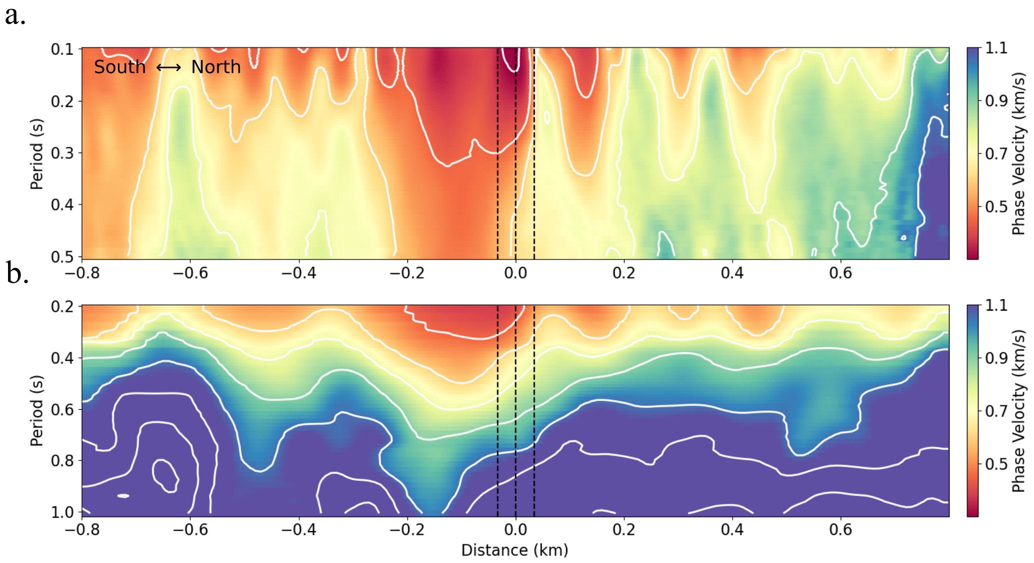

Figure 4.2: Dispersion curves from the active source experiment (a) and ambient noise cross-correlations (b) along the purple segment of the array in Fig. 4.1. Black dotted lines show locations of mapped strands of the Garlock Fault where they cross the velocity profile.

We separately perform an inversion using only ambient noise cross-correlation data for an extended portion of the array using the dispersion curves in Fig. 4.S2. Because of the lower spatial resolution of the ambient noise cross-correlation dataset, we use a dominant length scale of 200 m for this inversion. We merge this model with our higher resolution near-fault model; the discontinuity between these two models is removed by gradual averaging at the boundaries. The resultant extended model is plotted in Fig. 4.S2. We directly compare the near-fault velocity structure recovered using only the ambient noise data with the model recovered using the joint inversion in Fig. 4.S3. While these two models both recover the first-order low velocity feature near the fault, the joint model recovers a more detailed picture of the fault zone. The higher frequency phase velocity measurements from the active source experiment prevent the underestimation of velocities in the shallowest portion of the model, and the higher spatial frequency of the active source data uncovers the low wavelength variability near the fault trace.

The velocity model in Fig. 4.3 shows a rapid transition from lower-velocity material to higher-velocity material with depth. The heterogeneous lateral structure is responsible for sharp velocity perturbations at and across the fault. There is a clear, low-velocity feature biased towards the south side of the fault with a width of approximately 300 meters. This feature could be interpreted as the fault damage zone, but at this depth resolution, it could also be a shallow, potentially fault-associated, basin structure, as has been observed elsewhere (Song and Yang, 2022). Additionally, low velocities (less than 800 m/s) persist in the top 100 meters to the edges of our joint model. To determine if this is potentially a wider compliant zone associated with fault deformation, we can look at the extended model produced using ambient noise cross-correlation in Fig. 4.S2. This model suggests that these low velocities extend at similar depths several kilometers from the fault trace. We thus expect that these low velocities are associated with shallow sediment rather than deformation due to the fault zone. There is also a clear step in velocity across the fault, suggesting a sharp discontinuity due to displacement. The lateral heterogeneity at these depths suggests that the near-fault structure is highly varied, and because local structure plays a large role in ground motion amplification (Aki, 1993), these observations are important for assessing potential ground motion variability due to strong velocity perturbations near faults. Beyond these observations, this model is also a valuable correction term for isolating the fault structure at depth.

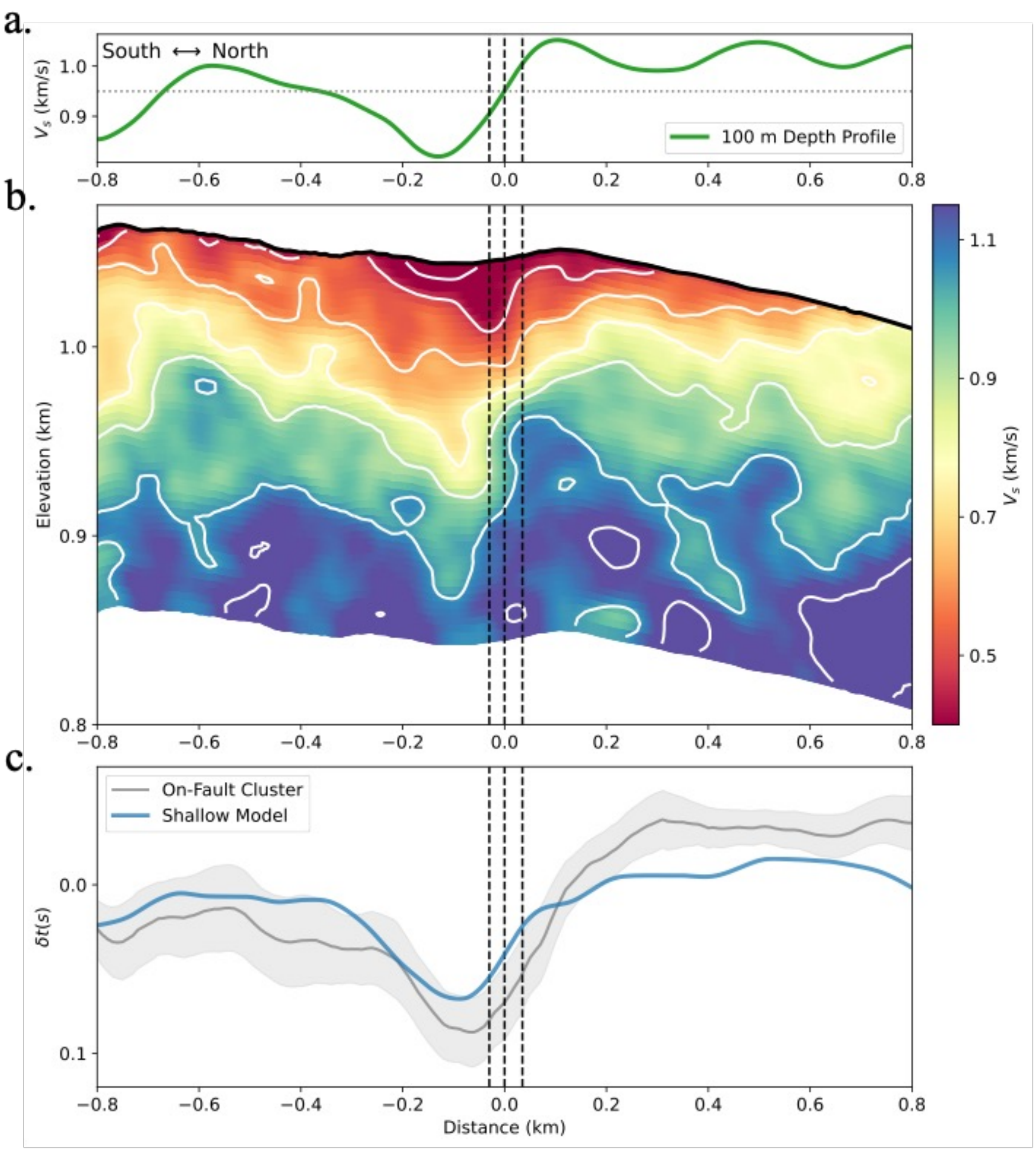

Figure 4.3: Shallow shear wave velocity model and corresponding model-travel-time perturbation comparison along the purple segment of the array shown in Fig. 4.1. a. Profile taken from the shallow velocity model around 100 meters depth (averaged from 80-120 m and smoothed over 200 m laterally) that clearly shows the discontinuity across the fault. b. Shear wave velocity model from the joint inversion of the active source and ambient noise data. Black dotted lines mark the locations of the array-crossing mapped traces of the Garlock Fault. c. Travel-time perturbations from the cluster of earthquakes on the fault in Fig. 4.1 and the expected perturbations from the shallow model. Shallow model perturbations are modified by applying a moving average filter corresponding to the gauge length of the fiber recording the earthquake for comparability.

4.3 An Upper Limit on Damage Zone Size

Earthquake travel-time measurements are sensitive to the velocity structure along the entire ray path, including both seismogenic depths and the shallow crust. Due to the highly productive 2019 Ridgecrest earthquake aftershock sequence, the area around the Garlock fault has produced many earthquakes with variable depths to the northeast of the array (Ross, Idini, et al., 2019). We first focus on a cluster of earthquakes near the Garlock Fault approximately 20 km east of the array and 9 km deep (Fig. 4.1). We use a deep learning algorithm, PhasenetDAS (Zhu et al., 2023), which is designed specifically for DAS data, to pick shear wave phase arrivals from these earthquakes. In short, PhasenetDAS generates training datasets by generating noisy labels for DAS data using Phasenet (Zhu and Beroza, 2018) and refining the labels using GaMMA (Zhu et al., 2022), a phase association algorithm. PhasenetDAS was partially trained using this dataset and, by visual inspection, performs very well for the events used in this study. Examples of these picks are shown in Fig. 4.1 and Fig. 4.S8. To compute the travel-time perturbations for each event, we compute the expected travel-times for a 1D model and subtract these from the observed travel-times. We modify a local 1D velocity profile from the SCEC Community Velocity Model (CVMS) (E. Lee et al., 2014) and compute the travel-times using TauP (Crotwell et al., 1999). The velocity profile used, and the approximate depth-sensitivity of the ray paths are shown in Fig. 4.S4. We then perform an elevation correction assuming an S-wave velocity from the top layer of the Hadley-Kanamori model (Hadley and Kanamori, 1977). The average travel-time perturbations for all events in the cluster are shown in Fig. 3.

We can compute the expected travel-time perturbations for the near-surface structure by computing the travel-time differences for a wavefront propagating through our shallow subsurface velocity model. As shown in Fig. 4.3, the travel-time perturbations very close to the fault are highly consistent between those measured from the earthquakes and the expected perturbations from our shallow velocity model. This would suggest that most of the depth integrated structural contributions near the fault are coming from top few hundred meters, and thus the structural variability at depth, including the variability resulting from the fault damage zone, is minor.

The earthquake travel-times are measured using waveform data with a power spectrum maximum at 6.5 Hz and substantial energy at 10 Hz, as shown in Fig. 4.S5. Assuming shear wave velocities directly below our shallow velocity model slightly higher than 1 km/s, as we observe at the base of our shallow velocity model, we may expect the wavelengths that control the sensitivity of our measurements to be between 100 and 200 m and potentially as large as 300 m. We can use these wavelength estimates to better understand the sensitivity of our measurements to low velocity zone parameters at depths below 200 meters. With this purpose, we perform an evaluation of travel-time perturbations due to different fault zone parameterizations using an Eikonal equation solver (Sethian, 1996; White et al., 2020), and we apply different moving average filters to approximate sensitivities at wavelengths of 100 m, 200 m, and 300 m. The results of these computations, shown in Fig. 4.S6, suggest our measurements are sensitive to low velocity zone features deeper than our velocity model with widths of at least 150 m, and potentially as narrow as 100 m, and velocity perturbation amplitudes above 5%. This would suggest that there is a rapid narrowing or decay of the low velocity zone below 200 meters depth, implying that the Garlock fault's damage zone does not host a wide or high amplitude low velocity feature at depth. The observed low-velocity feature is very small compared to some other faults, such as the Calico Fault, another major Southern California Fault late in its interseismic period, which hosts a substantial low-velocity feature (Fig. 4.S6) (Cochran et al., 2009).

The approach we employ in this section assumes that the across-fault velocity contribution along the ray path between the source and the receiver is representative of the velocity heterogeneity vertically below the shallow velocity profile. This is a reasonable assumption in the shallow crust, where ray paths are nearly vertical, but is less applicable at deeper depths. The velocity correction used to account for travel-time differences due to topography is an approximation. Though we cannot perfectly account for elevation, this correction is sufficient for our purposes, because in this section, we are mostly interested in the low velocity zone in our model. This feature is spatially compact and in a segment of the profile with a low topographic gradient. Additionally, the residual profile will be sensitive to contributions along ray paths that are distinct from those of a 1D model, due to 3D effects. We consider these effects by running the sensitivity tests, which incorporate 3D contributions to ray paths for different structural scenarios.

The reason for the absence of evidence for a low velocity zone at depth is unclear. If we consider the scaling of fault zone thickness with displacement (Savage and Brodsky, 2011) and the inferred cumulative displacement of approximately 50 km on the Garlock Fault (Davis and Burchfiel, 1973; Monastero et al., 1997; Smith, 1962), we may expect the Garlock Fault damage zone to be hundreds of meters thick at depth. One potential explanation is that we are by chance sampling a segment of the Garlock Fault with narrow damage because of along-strike variability in damage zone thickness due to lithological or geometrical changes (Lin and Yamashita, 2013). Such along-strike variability has been clearly observed both in regional tomographic models and systematic fault zone trapped wave studies (Lewis and Ben-Zion, 2010; Zigone et al., 2015). Given that Qiu et al. (2020) observed no compliant zone deformation in response to the Ridgecrest earthquake over an extensive region, we consider this hypothesis unlikely. Another potential explanation is that the Garlock Fault is simply on the low end of damage zone widths for mature faults. Fault damage zones can have a large variety of widths. For example, the Hector Mine and Landers Faults exhibit widths of approximately 100 m (Y.-G. Li, 2002) and 250 m (Li et al., 2007; Li et al., 2000), respectively. There is similar variability among mature faults; the Parkfield segment of the San Andreas Fault, which is far more active and mature than the Garlock Fault, hosts a relatively narrow damage zone between 200-250 m at depth (Hickman et al., 2007; Li et al., 2004). By contrast, the Calico and Anninghe Fault Zones, both late in their interseismic periods, host low velocities zones that in some places exceed widths of 1 km (Cochran et al., 2009; Mu et al., 2024). Mu et al. (2024) partially attribute the wide low velocity zone found at the Anninghe Fault to fault-associated sedimentation. This suggests that factors other than fault damage, such as local geology, may be attributable to the variability in low velocity zone width.

An alternative explanation for the spatially confined damage zone at the Garlock Fault is that considerable fault damage zone healing has potentially taken place over a large segment of the fault, allowing for significant recovery of the seismic velocities in our sensitivity range. This observation is consistent with the absence of fault zone trapped waves near the fault (Qiu et al., 2023) and the lack of compliant zone deformation around the fault following the Ridgecrest Earthquake (Qiu et al., 2020). The combination of these factors and the limit on the width of the low velocity zone determined in this study distinguishes the Garlock from the other fault zones mentioned. Because of these complimentary forms of evidence, we favor the hypothesis that the Garlock's damage zone has undergone substantial healing. This possibility has important implications, but it is difficult to verify without knowing the state of the low velocity zone at the beginning of the interseismic period.

4.4 A Hidden Bimaterial Contrast at Seismogenic Depth

At a broader scale, as shown in Fig. 4.S7, there is significant variability in the earthquake travel-time perturbations that is not captured by the shallow model. The consequences of this variability depend on whether it is localized above the seismogenic zone or present at seismogenic depths. To help resolve this question, we consider the differential travel-time perturbations between earthquakes. This is based on the observation that earthquakes of variant geographic location have distinct ray paths at depth, but that the ray paths become more similar as they approach the surface. This means that differential perturbations emphasize contributions from deeper depths. We first take the differential perturbations between the cluster of earthquakes on the fault and a different cluster farther to the north. Earthquake waveforms from these clusters are shown in Fig. 4.1 and Fig. 4.S8. The differential perturbation profile shows a consistent difference between perturbation profiles that changes polarity at the fault (Fig. 4.4). Since the earthquakes to the north preferentially sample the northern side of the fault at depth, this differential travel-time profile suggests that the southern side of the fault is faster at depth. Importantly, because of the density of the array and the sharpness of this polarity change, this observation localizes the contrast to the fault. This distinguishes this study from lower resolution tomography models, for which it is not possible to determine whether a velocity contrast is due to a fault or broader structural heterogeneity.

We quantify this observation with a Bayesian inversion using many of the M2+ earthquakes observed by the DAS array. The data in this inversion are the differential travel-time perturbations between every pair of earthquakes, and we solve for the necessary changes in computed travel-times in a simple model below the DAS array to match the data. We compute travel-time perturbations for all M2+ events within 30 km of the intersection between the array and the fault. For this analysis, we consider observations from a 20 km segment of the array centered on the Garlock Fault (yellow curve in Fig. 4.1). We remove any events with mean deviations that are greater than 0.2 seconds to ensure that we keep events with reliable hypocentral locations, and we subsequently compute the differential travel-time perturbations for each pair of remaining events. The events used in this analysis are plotted in Fig. 4.1 and the depths for these events are given in Fig. 4.S9. Since we are considering interevent travel-time differences recorded by the same channels, these measurements remove the contribution of receiver-side topography. To improve the quality of our data and obtain good estimates of the uncertainty on these measurements, we take the average and standard deviations, which are used as our uncertainties, of these perturbations

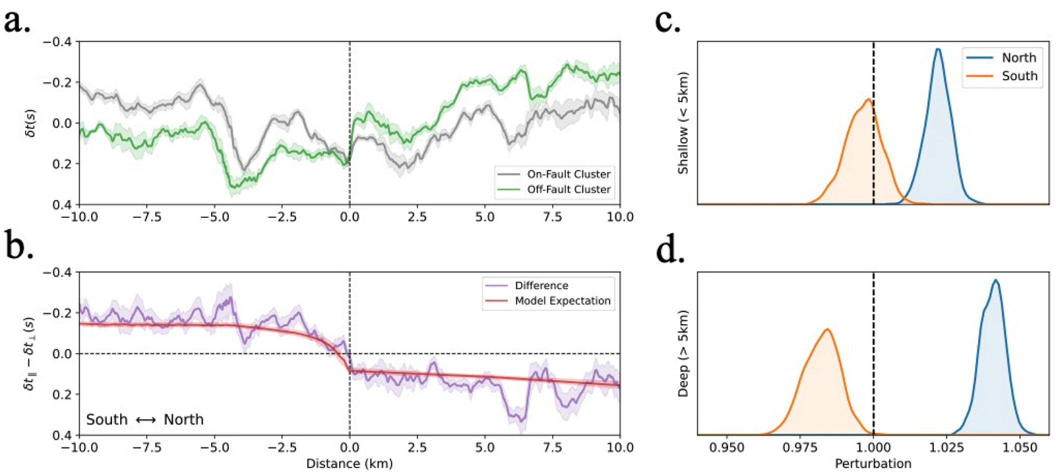

Figure 4.4: Cluster comparison and inversion results from differential travel-time measurements computed along the yellow segment in Fig. 4.1. a. Travel-time perturbations from on-fault (gray) and off-fault (green) clusters of earthquakes, shown in Fig. 4.1. b. difference between the two sets of perturbations (purple) plotted against the model fit from the inversion ensembles. c, d. Ensemble results using differential travel-times to invert for the necessary travel-time adjustments for the shallow (c) and deep (d) earth structure to the north and south of the fault. Joint distributions are shown in Fig. 4.5.

within 1 km bins. These measurements constitute our data vector. We additionally incorporate the standard deviation of the expected arrival time difference to our error estimates. Since the differential travel-times between the two clusters, and in general those between all event pairs used in this analysis, are simple and the polarity change is sharp and close to the fault, we parameterize a simple 4-block earth structure to resolve the velocity contrast across the fault. The lateral and vertical interfaces between blocks are the Garlock Fault and an approximation of the top of the seismogenic zone (5 km depth below sea level), respectively. We assume the Garlock Fault is vertical based on the fault zone reflected wave observation in Qiu et al. (2023). We formulate our inversion using the following equation:

$$d_{A_n - B_n} = \sum_i x_i (t_{A_{ni}} - t_{B_{ni}}) - (t_{An} - t_{Bn}), \tag{4.1}$$

where $t_{A_{ni}}$ and $t_{B_{ni}}$ are the expected travel-times of events A and B through block i in the model at station n, t_{An} and t_{Bn} are the expected total travel-times for events A and B at station n, and x_i is the necessary perturbation to the travel-times through block i to fit the data. The parameters x_i constitute our model vector. An important assumption of this analysis is that the bimaterial contrast does not significantly change between the earthquakes and the array. We also assume the effects of within-fault and broad-scale anisotropy are second order, as we are using a single component measurement and the across fault perturbation change is abrupt.

We apply a simple MCMC approach to solve this inverse problem because of the flexibility of the Bayesian framework and to evaluate tradeoffs between parameters in the inversion. We set a weak Gaussian prior at 1.0 with a standard deviation of 0.1 on each value of x_i to ensure that any perturbation is data informed. As shown in Fig. 4.4, we find that to fit the differential travel-time perturbation profiles, the southern side of the fault is required to be 4-7% faster than the northern side at seismogenic depths (>5 km). The joint distributions, shown in Fig. 4.5, suggest a narrower distribution of relative values, with a bimaterial contrast at depth well-constrained around 6%. This model matches our data, which requires an abrupt change in differential travel-time at the fault, as shown in Fig. 4.4. This velocity contrast is not apparent in the total travel-time measurements around the fault and was instead hidden by shallow crustal structure, which was largely removed by considering the differential times. Since the expected directivity from bimaterial contrasts corresponds to the sense of slip on the slow side of the fault, this would suggest an increased likelihood that future ruptures have a preferred rupture directivity towards Los Angeles and the San Andreas Fault.

Our measurements are consistent with the CVMS model locally at the array, as shown in Fig. 4.S10, and are also consistent with the tomography model of Tong et al. (2021), who find a similar velocity contrast across the central Garlock fault that reverses polarity at depth. But regional velocity models (Lee et al., 2014; White et al., 2021) do not yield a clear picture of a broader velocity contrast along strike. We can corroborate our observation by comparing these results to estimates of velocity profiles from cross-correlations between broadband stations. We consider a year of continuous vertical data on four Southern California Seismic Network broadband stations shown in Fig. 4.6. In a methodology like that described in section 2, we filter the data between 2 and 100 s and decompose the data into day-long segments. We subsequently perform absolute-average temporal normalization and spectral whitening and cross-correlate the waveforms in the frequency domain. We subsequently stack the correlograms and consider only the period band between 5 and 13.5 s for this analysis; these frequencies have high sensitivity to the seismogenic zone (approximately 5-15 km) and depths directly above the seismogenic zone.

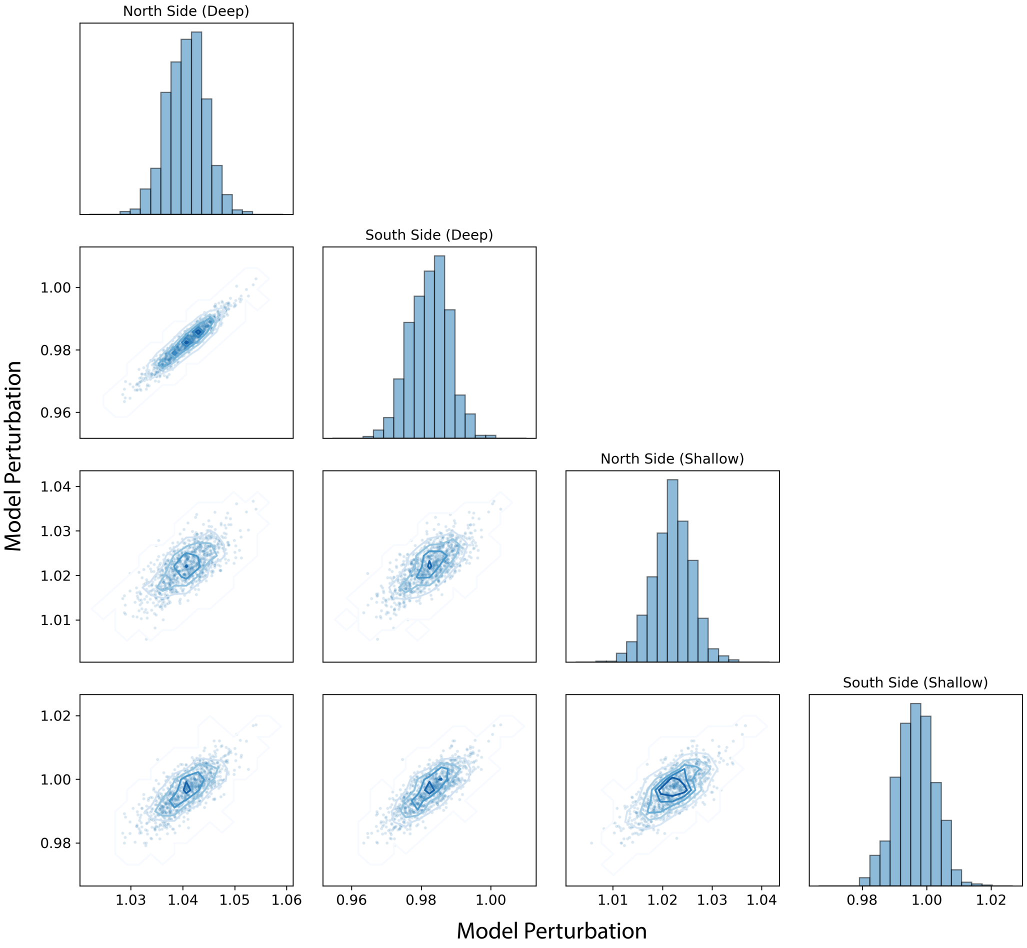

Figure 4.5: Joint probability distributions for ensembles of parameters from the differential travel-time inversion. Diagonal plots show the marginal distributions (also shown in Fig. 4.4), and the off-diagonal plots show the joint distribution for the row-column pairs. The values in these plots are unitless and correspond to the ratio between the time spent in each quadrant necessary to fit the arrival time data and the expected travel-time spent in each region computed using the initial velocity model.

Periods below 5 s did not achieve good convergence and periods above 13.5 s showed substantial phase interference.

We compute the phase dispersion curves by narrowband filtering the data at a set of frequencies and, for each frequency, combine the phase-amplitude relationship with the distance between stations to produce a frequency-velocity dispersion curve. These raw dispersion relationships are shown in Fig. 4.S11. We resolve the 2π ambiguity by picking the frequency-velocity relationship most closely aligned with the Preliminary Reference Earth Model (Dziewonski and Anderson, 1981). We estimate the uncertainty on these measurements using the width of the peak that we pick. We then use surf96 from the Computer Programs in Seismology package (Herrmann, 2013), which applies an iterative, weighted inversion, to recover the 1D shear wave velocity structure from these dispersion curves. The dispersion curves and corresponding velocity profiles are shown in Fig. 4.6. These profiles suggest that in a 100 km window along-strike, encompassing our array, the velocities to the north of the fault are faster at shallow depths but slower below 6 km, which is highly consistent with our local model. The amplitude of the velocity contrast across the fault at depth is also consistent with our local model. This suggests that what we observe in this study is perhaps an extensive rather than a local feature.

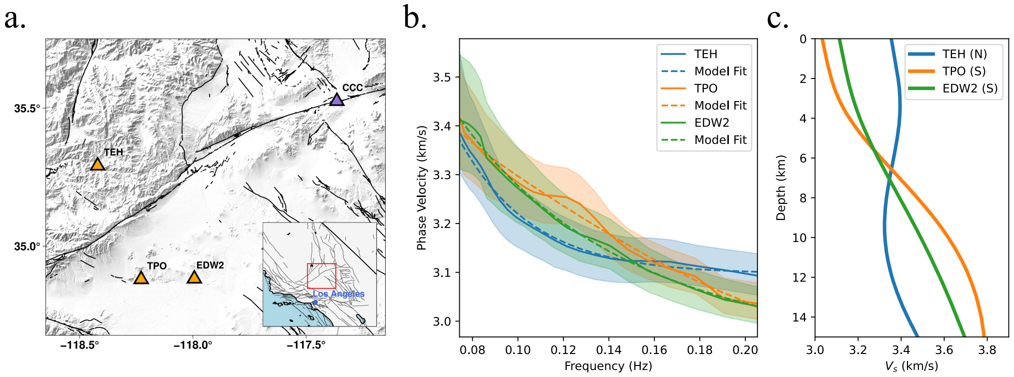

Figure 4.6: Results from the broadband seismic analysis. a. Station map showing the stations used in this analysis. Each off-fault station (orange) was cross-correlated with the on-fault station (purple) to produce the corresponding models. b. The dispersion curves from each of the cross-correlation measurements and c. the corresponding inverted shear wave velocity profiles.

4.5 Discussion and Conclusions

This study provides the depth-localized structure of a major fault zone in California through careful comparisons of multiple forms of analyses with collocated, high spatial density measurements. The deconvolution of measurement contributions from different parts of the fault zone suggests the fault zone model in Fig. 4.7. In particular, the near-surface component of the schematic is determined using the shallow velocity model that incorporates active source and ambient noise phase velocity measurements. The portion of the model at seismogenic depths is determined using the inversion of the differential travel-time perturbation measurements shown in Fig. 4.4. The shallow crust portion of the model is subsequently determined by measuring the residual between the measured travel-times of the cluster of earthquakes on the fault and the expected combined contributions from the near-surface and seismogenic depths. A summary of the travel-time contributions informing this schematic is shown in Fig. 4.S7. Deconvolving the different contributions to depth-integrated measurements is important because depth-integrated measurements may sometimes be misleading. For example, interpreting the fault zone structure using only the depth-integrated travel-time measurements near the fault zone may lead to the conclusion that the low velocity zone to the south of the fault is consistent with a typical persistent fault damage zone structure, and that seismic velocities are faster to the north and slower to the south at seismogenic depths, but these are the opposite conclusions of those presented in this study. These observations likely explain the differences between this study and that of Qiu et al. (2023), who used fault zone head waves to determine that the north side of the fault is faster than the south side of the fault. These head wave observations, which are depth-integrated, may have been dominated by the velocity contrast in the shallow crust that is evidenced in Figs. 4.S7 and 4.6 and illustrated in Fig. 4.7, rather than the contrast with the opposite polarity at seismogenic depth.

These results also show several strengths of DAS for making detailed observations of fault zones. The combined high spatial density of the channels and the low-effort maintenance allowing for long term deployments provide the tools necessary to both perform detailed imaging studies and make observations of many earthquakes with the same array. Performing these analyses with the same array allows for the direct comparison of the results and the subsequent localization of contributions to measurements from depth-localized structures in the fault zone. The application of DAS to fault zone related problems is not limited to the analyses performed in this study, and one can easily envision new possibilities for fault zone research that leverage the strengths of DAS data. For example, DAS arrays deployed across faults could potentially act as long-term, low-maintenance fault zone observatories that could be used to illuminate time-dependent changes in fault zones due to processes such as healing and to better capture seismicity along the fault.

The recovery of seismic velocities in the interseismic period is typically attributed to fault zone healing resulting from fracture closure due to mechanical (Brantley, 1992; Brantley et al., 1990; Brantut et al., 2013) and chemical (Aben et al., 2017; Lee and Morse, 1999; Renard et al., 2000) processes. Studies on fault zones immediately following earthquakes have shown measurable increases in seismic velocity and decreases in permeability with time, suggesting significant healing can take place

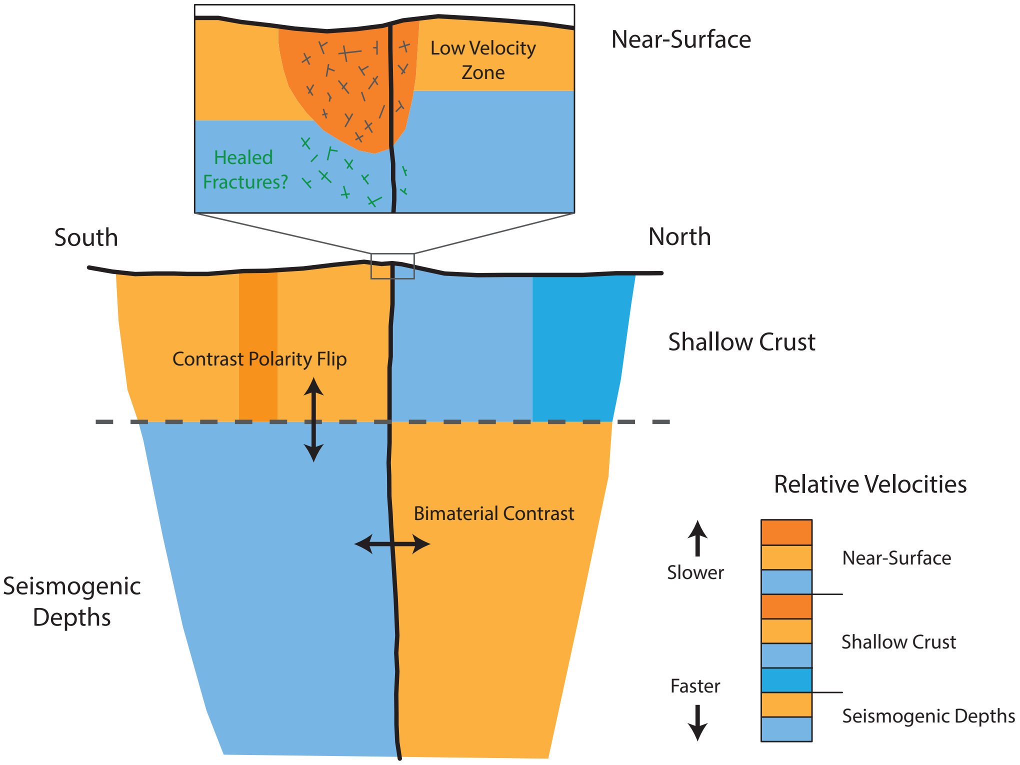

Figure 4.7: Schematic model summarizing the findings of this study.

shortly after an earthquake (Li and Vidale, 2001; Marone et al., 1995; Xue et al., 2013). The amount and rate of healing that takes place over the course of the interseismic period is likely highly variable. The presence of low velocity zones and fault zone trapped waves in faults that have not ruptured for decades suggest that some damage zones persist throughout the interseismic period (e.g., Cochran et al., 2009). Some studies suggest crack healing can occur rapidly, on the order of years (Hiramatsu et al., 2005), and others have observed substantial healing due to the sealing of fractures in exhumed fault zones (Rempe et al., 2018). A recent study using a borehole from the Alpine Fault, another fault late in its interseismic period, suggested that, for at least part of the fault zone, fractures near the fault had little impact on seismic velocity because of extensive mineral precipitation in the fractures (Williams et al., 2016). We speculate that the segment of the Garlock Fault, which is in a region of high hydrothermal activity (Sass et al., 1978), may have experienced similar healing as illustrated in Fig. 4.7. This is evidenced, not only by the low upper limit of damage zone width and velocity perturbation amplitude determined in this study, which is not sufficient evidence by itself, but also by the absence of damage zone indicators such as fault zone trapped waves (Qiu et al., 2023) and compliant zone deformation following the Ridgecrest earthquake (Qiu et al., 2020). We cannot definitively say whether this is the case, as the initial state of the damage zone following the last major earthquake is unknown. However, the enigmatic condition of the Garlock Fault's damage zone at depth warrants future study. One potential avenue for future research on this issue would be to investigate borehole data for evidence of healing as done in Williams et al. (2016).

Experimental and observational work investigating the relationship between bimaterial contrasts on faults and rupture directivity have discovered a range of behaviors (e.g., Harris and Day, 2005; Kane et al., 2013; Rubin and Gillard, 2000; Shlomai and Fineberg, 2016; Wang and Rubin, 2011; Xia et al., 2005). Dynamic simulations of sequences of ruptures on bimaterial interfaces suggest that, although a material contrast across a fault does not dictate the direction of rupture asymmetry invariably, the presence of a bimaterial contrast over an earthquake sequence creates favorable nucleation sites and increases the likelihood of asymmetric rupture in one direction over the other (Abdelmeguid and Elbanna, 2022; Erickson and Day, 2016). Further complications arise when fault complexity, such as fault curvature and along strike stress variability, is introduced. But, keeping these complications in mind, we can use the observed bimaterial contrast on the Garlock Fault to infer if there is an increased likelihood of a rupture propagating one direction over the other. The Garlock fault perhaps presents an ideal setting for this kind of analysis, as the highly limited low-compliance zone at depth suggests a potentially simpler fault structure. In the case of this study, the bimaterial contrast, which we have localized to seismogenic depths, suggests a future rupture on the Garlock Fault is more likely to propagate towards the San Andreas. This would suggest an increased likelihood of forward directivity ground motion amplitudes to the west of a given rupture, which is an important consideration for both the communities on the fault and those to the west, including Los Angeles. This would also greatly increase the dynamic stress change induced on the San Andreas, and thus may increase the likelihood of a rupture on the Garlock triggering a rupture on the San Andreas (Hill and Prejean, 2015; Toda and Stein, 2020).

Supplementary Materials

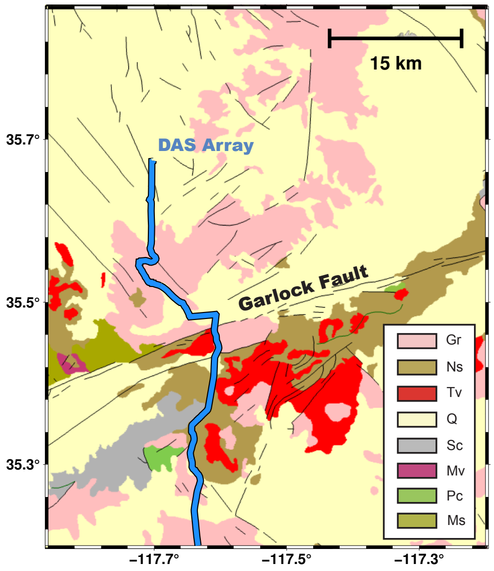

Figure 4.S1: Geologic map of the study region with units defined in the Geologic Map of California (Jennings et al., 1977). The dimensions of this map are the same as those in Fig. 4.1. Black lines are faults. Gr = Mesozoic granitic rocks | Ns = Plio-Pleistocene and Pliocene loosely consolidated deposits | Tv = Tertiary volcanic flow rocks | Q = Quaternary alluvium | Sc = schist of various types | Mv = Paleozoic metavolcanic rocks | Pc = Precambrian rocks | Ms = Paleozoic marine rocks.

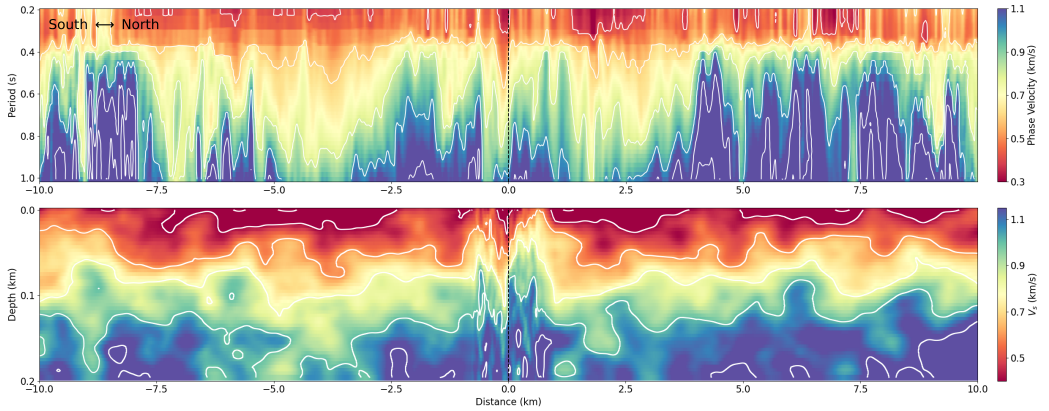

Figure 4.S2: Extended shallow imaging experiment phase (top) and shear wave velocity (bottom) models.

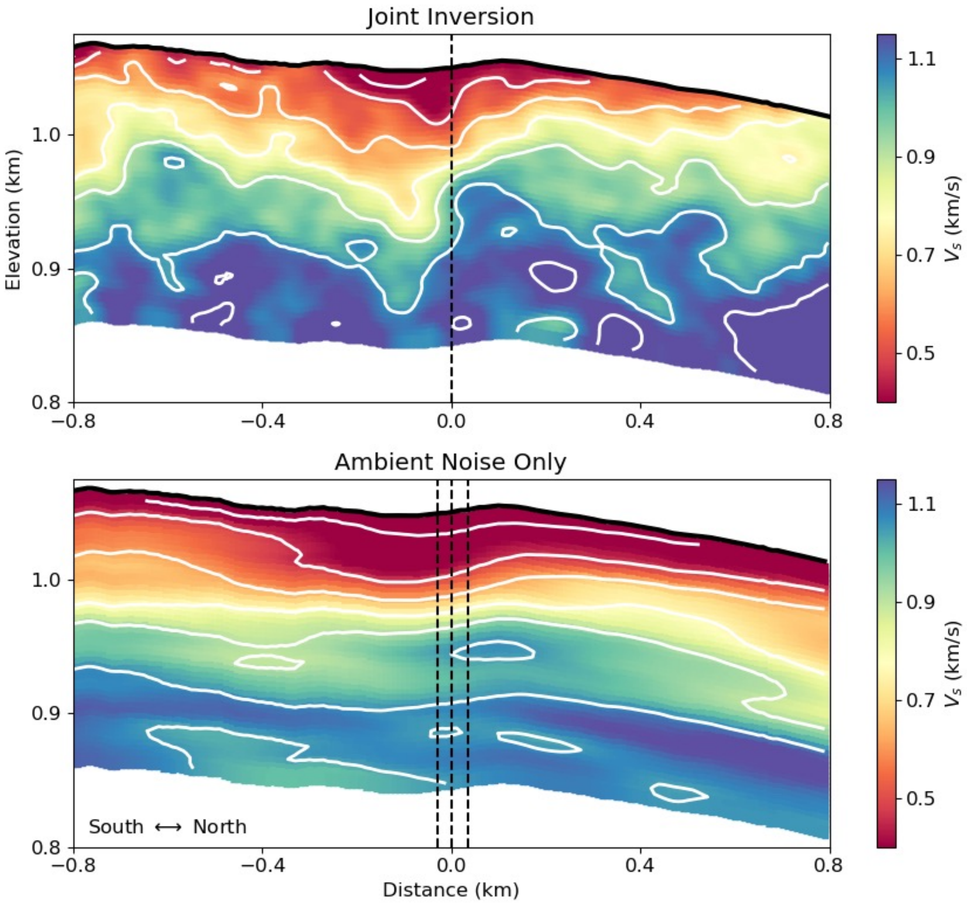

Figure 4.S3: Comparison of the near-fault velocity model recovered from the joint inversion (Fig. 4.3) and the inversion using only ambient noise data (Fig. 4.S2).

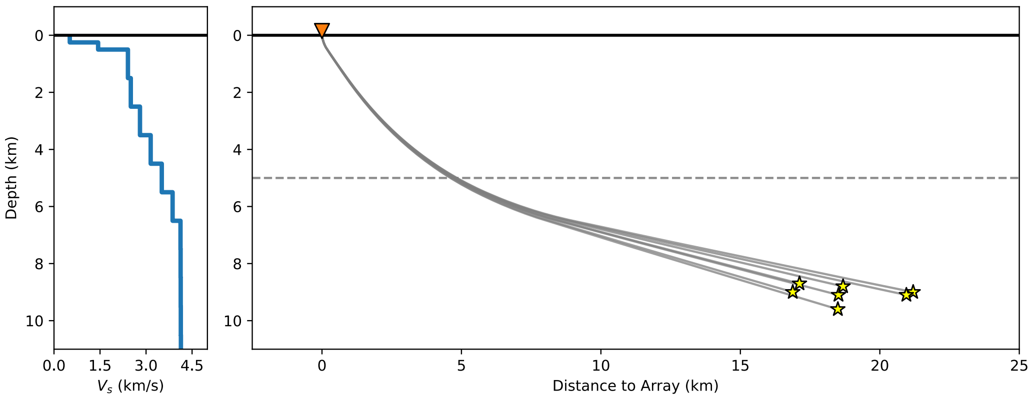

Figure 4.S4: 1D velocity model and approximate ray paths. Left: velocity profile used to isolate travel-time perturbations from 3D structure. Right: approximate ray-paths between near-fault event cluster and DAS channel collocated with the mapped trace of the Garlock Fault.

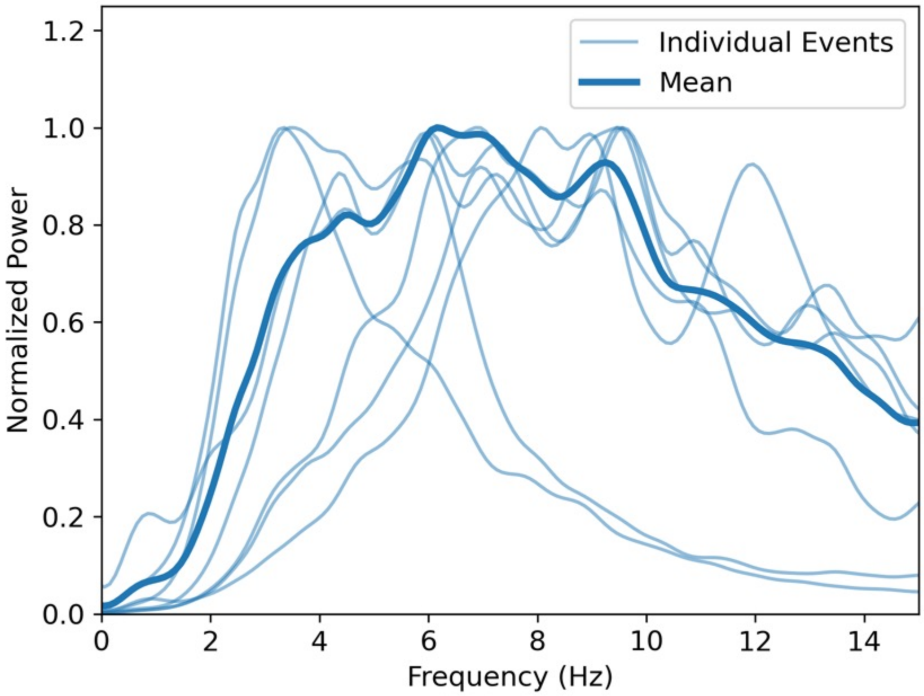

Figure 4.S5: Normalized power spectra of the earthquake wavefields of events in the cluster of earthquakes on the Garlock Fault.

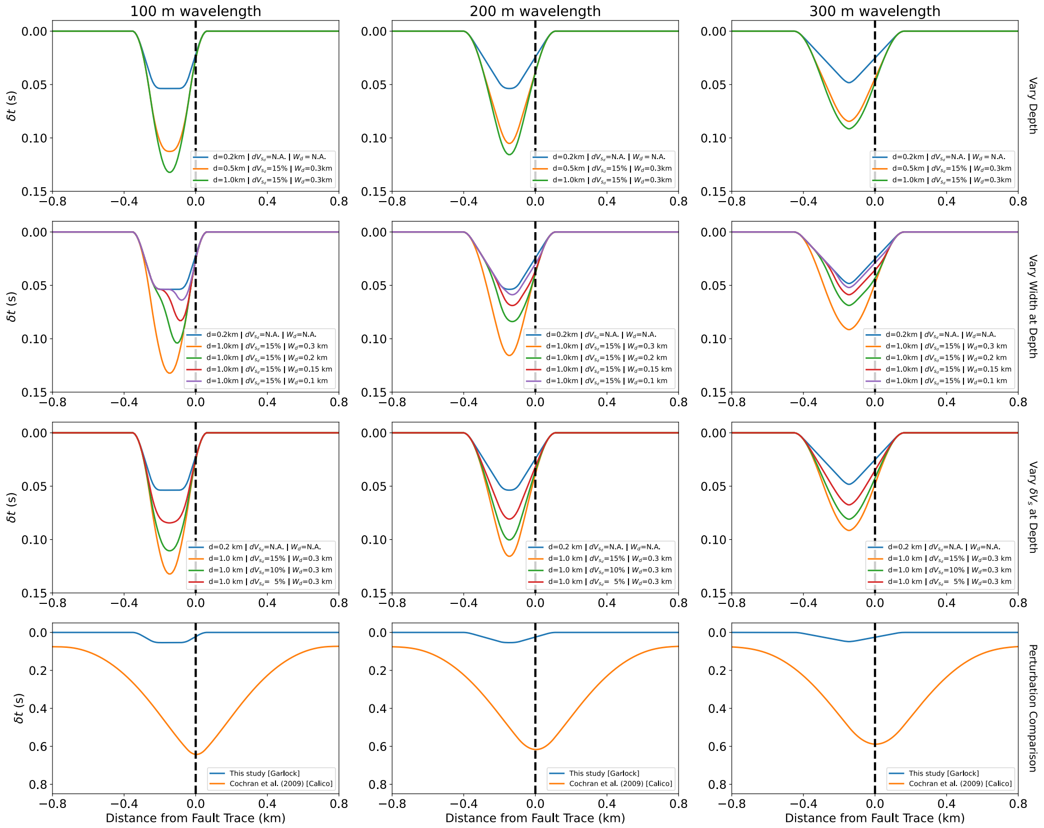

Figure 4.S6: Parametric evaluation of the sensitivity of our array to different velocity features at depth and comparison to velocity feature from Cochran et al. (2009). In this plot we vary depth of damage zone (d), velocity perturbation at depths greater than 0.2 km (dV_{sd}) and the width of the damage zone at depths greater than 0.2 km (W_d).

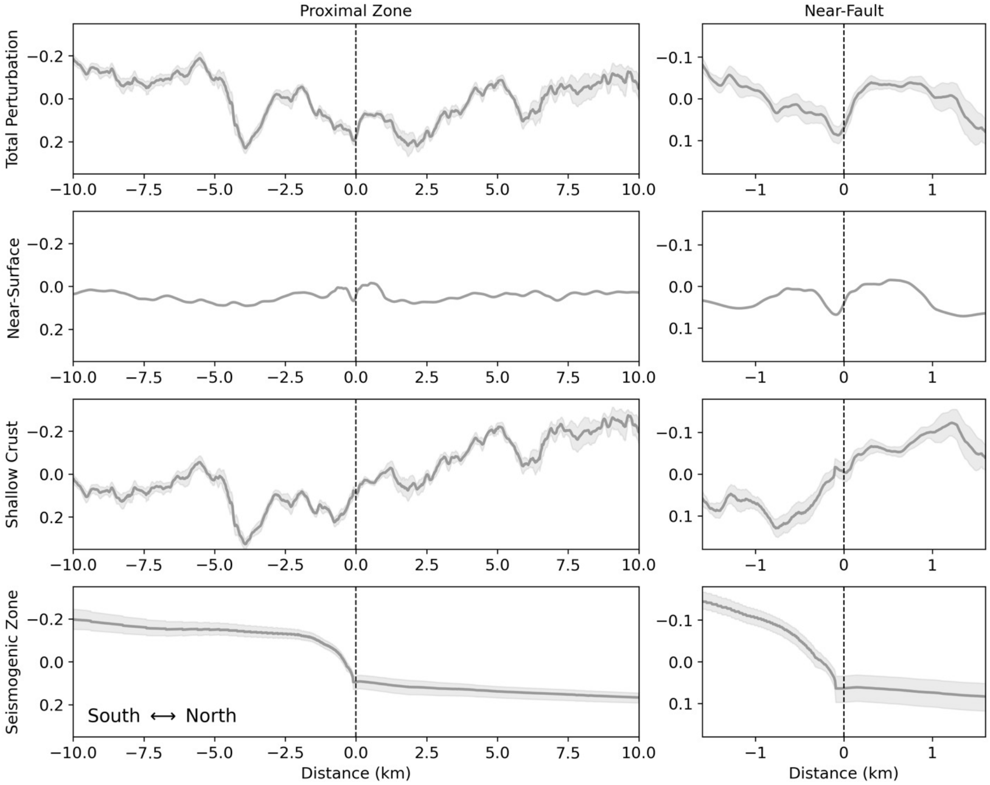

Figure 4.S7: Travel-time perturbations from the gray cluster of earthquakes shown in Fig. 4.1 at different distances from the Garlock fault for illustration. Near surface perturbations are computed using the model in Fig. 4.2. Seismogenic zone perturbations are computed using the model in Fig. 4.4. Shallow crust perturbations are computed as the difference between the total perturbations and the combined perturbations of the near surface and seismogenic zone. Black dotted line indicates location of Garlock fault in the USGS Quaternary Fault Database.

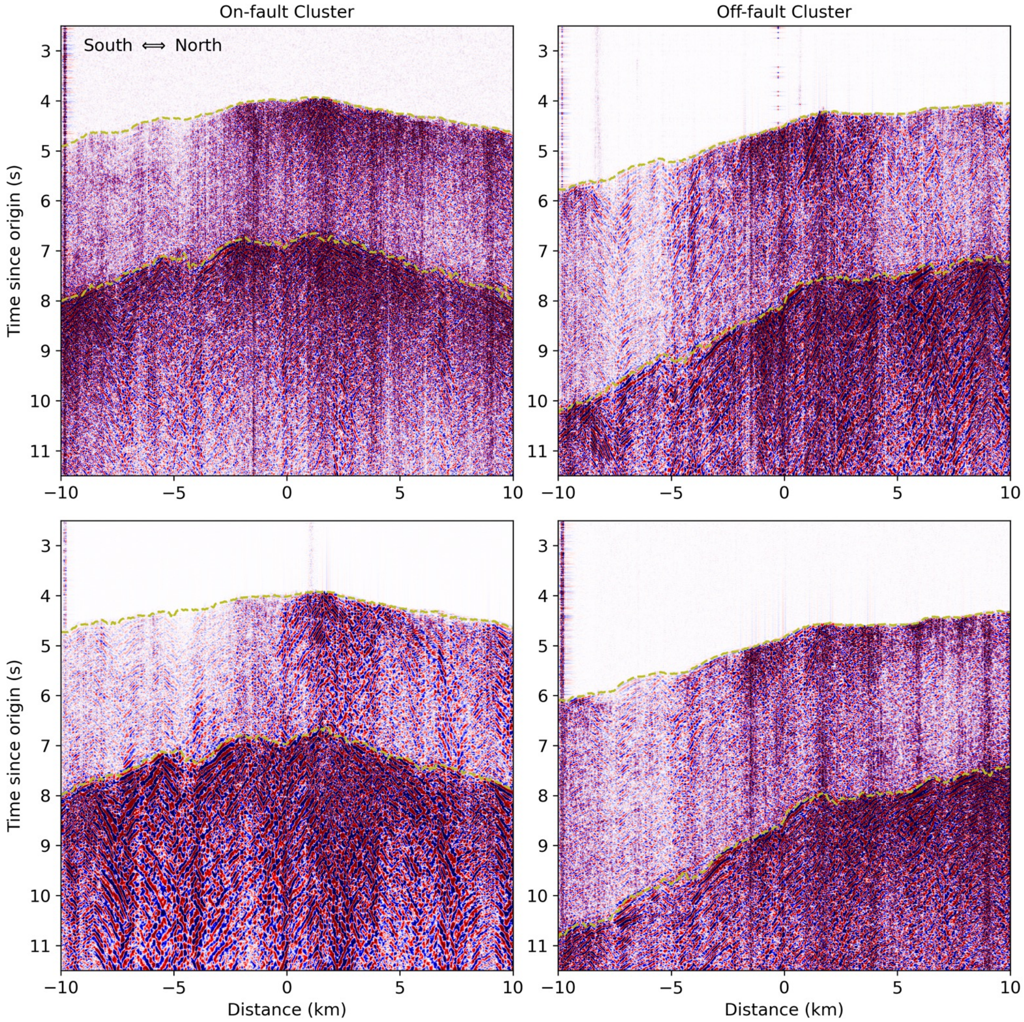

Figure 4.S8: Examples of earthquake wavefields from clusters of earthquakes on and off the Garlock Fault. Locations of these earthquakes are indicated by the diamond markers on the map in Fig. 4.1. Olive-colored dotted lines indicate the P and S phase picks made by PhasenetDAS.

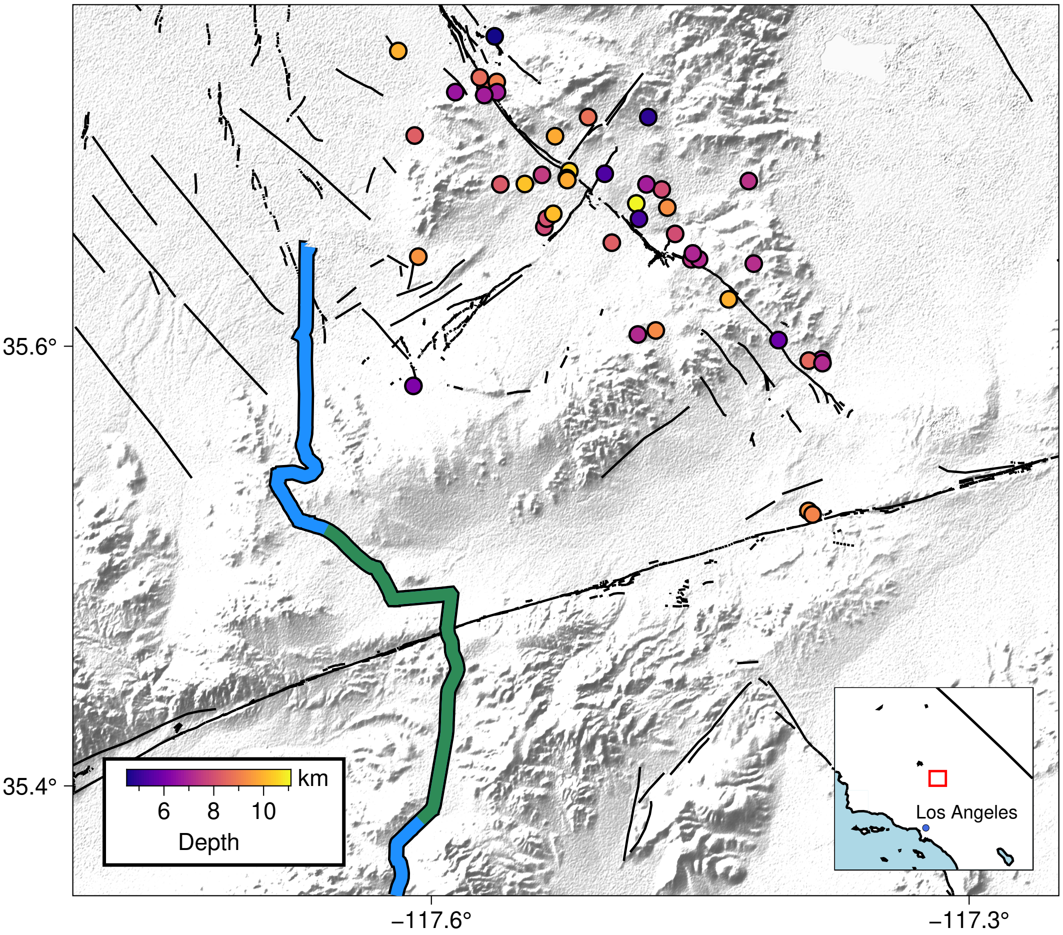

Figure 4.S9: Map of events used in the inversion for the bimaterial contrast across the fault. Green segment of the array indicates the channels from which travel-times were used.

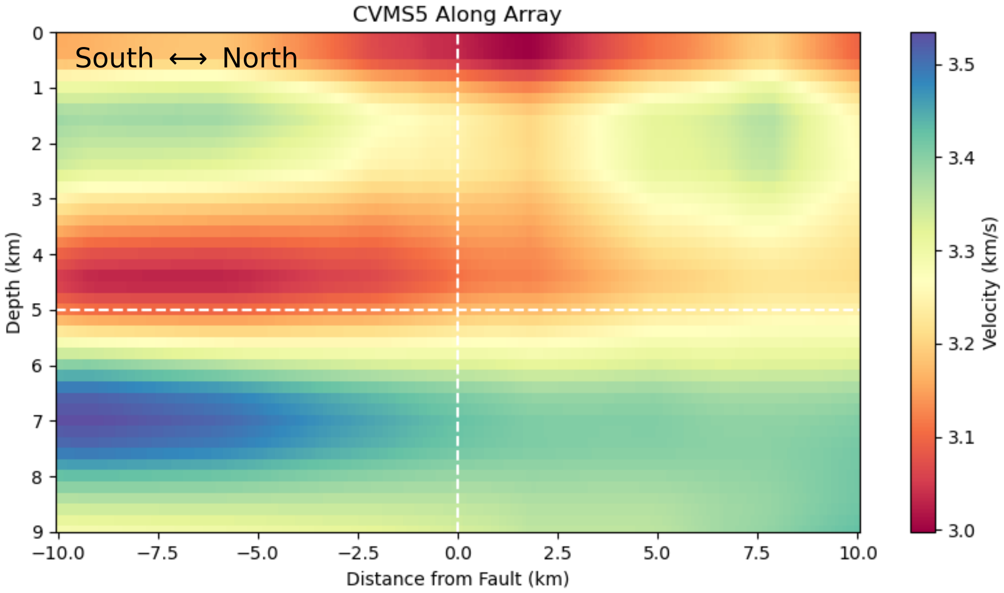

Figure 4.S10: The SCEC Community Velocity Model along a path collocated with the DAS array used in this study. Note the high velocity anomaly at depth on the south side of the model.

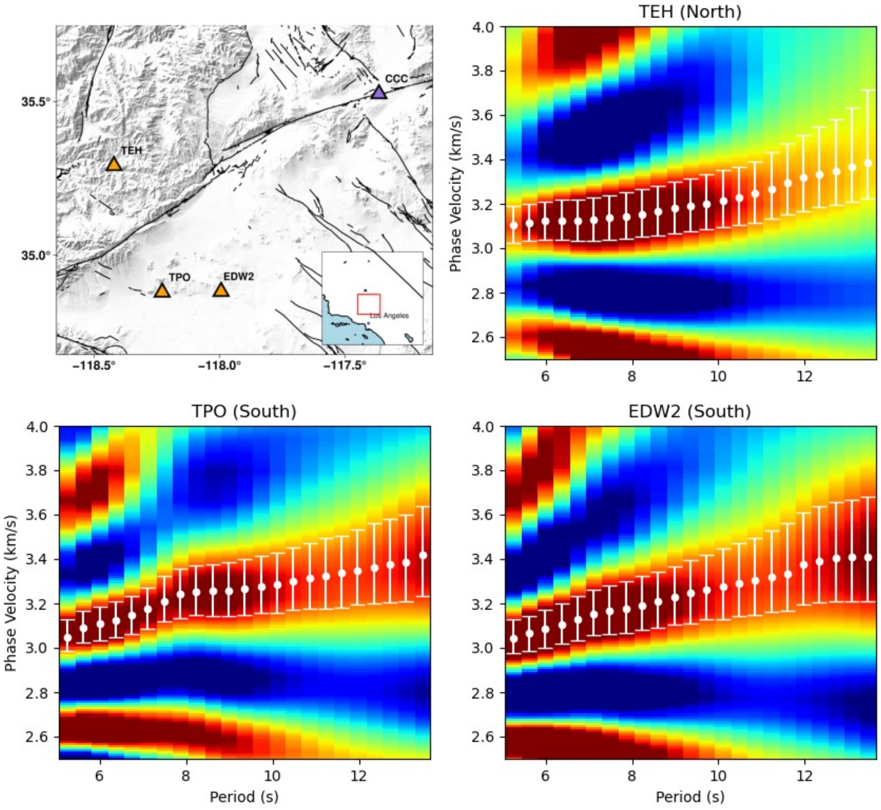

Figure 4.S11: Setting and phase velocity picks for the low-frequency broadband cross-correlation measurements. Top left plot shows station locations used in this analysis. The Christmas Canyon station (CCC) was a member of each cross-correlation pair. Other plots show measurements and error estimates of phase velocity dispersion measurements.

Chapter 5

MAPPING FINE-SCALE MOHO TOPOGRAPHY WITH DAS WAVEFIELDS

Atterholt, J. and Zhan, Z. (In Review). Fine scale Southern California Moho structure uncovered with distributed acoustic sensing.

Abstract

Moho topography can yield insights into the tectonic evolution of the lithosphere and the strength of the lower crust. The Moho-reflected phase (PmP) samples this key boundary and may be used in concert with the first arriving P phase to infer crustal thickness. The densely sampled station coverage of distributed acoustic sensing (DAS) arrays allows for the observation of the PmP phase at fine-scale intervals over many kilometers with individual events. We use the PmP phase recorded by a 100 km-long fiber that traverses a path between Ridgecrest, CA and Barstow, CA to explore the structural variability of the Moho in Southern California. With hundreds of well-recorded events, we verify that PmP is observable and develop a technique to identify and pick the relative arrival time between the first arrival and PmP with high confidence. We use these observations to constrain Moho depth throughout Southern California, and we find that low-wavelength variability in crustal thickness is abundant, with sharp changes across the Garlock Fault and Coso Volcanic Field.

5.1 Introduction

Observations of Moho structure are important because they provide evidence of processes that deform the lithosphere and yield constraints on the rheology of the lower crust (McKenzie et al., 2000; Zhu et al., 2006). Crustal thickness varies over many scales, and fine-scale variability is important because it constrains the depth-extent and depth-dependent behavior of localized tectonic processes observed at the surface (e.g., Liu et al., 2017; Luo et al., 2021; Yu et al., 2021; Zhu and Kanamori, 2000). The most popular methods for uncovering Moho structure are receiver functions and seismic reflection surveys. Receiver functions are a powerful tool for robustly determining Moho depth (e.g., Li et al., 2022; Sui et al., 2023; Yan and Clayton, 2007; Zhu, 2000), but are a low frequency measurement that requires seismometers near the measurement points, limiting their spatial resolution and geographic coverage. Reflection surveys can uncover Moho variability at impressive resolution (e.g., Cheadle et al., 1986; Fliedner et al., 2000; Li et al., 1992), but these surveys are expensive and often fail to penetrate Moho depths.

An alternative to these techniques is to use the Moho reflected phase (PmP), which provides constraints on Moho depth (Ding et al., 2022; Li et al., 2022; Nakajima et al., 2002; Richards-Dinger and Shearer, 1997; Salah and Zhao, 2004) and lower crustal velocity structure (Huang et al., 2016; Li et al., 2024; Wang et al., 2022; Xia et al., 2007). The advantage of using PmP over other methods is that measurements are made passively using higher frequency regional earthquakes and, with the right seismicity distribution, can resolve structure outside a seismic network. This technique has not been used as frequently as others because PmP is difficult to confidently identify on individual seismograms (Richards-Dinger and Shearer, 1997). Recent studies have found success using multi-event estimates of PmP moveout and machine learning techniques to generate expanded PmP catalogs (Ding et al., 2022; Li et al., 2022). These techniques are not readily transferrable to or ideal for dense array datasets that generally have lower data quality but high spatial sampling. The high frequency content of PmP observations combined with dense array datasets may allow for very high-resolution sampling of low wavelength features near the crust-mantle boundary.

Distributed acoustic sensing (DAS) is an increasingly popular technique in seismology that transforms fiber optic cables into dense arrays of strainmeters using phase interferometry of backscattered light (Zhan, 2020). This technique is powerful because it enables the deployment of extensive, dense seismic networks for long periods of time at low logistical burden. DAS is routinely employed for shallow crustal imaging (e.g., Cheng et al., 2021; Spica, Perton, et al., 2020; Yang, Atterholt, et al., 2022) and has recently been used to resolve structure in the middle crust using travel-time tomography (Biondi et al., 2023). The dense recordings enabled by DAS facilitate low-wavelength observations over large distances, and the long deployment times allow for the passive recording of high-quality earthquake wavefields with diverse source locations. While receiver functions have been successfully computed by combining DAS data with nearby broadband data (Yu et al., 2019), wider adoption of deep crustal imaging techniques with DAS has been slow, because DAS has high noise levels at low frequencies (R. Fernández-Ruiz et al., 2019). PmP is an especially promising avenue for realizing the potential of DAS for deep crustal imaging for a few reasons. Firstly, PmP is a high frequency phase, and DAS is most sensitive to higher frequency wavefields. Secondly, the high spatial density and abundance of channels in DAS arrays allows for both spatial coherence and array-side moveout to be used to identify PmP. Thirdly, although DAS arrays have many channels, the cable geometry often imposes a narrow geographic footprint; with PmP, Moho depth measurements may be made over a much larger area than is covered by the fiber.

In this study, we introduce a method with which to identify and pick relative arrival times of secondary phases in DAS data. We apply this method to a DAS array in the Mojave Desert to measure PmP differential times and use these observations to invert for Moho depth over a wide area. We find good correspondence with previous results, and we make novel observations of low-wavelength features in the Moho across the Garlock Fault and the Coso Volcanic Field. This technique offers a promising outlook for using DAS arrays to make fine-scale observations of lithospheric structure over broad geographic areas.

5.2 Autocorrelation for Secondary Phase Retrieval

In August of 2021, a DAS array was deployed on a 100 km segment of dark fiber between Ridgecrest, CA and Barstow, CA (Figure 5.1). This array has 10,000 channels with 10 m channel spacing and 100 m gauge length. Over the course of a two-year recording interval, the array recorded 440 M2.5+ regional earthquakes. Many of these earthquake wavefields exhibit strong secondary phase arrivals that coincide with the expected onset time of the Moho reflected phase (PmP) for a standard 1D earth model (e.g., Hadley and Kanamori, 1977). The relative arrival time between the first arriving P-phase and PmP provides a strong constraint on crustal thickness (Figure 5.2). Coupled with the spatial density of DAS, P-PmP differential times can yield very low wavelength profiles of Moho depth.

Identifying and measuring the relative arrival times of PmP on DAS data can be a challenging problem. Firstly, although PmP is often the strongest phase in P-wave coda, it has historically been very challenging to identify in broadband data, with only 1% of records showing readily identifiable PmP waveforms (Ding et al., 2022). DAS presents an advantage towards identifying this phase; the spatial density of DAS arrays allows for the evaluation of candidate phases across a broad spatial window. This spatial window allows for the use of spatial coherence and array-side moveout to assist in identifying secondary phases like PmP. Once identified, however, it is impractical to pick the thousands of phase arrivals recorded by DAS for

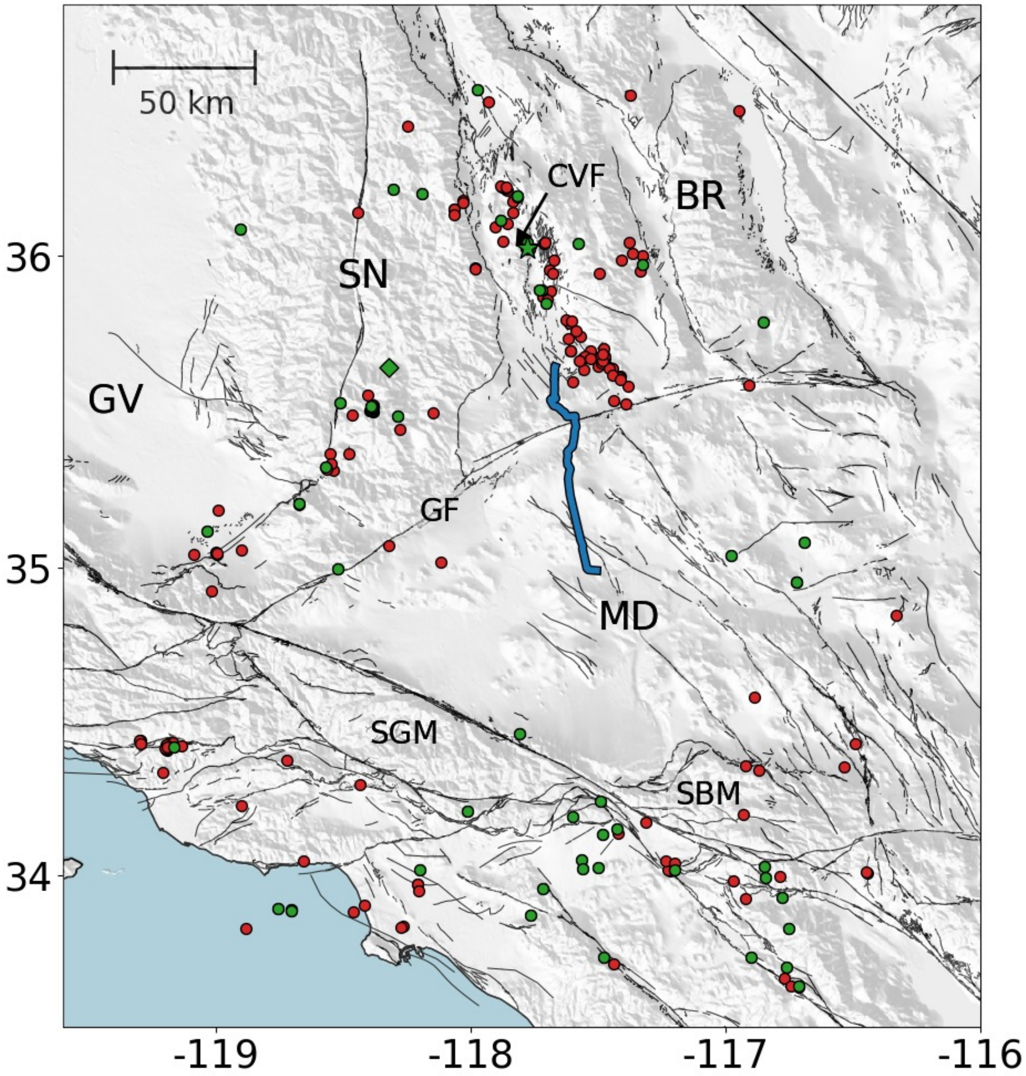

Figure 5.1: Experiment setting and data. The DAS array geometry (blue curve) plotted against the kept (green) and discarded (red) M2.5+ events recorded by the array. Also plotted are the fault traces included in the USGS Quaternary Fault Database (2018) and locations of relevant tectonic provinces and features (GV = Great Valley | SN = Sierra Nevada | BR = Basin and Range | MD = Mojave Desert | CVF = Coso Volcanic Field | GF = Garlock Fault | SGM = San Gabriel Mountains | SBM = Santa Barbara Mountains).

every earthquake wavefield by hand. Traditional automated phase picking methods are usually inadequate for these data because P-phase onsets are often weak and complicated in DAS due to broadside insensitivity of axial strainmeters and strong surface wave scattering due to local heterogeneities. Machine learning methods,

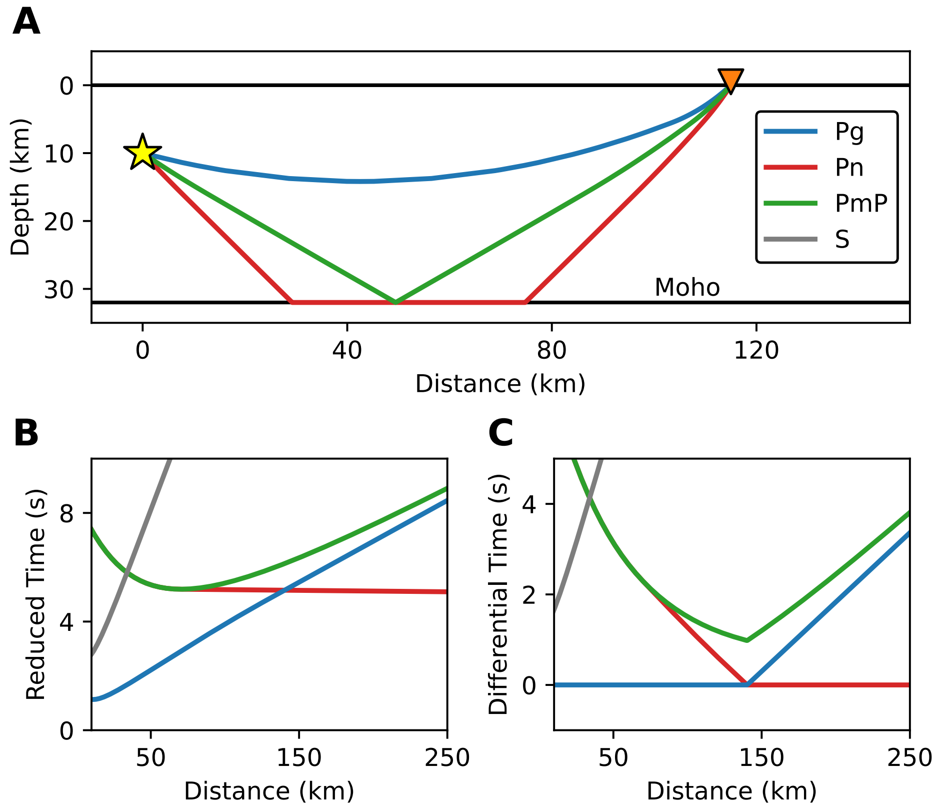

Figure 5.2: Important phases and relative arrival times. (A) Ray paths for the three phases of interest in this study for a fixed source-receiver distance and representative velocity model: the direct phase (Pg), the Moho head wave (Pn), and the Moho reflected wave (PmP) (S not pictured for simplicity). (B) Reduced (8.1 km/s) arrival times of phases plotted against source-receiver distance. (C) Differential times of phases relative to the first arriving P-phase plotted against source-receiver distance.

such as PhaseNet DAS (Zhu et al., 2023), have shown promise toward addressing this problem, but as of now they have not been adapted to secondary phases.

We develop a simple and effective approach to both identify and pick relative arrival times of secondary phases like PmP. Because the scattered surface waves that are nearly ubiquitous in DAS data are generated locally (Atterholt et al., 2022; Lindsey et al., 2019), these waves are common to both the first arrival and secondary arrivals. These phases consequently generate complicated but highly correlated wavefields. The autocorrelation of DAS-recorded earthquake wavefields is thus a potentially powerful tool for making highly accurate relative phase arrival time measurements. We apply a straightforward and semi-automated framework for identifying PmP and obtaining P-to-PmP differential times for DAS data (see Methods). This methodology is outlined using an example in Figure 5.3. Of the initial set of events, 229 events had visually identifiable P-phase onsets and some high-quality first arrival picks. Of this smaller subset of events, we can observe and pick PmP arrivals over large spatial windows for 72 events. Additionally, as shown in Figure 5.2, by evaluating the change in differential time with source-to-receiver distance, we determine for each observation whether PmP is trailing a direct wave (Pg) or a mantle head wave (Pn) first arrival. From this dataset, our workflow yields over 200,000 accurate and precise P-PmP differential times that may be used to constrain the velocity structure and crustal thickness throughout Southern California. These picks and the corresponding correlograms are shown in Figure 5.4.

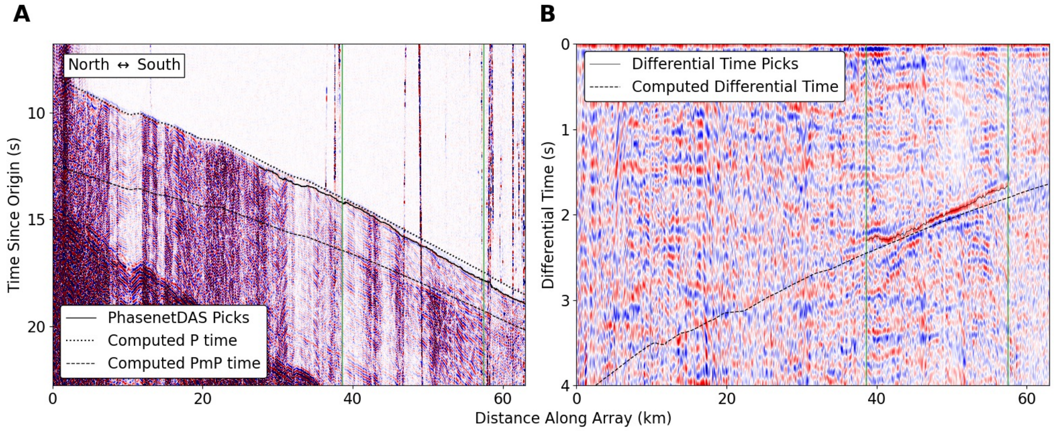

Figure 5.3: Example of autocorrelation for phase retrieval. (A) Earthquake wavefield with representative data quality. Included are the PhaseNet DAS picks and computed P and PmP times for the representative velocity model used in this study with a Moho depth of 32 km. Green bars are a reference for the channel bounds within which differential time picks were made. (B) Autocorrelation image created for the corresponding earthquake wavefield using the framework outlined in the text. Included are the computed P-PmP differential times and the picks made on the positive correlation peak associated with the PmP arrival. Location of this event is indicated as a green star in Fig. 5.1

5.3 Fine-Scale Crustal Thickness Variability from Dense Moho Depth Profiles

As shown in Figure 5.2, the differential time between Pg and PmP is both a function of the difference in path length between these two phases, which is dependent on the Moho depth, and the difference in the velocity structure to which these two phases are sensitive. Pn has a longer ray path than PmP, but it arrives earlier than PmP and eventually overtakes Pg because the upper mantle velocity is much higher than

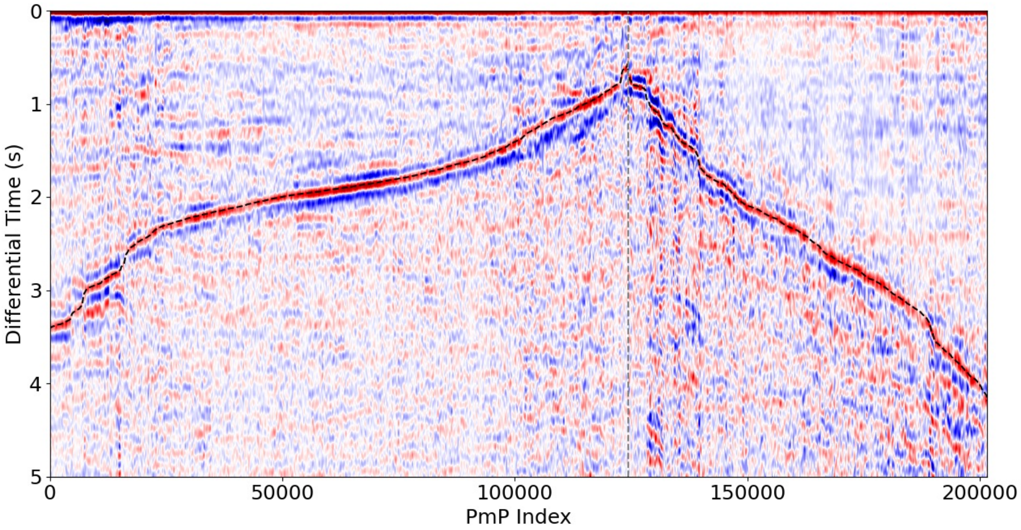

Figure 5.4: All PmP picks made in this study. Plotted are the autocorrelation correlograms for each channel for which estimates of P-PmP differential time could be made. Black dotted lines correspond to pick times, and correlograms are organized by decreasing pick times when following Pg and increasing pick times when following Pn. Gray dotted line marks the transition from Pg to Pn as first arrival.

the crustal velocity. When using P-PmP differential times, we thus need to consider three things: crustal structure, upper mantle velocity, and crustal thickness. Crustal structure and thickness trade off with each other and considering the two simultaneously would result in non-uniqueness, particularly because parameterizing the crust requires both seismic velocities and a layering structure. Low wavelength variability in PmP differential times is much more sensitive to changes in crustal thickness. This is because sensitivity due to crustal structure depends on integrated velocities along the ray path, not detailed velocity structure; we subsequently illustrate this with synthetic tests. Since we are most interested in sharp changes in the Moho, we choose to fix a representative crustal model (Figure 5.S1) using an ensemble of velocity profiles (see methods) and invert for Moho topography. The distance at which Pn supersedes Pg as the first arrival and the rate at which the Pn-PmP differential time increases with distance are functions of the upper mantle velocity integrated along the ray path. While this value also trades off with absolute Moho depth, we can resolve a robust estimate of a representative upper mantle velocity for the entire dataset in a straightforward way. We can then incorporate this velocity into our model when inverting for crustal thickness.

Using the representative crustal model, we determine a best fitting combination of Moho depth and upper mantle velocity for our entire dataset (see methods). We find that the optimal pair is a Moho depth of 31.5 km and an upper mantle velocity of 8.1 km/s. The representative model is shown in Figure 5.S1. This Moho depth is very similar to that of the Hadley-Kanamori model for Southern California (32 km) (Hadley and Kanamori, 1977), and the upper mantle velocity is consistent with Pn tomography results from this region (e.g., Buehler and Shearer, 2014; Richards-Dinger and Shearer, 1997). We then use our fixed crustal and optimal upper mantle velocities combined with our PmP differential times and first arrival classifications to invert for crustal thickness along each of our bounce-point profiles (see methods). The resultant profiles provide estimates of Moho depth at sub kilometer intervals, which is smaller than the minimum wavelength expected in the earthquake wavefields used in this experiment. These Moho depth estimates and select cross sections are shown in Figure 5.5.

These profiles yield Moho topography that is in close agreement with previously resolved high wavelength features in Southern California (Tape et al., 2012) and provide remarkably high spatial frequency resolution along profiles that illuminate highly localized changes in crustal thickness. Broadly, we observe a Moho depth of approximately 30 km throughout most of the Mojave block that shallows to the east. We also resolve a deep Moho over and around the Isabella anomaly (Raikes, 1980) that has been regularly observed in this region (e.g., L. Zhu and Kanamori, 2000). Consistent with other studies, the crust thickens sharply at the transition to the San Bernadino Mountains, corresponding to the mountain root. The Moho is relatively deep just to the northwest of these mountains, which is consistent with some recent results (Li et al., 2022). In general, the absolute values of Moho depth across the region agree with previous localized measurements of Moho depth made using receiver functions (Yan and Clayton, 2007), as is illustrated in Figure 5.5 and 5.S2.

There are indeed tradeoffs between variability in the velocity model and crustal thickness, and we evaluate and discuss these tradeoffs later. However, the primary advantage of combining a high-frequency measurement like P-PmP differential times and the high spatial sampling of DAS is towards resolving fine-scale variability in crustal thickness, rather than broad-scale absolute values. Velocity model variability will generally exert a longer wavelength effect on P-PmP differential times because the velocity contribution to the differential time is path integrated. Crustal thickness

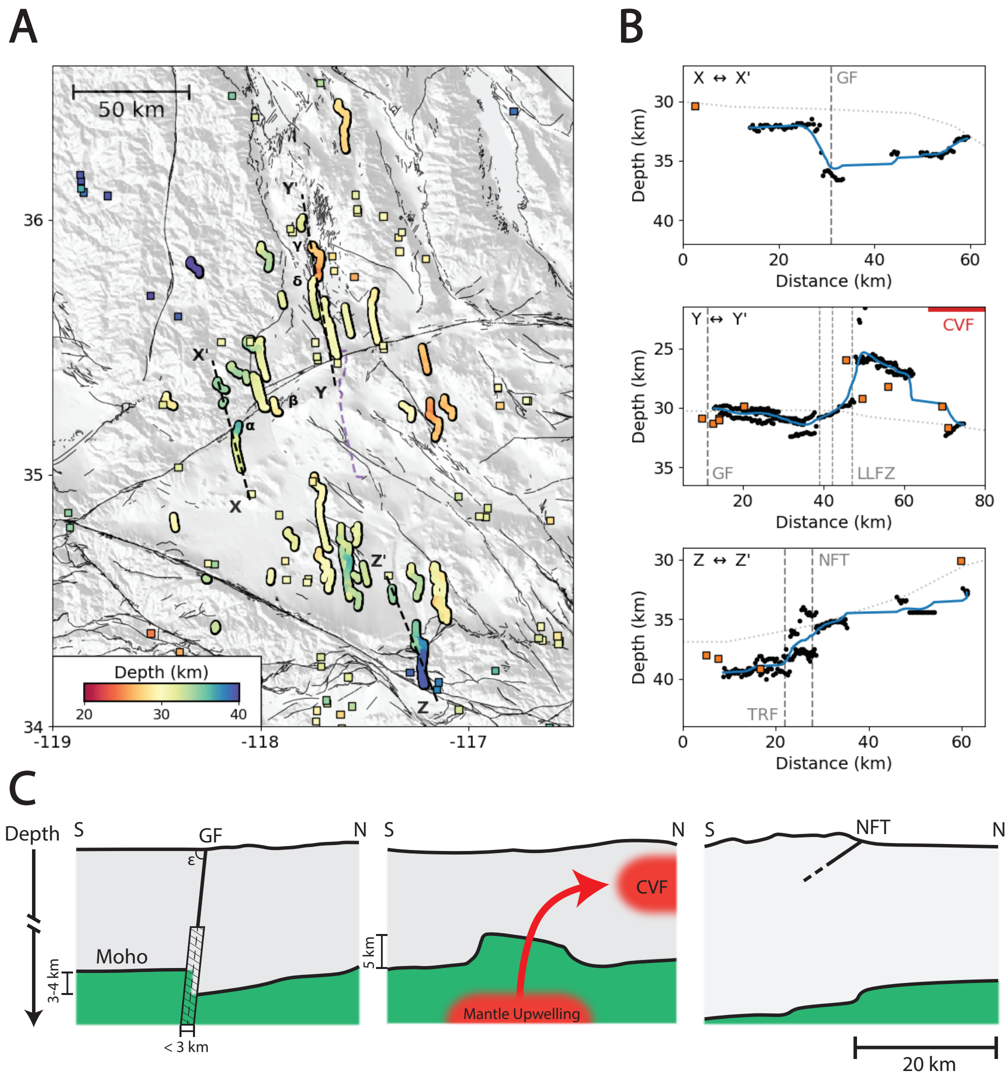

Figure 5.5: Summary of resolved Moho depth variability. (A) Moho depth inversion results along corresponding bounce-point locations for all events included in this study. Included as squares are Moho depth estimates reported in Yan and Clayton (2007). Purple dotted line marks the DAS array location. (B) Cross-sections of Moho depth corresponding the profiles mapped in (A). Included are all estimates of Moho depth within 10 km of the profile reported in this study (black dots) and all estimates of Moho depth within 20 km of the profile reported in Yan and Clayton (2007) (orange squares). Lettering indicates different structural features where they cross the profiles (GF=Garlock Fault | LLFZ=Little Lake Fault Zone | CVF=Coso Volcanic Field | TRF=Tunnel Ridge Fault | NFT=North Frontal Thrust). The CVF location marks the approximate southern extent of the mid-crustal low velocity zone reported in (Zhang and Lin, 2014). Lateral dotted line corresponds to smoothed Moho depth estimates from the Community Moho Model (Tape et al., 2012). (C) Schematic diagrams of the cross-sections in (B).

variability, however, can exert shorter wavelength effects on P-PmP differential times, because a sharp change in the Moho depth abruptly changes the path length of PmP. We demonstrate this using a set of synthetic tests (see methods) shown in Figure 5.6. These tests show that even very sharp and high amplitude local velocity perturbations have a smooth and muted effect on P-PmP differential time with source-to-receiver distance. Comparatively, a Moho step produces an abrupt jump in the P-PmP differential time that is representative of the amplitude of the step in the Moho.

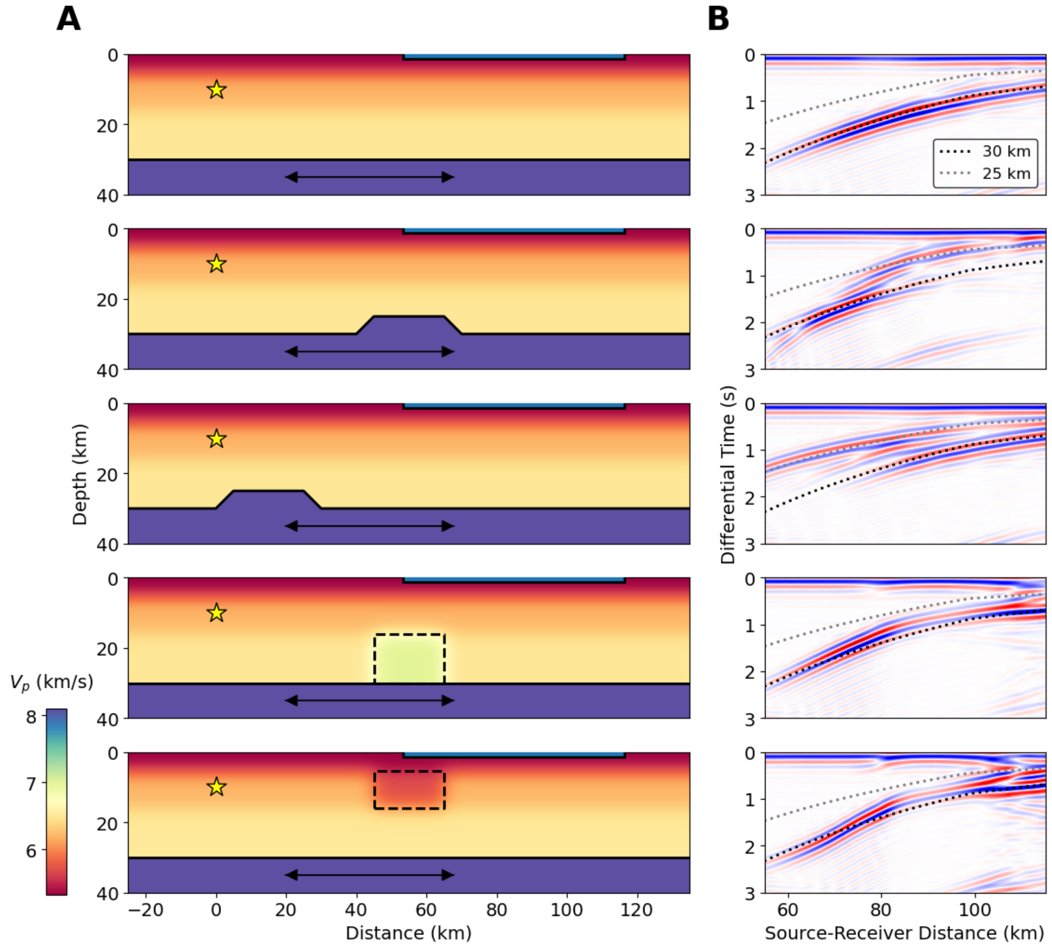

Figure 5.6: Synthetic tests. (A) Velocity models and source-array geometry used in these synthetic tests. Double-sided arrows correspond to the approximate extent and locations of bounce-points in these tests. Solid black line marks the Moho and dotted black lines outline velocity anomalies. (B) Differential times from autocorrelation wavefields for each synthetic test. Shown are reference relative arrival times of PmP for a flat Moho at 25 and 30 km depth.

5.4 Sharp Moho Changes Across the Garlock Fault and Coso Volcanic Field

Our results show that there is considerable variation in Moho depth along our crustal thickness profiles. We choose to focus on two low-wavelength features that are observable only because of the unique combination of the station density of DAS and the regional sensitivity of the PmP measurements. The correlogram profiles that inform these observations are shown in Figures 5.7 and 5.8. One of these interesting features shown in Figure 5.5 is a sharp step (3-4 km) in the Moho that is very close to the surface trace of the western segment of the Garlock Fault. As is shown in Figure 5.7, this step is clear in the data and occurs over only a few kilometers. Because this profile is recovered using individual event wavefields, uncertainties related to source location do not affect the relative change. A less precise but more objective way to confirm the presence of the step is to sum the envelope of these correlograms along the expected P-PmP differential times for a range of Moho depths. When we do this along the spatial windows to the north and south of the expected step location, we find that there are peaks at distinct Moho depths (Figure 5.9). Another shorter profile to the east, also shown in Figure 5.7, shows a step-like feature of the same polarity, providing additional evidence for this Moho discontinuity.

This observation may be attributed to a discontinuity in the crust imposed by the Garlock Fault and would suggest that the western segment of the fault penetrates the Moho. This observation is distinct from some early results suggesting that the Garlock Fault is truncated (Cheadle et al., 1986) or approaches a horizontal angle in the middle crust (Louie and Qin, 1991). The results presented in this study have deeper penetration depths and require fewer assumptions than these earlier studies. The deeper penetration depths resolved in this study add increased importance to the Garlock Fault as a physical boundary between the Mohave and the Sierra Nevada and Basin and Range terrains to the north (Figure 5.1). This agrees with some geologic studies that suggest the Garlock Fault delineates, and slip on the fault may be driven by a difference in extensional behavior between the Basin and Range and the Mojave (Wernicke et al., 1982). Additionally, this feature suggests that along this segment of the fault the Garlock is nearly vertical through the entire crust. This extends the results of earlier studies that used focal mechanisms (Bailey et al., 2010) and imaging techniques (Qiu et al., 2023) to infer a near vertical dipping fault at seismogenic depths. The width of this step is intriguing, because the behavior of continental faults at depth can shed light on the strength of the lower crust and upper mantle (e.g., Molnar et al., 1999; Zhu and Kanamori, 2000). Since the Garlock fault consists of a narrow step, this observation supports the possibility of a narrow shear zone at depth, rather than a broad deformational zone, The wavelength of this step observed at the Garlock Fault (<3 km) suggests an upper bound for the width of the deformation zone at the crust-mantle boundary. The PmP observation becomes faint in the narrow spatial interval at the step, and we cannot further characterize the properties of the step within this interval. That such a narrow zone with steep offset is maintained on a relatively slow slipping fault (e.g., Chuang and Johnson, 2011) may help constrain the strength contrast at the crust mantle boundary. This observation is comparable to that of the Denali Fault, another intracontinental strike-slip fault with a sharp Moho step at depth (Allam et al., 2017). A schematic representation of the observations made at the Garlock is shown in Figure 5.5C.

Another important feature is the thinning of the crust near the Coso Volcanic Field (CVF) that is illuminated by several profiles. Two of the correlograms that inform this result are shown in Figure 5.8. Again, we can confirm the distinction between these profiles by summing the envelopes of the correlograms for these two profiles along computed P-PmP differential times (Figure 5.9). We find that this confirms the P-PmP differential times evidence distinct Moho depths at each profile. This observation is supported by a resolved shallowing of the Moho observed with receiver functions nearby (Yan and Clayton, 2007). The crustal thinning may be explained as a highly localized feature that evidences a regional tectonic phenomenon. The deep Moho to the west, that is also resolved in our data, has been explained as a subduction-induced lithospheric drip of the ultramafic base of the Sierra Nevada batholith (Saleeby et al., 2003; Zandt et al., 2004) or as a fragment of the Farallon Plate (Dougherty et al., 2020; Wang et al., 2013). In either case, these structures are expected to induce a counterflow that results in mantle upwelling and crustal thinning to the east (Bernardino et al., 2019). There are several recent tomography results that suggest that the CVF is collocated with a regionally significant low-velocity anomaly in the upper mantle and lower crust that are slightly to the south of the associated mid-crustal magma reservoir (Jiang et al., 2018; Wang et al., 2022; Wang et al., 2013). Our results may provide additional constraints at the crust-mantle boundary on the location of the mantle source of the mid-crustal magma reservoir. The feature we resolve is more local and biased further to the north than the features described in deeper tomography studies, which may be due either to distinct responses of velocity structure and Moho depth to the thermal anomaly or the different sensitivities of these methods. A schematic representation of the connection between this observed section of thinned crust and the Coso system is shown in Figure 5.5C.

The known low velocity anomaly in the middle crust associated with this reservoir (e.g., Zhang and Lin, 2014) raises questions as to whether we are indeed observing a true crustal thickness anomaly or an apparent thickness anomaly due to sharp velocity heterogeneity. A low velocity anomaly in the lower crust would make the Moho apparently deeper, rather than shallower, but a low velocity anomaly in the middle crust could indeed preferentially delay Pg and produce an apparent thinning of the crust. But, as shown in our synthetics in Figure 5.6, even a high-amplitude low-velocity anomaly in the middle crust, one much stronger than what is resolved in Zhang and Lin (2014), and comparable to the volume expected at CVF produces a small perturbation in P-PmP times relative to a 5 km high Moho platform. Additionally, the synthetics show a diffracted phase generated at the transition to bounce points off the step that may be observable in the data. We observe a weak phase preceding the PmP phase in the autocorrelation profile just south of the shallow Moho anomaly; our preferred interpretation is that this is the diffracted phase (Figure 5.8).

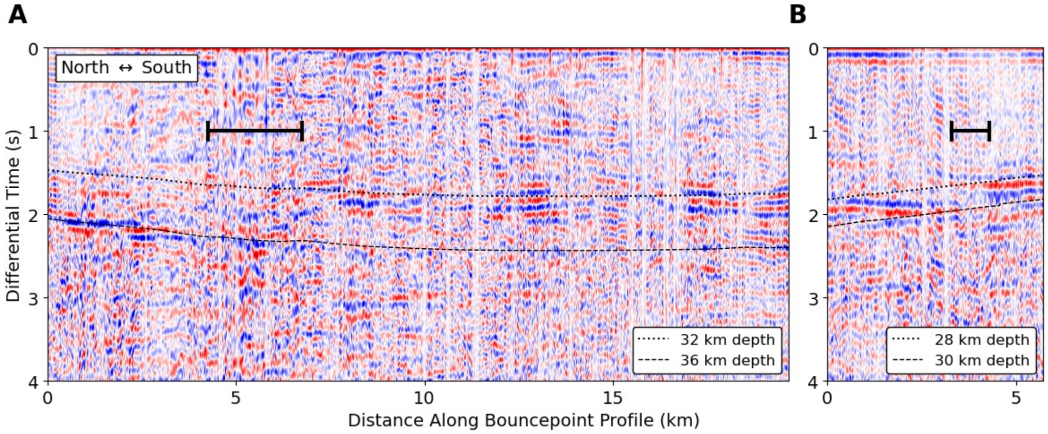

Figure 5.7: Auto-correlograms across Garlock Fault. (A) and (B) are correlograms for long and short bounce-point profiles across the Garlock fault, respectively. Plotted are reference curves of expected P-PmP differential times for different Moho depths. Also plotted are the estimates of the width of uncertain Moho depths on either side of which we can confidently identify distinct PmP peaks. Locations of these profiles are indicated as α and β in Figure 5.5.

5.5 Discussion of Ambiguity and Uncertainty

There will always be uncertainty when attempting to classify secondary phases; our objective is to minimize this uncertainty. It is thus important to evaluate the confidence with which we can ascribe the secondary phase arrivals made in this study

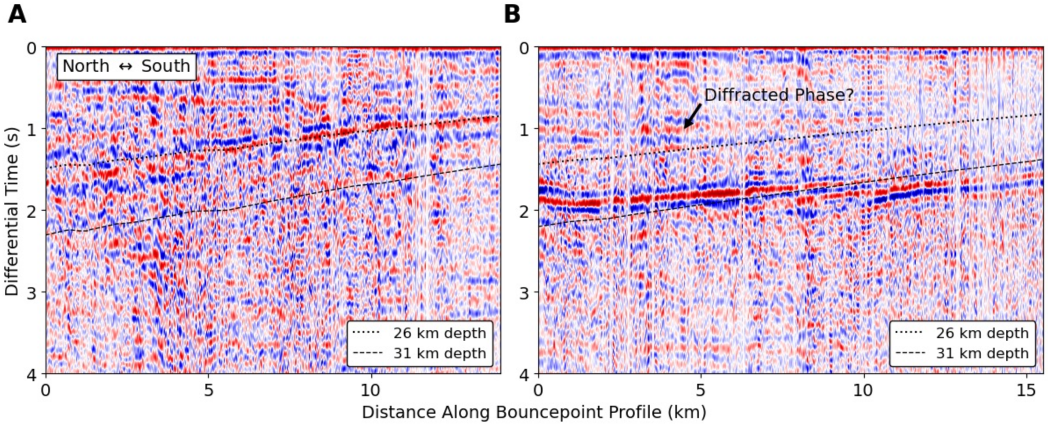

Figure 5.8: Auto-correlograms near Coso Volcanic Field. (A) and (B) are correlograms for bounce-point profiles on and just south of the shallow Moho depth anomaly near Coso, respectively. Plotted are reference curves of expected P-PmP differential times for different Moho depths. Also identified is a correlogram peak that we speculate is the diffracted phase off nearby shallow Moho anomaly. Locations of these profiles are indicated as γ and δ in Figure 5.5.

to a specific phase. There are several reasons why we expect our observations to correspond to PmP. Each identification was made using prominent phases recorded by at least hundreds of channels that were highly correlated with the first arriving P-phase. This would suggest that we are not identifying spurious arrivals, but rather phases associated with a sharp and coherent discontinuity with a similar scattering behavior to the P-phase. It is well documented that PmP is often the most prominent phase in the P-wave coda (e.g. Grad et al., 2009; Richards-Dinger and Shearer, 1997), and so we would expect it to show a high relative amplitude to the first arriving P. We only identified a phase as PmP if the phase approximately paralleled the expected P-PmP differential time and moveout for a representative lithospheric model of the region. This correspondence was usually evaluated over tens of kilometers at meter-scale intervals for each event, as shown in Figure 5.3. This array-side moveout evaluation is an effective tool for identifying secondary phases that is available only to dense arrays. Other studies have been successful in identifying PmP using reciprocity to evaluate P-PmP moveout using multiple events (Li et al., 2022). Our technique is similar; however, it has the added benefit of removing the uncertainty associated with potential errors in the source location and depth. A related verification of our observations comes from the fact that a global inversion for the sensitive parameters of Moho depth and upper mantle velocity under the assumption that our observations were PmP produced results that are highly consistent with prior studies for the region made using independent methods (Buehler and Shearer, 2014; Hadley and Kanamori, 1977; Tape et al., 2012). The regional variability, both in terms of absolute and relative values, of Moho depth is also in close agreement with the expected variability for Southern California resolved using receiver functions (Li et al., 2022; Yan and Clayton, 2007; Zhu, 2000).

As is shown in Figure 5.2, for some arrivals before the triplication point, Pn is expected to arrive between Pg and PmP, and for arrivals after the triplication point, Pg is expected to arrive between Pn and PmP. This may lead to the problem that in some cases, Pn or Pg may be misidentified as PmP. It is highly unlikely that Pn would be misidentified as PmP, as Pn is expectedly much lower amplitude than either Pg or PmP in our synthetic tests (Figure 5.S3). The case of Pg following Pn is more problematic; judging by our synthetic tests, Pg is expected to have comparable amplitude to PmP for a range of source-to-receiver distances beyond the triplication point. However, as is shown in Figure 5.4, for observations on or shortly beyond the triplication point, the correlograms show no evidence of exceptionally early PmP arrivals, as would be expected if we were misclassifying Pg as PmP. Further, there is little evidence of multiple, high amplitude peaks in the correlograms following Pn, as would be expected if Pg were observable in the coda. Supplementary evidence can be found in the fact that the Moho variability computed using PmP following Pn agrees with previous studies, as is made abundantly clear by the consistently resolved deepening of the Moho across the Northern Frontal Thrust (Li et al., 2022; Li et al., 1992; Yan and Clayton, 2007; Zhu, 2000), shown in Figure 5.5, and that the resolved upper mantle velocity is consistent with Pn tomography models (Buehler and Shearer, 2010; Buehler and Shearer, 2014). The step across the Garlock Fault and the shallowing the Moho near Coso, are made using PmP picks that follow a Pg first arrival. We also note that for low-angle reflections, there is expectedly phase distortion (Aki and Richards, 2002). For simplicity and precision, we pick the maximum positive correlation peak, and we expect errors due to phase distortion to be small. This expectation is supported by the fact that the dominant frequency content of PmP in this study is high (4 Hz), as illustrated in the stacked cross-correlation wavelet in Figure 5.S4. The upper bound for error due to phase distortion (0.1 s) is thus quite small compared to the differential time differences important in this study, as shown in Figures 5.7 and 5.8.

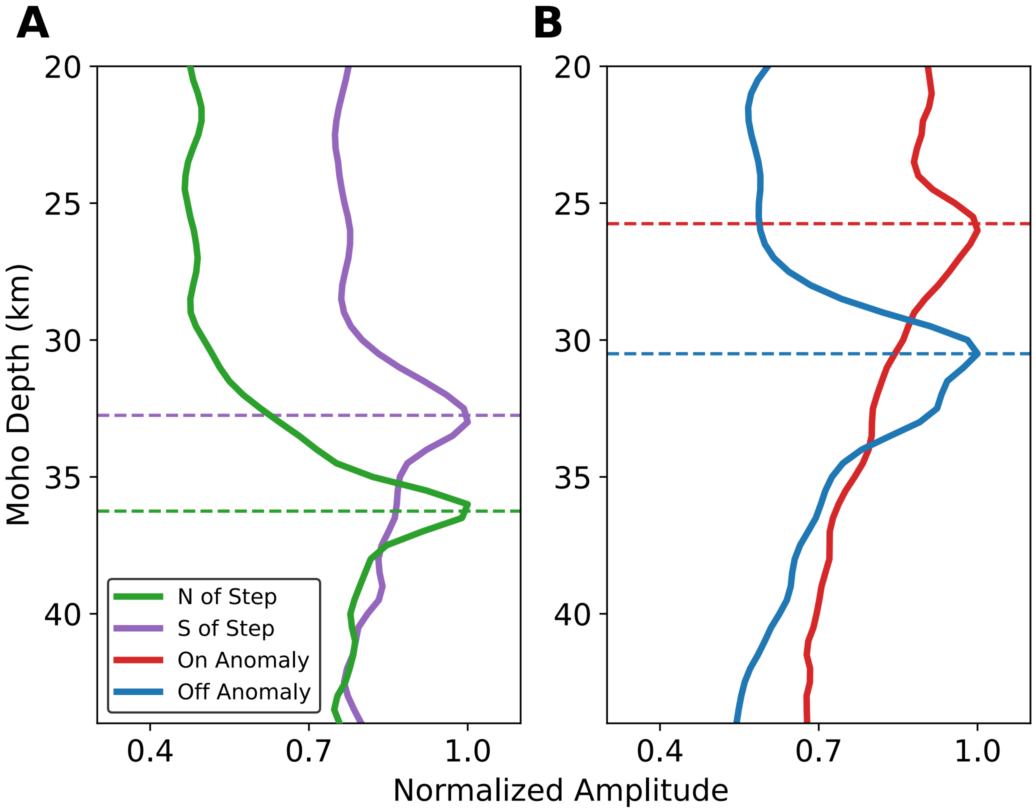

Figure 5.9: Correlogram envelope summation results. (A) and (B) show profiles that summarize the amplitude of the summation of the envelopes of the correlogram profiles shown in Figures 5.7 and 5.8 along expected P-PmP differential times for different Moho depths. (A) shows the results of this operation performed along the spatial windows to the north and south of the expected step location for profile shown in Figure 5.7. (B) shows the results of this operation performed on profiles (on anomaly) and (off anomaly). Both (A) and (B) suggest the data between profiles are consistent with variant crustal thickness values.

The depth phases sP and sPmP are also of interest because they can produce amplitudes comparable to PmP and in some cases are expected to arrive at times similar to PmP. As shown in Figure 5.S4, the phase sP can have comparable differential times at certain source-to-receiver distances for specific source depths; however, the moveout of the P-sP differential time is markedly different from P-PmP and can easily be distinguished using the moveout criterion of the PmP selection. Also shown in Figure 5.S5, for very shallow events (<2.5 km), the expected arrival times of sPmP assuming a shallower Moho and PmP assuming a deeper Moho can be similar. This is a concern for a small number of earthquakes in this study with shallow source depths. One such important event is the event whose data are shown in Figure 5.8b; we describe the uncertainties associated with the shallow depth of this event subsequently. We also note that SmS is observable in these data. SmS is a uniquely important phase because it is sensitive to shear wave velocities in the lower crust (Kay et al., 1999; Zhan et al., 2010), and it often produces the strongest ground shaking at regional distances (Liu and Tsai, 2009; Somerville and Yoshimura, 1990). We show an example of an SmS observation next to a PmP inversion for one of the earthquake wavefields used in this study in Figure 5.S6. Picking and identifying first S arrivals at regional distances is often challenging and the SmS cross-correlation peaks are generally not as clear as those of PmP. We thus reserve the systematic identification and analysis of SmS phase differential times for future work.

An important result of this study is that PmP is commonly observable in DAS data; however, we also found PmP is more commonly not observable. The fact that PmP is observable in some seismograms but not others has been extensively documented (see Ding et al. (2022) for a summary), but the reason for this observation has not been conclusively determined. We do not attempt to resolve this question in this study, but we evaluate how several source and array parameters affect the observability of PmP (Figure 5.S7). We found strong positive correlations between source magnitude and source-to-receiver distance with PmP observability, and a weak positive correlation between source depth and PmP observability. Additionally, for the sources for which there was a focal mechanism solution, we computed the minimum angular distance between the expected takeoff ray of PmP and the nearest nodal plane to the observability of PmP. As expected, we see a positive correlation between these two parameters, suggesting that PmP observability is partially a source effect. Additionally, since DAS is a uniaxial strainmeter, the array geometry may play a role in the observability of PmP. To determine the strength of this effect, we compare the angle between the expected incidence path of PmP and the local source geometry to the observability of PmP. We find a negative correlation between these two parameters, which is consistent with the expected broadside insensitivity of DAS. The combination of source effect and array geometry produces a stronger correlation. None of these parameters completely explain the common lack of observability of PmP. There are likely large contributions from parameters that are not so easily tested, such as focusing and defocusing of PmP due to crustal structural variability, energy partitioning due to complex geologic structure (Mori and Helmberger, 1996), and the strengthening or weakening of PmP due to differences in the sharpness of the Moho (Levin et al., 2016).

In this study, we use fixed crustal and upper mantle velocities to invert for Moho depth. There are tradeoffs between the absolute value of the Moho depth and the velocity model used to infer expected P-PmP differential times. Although in this study we are mostly concerned with low-wavelength, relative changes in Moho depth, we can also evaluate the potential variability in the resolved absolute values due to uncertainties in the velocity model. The Moho depth values are especially sensitive to changes in the lower crustal velocity and, for Moho depths resolved using P-PmP differential times when Pn is the first arrival, upper mantle velocity. Our fixed crustal model considers a set of 1D profiles drawn from the Community Velocity Model (CVM) (Lee et al., 2014) at expected bounce point, source, and receiver locations, and the variance of these 1D profiles can be used to estimate the potential broad deviations of the lower crustal velocity within our study area (±0.15 km/s). Additionally, we can perturb our best fitting upper mantle velocities by a small value (±0.1 km/s) and continue to fit our data reasonably well. We invert for Moho depth along the bounce-point profiles using perturbed values (see methods) and plot the results in Figure 5.S8. In general, as shown in Figure 5.S9, the deviations are quite small. Varying the lower crustal velocity produces the most substantial change in absolute value, but this is contained within 5 km and the key features in the relative variability are unchanged. Varying the upper mantle velocity shifts only the measurements that trail a Pn first arrival, and these shifts are within 3 km.

Multiple events are necessary to support the observation of shallowing of the Moho near the Coso Volcanic Field, meaning we must carefully consider source uncertainty. The two events that suggest a thin crust near Coso are approximately collocated, with depths of 6.9 and 7.1 km in the SCSN catalog and 7.75 and 7.87 km in the focal mechanism catalog developed following Yang et al. (2012). If this feature was an artifact of incorrect event location, both events would need to be severely mislocated in both catalogs, as removal of this anomaly would require these events to be substantially deeper, approximately 15 km depth. We can estimate the potential error in the depths of the SCSN catalog by plotting a distribution of differences between the depths of the events used in this study in the SCSN catalog and the available depths in the waveform relocated Hauksson et al. (2012) seismicity catalog. The vast majority of these differences are within 3 km, and there is no difference present that would be large enough to negate the shallow Moho anomaly. The profile just south of the anomaly that marks the recovery of the Moho to deeper depths is generated by a shallow event (2.4 km). Making the Moho shallower along this profile would require a much shallower event depth, which is highly unlikely given the already shallow depth. We can systematically evaluate the dependence of our Moho depth estimates on source depth by inverting for Moho depths shifted according to the estimated depth uncertainty illustrated in figure 5.S10 (-1 km to +3 km). The resultant changes in Moho depth are minor and are plotted in Figures 5.S8 and 5.S9. Finally, although we interpret the weak phase in Figure 5.8b to be the diffracted phase, this peak could also be a correlogram artifact or the true PmP phase, with the strong peak corresponding to the depth phase (sPmP). If true, the third possibility would only extend the expected region of shallow depths slightly south, at which point there are several profiles with a variety of source depths which all suggest a roughly uniform Moho depth that is consistent with previous results for the region.

5.6 Materials and Methods

Earthquake Selection and Quality Control

For the recording period between August 2021 and August 2023, the DAS array recorded several hundred M2.5+ earthquakes that we identify using the Southern California Seismic Network catalog. Earthquakes of these magnitudes are sufficiently large to exhibit a consistently observable P-phase at regional distances in DAS data, which generally have higher noise than broadband data, and thus we consider only these earthquakes this study. Of these earthquakes, we consider all events that have at least one source-to-receiver epicentral distance between 70 km and 250 km. The lower bound is selected to ensure that each event analyzed could show observable PmP (i.e., arrives before the S-wave) over a substantial segment of the fiber and thus may be identified with spatial coherence. This lower bound also increases the likelihood that some observations will be made at postcritical distances and thus more easily identifiable. The upper bound is an estimate of the source-to-receiver distance at which the signal-to-noise ratio of the earthquake wavefield is too low to identify the phases of interest in this study. After this initial quality control, there are 440 candidate earthquakes distributed throughout Southern California with likely high-quality wavefields and potentially estimable P-phase onsets with which we may analyze the Moho reflected phase.

We apply a straightforward and semi-automated framework for obtaining P-to-PmP differential times via autocorrelation. We first select a window for each of the candidate earthquakes starting 30 seconds before and ending 90 seconds after the cataloged origin time and make travel-time picks on these events using PhaseNet

DAS (W. Zhu et al., 2023). We then visually evaluate these picks, keeping only first arrival picks that we can confidently attribute to the first arriving P-phase. Of the initial set of events, 229 events had visually identifiable P-phase onsets and some preserved first arrival picks. We then compute the expected first arrivals for each event using the Hadley-Kanamori (HK) 1D model (Hadley and Kanamori, 1977) and the software TauP (Crotwell et al., 1999) and correct the absolute times of these computed arrivals using the preserved pick times. This workflow provides us with calibrated approximate onset times for every channel for each event. Once we have these onset times, we select a time window for each record that is 4 seconds before and 8 seconds after the approximate onset time. We then spectrally whiten the signal and filter the signal between 0.2 and 5 Hz, a filter band that balances maintaining as much of the earthquake spectra as possible while reducing high and low frequency noise. We then select a 1 second window around the approximate first arrival (0.3 seconds before and 0.7 seconds after) and correlate this time window with the full-time window. This is distinct from other autocorrelation workflows that simply autocorrelate the full-time window (Delph et al., 2019). We make this choice because the first arrivals in these data are often very low amplitude and using this narrow window scales the contribution of the first arriving P-phase to make the P-PmP correlation peak identifiable. We then visually inspect each of the autocorrelated wavefields, using P-PmP relative arrival time computed using the HK model as a reference. We manually select spatial windows that encompass high-amplitude, spatially coherent correlation peaks that maintain a reasonable moveout for PmP at the respective source-to-receiver distances. From this manual selection we obtain large spatial windows of PmP observations for 72 events. For each of these spatial windows, we pick P-PmP differential times by selecting the local maxima corresponding the PmP onset in the autocorrelation profiles. These local maxima are selected using a visually identified time window within which the P-PmP autocorrelation peak is observed. Additionally, by visually evaluating the change in differential time with source-to-receiver distance, we determine for each observation whether PmP is trailing Pg or Pn. A decrease in the differential time with duration corresponds to PmP trailing Pg, and the opposite is the case for PmP trailing Pn. Using this workflow, we select over 200,000 accurate and precise P-PmP differential times shown in Figure 5.4.

Inverting for Upper Mantle Velocity and Crustal Thickness Variability

In this study, we fix the crustal velocity according to an ensemble of profiles from the Community Velocity Model (Lee et al., 2014). These profiles are drawn from the source, bounce-point, and channel locations used in this study. We reduce these models for comparability and simplicity by depth-averaging the upper (0-5.5 km), middle (5.5-16 km), and lower (16 km-Moho) crustal velocities to generate 3-layer models and take a representative model as our fixed crustal model. We then perform a grid-search for a representative crustal thickness and upper mantle velocity for our entire dataset. We bootstrap by randomly sampling which events we use in the inversion to estimate the error. For each P-PmP differential time observation, we compute an expected differential time using TauP for a set of Moho depth and upper mantle velocity pairs, and we determine the pair that minimizes the misfit to all our observations. We find that the optimal pair is a Moho depth of 31.5 km and an upper mantle velocity of 8.1 km/s. We then use our fixed crustal and optimal upper mantle velocities and invert for crustal thickness along each of our bounce-point profiles. For each source-receiver pair, we compute expected P-PmP differential times for a suite of Moho depths and determine which Moho depths minimize the misfit to the data for 100 sample segments (1 km) along the fiber; this segment length is selected to improve the stability of the inversion and is shorter than the minimum wavelength in our data. The loss is evaluated as the L2 Norm. Additionally, since we have observations of whether our PmP phase trails a Pg or Pn first arrival, we penalize any mismatch between our observed first arrival and the modeled first arrivals. To accomplish this, we multiply the loss by $n/(m+\epsilon)$ where n is the number of observations within a segment, m is the number of observations for which the observed and the expected first arrivals match, and ϵ is a small number incorporated to prevent singularities. Once we have a best fitting solution, we compute the expected bounce point locations using the source location, velocity model, and best fitting Moho depth to determine the location of the Moho depth measurement.

Performing Synthetic Tests

To generate the synthetic results shown in Figure 5.6, we use the software Salvus (Afanasiev et al., 2019), which uses the spectral element method to simulate wavefield propagation. We parameterize the velocity model using our 1D model derived from a sampling of the CVM and our inverted upper mantle velocity for the region, and we set the Moho depth to be 30 km. We smooth the a priori defined layer boundaries within our 1D model to minimize artifact reflections in the synthetics.

We parameterize our model as a 60 km segment of strainmeters at the surface of our model and emplace an isotropic source with an impulsive source time function at 10 km depth and 55 km lateral distance from the first station. The step we impose in the Moho is 5 km high and has a 20 km plateau with 5 km linear ramps on either side of the step. The high velocity zone imposed in the lower crust is a 7.5% velocity increase with 20 km width. The low velocity zone imposed in the middle crust is a 9% velocity reduction with 20 km width. These velocity anomalies have smoothed edges imposed using a Gaussian filter with a standard deviation of 250 m. The expected arrival times of P and PmP are computed using TauP (Crotwell et al., 1999) and the 1D model used to parameterize the synthetic with an unmodified Moho structure. The plotted synthetic autocorrelations are produced using the processing describe above, and we use the computed P times as our first arrival times for the autocorrelation.

Supplementary Materials

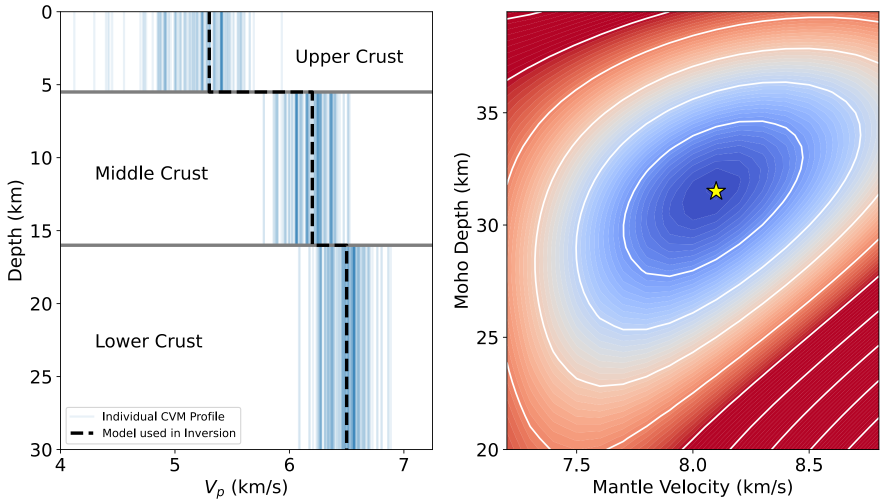

Figure 5.S1: 1D crustal model and average upper mantle velocity inversion. Left: Ensemble of crustal models drawn from the Community Velocity Model. Light blue lines are each a profile included in the ensemble. Black dotted line is the representative model used throughout this study. Right: Global Moho depth and upper mantle velocity loss distribution described in the main text. Red and blue indicate higher and lower loss, respectively. Yellow star indicates best fitting solution.

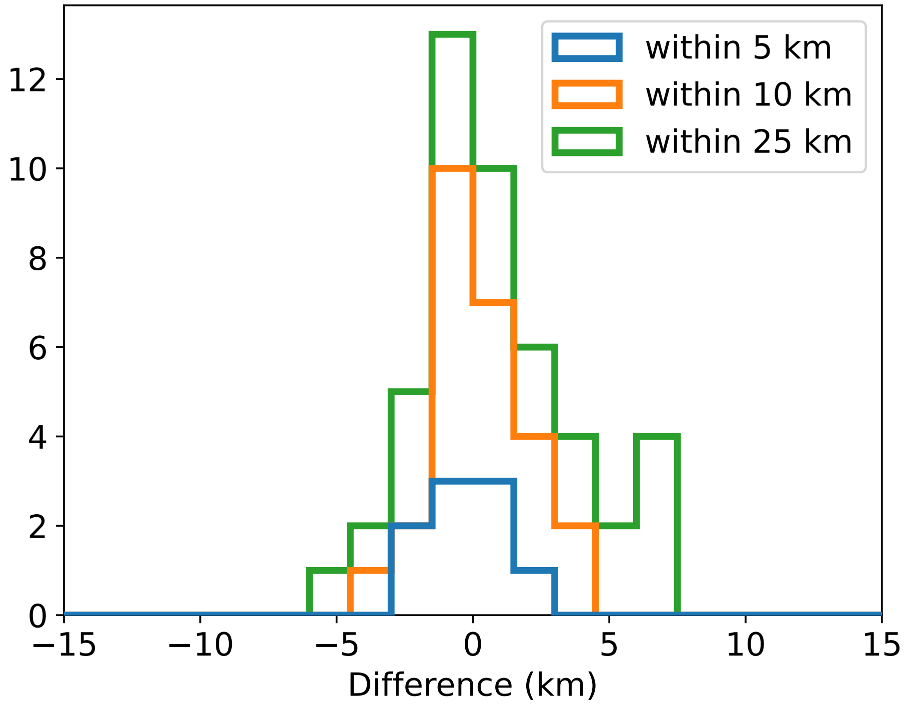

Figure 5.S2: Histogram of differences between nearby Moho depth estimates made in this study and those of Yan and Clayton (2007). Different colors correspond to different maximum distances between measurement points used as prerequisites for inclusion in the histogram. Measurements from Yan and Clayton (2007) are included only once using the nearest measurement from this study.

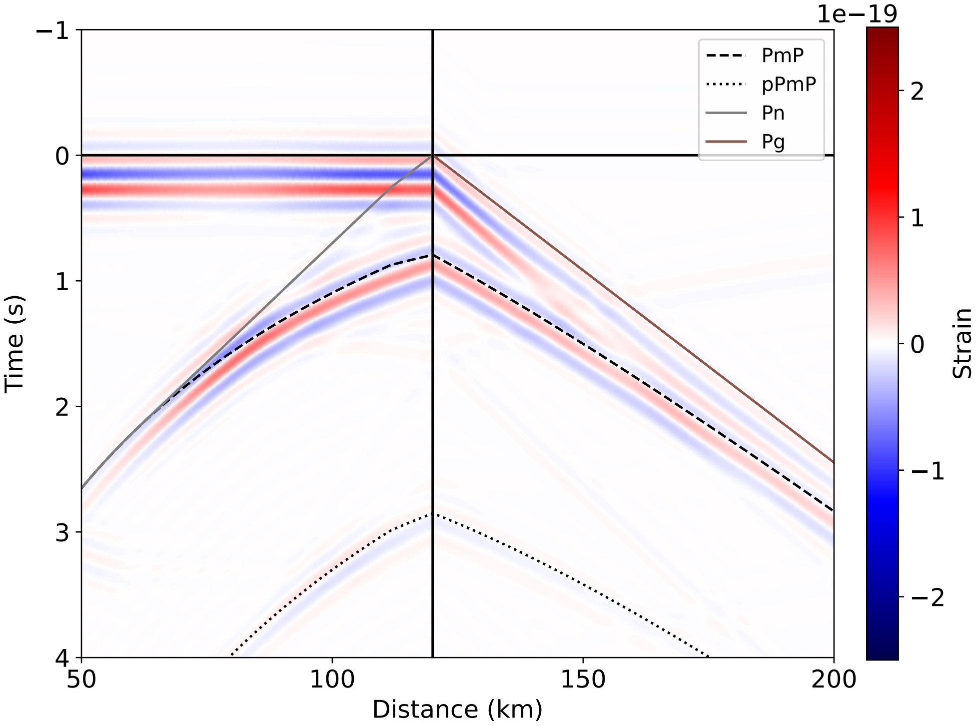

Figure 5.S3: Synthetic wavefield generated using the same parameters as the flat Moho model in Figure 5.6, but with an extended measuring array.

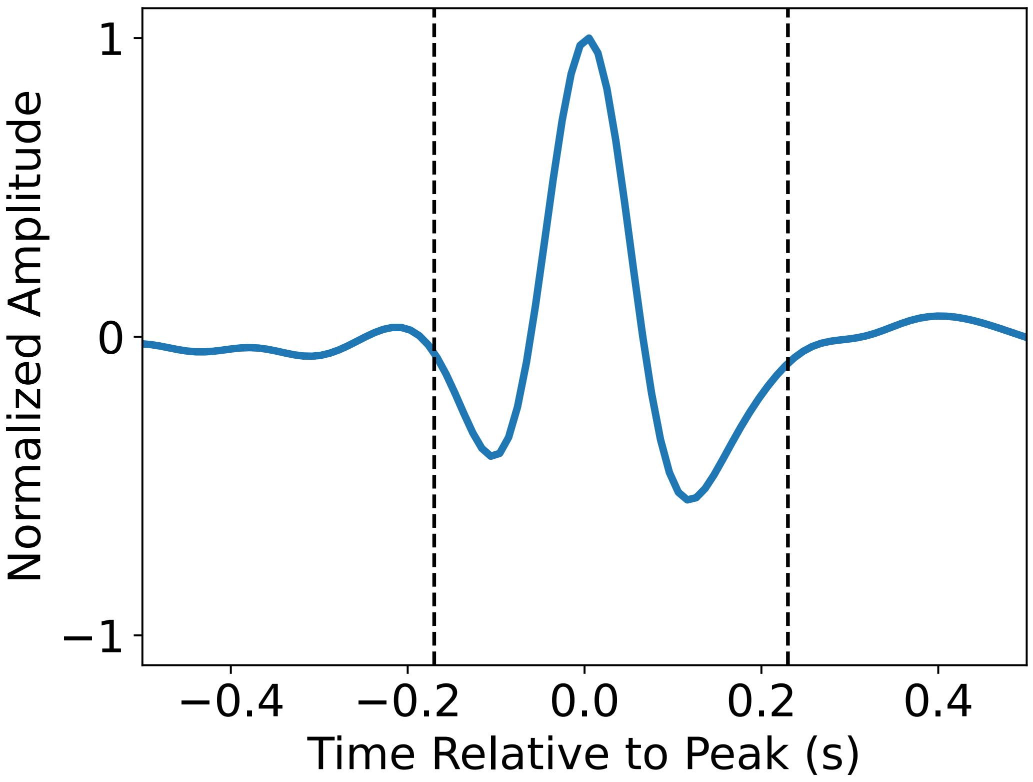

Figure 5.S4: Full stack of all cross-correlation wavelets associated with PmP used in this study. Alignment is performed using the peak picks shown in Figure 5.4. Black dotted lines encompass 1.5 wavelengths.

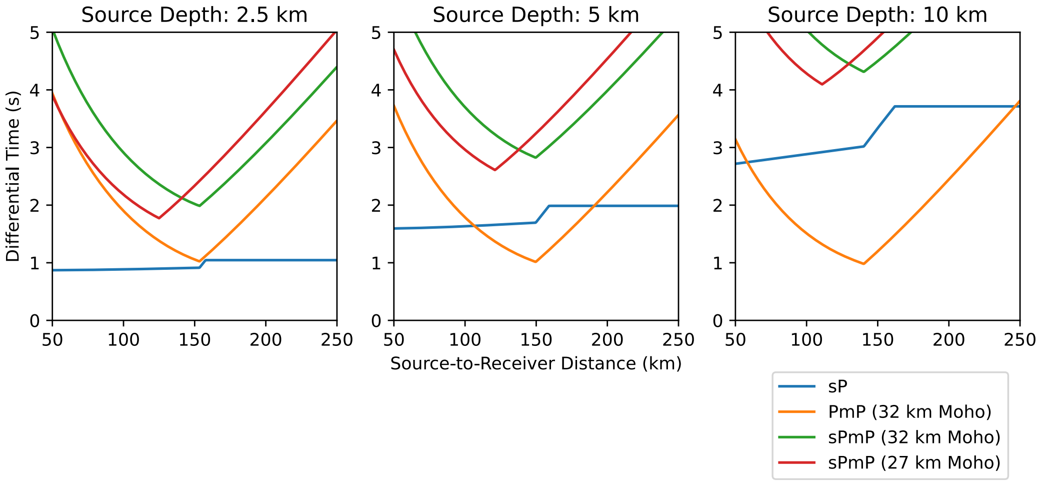

Figure 5.S5: Phase-P differential times for a diversity of source depth, Moho depth, and source-to-receiver distance combinations.

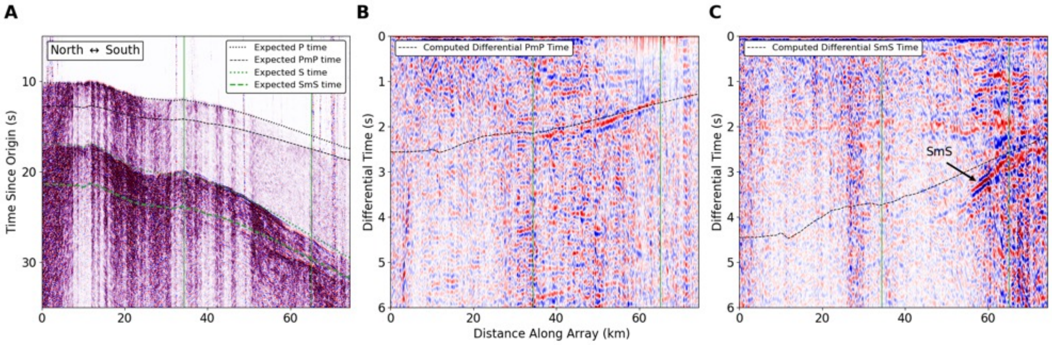

Figure 5.S6: Example of an SmS observation made using one of the earthquakes in this study. Earthquake location is indicated with a diamond marker in Figure 5.1. Vertical green lines mark the bounds over which PmP is observable.

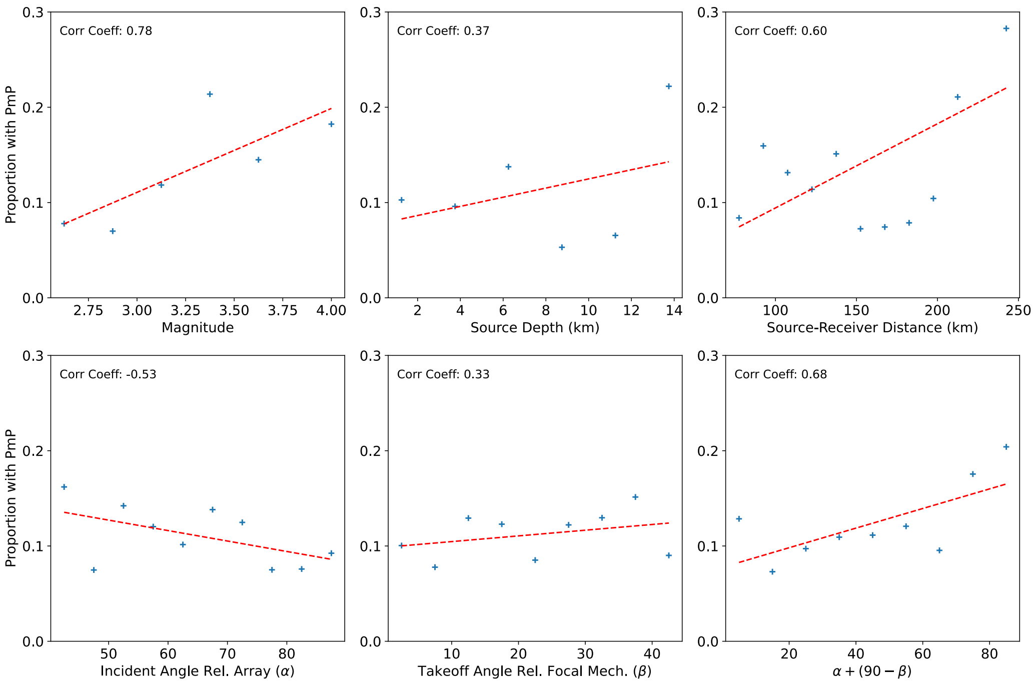

Figure 5.S7: Comparison of several parameters with the proportion of station-channel pairs for which PmP was observable in this study.

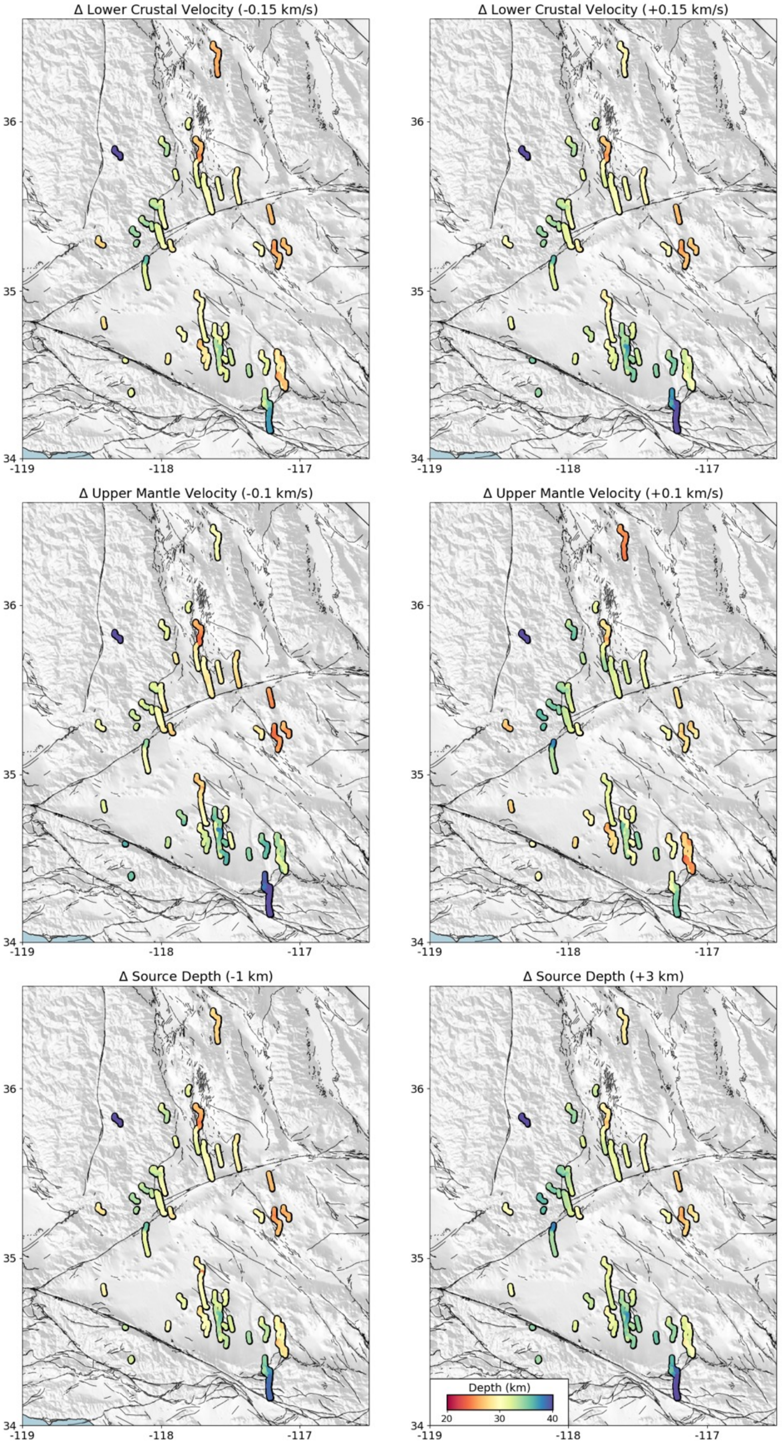

Figure 5.S8: Moho depth distributions computed using modified velocity model parameters and shifted source depths.

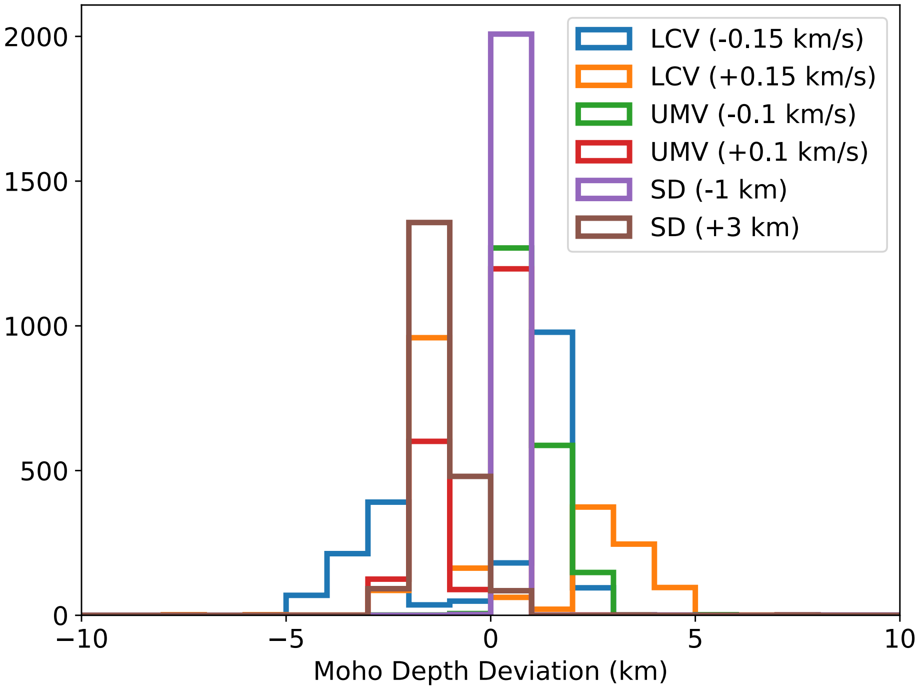

Figure 5.S9: Distribution of differences between Moho depth values determined using the perturbations shown in Figure S8 and those of the preferred model shown in Figure 5.5.

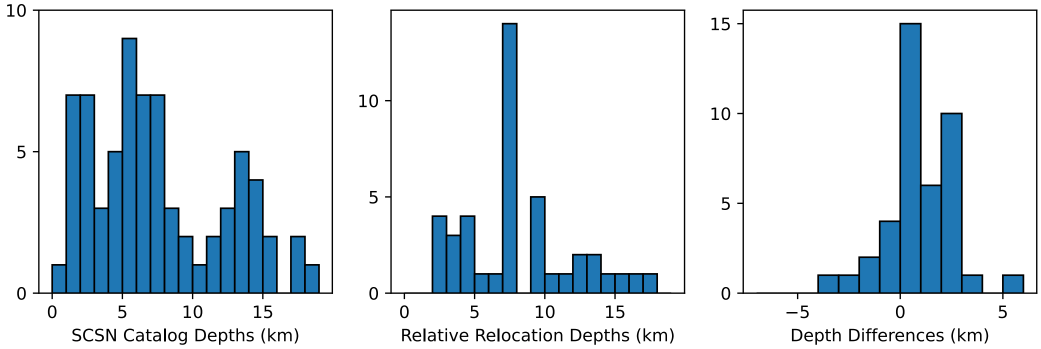

Figure 5.S10: Distribution of depths for the SCSN catalog and the Hauksson et al. (2012) waveform cross-correlation relocation catalog for events used in the study and the distribution of depth differences between catalogs.

Chapter 6

COMPUTING EARTHQUAKE SECOND MOMENTS IN A BAYESIAN FRAMEWORK

Atterholt, J. and Ross, Z. E. (2022). Bayesian framework for inversion of second-order stress glut moments: application to the 2019 Ridgecrest Sequence mainshock. *Journal of Geophysical Research: Solid Earth* 127. DOI: `10.1029/2021JB023780`. e2021JB023780.

Abstract

We present a fully Bayesian inverse scheme to determine second moments of the stress glut using teleseismic earthquake seismograms. The second moments form a low-dimensional, physically-motivated representation of the rupture process that captures its spatial extent, source duration, and directivity effects. We determine an ensemble of second moment solutions by employing Hamiltonian Monte Carlo and automatic differentiation to efficiently approximate the posterior. This method explicitly constrains the parameter space to be symmetric positive definite, ensuring the derived source properties have physically meaningful values. The framework accounts for the autocorrelation structure of the errors and incorporates hyperpriors on the uncertainty. We validate this methodology using a synthetic test and subsequently apply it to the 2019 $M_w 7.1$ Ridgecrest earthquake using teleseismic data. The distributions of second moments determined for this event provide probabilistic descriptions of low-dimensional rupture characteristics that are generally consistent with results from previous studies. The success of this case study suggests that probabilistic and comparable finite source properties may be discerned for large global events regardless of the quality and coverage of local instrumentation.

6.1 Introduction

Earthquakes are known to exhibit complex rupture processes that vary strongly in space and time. A better understanding of the factors controlling earthquake behavior consequently requires constraining the finite source properties of earthquakes. Today, high dimensional estimates ($\sim$ 1000 parameters) of finite source properties are routinely computed for significant earthquakes (e.g., Wald and Heaton, 1992; Ammon, 2005; Moreno et al., 2010; Ide et al., 2011; Ross, Idini, et al., 2019).

These estimates usually involve the inversion for slip on a predefined fault plane using some combination of seismic, geodetic, and tsunami data with kinematic constraints placed on the rupture propagation (Hartzell and Heaton, 1983; Du et al., 1992; Saito et al., 2011). These solutions, termed finite-fault slip distributions, provide a detailed image of time-dependent slip behavior during an earthquake rupture. However, these inversions require often arbitrary parameterization of the source geometry, have a general lack of sensitivity to rupture velocity, and need substantial regularization due to the non-uniqueness of the inverse problem (e.g., Lay, 2018; Wang et al., 2020). This nonuniqueness presents challenges to objectively comparing finite source properties between events, and thus limits our ability to discern patterns in earthquake behavior that could inform a deeper understanding of earthquake phenomenology.

The limitations of routinely computed estimates of finite source properties motivates the development of alternative estimates that overcome these limitations. One potential alternative is the second moment formulation (Backus and Mulcahy, 1976a; Backus and Mulcahy, 1976b), in which higher-order mathematical moments of the stress glut, a source representational quantity, are used to describe basic properties of the rupture process in space and time. Higher-order stress glut moments have been successfully computed in the past (Bukchin, 1995; McGuire et al., 2000; McGuire et al., 2001; McGuire et al., 2002; McGuire, 2004; Chen, 2005; Meng et al., 2020), but this methodology has received little attention compared to slip inversions. The second-moment formulation yields low-dimensional, physically-motivated estimates of the spatial extent, directivity, and duration of earthquake ruptures. It requires no prior knowledge of the rupture velocity, and makes only mild assumptions about the source geometry. Being free of gridding and associated discretization issues that complicate slip inversions, the second moment formulation can more objectively facilitate comparisons between events, helping to find common patterns, albeit at a lower resolution. Illuminating these patterns may help address outstanding questions in earthquake science relating to how fault zones may facilitate or impede earthquake ruptures.

In this study, we use the well-studied 2019 $\mathrm{M_w}7.1$ Ridgecrest earthquake as a vehicle to demonstrate our methodology (e.g., Ross, Idini, et al., 2019; Barnhart et al., 2019). The wealth of high quality geodetic data and dense seismic instrumentation have been incorporated into numerous finite-fault slip distribution models (Ross, Idini, et al., 2019; Barnhart et al., 2019; Liu et al., 2019; Xu et al., 2020; Goldberg et al., 2020; Wang et al., 2020; Jin and Fialko, 2020; Yue et al., 2021). Additionally, rapid field response studies have provided high resolution characterizations of the surface fault rupture and displacement (Ponti et al., 2020; DuRoss et al., 2020). Further, other source estimation techniques such as subevent inversion (Jia, Wang, et al., 2020) and multi-array backprojection (Xie et al., 2021) have yielded additional constraints on the time-dependence of moment release during the mainshock.

Our contributions in this paper are as follows. We develop a Bayesian inverse scheme for second moments using teleseismic data. We employ Hamiltonian Monte Carlo sampling and automatic differentiation to efficiently sample from the posterior distribution. In doing so, we apply a set of transformations that ensure positive definiteness of the second moments. We demonstrate the efficacy of our methodology by applying the inversion scheme to the Ridgecrest mainshock. We show that our methodology is useful for determining probabilistic and comparable descriptions of low-dimensional rupture parameters with few a priori assumptions.

6.2 Preliminaries

Because an earthquake is constituted by a localized zone of inelastic deformation, we can represent the source region as a localized departure from elasticity. These departures can be quantified using the so-called stress glut, $\mathbf{\Gamma}$, the tensor field computed by applying an idealized Hooke's law to the inelastic component of strain in a system (Backus and Mulcahy, 1976a; Backus and Mulcahy, 1976b). The stress glut is nonzero only within the source region. The stress glut is a complete representation of a seismic source in space and time that can be used to reproduce displacements everywhere on Earth for an arbitrary source (Dahlen and Tromp, 1998). Given the typically sparse distribution of seismic observations, solving for the full stress glut is an ill-posed problem. We can simplify the stress glut by assuming the source geometry is constant in space and time:

$$\Gamma_{ij}(\boldsymbol{\xi}, \tau) = \hat{M}_{ij} f(\boldsymbol{\xi}, \tau) \tag{6.1}$$

where $\hat{\mathbf{M}}$ is the normalized mean seismic moment tensor and f is the scalar function defined at the position $\boldsymbol{\xi}$ and time τ. This approximation reduces the solution from a tensor field to a scalar field and is most valid for seismic sources with stable source mechanisms.

We can further reduce the dimensionality of the stress glut by first recognizing that any scalar function in a bounded interval may be uniquely determined by its collection of polynomial moments. Because f captures a static displacement, f is nonzero for infinite time and thus occupies an unbounded interval, but $\dot{f}$ vanishes to zero at the cessation of rupture and is thus captured within a bounded interval. Hence, considering that the stress glut prescribes displacements due to an arbitrary seismic source, we can represent seismic displacements as the superposition of the spatiotemporal moments of the rate function $\dot{f}$. We represent the spatial and temporal components of these moments separately, with spatial order m and temporal order n. At low frequencies, we can truncate this infinite series such that we only include terms with moments of order $m + n \leq 2$. We can then explicitly define the measured displacements for a station i at low frequencies as:

$$\begin{aligned} u_i(\mathbf{r},t) \quad = \quad & \dot{f}^{(0,0)}(\boldsymbol{\xi}^c,\tau^c)\hat{M}_{jl}\frac{d}{d\xi_l}\int_{-\infty}^{+\infty} G_{ij}(\boldsymbol{\xi}^c,\tau^c,\mathbf{r},t)dt \\ & -\dot{f}_x^{(1,1)}(\boldsymbol{\xi}^c,\tau^c)\hat{M}_{jl}\frac{d}{d\xi_x}\frac{d}{d\xi_l}G_{ij}(\boldsymbol{\xi}^c,\tau^c,\mathbf{r},t) \\ & +\frac{1}{2}\dot{f}_{xy}^{(2,0)}(\boldsymbol{\xi}^c,\tau^c)\hat{M}_{jl}\frac{d}{d\xi_x}\frac{d}{d\xi_y}\frac{d}{d\xi_l}\int_{-\infty}^{+\infty} G_{ij}(\boldsymbol{\xi}^c,\tau^c,\mathbf{r},t)dt \\ & +\frac{1}{2}\dot{f}^{(0,2)}(\boldsymbol{\xi}^c,\tau^c)\hat{M}_{jl}\frac{d}{d\xi_l}\frac{d}{dt}G_{ij}(\boldsymbol{\xi}^c,\tau^c,\mathbf{r},t) \end{aligned} \tag{6.2}$$

where $\mathbf{G}$ is a Green's tensor prescribing the path effects from a source with the centroid location $\boldsymbol{\xi}^c$ and centroid time τ^c to an arbitrary station with the location $\mathbf{r}$ at time t, and $\dot{f}^{(m,n)}(\boldsymbol{\xi}^c,\tau^c)$ is the moment of the scalar rate function $\dot{f}(\boldsymbol{\xi},\tau)$ of spatial order m and temporal order n taken about the source centroid in space and time (Bukchin, 1995). Equation 6.2 is only valid at low-enough frequencies, and the determination of "low-enough" depends on the spatiotemporal dimensions of the source.

Several of the moments are of routine use in seismology, while the rest are worked with sparingly. The moment of order $m + n = 0$ is the scalar moment of the source. The moments of order $m + n = 1$ correspond to the spatial ($m = 1$) and temporal ($n = 1$) centroids of the source. Perhaps unfamiliar are the moments of order $m + n = 2$; these moments describe low-dimensional finite properties of earthquake sources. In particular, $\dot{\boldsymbol{f}}^{(2,0)}(\boldsymbol{\xi}^c,\tau^c)$ is the spatial covariance of the stress glut, $\dot{\boldsymbol{f}}^{(1,1)}(\boldsymbol{\xi}^c,\tau^c)$ is the spatiotemporal covariance of the stress glut, and $\dot{f}^{(0,2)}(\boldsymbol{\xi}^c,\tau^c)$ is the temporal variance of the stress glut. These so-called second moments yield low-dimensional, physically-motivated approximations of the source volume, source directivity, and source duration respectively (Backus, 1977).

To understand the physical significance of these second moments, we emphasize that the spatial second moments and the temporal second moments are covariances and variances respectively. From these quantities we can thus obtain the standard deviation of the stress-glut distribution, and the standard deviation is a measure of the width of the distribution. We can then define characteristic dimensions of the source using standard deviations of the stress glut derived from the second moments (Backus, 1977; Silver and Jordan, 1983). These characteristic dimensions may be defined using a metric of ±1 standard deviation from the centroid:

$$r^c(\hat{\mathbf{n}}) = \sqrt{\hat{\mathbf{n}}^{\mathbf{T}} \cdot [\dot{\boldsymbol{f}}^{(2,0)}(\boldsymbol{\xi}^c, \tau^c)/\dot{f}^{(0,0)}(\boldsymbol{\xi}^c, \tau^c)] \cdot \hat{\mathbf{n}}},$$

$$t^c = 2\sqrt{\dot{f}^{(0,2)}(\boldsymbol{\xi}^c, \tau^c)/\dot{f}^{(0,0)}(\boldsymbol{\xi}^c, \tau^c)}, \tag{6.3}$$

where $r^c(\hat{\mathbf{n}})$ is the extent of the characteristic volume from the centroid in the direction of arbitrary unit vector $\hat{\mathbf{n}}$ and t^c is the characteristic duration of the source. We will also define a characteristic length of the source, L^c, as $2 \cdot r^c(\boldsymbol{\eta})$, where $\boldsymbol{\eta}$ is the principal eigenvector of $\dot{\boldsymbol{f}}^{(2,0)}(\boldsymbol{\xi}^c, \tau^c)$. Using the mixed second moments and the characteristic dimensions described in equation 6.3, we can get estimates of the velocity of the rupture:

$$\mathbf{v_0} = \dot{\boldsymbol{f}}^{(1,1)}(\boldsymbol{\xi}^c, \tau^c)/\dot{f}^{(0,2)}(\boldsymbol{\xi}^c, \tau^c),$$

$$v^u = L^c/t^c \tag{6.4}$$

where $\mathbf{v_0}$ is the average instantaneous velocity of the centroid of the rupture and v^u is an upper bound on the average velocity of the rupture. The quantities described in equations 3 and 4 thus yield physically interpretable values with which we can evaluate and compare stress glut second moment solutions and contextualize these solutions in the broader source characterization literature.

6.3 Methods

Data and Preprocessing

In this study we work with both real and synthetic seismic waveform data. The real data are vertical component seismic data from 48 Global Seismographic Network

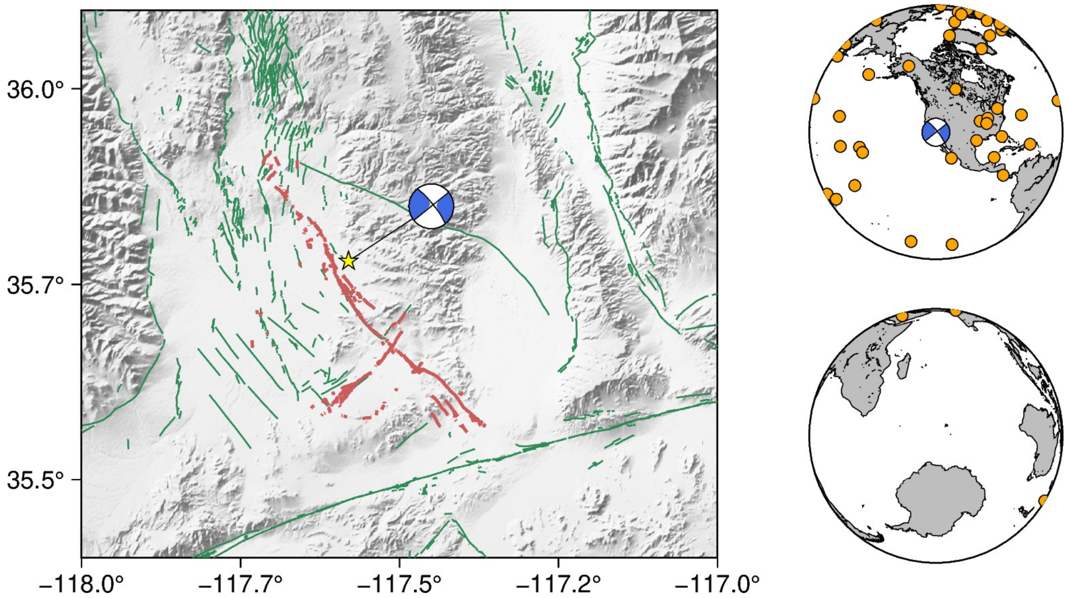

Figure 6.1: Geographic setting and data coverage. Left: Geographic setting of the 2019 Ridgecrest Sequence. Focal mechanism is the gCMT solution for the sequence mainshock. Yellow star indicates the gCMT solution centroid position. Green and red lines indicate USGS mapped quaternary faults (USGS and CGS, 2022) and faults that were activated during the Ridgecrest Earthquake sequence (Ross, Idini, et al., 2019). The strike, dip, and rake of the true nodal plane as given by the gCMT solution are 321°, 81°, and 180°, respectively. Map coloring is reflective of elevation. Right: Global distribution of stations from which waveforms were used in this study.

(GSN) stations (Figure 6.1). We selected these stations both by the source-to-receiver distance and by evaluating how well the waveforms were approximated by point source synthetics computed using the gCMT solution. The seismograms used in the inversion are 700 second windows about the surface wave packet that we manually selected from 7200 second windows that start at the gCMT centroid time for the Ridgecrest mainshock. In this study, we only use the vertical component of the seismograms and only include R1 arrivals. The addition of other phases like body waves and G1 arrivals, as well as R2 and G2 arrivals, would further constrain the posterior distribution, but we reserve the inclusion of these additional phases for future studies. Using additional phases presents some challenges. For example, including body waves, which are of higher velocity than surface waves, requires computing higher frequency Green’s functions; including the G1 phase, which has a different sensitivity than the R1 phase (Bozdağ and Trampert, 2008), may require better accounting for shallower structure when attempting to match our

Green's functions to observations. We down-sample the waveform data to a 0.05 Hz sampling rate, which reduces the correlation between samples and minimizes the computational demands of the inversion. As part of the construction of the forward propagation matrix, we computed the Green's tensor using the gCMT moment tensor and centroid location, which we perturbed to compute the requisite spatial derivatives numerically.

To compute the Green's tensor, we use the 3D Earth model S362ANI + M (Moulik and Ekström, 2014) and the full waveform modeling software Salvus (Afanasiev et al., 2019), which employs the spectral element method to simulate wave propagation. After computing this Green's tensor, we initially keep these waveforms at a high frequency (4 Hz) to improve numerical stability when approximating integrals and derivatives. We take the necessary temporal and spatial derivatives and integrals of this Green's tensor numerically using a centered finite difference approximation. For the spatial derivatives, we tested numerous finite difference offsets from the spatial centroid using synthetic tests, which are described subsequently. Given these tests, we prefer a perturbation distance of 150 m because this distance is both small enough to yield a reasonable approximation of the spatial derivative and large enough to be numerically stable. We consider both the results from a synthetic test, which we describe subsequently, and finite-fault slip distribution solutions with geodetic constraints for the Ridgecrest earthquake when evaluating our choice of perturbation distance. The construction of the forward propagation matrix, which we describe subsequently, requires both the gCMT moment tensor and the Green's tensor derivatives and integrals.

A particularly important step in the preprocessing of these waveforms is selecting which frequency band to use in the inversion. There are two key issues that need to be balanced when making this determination. Firstly, equation 6.2 is a low frequency approximation; at higher frequencies, moments of order $m + n > 2$ become more significant. This means that the frequency band needs to be low enough such that we exclude moments of order $m + n > 2$, or else the inversion will be biased by these higher-order terms. Secondly, moments of order $m + n = 0$ and $m + n = 1$ are used. The values used for these lower-order terms are robust, but are subject to error. Thus, we need to ensure that the contributions from moments of order $m + n = 2$ are large enough such that they exceed the magnitude of error of the lower order terms, otherwise the inversion will be dominated by this error. In short, the frequency band should be high enough such that the contribution of the second moments markedly exceeds the error on the solutions for the zeroth and first moments, and be low enough such that the contribution of the third moments is reasonably small. A good metric by which to make this selection is to use the observation that the contribution of moments of order $m + n$ is approximately proportional to $(D/P)^{m+n}$ (assuming $(D/P) < 1$) where D is the source duration and P is the period (Backus, 1977). Looking at the distribution of scalar moment estimations for the Ridgecrest mainshock obtained using teleseismic data (GCMT, 2019; USGS, 2019; Liu et al., 2019), we likely approach the order of the error on the zeroth moment when the contribution of the second moments exceeds 5% of the zeroth moment. To obtain a period band where the second moments are significant compared to the error on the lower-order terms and the contribution of the higher-order terms are always small compared to the second moments, we select a period band that obeys both $(D/P)^2 > 0.05$ and $(D/P)^3 < 0.05$. Taking 25 s as an approximate source duration for the Ridgecrest mainshock, this yields a period band of 70-110 s. Since source durations are routinely estimated for global events (e.g., Vallée and Douet, 2016), this method of frequency-band selection is applicable to most other global events.

We only use stations in the distance range $10 - 90°$, with the exception of a few stations with exceptional fits at distances just above 90° (see Figure 6.1), to minimize the bias imposed by the integrated effect of Earth model error. We then align the Green's tensor and observed displacements of the remaining stations via cross correlation and select a 700 s window that encompasses the surface wave packets at each station. The time shifts, which are intended to correct for time errors due to variable Earth model inaccuracy, are performed at a frequency band at which the third moments are small. There is thus assumed to be minimal skewness in the source time function, and we then expect the cross-correlation to account for the Earth-model effected timing error without misaligning the centroid time. We apply a Hamming taper to the surface wave packet to minimize the contributions of signal at the start and end of the time window. These time windows constitute the time-segments of the Green's tensor and data. Because the contribution of moments of order $m + n = 2$ should still be relatively small in the selected frequency band, the synthetic waveforms produced using a point source approximation should be similar to the observed waveforms. We thus perform an additional manual quality control of the remaining stations, and we remove stations that show a poor match between the data and the point source waveforms. Both the waveforms that were kept and the waveforms that were thrown out in the course of this quality control are shown in Figure 6.S1.

Before applying this methodology to real data, we will show a test of the outlined inversion procedure using a synthetic source. For this test, we prescribe a 55x15 km rectangular fault with a strike and dip corresponding to the nodal plane of the gCMT solution associated with the true rupture surface. We then define a grid of point sources, each with the gCMT source mechanism and equal fraction of the gCMT moment, along this prescribed fault such that the spatial release of moment can be approximated as uniform distributions of moment release along the strike and dip of the fault. We delay the activation of these point sources according to a prescribed rupture velocity of 2.5 km/s along strike, resulting in an event duration of 22 s, such that the moment release with time can also be approximated as a uniform distribution. Using the fact that the width of a uniform distribution is equal to $2\sqrt{3}\sigma$, where σ is the standard deviation of the Gaussian approximation of that uniform distribution, we can determine the true second moment solution for this synthetic source.

Inversion

Equation 6.2 describes the forward model for a second moment tensor source. While it appears unruly, many of the terms that constitute it are easily accessible. For a given source, we can observe $u_i(\mathbf{r}, t)$ using seismic instrumentation; we can solve for $\mathbf{G}$, $\mathbf{M}$, and $(\boldsymbol{\xi}^c, \tau^c)$ using routine techniques; and we can compute the necessary derivatives and integrals using numerical methods. Thus, in equation 6.2, only the moments of the scalar function $\dot{f}$ are unknown. We can then pose equation 6.2 as a linear inverse problem:

$$\mathbf{d} = \mathbf{F}\mathbf{p} \tag{6.5}$$

where $\mathbf{d}$ is a vector of measured displacements, $\mathbf{F}$ is a forward propagation matrix of spatial and temporal integrals and derivatives of $\mathbf{G}$, the columns of which are weighted by the components of $\mathbf{M}$, and $\mathbf{p}$ is a vector of parameters which constitute the lower-order moments of the stress glut.

Numerous Bayesian methods for source parameter inversion have been proposed for problems such as focal mechanism estimation (Wéber, 2006; Walsh et al., 2009; Lee et al., 2011; Duputel et al., 2014) and finite-fault slip distribution estimation (Monelli et al., 2009; Minson et al., 2013). Bayesian inference has been growing increasingly popular because it provides an ensemble of solutions that are informed by both data and prior distributions determined by physical constraints or ground truth. The Bayesian formulation described here allows for the computation of an ensemble of second moment solutions, with each providing a low dimensional estimate of the source process.

The posterior distribution for this problem can be written as follows (e.g., Tarantola, 2005),

$$p(\mathbf{p}, \sigma|\mathbf{d}) \propto p(\mathbf{d}|\sigma, \mathbf{p})\ p(\sigma)\ p(\mathbf{p}), \tag{6.6}$$

where σ is a hyperparameter. For the likelihood term, $p(\mathbf{d}|\sigma, \mathbf{p})$, we use a multivariate normal distribution,

$$p(\mathbf{d}|\sigma, \mathbf{p}) \propto \frac{1}{\sqrt{|\Sigma|}} \exp(-\frac{1}{2}(\mathbf{d} - \mathbf{Fp})^{\mathrm{T}}\, \boldsymbol{\Sigma}^{-1}\, (\mathbf{d} - \mathbf{Fp})). \tag{6.7}$$

Since the observations are time-series data, errors in the forward model will be subject to temporal autocorrelation. We can account for this correlation structure through the data covariance matrix, $\boldsymbol{\Sigma}$, as outlined in (Duputel et al., 2014). If d_i and d_j are measured displacements that are on the same trace and are recorded by the same station:

$$\Sigma_{ij} = \sigma \cdot \exp(-|i - j|\delta t/\Delta t), \tag{6.8}$$

where σ is the hyperparameter included in equations 6 and 7, δt is the sampling rate, and Δt is the period of the shortest period information included in the time-series. This prescribes a block diagonal matrix where the blocks have the same length as the time windows taken from each station. This correlation structure accounts for temporal correlation in the errors, but not any spatial correlation. In this paper we assume that the observations are spatially distributed sparsely enough that spatially-correlated errors are negligible.

We use uninformed priors in this case study, but note that informed priors can easily be incorporated (Gelman et al., 2010). That is, with the physical interpretation of the second moment properties that we will describe shortly, priors on the spatial extent, directivity, and duration may be imposed given observational ground truth. For example, if the true nodal plane of an earthquake is known, Gaussian priors may be placed on the spatial second moment parameters to restrict the principal eigenvector of the spatial covariance matrix to abut the true nodal plane.

The total number of parameters in this inverse problem is 11, and we approximate $p(\mathbf{p}, \sigma|\mathbf{d})$ using Markov Chain Monte Carlo (MCMC) sampling to obtain an ensemble of solutions. We do not solve for the zeroth or first order moments, and instead use the gCMT solution as our moment tensor and centroid location. Future work will focus on jointly solving for the lower order moments together with the second moments. As the parameter space is too large for efficient inference with standard Metropolis-Hastings type samplers, we instead sample from the posterior distribution using Hamiltonian Monte Carlo (HMC) sampling (Neal, 2010), which is an instance of the Metropolis-Hastings algorithm that can efficiently sample large parameter spaces using principles from Hamiltonian dynamics. This is accomplished in part by incorporating gradient information into the sampling process; however, it requires a means to also compute gradients efficiently. Here, we accomplish this through the use of reverse-mode automatic differentiation (Innes, 2019).

For each Markov chain in the inversion, we draw 5000 samples from the posterior distributions after drawing 5000 burn-in samples. The momentum distribution has a diagonal mass matrix and the samples are updated using an ordinary leapfrog integrator (Neal, 2010). To evaluate convergence, we run at least 3 chains of the inversion and compute the Gelman-Rubin diagnostic using the computed set of chains (Gelman and Rubin, 1992). That is, we compare the variability within chains to the variability between chains to determine if the chains all converge to the same target distributions.

Additionally, as described in prior work on this subject (Bukchin, 1995; McGuire et al., 2001), the second moments of the stress glut are covariances, and therefore only a subset of the parameter space produces valid solutions. Specifically, the second moments are symmetric positive definite,

$$\mathbf{X} = \begin{bmatrix} \dot{\boldsymbol{f}}^{(2,0)}(\boldsymbol{\xi}^c, \tau^c) & \dot{\boldsymbol{f}}^{(1,1)}(\boldsymbol{\xi}^c, \tau^c) \\ \dot{\boldsymbol{f}}^{(1,1)}(\boldsymbol{\xi}^c, \tau^c)^T & \dot{f}^{(0,2)}(\boldsymbol{\xi}^c, \tau^c) \end{bmatrix} \succeq 0. \tag{6.9}$$

Physically, this is equivalent to saying that the spatial extent and duration of the source are both non-negative. Typically, when performing a constrained Bayesian inversion, the easiest course of action is to sample under an unconstrained parameter space and subsequently transform those parameters into the necessarily constrained parameter space (Gelman et al., 2010). To this end, we note that, by the Cholesky Factorization Theorem, every symmetric positive-definite matrix can be decomposed into the product of some lower triangular matrix with a positive diagonal and the transpose of that same lower triangular matrix. This means that given **X**, there exists a lower triangular matrix **L** with positive diagonal components such that:

$$\mathbf{X} = \mathbf{L}\mathbf{L}^T. \tag{6.10}$$

Thus, we can sample freely from the unconstrained off-diagonal components of **L** and from the natural logarithm of the diagonal components of **L**. Then, to evaluate our sample against our data, we can simply build **L** using our sample components and then construct **X** using equation 6.10. From **X** we can extract a valid **p** with which we evaluate the likelihood of our sample. A keen observer may notice that while **X** need only be symmetric positive semi-definite, the Cholesky factorization forces **X** to be positive definite. In practice, this distinction is inconsequential, as a positive semi-definite **X** suggests that at least one dimension of the source is identically zero, which will never be true in reality.

6.4 Results

We first perform our inversion on the synthetic test described in the Methods section. In the interest of evaluating the resolvability of parameters for the Ridgecrest mainshock, we invert for these second moments using the same distribution of stations and the same windowing procedure that we use for the real event. For this test, we also use the mean σ from the to-be-described inversion of real data so we can test this inversion in the presence of realistic error. The marginal probability distributions for each parameter and the joint probability distributions for each pair of parameters are shown in Figure 6.2. These plots show that most of the parameters are either uncorrelated or weakly correlated with each other. Some terms, however, present noteworthy correlations with each other. These terms include closely related spatial terms, such as the E-E and E-N terms of the spatial covariance matrix and the N-N and E-N terms of the spatial covariance matrix. Notable correlations are also found between the spatial and temporal components, namely, the diagonal components of the spatial covariance matrix with the temporal variance. These plots also show that almost all the components of the expected second moment covariance matrix fall well within the ensemble of solutions, with the exception of a slight underestimate of the magnitude of the east and north components of the mixed second moment. This discrepancy may be due to the imperfect assumption of uniform moment release with time for this test due to the discretization of the source.

We can further test the fidelity of our inversion results by computing synthetic waveforms using equation 6.2 and evaluating the fit to the observed waveforms generated for this synthetic example. The waveforms for an ensemble of second

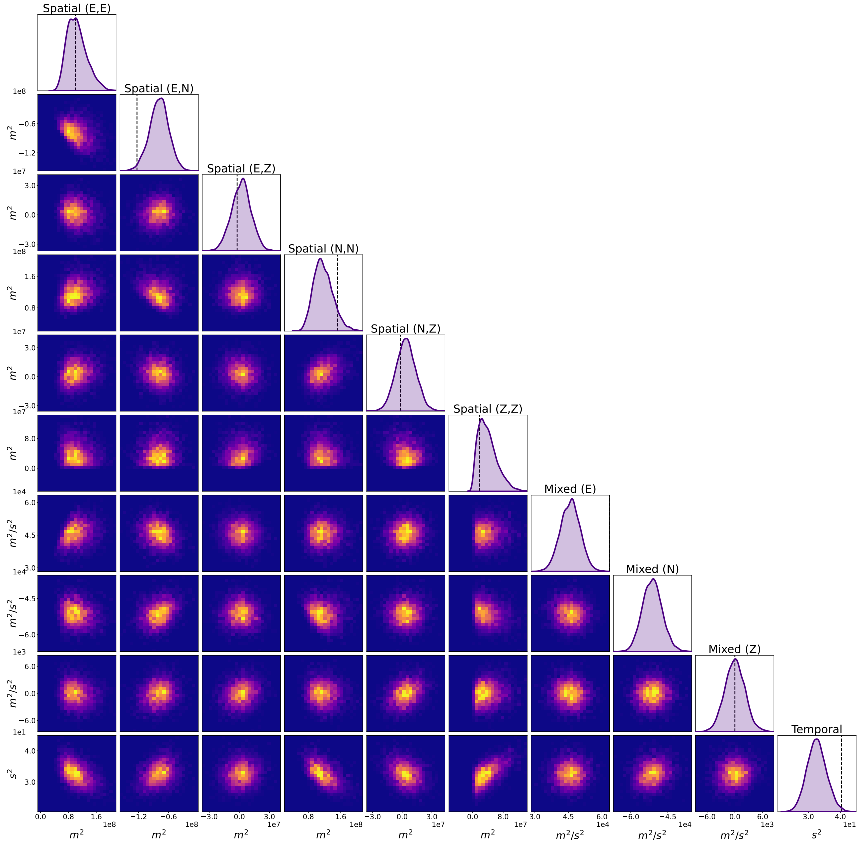

Figure 6.2: Marginal and joint probability density plots for the 10 independent parameters inverted for the synthetic test in this study. Off-diagonal plots are 2-dimensional histogram plots representing the joint probability distribution for each pair of independent parameters. On-diagonal plots are kernel density estimate plots for the marginal distributions of the adjacent joint probability distributions. Black dotted lines indicated the anticipated solution for each parameter in the inversion.

moment solutions from a single chain for the synthetic test are shown for a subset of stations with a large diversity of azimuths and distances in Figure 6.3. The waveform fits match the synthetic observations very well, particularly when the full ensemble of solutions is considered. As is shown in this figure, the inclusion of the inverted-for second moments of the stress glut perturb the point-source waveforms to fit the synthetic observations, thus successfully accounting for the finiteness of the source.

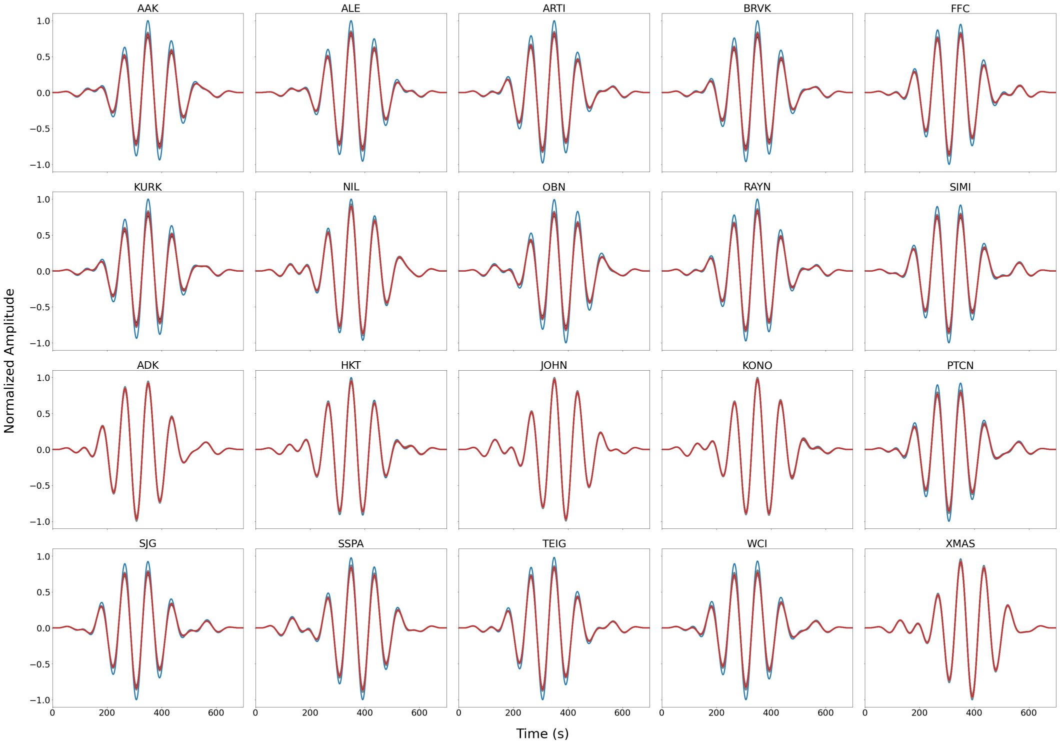

Figure 6.3: Waveform fits for a large subset of the windowed waveforms for the synthetic test conducted in this study. Waveforms are labeled according to the GSN station at which they were generated. Black waveforms are synthetic observations. Gray waveforms are generated using a single solution from the ensemble of solutions from our inversion. Waveforms from each solution in the ensemble are plotted. Red waveforms are generated using the mean solution of the ensemble of solutions from our inversion. Blue waveforms are generated using only the gCMT solution and exclude any consideration of the second moments of the stress glut.

In order to represent the second moment solutions for the synthetic test in a more physically interpretable way, we convert the ensembles of second moments into ensembles of L^c, t^c, $|\mathbf{v_0}|$, and v^u; the anticipated values for these parameters are 31.8 km, 12.7 s, 2.5 km/s and 2.5 km/s, respectively. Additionally, because the directions associated with L^c and $|\mathbf{v_0}|$ are important, we consider the strike (θ) and plunge (ϕ) associated with these quantities as well; the anticipated values for these parameters are 321° and 0° for rupture strike and plunge and 141° and 0° for directivity strike and plunge. We plot the ensembles of these quantities in Figure 6.4. We find that the ensembles of these converted parameters are largely normally distributed, and the values associated with the anticipated solution for the synthetic test all fall within these ensembles. In particular, we find that, within two standard deviations, the characteristic length for this test is 27.7 ± 4.8 km with strike and plunge of 317.5 ± 13.5° and −0.1 ± 9.9°, respectively. The characteristic duration of this test is 11.4 ± 1.1 s. The instantaneous centroid velocity of this test has magnitude 2.1 ± 0.5 km/s with strike and plunge of 138.2 ± 6.8° and 0.0 ± 3.6°, respectively. Finally, the average velocity upper bound for this test is 2.4 ± 0.6 km/s. These plots additionally make clear how well constrained certain parameters may be given waveform data in the presence of error. Notably, the width of the distribution on the instantaneous centroid velocity in Figure 6.4E suggests that this directivity is the least constrained of these parameters.

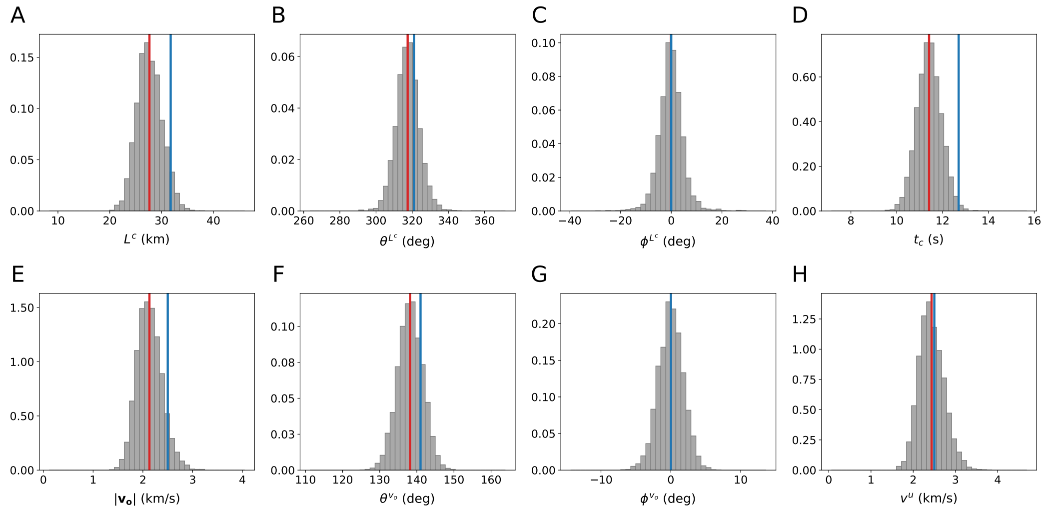

Figure 6.4: Physically motivated representations of the ensembles of second moment solutions for the synthetic test. A. characteristic length (L^c), B. characteristic length strike (θ^{L^c}), C. characteristic length plunge (ϕ^{L^c}), D. characteristic duration (t^c), E. instantaneous centroid velocity magnitude ($|\mathbf{v_0}|$), F. instantaneous centroid velocity strike ($\theta^{\mathbf{v_0}}$), G. instantaneous centroid velocity plunge ($\phi^{\mathbf{v_0}}$), H. average velocity upper bound (v^u). Histogram shows density of realizations in the ensemble. Red vertical line shows the mean realization. Blue line shows the anticipated realization.

Now, we invert for the second moments of the 2019 Ridgecrest mainshock using the real data. The distributions of the 10 independent parameters of the second moments for a single chain of the inversion using the real data are shown in Figure 6.5. We run the inversion for a set of chains, shown in Figure 6.S2, and compute the Gelman-Rubin diagnostic (Gelman and Rubin, 1992) using these chains. The Gelman-Rubin values are far less than 1.1, suggesting that the chains have converged to the target posterior distributions for the second moments. The joint probability distributions for each pair of parameters are shown in Figure 6.5. As with the synthetic test, these joint distributions show that the inverted parameters are mostly uncorrelated with each other. Some of the marginal distributions of the second moments are skewed due to the positive-definite constraint placed on the inversion. The distribution for the hyperparameter σ is shown in Figure 6.S3. We can also evaluate the waveform fits for the inversion using real data. A representative subset of these waveform fits is shown in Figure 7.2. The computed waveforms for the ensemble of solutions inverted for under this framework fit the observed waveforms reasonably well.

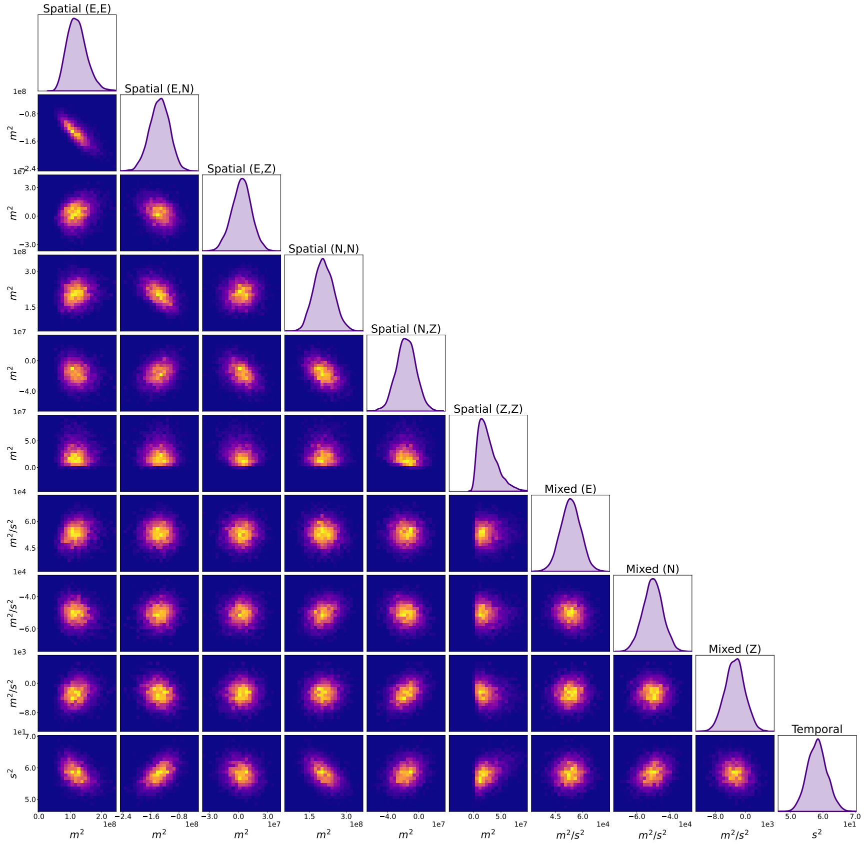

Figure 6.5: Marginal and joint probability density plots for the 10 independent parameters inverted for in this study. Off-diagonal plots are 2-dimensional histogram plots representing the joint probability distribution for each pair of independent parameters. On-diagonal plots are kernel density estimate plots for the marginal distributions of the adjacent joint probability distributions.

Using these ensembles of second moments, we can summarize the physical parameters of the Ridgecrest mainshock. We show these distributions in Figure 6.7. As

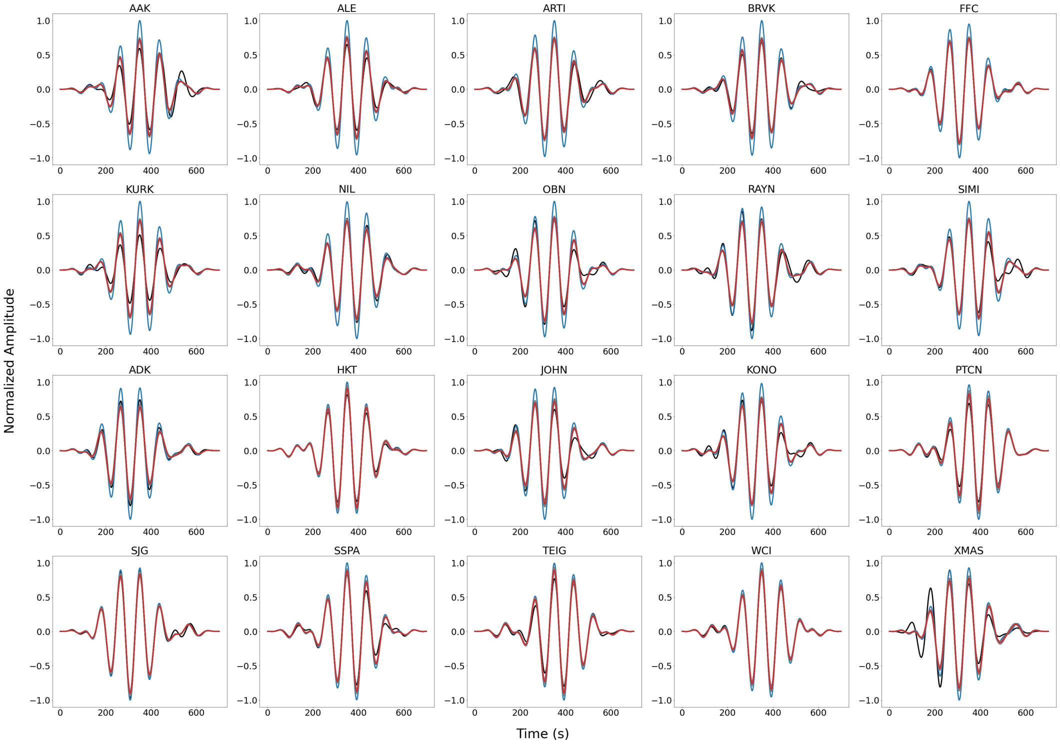

Figure 6.6: Waveform fits for a subset of the windowed waveforms used in this study. Waveforms are labeled according to the GSN station at which they were recorded. Black waveforms are observations. Gray waveforms are generated using a single solution from the ensemble of solutions from our inversion. Waveforms from each solution in the ensemble are plotted. Red waveforms are generated using the mean solution of the ensemble of solutions from our inversion. Blue waveforms are generated using only the gCMT solution and exclude any consideration of the second moments of the stress glut.

with the synthetic test, most of these ensembles are normally distributed, with the exception of ϕ^{L^c}, which is bimodal, which reflects some nonlinearity in the mapping between the raw second moments and the derived parameters. We find that, within two standard deviations, the characteristic length of the rupture is 35.2 ± 6.0 km with strike and plunge of $324.1 \pm 10.0°$ and $0.1 \pm 8.1°$, respectively. The characteristic duration of the rupture is 15.3 ± 0.8 s. The instantaneous centroid velocity of the Ridgecrest mainshock has a magnitude of 1.3 ± 0.3 km/s with strike and plunge of $133.3 \pm 8.3°$ and $-2.2 \pm 4.1°$, respectively. Finally, the average velocity upper bound is 2.3 ± 0.5 km/s. Additionally, some finite-fault slip distributions are easily available through the SRCMOD database (Mai and Thingbaijam, 2014). For comparison with our solution, we can compute the centered spatial second moments of the stress-glut for these finite-fault slip distributions. We plot the resultant characteristic values from these finite-fault slip distributions in Figure 6.7. These characteristic values fall well within the ensemble of characteristic values computed using this inversion procedure. We summarize the results for the spatial and mixed second moments by plotting projections of ellipsoids defined using $r^c(\hat{\mathbf{n}})$ from equation 6.3, which yield descriptions of the volume in which most of the moment of the source was released, and $\mathbf{v_0}$ for a subset of 500 solutions from our ensemble of second moment solutions for this source in Figure 6.8.

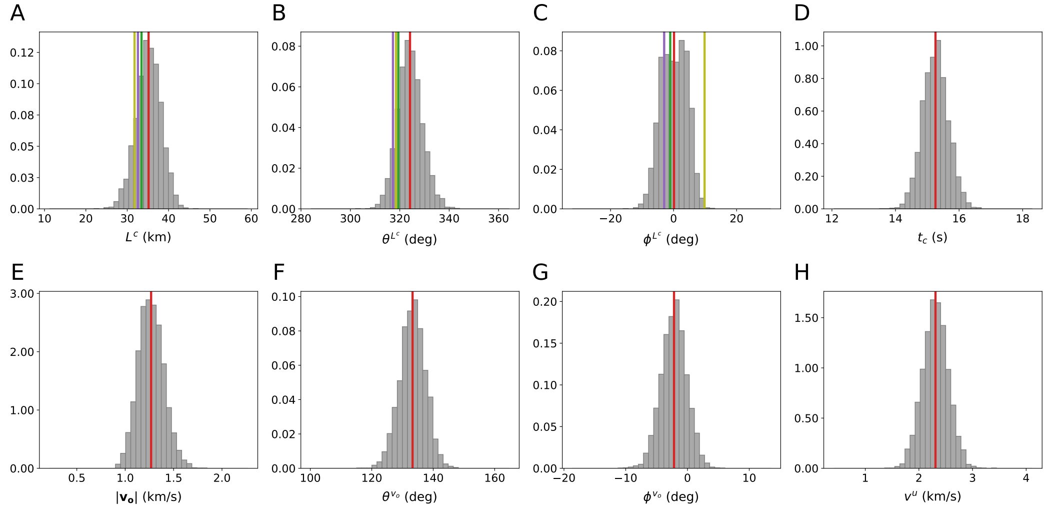

Figure 6.7: Physically motivated representations of the ensembles of second moment solutions for the 2019 Ridgecrest mainshock. A. characteristic length (L^c), B. characteristic length strike (θ^{L^c}), C. characteristic length plunge (ϕ^{L^c}), D. characteristic duration (t^c), E. instantaneous centroid velocity magnitude ($|\mathbf{v_0}|$), F. instantaneous centroid velocity strike ($\theta^{\mathbf{v_0}}$), G. instantaneous centroid velocity plunge ($\phi^{\mathbf{v_0}}$), H. average velocity upper bound (v^u). Histogram shows density of realizations in the ensemble. Red vertical line shows the mean realization. Green, purple, and yellow vertical lines correspond to the fault-slip distribution results from prior studies, simplified into spatial second moments, from Ross, Idini, et al. (2019), Xu et al. (2020), and Jin and Fialko (2020), respectively.

6.5 Discussion

When evaluating the solutions described in Figures 6.4, 6.7, and 6.8 and when contextualizing these solutions with previous results, it is important to keep in mind that these quantities are derived parameters from the variance of the stress glut distribution. This is distinct from other types of source parameterizations, such as finite-fault slip distributions, which attempt to solve for an approximation of the full stress glut distribution. Thus, the solutions presented in this study,

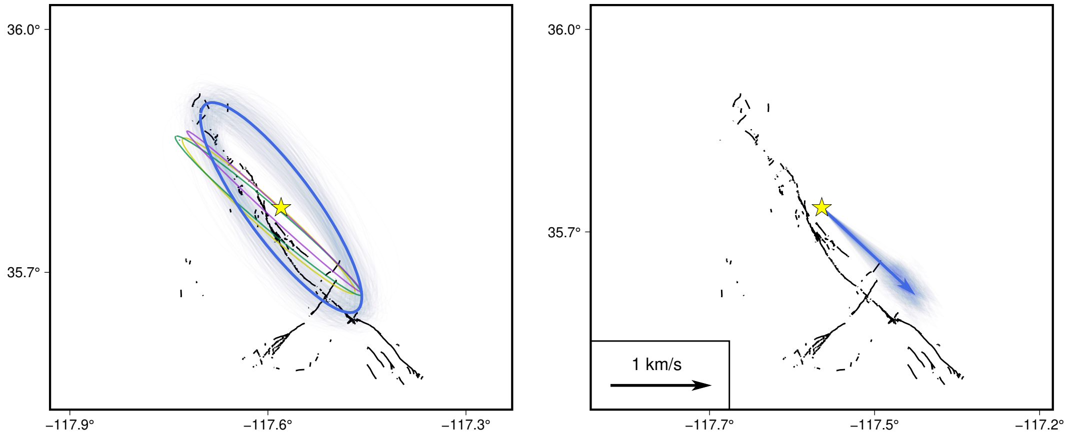

Figure 6.8: Summary figure of the map-view spatial and directivity features of the 2019 Ridgecrest mainshock as derived from the second moment inversion. Left: Map-view projections of a 500-solution subset of the ensemble of second spatial moment ellipsoids solved for in this study. Ellipsoids are defined using $r_c(\hat{\mathbf{n}})$ in equation 6.3, and the largest principal semi-axis is L_c. Right: Map-view projections of a 500-solution subset of the ensemble of $\mathbf{v_0}$, as defined in equation 6.4, solved for in this study. Black lines represent the surface-rupture faults mapped after the Ridgecrest mainshock. Yellow star marks the location of the gCMT centroid of the Ridgecrest mainshock. Transparent blue lines represent a single solution from the ensemble of second moment solutions. Solid blue lines represent the mean solution from the ensemble second moment solutions. Green, purple, and yellow vertical lines correspond to the fault-slip distribution results from prior studies, simplified into spatial second moments, from Ross, Idini, et al. (2019), Xu et al. (2020), and Jin and Fialko (2020), respectively.

while physically meaningful, ought to be considered as a separate category of rupture parameterization that should be compared to other rupture parameterizations cautiously. With this in mind, we can begin to assess whether the solutions given in this study yield a reasonable low-dimensional story of the Ridgecrest mainshock rupture.

In general, the ensemble of solutions for the Ridgecrest mainshock is well constrained and largely agrees with what is already known about the event. As is shown in Figure 6.8, the largest principal axis of the ellipsoid representation is well-aligned with the faults that are known to have ruptured during the mainshock. As is made clear in Figures 6.7 and 6.8, the characteristic length of this rupture is in close agreement with other estimates of the rupture extent for this event. Also shown in Figure 6.8, the directivity vectors are aligned with these faults and suggest a rupture scenario in which the instantaneous centroid propagates from the NW to the SE. This unilateral behavior is in agreement with other estimates of the directivity of the event. The characteristic durations for this event, which suggest the period of time in which the majority of the moment, but importantly not all of the moment, was released, is also in agreement with other estimates of duration for this earthquake.

The joint probability distributions shown in Figures 6.2 and 6.5 suggest that most of the independent parameters of the second moments of the stress glut are weakly correlated. In general, this weak correlation suggests that a perturbation in one parameter will likely have little effect on the values of other parameters. Perhaps most interesting are the weak correlations between the spatial second moments and the temporal second moments. These suggest the intuitive conclusion that changing the amount of time available for rupture changes the volume through which a rupture of fixed velocity can propagate.

The low dimensional second moment estimate of the 2019 Ridgecrest mainshock illustrates the unique potential of this methodology for producing probabilistic estimates of finite source properties with few a priori assumptions on the fault geometry and rupture dynamics. The only requirement is a centroid moment tensor solution, which fits nicely into this framework, as the zeroth and first moments represent the scalar moment and centroid position of the earthquake, respectively. In fact, the centroid moment tensor solution may be solved concurrently with the second moment solution (McGuire et al., 2000), but this introduces nonlinearity and significant additional computational/numerical complexity, which we reserve for future studies. The only constraint required in the inversion is that the source be non-negative in extent, which does not exclude any possible source scenarios. However, it is indeed easy to impose additional constraints on the second moments through the use of informed priors on the inversion parameters. Such informed priors should be imposed with the understanding that the second moments describe a covariance matrix of a 4-dimensional stress glut distribution. That is, informed priors are not necessarily being placed on the possible source dimensions, but instead are being placed on the possible covariances of the source distribution.

The 2019 Ridgecrest mainshock is a well-studied event, and many of the features of the rupture that are illuminated by this inversion were already known. However, this study serves as an illustration of some key strengths of this technique. Firstly, this methodology provides an estimate of the full posterior distribution of these solutions. So, claims regarding rupture finiteness can be made in the context of the full range of possible solutions given the uncertainty in the problem. Having a posterior distribution thus allows us to apply some degree of confidence to specific claims about an earthquake rupture. Consequently, with this methodology, we can make probabilistically supported assessments of the significance of similarities and differences between solutions for different events. Another benefit of this approach is that, given a prescribed correlation structure in the data, the data covariance matrix is solved for as a hyperparameter in the inversion. This means that the uncertainty of the posterior is reflective of data uncertainty that is solved for dynamically according to the structure of the data and the model.

Additionally, this methodology requires few of the a priori assumptions that present challenges and inaccuracies in other source finiteness estimation techniques, like finite-fault slip distributions. For example, this inversion technique does not require any prior characterization of the fault surface. Although the fault surface for Ridgecrest is well-approximated, for many global events, like offshore earthquakes, determining a fault surface is challenging, and so this methodology presents a substantial advantage for these events. Indeed, this methodology does not even require that all of the slip take place on a surface, but instead allows for moment release in a volume. This is apparent in Figure 6.8, where the spatial second moment is represented as an ellipsoid with a finite width orthogonal to the major axis of the ellipsoid. Indeed, with this methodology, scientifically interesting properties like the fault-normal width of rupture can be probabilistically constrained and compared between events. This width parameter for the Ridgecrest event can be quantified by assuming a fault plane derived from the direction of the principal eigenvector and the dip of the true nodal plane of the gCMT focal mechanism. Then, we can compute a maximum off-fault distance as the maximum distance of the spatial covariance ellipsoid computed using equation 6.3 from this fault plane. The ensembles of maximum off-fault distances for the solutions shown in Figures 6.4 and 6.7 are shown in Figure 6.S4. Indeed, Figure 6.S4 shows that, for this event, the off-fault distance for the Ridgecrest rupture is not distinct from the off-fault distance of the synthetic test, for which the true width is zero. However, for an event of larger width, or an event with a lower inferred error (e.g., a larger event with signficant second moments at lower frequencies), this parameter may significantly exceed zero, suggesting moment release in a volume.

Another strength of this methodology is implicit in the fact that we employed this methodology using only GSN teleseismic data. Although the Ridgecrest earthquake occurred in an exceptionally well-instrumented area, for many global events teleseismic data is the only available information for characterizing the coseismic rupture. Thus for numerous events, given this limitation in data availability, robust information concerning rupture finiteness is scarce. This methodology then serves as a potentially pivotal tool in discerning probabilistic characterizations of earthquakes globally. Relatedly, large global events occur infrequently, and thus historic events are a crucial component in our understanding of large earthquakes. The continuity of teleseismic data collection by the GSN for over two decades thus allows for this methodology to be readily applied to a large number of previous global earthquakes.

6.6 Conclusions

In this study, we develop a Bayesian framework for computing second moments of the stress glut of earthquakes using teleseismic data. This framework incorporates a positive-definite constraint under Cholesky decomposition and employs Hamiltonian Monte Carlo sampling to efficiently probe the parameter space. This methodology provides robust estimates of uncertainty by sampling the posterior distribution of solutions with dynamic error computation and accounting for the temporal correlation structure in the waveform data. These second moments of the stress glut provide a low-dimensional, physically-motivated representation of source volume, directivity, and duration that requires few *a priori* assumptions and is repeatable and comparable between events. We verify this methodology using a synthetic test and apply this framework to the 2019 Ridgecrest Sequence mainshock. We show that our solutions for this event yield event parameters that largely agree with what is known about this event and includes an estimate of the full posterior distribution. Our solution also illustrates some key strengths of this rupture-parameterization, namely the independence of this solution from a prescribed fault surface and the reliance of this inversion on only teleseismic data.

Supplementary Materials

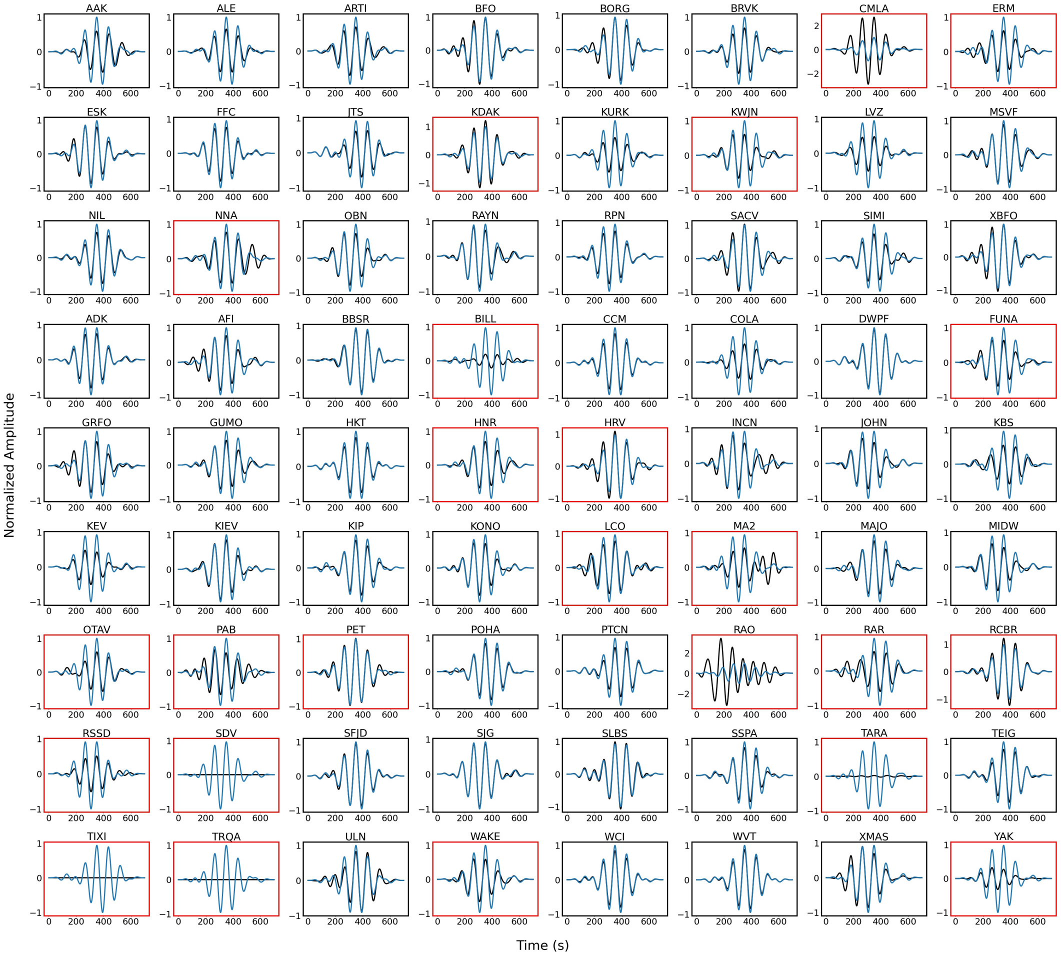

Figure 6.S1: Traces of stations submitted to manual quality control in this study. Station plots with black outlines indicate stations that were kept. Station plots with red outlines indicate stations that were not kept

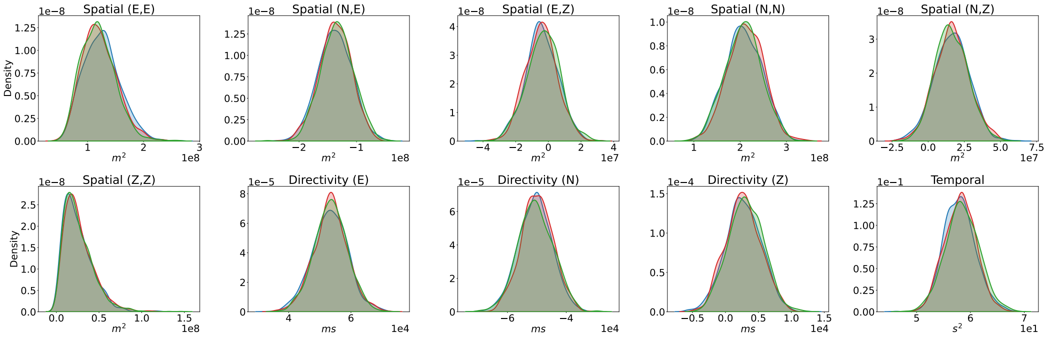

Figure 6.S2: Kernel density estimate plots for multiple chains describing the distributions of independent components of the second moments of the stress glut for the 2019 Ridgecrest sequence mainshock. Different colors (blue, red, and green) represent different chains of the inversion.

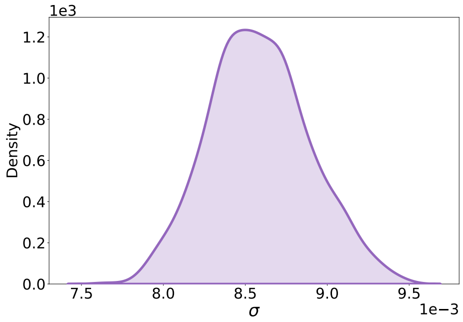

Figure 6.S3: Distribution of hyperparameter σ determined in the inversion using real data and included in the inversion using synthetic data.

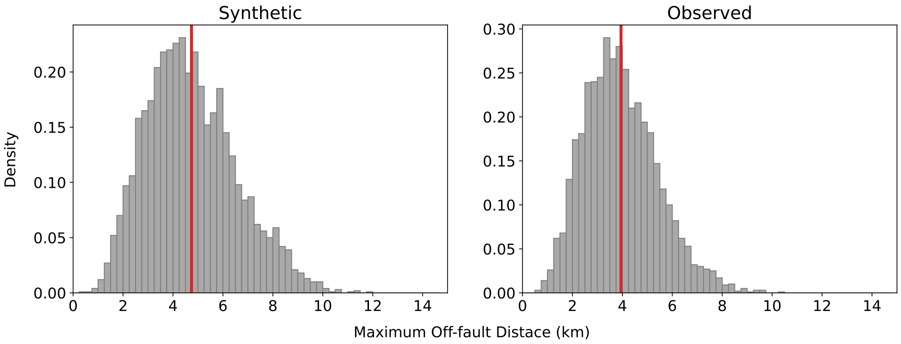

Figure 6.S4: Posterior distribution of the maximum off-fault distance derived using the ensemble of spatial covariance matrices and assuming a vertically dipping fault plane. Left plot is the ensemble for the synthetic test. Right plot is the ensemble for the test using observations. Red vertical lines delineate the mean of the ensemble.

Chapter 7

COMPARING SECOND MOMENTS OF LARGE STRIKE-SLIP EARTHQUAKES

Atterholt, J. and Ross, Z. E. (2023). Finite source properties of large strike-slip earthquakes. *Geophysical Journal International* 236. DOI: `10.1093/gji/ggad459`. Pp. 889–903.

Abstract

Earthquake ruptures are complex physical processes that may vary with the structure and tectonics of the region in which they occur. Characterizing the factors controlling this variability would provide fundamental constraints on the physics of earthquakes and faults. We investigate this by determining finite source properties from second moments of the stress glut for a global dataset of large strike-slip earthquakes. Our approach uses a Bayesian inverse formulation with teleseismic body and surface waves, which yields a low-dimensional probabilistic description of rupture properties including the spatial deviation, directivity, and temporal deviation of the source. This technique is useful for comparing events because it makes only minor geometric constraints, avoids bias due to rupture velocity parameterization, and yields a full ensemble of possible solutions given the uncertainties of the data. We apply this framework to all great strike-slip earthquakes of the past three decades, and we use the resultant second moments to compare source quantities like directivity ratio, rectilinearity, average moment density, and vertical deviation. We find that most strike-slip earthquakes have a large component of unilateral directivity, and many of these earthquakes show a mixture of unilateral and bilateral behavior. We notice that oceanic intraplate earthquakes usually rupture a much larger width of the seismogenic zone than other strike-slip earthquakes, suggesting these earthquakes may often breach the expected thermal boundary for oceanic ruptures. We also use these second moments to resolve nodal plane ambiguity for the large oceanic intraplate earthquakes and find that the rupture orientation is usually unaligned with encompassing fossil fracture zones.

7.1 Introduction

Large earthquakes involve complex ruptures that can vary strongly between events. The characteristics of these ruptures may be controlled by the structural and tectonic characteristics of the fault zone, and understanding patterns in these ruptures may improve our understanding of the interplay between source phenomenology and the rupture zone. In particular, large strike-slip earthquakes are known to show considerable variability in rupture properties between events (e.g., Hayes, 2017; Yin et al., 2021; Bao et al., 2022). Systematically characterizing this variability has the potential to yield insights into the underlying controls on the rupture process. These insights are of societal and scientific interest because these earthquakes present significant global hazard and provide unique windows into the structure and rheology of the lithosphere. Several faults known to host large strike-slip earthquakes are in close proximity to dense population centers. There is also wide speculation that the propagation behavior and rupture dimensions are dictated by the structural (Ben-Zion and Andrews, 1998; Wesnousky, 2008) and rheological properties (Abercrombie and Ekström, 2001; Boettcher et al., 2007) of the host fault zone. Intraplate oceanic earthquakes are particularly enigmatic, because the explanation for the weakening of the oceanic lithosphere that accommodates these events remains elusive (Lay, 2019).

A general quantity for describing the space-time kinematics of earthquake ruptures is the so-called stress glut (Backus and Mulcahy, 1976a), which quantifies the breakdown of linear elasticity in space and time (Dahlen and Tromp, 1998). Finite-fault slip distributions, which approximate the stress glut as discretized slip on a predefined fault plane, are routinely computed for large events (Mai and Thingbaijam, 2014). These solutions provide a high dimensional view of fault ruptures but in practice are challenging to compare between events due to pervasive nonuniqueness in the inverse problem, a priori fault plane parameterization, poor rupture velocity sensitivity, and regularization. An alternative technique for characterizing earthquake source properties is the second-moment formulation (Backus and Mulcahy, 1976a; Backus and Mulcahy, 1976b). Instead of approximating the stress glut as a superposition of assigned subevents, this approach involves solving for the second order polynomial moments of the stress glut, yielding a source covariance matrix that approximates the spatiotemporal extent of the source. This technique has been successfully applied in the past (Bukchin, 1995; McGuire et al., 2000; McGuire et al., 2001; McGuire et al., 2002; Clévédé et al., 2004; Chen, 2005; Meng et al., 2020), but has received far less attention than slip inversions. This low-dimensional

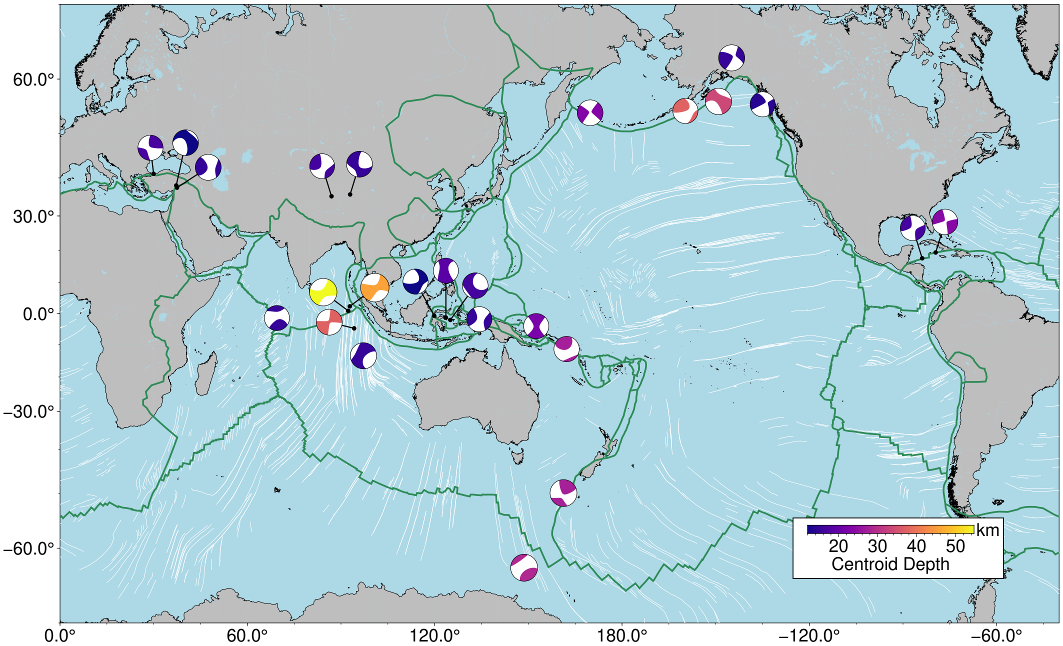

Figure 7.1: Centroid locations and centroid depths of the earthquakes used in this study. White lines are fossil fracture zone locations from Seton et al. (2014) and Wessel et al. (2015). Green lines are plate boundaries from Bird (2003).

framework makes only minor assumptions about rupture geometries and has the advantages of not requiring an explicitly paramaterized rupture velocity and avoiding the discretization challenges that arise when performing slip inversions. The low dimensionality of the solution also facilitates computation of these moments with a Bayesian approach (Atterholt and Ross, 2022), which can provide uncertainty estimates crucial for comparing the source processes of different earthquakes.

Our contributions to this study are as follows. We compute second moments for all of the $M_w \geq 7.5$ strike-slip earthquakes of the past three decades using a Bayesian inference approach. We use this catalog to establish baselines for the range of values observed globally and compare values between events, subgroups, and other tectonic features. From these analyses we conclude that (i) large strike-slip earthquakes almost always show unilateral or a comparable amount of unilateral and bilateral directivity behavior, (ii) that large intraplate oceanic earthquakes usually rupture over a much wider depth range, and (iii) that oceanic intraplate strike-slip earthquakes are not systematically aligned with fossil fracture zones.

7.2 Preliminaries

The stress glut is a tensor field representing the expected stress due to the application of Hooke's law to inelastic strain in a body (Backus and Mulcahy, 1976a; Backus and Mulcahy, 1976b). The stress glut is a useful source characterization quantity, because the stress glut is identically zero outside the source region and can be used to compute displacements anywhere on Earth resulting from an arbitrary source (Dahlen and Tromp, 1998). The dimensionality of the stress glut can be significantly reduced by assuming the source mechanism does not change throughout the rupture:

$$\Gamma_{ij}(\boldsymbol{\xi}, \tau) = \hat{M}_{ij} f(\boldsymbol{\xi}, \tau). \tag{7.1}$$

Here, $\boldsymbol{\Gamma}$ is the stress glut, $\hat{\mathbf{M}}$ is the normalized mean seismic moment tensor, and f is a scalar function of position $\boldsymbol{\xi}$ and time τ. The second moment formulation is defined by taking the second central moment of the scalar stress glut rate function ($\dot{f}$) with terms for the spatial and temporal components. The equation for these moments is given by:

$$\dot{f}(\boldsymbol{\xi}^c, \tau^c)^{(m,n)} = \int \int \dot{f}(\boldsymbol{\xi}, \tau)(\boldsymbol{\xi} - \boldsymbol{\xi}^c)^m (\tau - \tau^c)^n d\boldsymbol{\xi} d\tau, \tag{7.2}$$

where $\boldsymbol{\xi}$ and τ are position and time, $\boldsymbol{\xi}^c$ and τ^c are the centroid position and centroid time, which are the first moments of the distribution, and m and n are the spatial order and temporal order of the moment. The central moments of order $m + n = 2$ correspond to the covariance of the source. Specifically, $f(\boldsymbol{\xi}^c, \tau^c)^{(2,0)}$ is the spatial covariance, $f(\boldsymbol{\xi}^c, \tau^c)^{(0,2)}$ is the temporal variance, and $f(\boldsymbol{\xi}^c, \tau^c)^{(1,1)}$ is the spatiotemporal covariance. The distribution $\dot{f}$ is defined by the superposition of its polynomial moments, and at low-enough frequencies, the contribution of moments of order three or greater may be approximated as zero. Under this approximation, the second moments can be linearly related to displacement:

$$\mathbf{d} = \mathbf{F}\mathbf{p} \tag{7.3}$$

where $\mathbf{d}$ is a vector of the difference between the measured displacements and the theoretical Green's functions, $\mathbf{F}$ is a forward propagation matrix of spatial and temporal integrals and derivatives of the Green's tensor weighted by the components of the moment tensor $\mathbf{M}$, and $\mathbf{p}$ is a vector that contains the independent parameters of the second order stress-glut moments.

Since the standard deviation of a distribution gives a low-dimensional estimate of the width of a distribution, these second moments, which are the covariance of the stress-glut, can be used to compute low-dimensional measures of the volume, duration, and directivity of a source distribution. In particular, we define dimensional quantities of the source that describe the shape of the stress-glut distribution about the centroid. These are:

$$\begin{aligned}
r^c(\hat{\mathbf{n}}) &= \sqrt{\hat{\mathbf{n}}^{\mathbf{T}} \cdot [\dot{\boldsymbol{f}}^{(2,0)}(\boldsymbol{\xi}^c, \tau^c) / \dot{f}^{(0,0)}(\boldsymbol{\xi}^c, \tau^c)] \cdot \hat{\mathbf{n}}}, \\
t^c &= 2\sqrt{\dot{f}^{(0,2)}(\boldsymbol{\xi}^c, \tau^c) / \dot{f}^{(0,0)}(\boldsymbol{\xi}^c, \tau^c)}, \\
\mathbf{v_0} &= \dot{\boldsymbol{f}}^{(1,1)}(\boldsymbol{\xi}^c, \tau^c) / \dot{f}^{(0,2)}(\boldsymbol{\xi}^c, \tau^c).
\end{aligned} \tag{7.4}$$

Here, $r^c(\hat{\mathbf{n}})$ is the distance from the centroid in the direction of a unit vector $\hat{n}$ that defines a spatial deviation ellipsoid in which most of the moment was released. The characteristic spatial deviation of the source is given by $L^c = 2r^c(\boldsymbol{\eta})$, where $\boldsymbol{\eta}$ is the principal eigenvector of $\dot{\boldsymbol{f}}^{(2,0)}$. t^c is the characteristic temporal deviation that captures a time interval in which most of the moment was released. $\mathbf{v_0}$ is the average instantaneous velocity of the rupture centroid. These quantities together provide a physically interpretable, low-dimensional estimate of a rupture's spatiotemporal behavior (Backus, 1977; Silver and Jordan, 1983).

From the aforementioned quantities, we can compute ensembles of parameters that may further illuminate potential differences between ruptures. In particular, we inspect four derived parameters in this study: rectilinearity (R), directivity ratio (α), average moment density ($\bar{m}$), and vertical deviation (Z). Rectilinearity is a measure of the degree of elongation along an axis and has been used in seismology to evaluate particle motion (Vidale, 1986; Jurkevics, 1988). We instead use this measure to evaluate the elongation of ruptures along the principal axis, and define it so the values are bounded between 0 (spherical source) and 1 (linear source):

$$R = 1 - \frac{\frac{1}{2}(\lambda_2 + \lambda_3)}{\lambda_1}. \tag{7.5}$$

The variables λ_1, λ_2, and λ_3 are the eigenvalues of the spatial second moment, in order of largest to smallest, and yield estimates of the dimensions of the source along its principal axes. The directivity ratio provides an estimate of the degree of directivity of a rupture by comparing the average centroid velocity to the maximum possible average centroid velocity, and has been used in the second moment literature previously (McGuire et al., 2002):

$$\alpha = \frac{||\mathbf{v_0}||}{(L^c/t^c)}. \tag{7.6}$$

The average moment density comes from the moment tensor density formulation (Aki and Richards, 2002) and compares the scalar moment, M_0, to the volume of the ellipsoid representation of the spatial second moments:

$$\bar{m} = \frac{M_0}{(2)^3 \frac{4}{3} \pi \lambda_1 \lambda_2 \lambda_3}. \tag{7.7}$$

As is apparent, the equation for $\bar{m}$ is very similar to analytic solutions for the stress drop on planar sources e.g. Eshelby, 1957 and has units of stress. Finally, we define a measure of the vertical extent of the source:

$$Z = 2\gamma_z r^c(\boldsymbol{\gamma}). \tag{7.8}$$

Here, $\boldsymbol{\gamma}$ is the unit vector pointing in the direction with the maximum vertical component. Each of these quantities yield estimates of the source dimensions that have historically been difficult to obtain. In this framework, we can systematically solve for full posterior distributions on these parameters and consequently perform error-informed comparisons.

Because we will subsequently apply this inversion framework to large strike-slip earthquakes, an important point about the assumption of a constant source mechanism should be made here. Several large strike-slip earthquakes, such as the 2012 Wharton Basin and the 2018 Gulf of Alaska Earthquakes, have been shown to rupture multiple conjugate, near-orthogonal faults. This presents no problem in our framework because the faults are nearly orthogonal and have opposite senses of slip, making the source mechanism approximately constant between faults. There is no assumption that the rupture be constrained to a single fault. The orthogonality of the faults in these ruptures is likely not a coincidence, and may be systematic for large fault zones (Thatcher and Hill, 1991; Scholz and Choi, 2022); thus we may expect that for other ruptures of this type, the assumption of a constant source mechanism is also reasonable. This assumption is less valid for faults with significant curvature

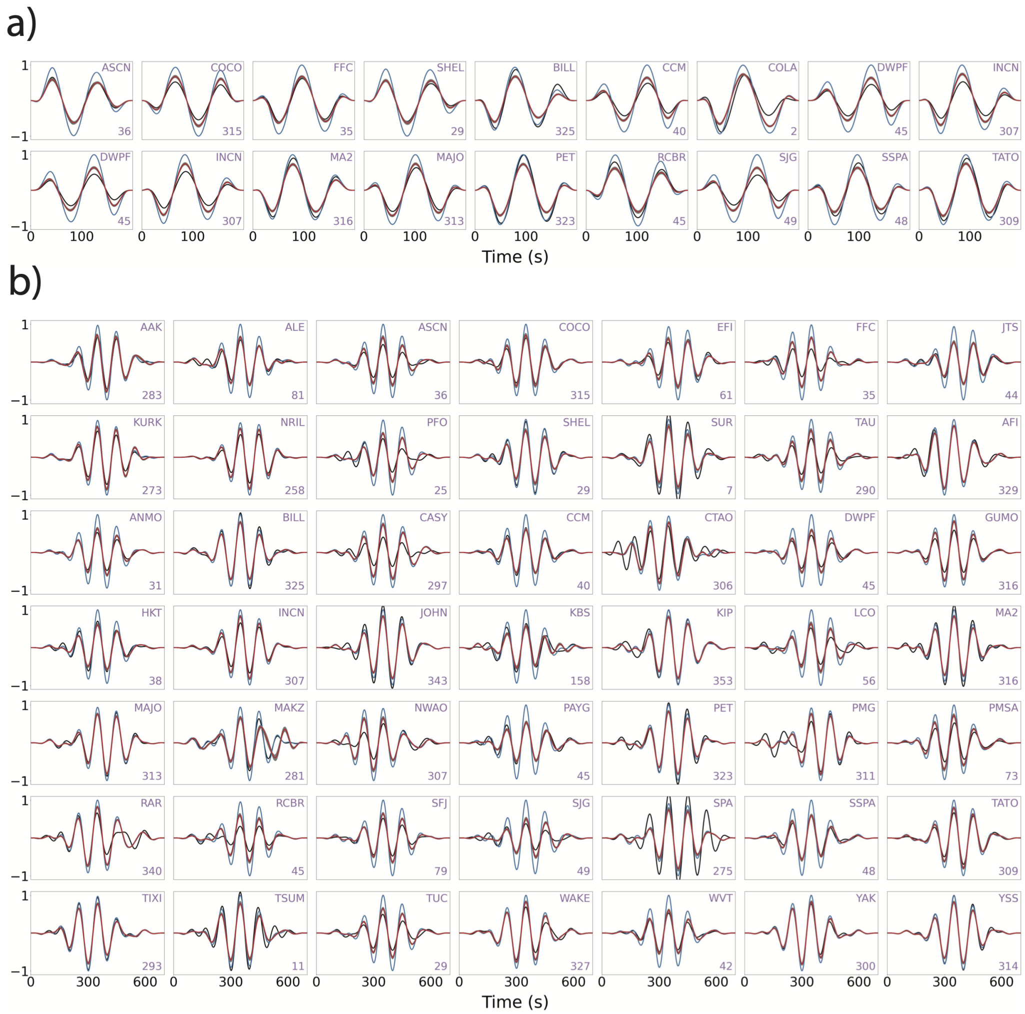

Figure 7.2: Examples of waveform fits for the 1999 M_w7.61 Izmit earthquake. The waveforms in the top grouping are fits to the SH phase. The waveforms in the bottom grouping are fits to the R1 phase. Each waveform panel includes corresponding station name and back-azmith. The black and blue lines correspond to the observed waveforms and the point source theoretical Green's functions at each respective station. The red and gray lines correspond to the waveform fit of the mean solution and the distribution of fits for the ensemble of solutions, respectively. Waveforms are filtered between 7.5 and 12.3 mHz according to the described bandpass framework.

(Shimizu et al., 2020), ruptures in which the slip direction changes significantly, or ruptures of multiple faults that are highly non-parallel and non-orthogonal. Though this assumption is a limitation of this methodology, this methodology is strengthened by avoiding constraints of slip to a user-defined fault plane that is typically necessary for fault slip distributions.

7.3 Methods

Data and Preprocessing

We use the Global Centroid Moment Tensor (gCMT) catalog to select large strike-slip earthquakes of the past three decades (Ekström et al., 2012). To find these events, we search the gCMT catalog for events with $M_w \geq 7.5$ and with nodal axis plunges greater than 45°. We then manually evaluate these events to ensure that each event shows predominantly strike-slip behavior, resulting in the set of events shown in Figure 7.1 and Table 7.1. We choose events of this magnitude because the frequency to which the waveforms for these events need to be fit to resolve stress-glut second moments is inversely related to the duration of the event. Consequently, larger events with correspondingly larger durations may be fit with theoretical Green's functions at lower frequencies. We directly fit the displacement waveforms from Global Seismographic Network (GSN) stations for data consistency between events. The waveforms used in these inversions are SH and R1 waveforms selected using travel times from the Preliminary Reference Earth Model (PREM) (Dziewonski and Anderson, 1981) specific to the selected frequency bands in this study. The inclusion of the P waveforms would further constrain the posterior distributions, but we decide not to include these because this would require the computation of theoretical Green's functions at much higher frequencies. We select 200-second windows around the SH waveforms and 700-second windows around the R1 waveforms. Waveforms at distances less than 30 degrees are excluded to avoid the convolution of the SH waves with the R1 waves, because at short distances these phases have not diverged enough to select SH windows with no R1 waveforms present. An example set of waveforms for the 1999 Izmit earthquake are shown in Figure 7.2. We compute the Green's tensors using the gCMT moment tensor solutions (Ekström et al., 2012). We use the spectral element method software Salvus (Afanasiev et al., 2019) in combination with the 3D Earth model S362ANI+M (Moulik and Ekström, 2014) to compute the Green's tensors. The derivatives of the Green's functions needed for the forward propagation matrices are computed using a centered finite difference approximation. For the spatial finite difference, we compute the wavefield for a grid of source locations centered on the centroid solution.

As in Atterholt and Ross (2022), we select the frequency bands used in these inversions using duration estimates for each event. In particular, we consider the observation that the contribution of moments of order $m + n$ is approximately proportional to $(D/P)^{m+n}$ (where $(D/P) < 1$), where D and P are the event duration

Table 7.1: Global strike-slip earthquakes considered in this study. The hypocenter locations and magnitudes are drawn from the gCMT catalog (Ekström et al., 2012). Categories of earthquakes are continental (C), oceanic interplate (E), and oceanic intraplate (A).

Name	Date	Longitude	Latitude	Depth (km)	M_w	Category
Tibet	1997-11-11	86.96	35.33	16.4	7.53	C
Balleny Is.	1998-03-25	148.64	-62.99	28.8	8.14	A
Ceram Sea	1998-11-29	125.0	-2.03	16.4	7.75	A
Izmit	1999-10-17	29.97	41.01	17.0	7.61	C
Sulawesi	2000-05-04	123.59	-1.29	18.6	7.57	A
Whar. Basin (1)	2000-06-18	97.17	-13.47	15.0	7.92	A
Kunlun	2001-11-14	92.91	35.8	15.0	7.81	C
Irian Jaya	2002-10-10	134.3	-1.79	15.0	7.58	A
Denali	2002-11-03	-144.89	63.23	15.0	7.88	C
Carlsberg Rdg.	2003-07-15	69.47	-1.42	15.0	7.57	E
Macquarie Is.	2004-12-23	161.25	-49.91	27.5	8.11	A
Whar. Basin (2)	2012-04-11	92.82	2.35	45.6	8.6	A
Whar. Basin (3)	2012-04-11	92.31	0.90	54.7	8.28	A
S.E. of Alaska	2013-01-05	-134.97	55.69	13.8	7.56	E
Solomon Is.	2014-04-12	162.24	-11.35	27.3	7.66	E
Whar. Basin (4)	2016-03-02	94.22	-4.75	37.2	7.82	A
Komandorski Is.	2017-07-17	169.78	54.13	23.2	7.79	E
Honduras	2018-01-10	-83.86	17.56	16.5	7.55	E
Gulf of Alaska	2018-01-23	-149.12	56.22	33.6	7.96	A
Palu	2018-09-28	119.86	-0.72	12.0	7.60	C
Papua N.G.	2019-05-14	152.52	-4.03	22.1	7.60	C
Canary Is.	2020-01-28	-79.55	19.33	23.9	7.72	E
S. of Alaska	2020-10-19	-159.7	54.48	37.4	7.62	A
Turkey-Syria (1)	2023-02-06	37.47	37.56	14.9	7.83	C
Turkey-Syria (2)	2023-02-06	37.22	38.11	12.0	7.78	C

and period of the signal respectively (Backus, 1977). We select a frequency band such that $(D/P)^2 > 0.05$ and $(D/P)^3 < 0.05$ in order to balance maximizing the second moments relative to the zeroth and first moments while minimizing the contribution of moments of order three and greater. For an estimate of duration, we use the empirical relationship used for the gCMT catalog (Ekström et al., 2012). These frequency bands are given in Table 7.S1. We subsequently show that this relationship provides a fairly reasonable estimate for the source duration for these events. With the aforementioned inequality and duration estimates, we can compute a frequency band for filtering the data, and we filter the waveforms using a Butterworth filter. Once filtered, we visually inspect the fit of the theoretical Green's functions to the data for quality control.

Inversion

For the second moment inversion, we follow the procedure outlined in Atterholt and Ross (2022), and we summarize the method here. In essence, our objective is to use the relationship described in equation 7.3 to invert for a model vector of stress glut moments that better fits displacement waveforms by accounting for the finiteness of the source. An example of the waveform fits for the 1999 Izmit, 2002 Denali, and 2018 Palu earthquakes using the subsequently-described inversion are shown in Figures 7.2, S1, and S2, respectively. The azimuthal distributions for these earthquakes, which are representative of the azimuthal distributions for the earthquakes used in this study, are shown in Figure 7.S3. We solve this inverse problem using a Bayesian formulation that produces an ensemble of potential solutions given the uncertainty of the inverse problem, outlined in detail by Atterholt and Ross (2022). The posterior distribution for this problem can be written using the relationship:

$$p(\mathbf{p}, \sigma|\mathbf{d}) \propto p(\mathbf{d}|\sigma, \mathbf{p})\ p(\sigma)\ p(\mathbf{p}), \tag{7.9}$$

where σ is a parameter that is updated every sample and quantifies the uncertainty by estimating the inability of the model to fit the data (Gelman et al., 2010). $p(\mathbf{p})$ is the prior distribution on the model parameters; in this study we use uninformed priors. We compute the likelihood using a multivariate normal distribution:

$$p(\mathbf{d}|\sigma, \mathbf{p}) \propto \frac{1}{\sqrt{|\Sigma|}} \exp(-\frac{1}{2}(\mathbf{d} - \mathbf{Fp})^{\mathrm{T}}\, \mathbf{\Sigma}^{-1}\, (\mathbf{d} - \mathbf{Fp})) \tag{7.10}$$

Where Σ is a block diagonal covariance matrix that incorporates the temporal correlation structure, which is a function of the parameter σ and the minimum period of the bandpass filter. A limitation of this methodology is that the parameter σ accounts for random, but not systematic, errors in the Green's functions.

Prior studies on stress-glut second moment inversions (Bukchin, 1995; McGuire et al., 2001) have applied the constraint that since second moments constitute a covariance matrix, only the solutions that ensure the second moments are positive definite are valid, or:

$$\mathbf{X} = \begin{bmatrix} \dot{\boldsymbol{f}}^{(2,0)}(\boldsymbol{\xi}^c, \tau^c) & \dot{\boldsymbol{f}}^{(1,1)}(\boldsymbol{\xi}^c, \tau^c) \\ \dot{\boldsymbol{f}}^{(1,1)}(\boldsymbol{\xi}^c, \tau^c)^T & \dot{f}^{(0,2)}(\boldsymbol{\xi}^c, \tau^c) \end{bmatrix} \succeq 0. \tag{7.11}$$

To ensure our samples of the posterior are positive definite, we take advantage of the Cholesky Factorization Theorem, which states that every symmetric, positive definite matrix can be represented as the product of a lower triangular matrix and its transpose. For $\mathbf{X}$, there thus exists a matrix $\mathbf{L}$ such that $\mathbf{X} = \mathbf{L}\mathbf{L}^T$. We thus sample over $\mathbf{L}$ and construct $\mathbf{X}$ from $\mathbf{L}$ when computing the likelihood of the sample. This framework allows for the inclusion of prior distributions on the source model; for example, it would be possible to impose a prior on the azimuth of the principal eigenvector or the size of the characteristic values using information from previous source characterizations or empirical scaling relationships. In this study, we use uninformed priors to maximize the independence of this catalog of solutions from other source studies. We probe the solution manifold using Hamiltonian Monte Carlo (HMC) sampling (Neal, 2010), an instance of Metropolis Hastings sampling that uses an analog from Hamiltonian Dynamics. We choose HMC sampling because our parameter space is large, and HMC sampling applies gradient information to sample large parameter spaces efficiently. To take these gradients, we use reverse-mode automatic differentiation (Innes, 2019). In total, we take 10,000 samples, and in each subsequent representation of solution ensembles, we show the final 500 unique samples. In Atterholt and Ross (2022), we demonstrated that this parameterization was appropriate to conservatively achieve convergence for this type of inverse problem using the Gelman-Rubin diagnostic (Gelman and Rubin, 1992). The computational time for this inversion varied according to the number of waveforms used, but in general was executed for each event within between 2 to 10 hours on a single CPU core.

7.4 Results and Discussion

Patterns in rupture behavior

Using the definitions in Equations 7.4-7.8, we compute ensembles of quantities that capture low dimensional rupture characteristics. We summarize these ensembles in Table 7.2 and show the full posterior of these quantities in Figures 7.S4, 7.S5, and 7.S6. In Figure 7.3 we plot the ensembles of temporal deviations, which show good agreement with the empirical magnitude-duration relationship used to determine the frequency bands used in this study. The initial duration estimates control the quality of the solution by reducing biases from the error of the moments of order $m+n \leq 1$ and from the contributions of the moments of order $m+n \geq 3$, but this does not suggest a causal relationship between the initial duration estimates and the second temporal moments. These moments thus show that this empirical relationship is a reasonable model for these data.

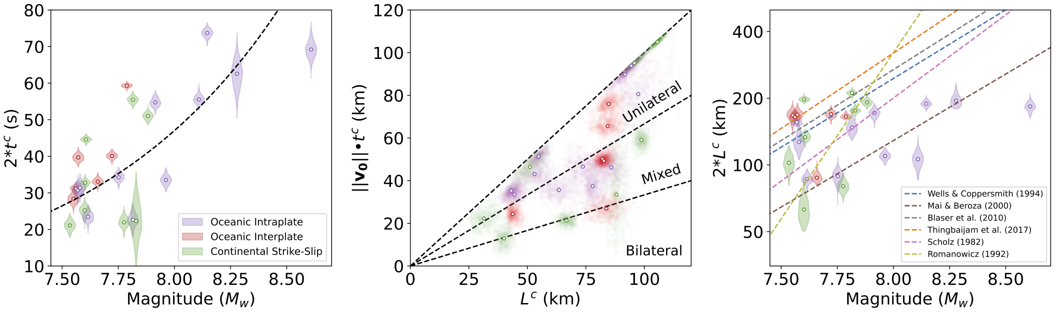

Figure 7.3: Summary of characteristic values. Left: Twice the characteristic temporal deviation (±2σ of moment rate function) for each event plotted against event moment magnitude. Black dotted line is the empirical magnitude-duration relationship used in (Ekström et al., 2012). Center: Characteristic spatial deviation plotted against centroid propagation length. Black dotted lines separate bilateral, mixed, and unilateral categories described in the text. Right: Twice the characteristic spatial deviation plotted against event moment magnitude; several scaling relationships from prior studies are plotted as dotted lines (Wells and Coppersmith, 1994; Mai and Beroza, 2000; Blaser et al., 2010; Thingbaijam et al., 2017; Scholz, 1982; Romanowicz, 1992). Green, red, and purple correspond to continental strike-slip, oceanic interplate, and oceanic intraplate, respectively.

Also shown in Figure 7.3 is a comparison between the characteristic spatial deviation of the rupture, L_c, and the propagation length of the rupture centroid $||\boldsymbol{v}_0|| \cdot t^c$. The ratio between these two quantities reflects the degree of directivity of the rupture (McGuire et al., 2002). We separate these quantities into 3 categories of our design: bilateral ($||\boldsymbol{v}_0|| \cdot t^c / L_c \leq \frac{1}{3}$), mixed ($\frac{1}{3} \leq ||\boldsymbol{v}_0|| \cdot t^c / L_c \leq \frac{2}{3}$), and unilateral ($||\boldsymbol{v}_0|| \cdot t^c / L_c \geq \frac{2}{3}$). As is made clear in Figure 7.3, almost no ruptures fall in the bilateral category, suggesting that the vast majority of these ruptures have a large component of unilateral directivity, which is consistent with previous results (McGuire et al., 2002; Ross et al., 2020). But, while many of these ruptures fall in the unilateral category, suggesting these ruptures favor unilateral directivity over bilateral directivity, many of the ruptures also fall in the mixed category. Mixed directivity in ruptures may point to a more complicated rupture process and are difficult to achieve by chance. McGuire et al. (2002) computed the expected distribution of directivity ratios given a 1-dimensional predefined fault with uniform slip and hypocenter location and found that the distribution is heavily skewed towards unilateral ruptures. We reproduce this distribution and compare it to our observed distribution of directivity ratios. For this comparison, we choose the median as the test statistic, because the median is a good estimate of the central tendency of skewed distributions. We create a distribution of possible median values for our observed distribution by computing them for random ensemble member draws from the source directivity distributions and comparing these values to the distribution of medians from random draws of the same size from the simulated distribution. This workflow is summarized in Figure 7.S7. We find that the vast majority of the ensemble draws from our observed distribution are unlikely to be drawn from the simulated distribution, suggesting the difference between these distributions is significant. This would suggest that the simple hypothesis that ruptures start at random positions on a predefined fault with uniform slip cannot explain our data. In reality, fault ruptures are more complex than this simple model, and a number of factors contributing to this complexity may explain the difference between these distributions. For example, ruptures may preferentially start near high strength regions (Mai et al., 2005; Melgar and Hayes, 2019) which may be biased towards the center of ruptures (e.g., Manighetti et al., 2005) and thus bias ruptures towards bilateral behavior. With additional observations and tests against simulations of more complicated ruptures, this type of data may supplement arguments for specific rupture behaviors that prefer bilateral propagation.

Finally, in Figure 7.3, we plot twice the characteristic spatial deviation of the rupture against magnitude to observe the scaling relationship present in this catalog. Additionally, we plot best-fitting solutions for L model (Scholz, 1982) and W model (Romanowicz, 1992) scaling relationships and empirical scaling relationships from previous studies that use independent slip distribution catalogs (Wells and Coppersmith, 1994; Mai and Beroza, 2000; Blaser et al., 2010; Thingbaijam et al., 2017). We find the trend of our L_c values, in general, matches the trends of the scaling relationships, but there is not sufficient coverage along the magnitude axis to determine with which scaling relationship this catalog is best aligned. However, among the intraplate oceanic events, which have more diverse observations with magnitude, the trend between M_w and L_c appears to deviate from these of the scaling relationships; the significance of this is described subsequently.

We compute ensembles for the quantities described in Equations 7.5-7.8 for all the events considered in this study and plot the kernel density estimates of the underlying probability distributions of these ensembles in Figure 7.4. Almost all rectilinearity values for these events are well-above 0.5, suggesting that most of these ruptures are elongated along a single dimension. Large strike-slip earthquakes are large-enough to be constrained by the width of the seismogenic zone, and thus elongation of the spatial deviation ellipsoid in the strike-parallel direction is expected. The directivity ratio, also represented in Figure 7.3 and discussed in the previous section, yields a wide distribution that is biased towards values closer to one. Average moment densities for these events vary by over two orders of magnitude (1-100 MPa) with a median value near 10 MPa. The distributions of these values should be interpreted carefully, as the average moment density estimates are computed using the smallest eigenvalue, λ_3, of the spatial covariance matrix; this value is poorly constrained by our data. We expect λ_3 to be small for most ruptures, but since the data do not constrain λ_3 well, the posterior distributions of λ_3 can be very broad above zero, and thus skew the distributions of source volume upward. This issue may be addressed by assigning a well-justified prior distribution on the size of λ_3, but we leave this for future work. The distribution of vertical deviations is mostly below 20 km with a noteworthy tail extending up to 40 km. The ensembles of these parameters for each event are shown in Figures 7.S4, 7.S5, and 7.S6 and are summarized in Table 7.2.

We separate these events into 3 categories: continental strike-slip, oceanic interplate, and oceanic intraplate. For oceanic events, we make classifications by cross-referencing the event locations with the plate boundary types outlined in Bird (2003). This classification is not always simple. For example, the 2003 Carlsberg Ridge event ruptured close to the active spreading center and is expected to be aligned with the spreading-associated transform faults in the vicinity (Antolik et al., 2006), but it has an opposite sense of slip as expected for these faults. We nonetheless classified this event as interplate because of it's proximity to the plate boundary assuming the true nodal plane is that aligned with the nearby active transform faults. Classifying this event as intraplate does not change the conclusions of this study. We classify all continental strike-slip events together to ensure that there are enough events in the group to evaluate potential systematic behavior. These classifications are given in Table 7.1. The rectilinearity and directivity of these events are too variable within groups to make statements regarding differences between groups, but these ensembles demonstrate the potential of this second-moment framework to objectively obtain quantities that potentially illuminate rupture features that have historically been difficult to obtain independently of the necessary assumptions associated with fault slip distributions. Some differences in average moment densities are evident in these distributions; namely, the ensembles of average moment densities for oceanic interplate earthquakes create a distribution that is much narrower than

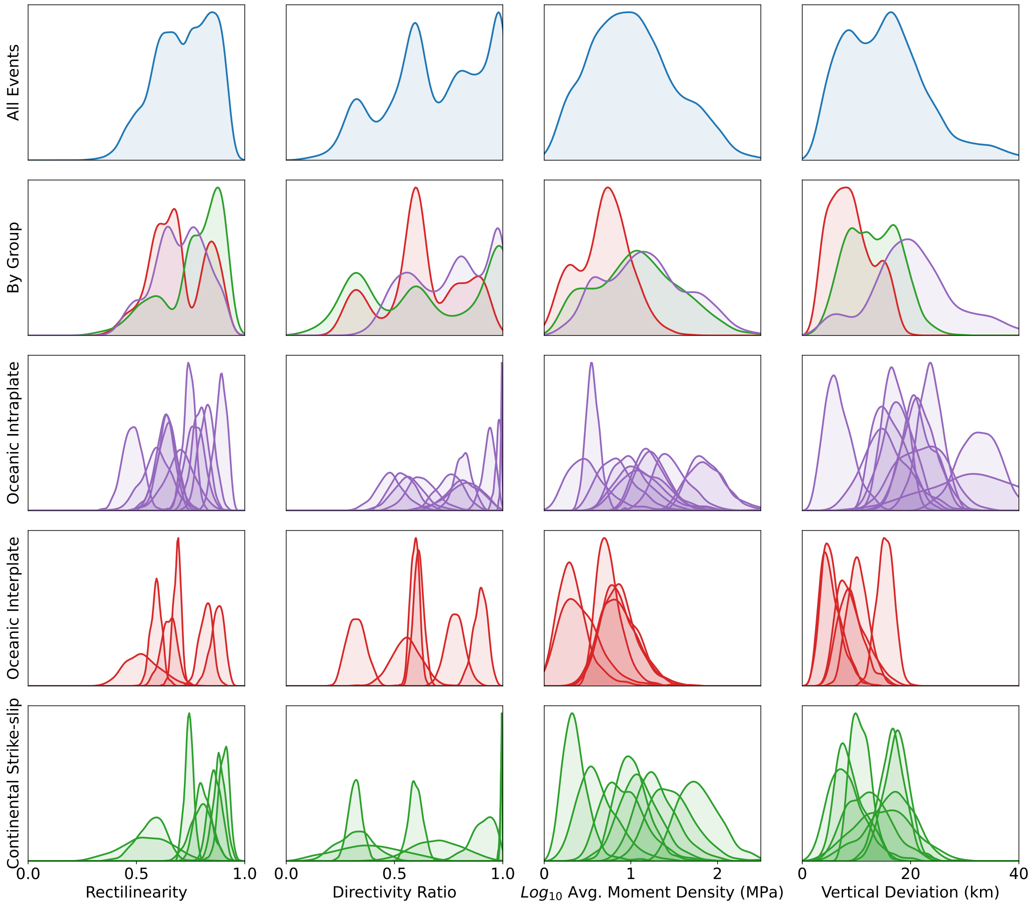

Figure 7.4: Derived source quantities described in the text. Top row: Distributions of all event ensembles for each quantity. Second row from the top: Distributions of all ensembles within individual tectonic groups for each quantity. Green, red, and purple correspond to continental strike-slip, oceanic interplate, and oceanic intraplate, respectively. Bottom three rows: ensemble distributions for individual events within each tectonic category for each quantity. The relative heights of a few distributions of directivity ratios for individual sources were reduced for visualization purposes.

that of other strike-slip earthquakes, because the other types of events include the contributions of several earthquakes with ensembles of exceptionally high average moment density values.

The depth-dependence of slip distributions has historically been difficult to constrain because surface observations typically have poor sensitivity to variability with depth (e.g., Duputel et al., 2014). As is shown in Figure 7.4, the uncertainty of the vertical deviation parameter in this study is quite high. However, because we estimate the full posterior of our solutions, we have a good estimate of the uncertainty present in these solutions. We can thus make error-informed conclusions while accounting for the high uncertainty inherent to resolving parameters related to the source distribution with depth. The distributions of vertical deviations of these events suggest a clear difference between oceanic intraplate earthquakes and other strike-slip earthquakes. The oceanic intraplate earthquakes exhibit much wider ruptures than other strike-slip earthquakes; this has been suspected before, particularly for Wharton Basin events (Aderhold and Abercrombie, 2016). The observations in this study provide some evidence for this difference globally. Mindful that the vertical deviation measure only accounts for $\pm 1\sigma$ of the source distribution's vertical width, it is reasonable to expect that the source distribution extends over an even larger width than the estimated vertical deviation of the rupture. Given that these intraplate oceanic earthquakes generally rupture colder lithosphere, some difference in vertical deviation between rupture types is to be expected. For earthquakes that ruptured oceanic crust with measured age, we can account for the expected thermal differences by comparing the age of the oceanic crust encompassing the centroid, taken from Seton et al. (2020), to the expected thermal profile of a half space cooling model with an ambient mantle temperature of 1350° and thermal diffusivity of $10^6 \mathrm{m}^2/\mathrm{s}$ as in Aderhold and Abercrombie (2016). Noting that the vertical extents are estimates of the variance of the stress glut from the centroid, we can estimate the depth extent of these earthquakes by summing the centroid depth with quantities proportional to the vertical deviation of the source.

We plot these distributions of depth extent assuming the depth extents given by the conservative estimates of $\boldsymbol{\xi}^c(z) + \frac{1}{2}Z$ and $\boldsymbol{\xi}^c(z) + \frac{\sqrt{2}}{2}Z$ in Figure 7.5. The $\boldsymbol{\xi}^c(z) + \frac{1}{2}Z$ values assume slip only occurred within a single standard deviation of the source distribution below the source centroid, and the $\boldsymbol{\xi}^c(z) + \frac{\sqrt{2}}{2}Z$ values would yield the exact depth extents for source distributions with uniform slip. We note here that there may be some inaccuracies in the Green's functions due to the crustal model when generating sources in oceanic crust. These inaccuracies would increase the modeled excitation of the surface waves (Abercrombie and Ekström, 2003) which we would expect to increase the radial spatial gradients incorporated in Equation 7.3. This bias would serve to decrease the estimated depth extent of the earthquakes, and thus would not change subsequent conclusions of this study. Additionally, because the Wharton Basin (3) event was an aftershock that occurred only two hours after the Wharton Basin (2) event, the Wharton Basin (3) event waveforms show long-period noise that is likely causing the high uncertainty for that event in Figure 7.8, this solution should thus be considered in that context. An estimate of how well resolved the vertical extent values are can be made by comparing the ratio of λ_2/λ_3. Since λ_3 is expectedly small, larger values of λ_3 may be interpreted as an approximate noise level. These ratios are plotted in Figure 7.S8. In general, while some ensemble members for some sources are lower, these ratios greatly exceed 2; however, these values are not purely estimates of the signal-to-noise ratio, as physical characteristics of the source can contribute to elevated λ_3 values.

As is apparent in Figure 7.5, for interplate events these values generally fall above the 800° isotherm and for intraplate events these values generally fall below the 800° isotherm. While there is some variability in estimates of the limiting temperature for slip on oceanic transform faults (e.g, Wiens and Stein, 1983; Abercrombie and Ekström, 2001), the estimates of depth extent of the slip for oceanic intraplate earthquakes frequently exceed even the highest expected slip-limiting temperatures. These observations are supported by the L_c values, which are better constrained, for the intraplate oceanic ruptures shown in Figure 7.3. These values shows that the intraplate events, L_c, when plotted against magnitude, follow a trend that is distinct from expected scaling relationships for strike-slip earthquakes which are expectedly restricted by their widths. These results motivate the consideration of a mechanism for coseismic slip below the brittle-ductile transition zone for large intraplate earthquakes. One potential mechanism for such a large amount of moment released below the brittle-ductile transition zone, proposed as an explanation for the slip in 2012 Wharton Basin Earthquake, is a large component of deep viscous failure, rather than frictional failure, resulting from a runaway feedback system due to heating of the shear zone (Kelemen and Hirth, 2007; McGuire and Beroza, 2012). This mechanism, however, would only account for moment released between 600° and 800°. Another potential explanation is that diffuse deformation zones in the interior of oceanic lithosphere may be hydrated at depth, altering the rheological profile of the fault (Bishop et al., 2023) and thus allowing for deeper rupture.

Orientations of ruptures and crustal fabric

For large strike-slip earthquakes that occur on plate boundaries or in continental crust, the fault associated with the majority of slip is typically well resolved or easy to infer from the focal mechanism, and in most cases, the processing involved in computing a fault slip distribution helps discern the true nodal plane (Hayes, 2017). However, for intraplate oceanic earthquakes, the true fault plane is often not easily resolved (e.g., Nettles et al., 1999; Abercrombie et al., 2003; Robinson, 2011; Meng et al., 2012; Lay et al., 2018). The determination of the primary

Table 7.2: Ensembles of parameters defined in Equations 7.4-7.8 summarized for the events in this study. For each parameter, the median value and a credible interval (5^{th} to 95^{th} percentile) are given.

Name	L_c (km)	$\|\|\boldsymbol{v_0}\|\|$ (km/s)	t_c (s)	R	α	$Log_{10}(\bar{m})$ (MPa)	Z (km)
Tibet	51.1 (45.4-57.9)	4.39 (3.54-5.51)	10.55 (9.5-11.6)	0.6 (0.5-0.7)	0.91 (0.79-0.98)	0.58 (0.3-1.1)	7.72 (3.5-13.7)
Balleny Is.	94.4 (90.4-98.9)	2.55 (2.43-2.69)	36.86 (35.9-37.6)	0.7 (0.7-0.8)	0.99 (0.98-1.0)	1.25 (1.0-1.7)	15.94 (12.0-21.8)
Ceram Sea	44.5 (39.6-48.9)	1.96 (1.73-2.19)	17.13 (16.2-18.0)	0.6 (0.6-0.7)	0.76 (0.66-0.86)	1.21 (1.0-1.6)	21.16 (16.9-27.2)
Izmit	66.7 (63.0-70.4)	0.95 (0.81-1.1)	22.31 (21.8-22.8)	0.8 (0.8-0.9)	0.32 (0.27-0.37)	1.0 (0.7-1.3)	16.65 (8.2-22.7)
Sulawesi	77.9 (75.4-81.9)	2.42 (1.84-3.22)	15.34 (14.3-16.3)	0.9 (0.8-0.9)	0.48 (0.37-0.59)	1.12 (0.8-1.7)	6.32 (3.1-11.7)
Whar. Basin (1)	85.8 (80.0-91.5)	1.68 (1.41-2.0)	27.37 (26.5-28.3)	0.8 (0.7-0.9)	0.54 (0.45-0.64)	0.98 (0.7-1.4)	15.23 (9.0-24.1)
Kunlun	105.6 (102.1-109.0)	3.79 (3.61-3.97)	27.74 (27.0-28.5)	0.9 (0.8-0.9)	0.99 (0.99-1.0)	0.89 (0.6-1.4)	15.18 (6.7-24.3)
Irian Jaya	63.5 (56.0-72.2)	2.25 (1.89-2.73)	15.71 (14.7-16.7)	0.6 (0.6-0.7)	0.56 (0.46-0.69)	0.47 (0.2-0.9)	17.74 (12.9-22.6)
Denali	95.7 (91.9-100.1)	3.73 (3.49-3.97)	25.51 (24.7-26.2)	0.9 (0.8-0.9)	0.99 (0.98-1.0)	1.26 (1.0-1.8)	8.42 (5.6-14.5)
Carlsberg Rdg.	84.3 (78.3-90.4)	3.31 (3.06-3.6)	19.84 (19.1-20.6)	0.7 (0.6-0.7)	0.78 (0.71-0.85)	0.31 (0.1-0.7)	10.23 (7.4-13.7)
Macquarie Is.	53.1 (46.1-59.7)	1.55 (1.39-1.75)	27.76 (27.0-28.7)	0.6 (0.5-0.7)	0.82 (0.7-0.94)	1.45 (1.2-1.9)	22.32 (15.0-29.5)
Whar. Basin (2)	91.8 (85.2-98.0)	2.6 (2.39-2.84)	34.6 (32.8-36.5)	0.8 (0.7-0.8)	0.98 (0.95-1.0)	1.85 (1.6-2.2)	32.73 (26.2-39.0)
Whar. Basin (3)	97.4 (90.8-109.2)	2.58 (2.12-3.06)	31.29 (28.0-34.1)	0.7 (0.6-0.8)	0.83 (0.67-0.94)	1.07 (0.7-1.6)	32.07 (17.4-47.5)
S.E. Alaska	82.2 (78.8-86.4)	3.22 (2.96-3.55)	15.59 (14.9-16.1)	0.6 (0.6-0.6)	0.61 (0.57-0.65)	0.38 (0.1-0.8)	4.95 (2.6-9.2)
Solomon Is.	43.8 (41.7-47.5)	1.48 (1.21-1.75)	16.53 (15.8-17.2)	0.5 (0.4-0.7)	0.55 (0.45-0.66)	0.73 (0.6-1.0)	15.34 (12.8-17.8)
Whar. Basin (4)	73.7 (67.5-83.1)	4.08 (3.37-5.01)	11.3 (10.0-12.8)	0.6 (0.6-0.7)	0.63 (0.52-0.75)	0.83 (0.5-1.2)	21.5 (17.1-26.5)
Komandorsky Is.	82.7 (80.6-86.0)	1.66 (1.57-1.75)	29.65 (29.3-30.0)	0.7 (0.7-0.7)	0.59 (0.56-0.63)	0.84 (0.6-1.2)	5.13 (2.8-9.1)
Honduras	83.7 (75.4-90.2)	1.89 (1.47-2.42)	14.18 (13.2-15.2)	0.9 (0.8-0.9)	0.32 (0.26-0.4)	0.84 (0.5-1.3)	9.1 (5.8-14.7)
Gulf of Alaska	54.8 (51.6-58.4)	3.07 (2.77-3.42)	16.76 (15.7-17.8)	0.8 (0.8-0.9)	0.94 (0.88-0.98)	1.86 (1.6-2.3)	16.92 (13.6-20.5)
Palu	98.7 (96.0-101.6)	3.61 (3.21-4.01)	16.39 (15.7-17.0)	0.7 (0.7-0.8)	0.6 (0.55-0.65)	0.34 (0.2-0.6)	10.63 (8.1-14.2)
Papua N.G.	31.5 (26.5-38.5)	1.75 (1.3-2.25)	12.62 (11.5-13.6)	0.6 (0.3-0.7)	0.7 (0.51-0.88)	1.09 (0.8-1.5)	12.12 (6.5-19.9)
Canary Is.	84.8 (80.8-89.6)	3.78 (3.48-4.1)	20.05 (19.4-20.7)	0.8 (0.8-0.9)	0.9 (0.84-0.94)	0.86 (0.6-1.2)	8.38 (5.5-13.6)
S. of Alaska	43.1 (40.4-46.3)	3.0 (2.61-3.45)	11.73 (10.8-12.7)	0.5 (0.4-0.6)	0.82 (0.75-0.88)	0.56 (0.4-0.7)	23.61 (19.5-27.3)
Turkey-Syria (1)	88.0 (84.2-92.1)	2.89 (0.93-6.56)	11.14 (7.0-15.2)	0.9 (0.9-0.9)	0.38 (0.13-0.63)	1.46 (1.1-2.0)	16.65 (12.7-20.5)
Turkey-Syria (2)	40.0 (36.5-43.6)	1.17 (0.65-1.69)	10.96 (9.8-12.1)	0.8 (0.7-0.9)	0.32 (0.18-0.46)	1.77 (1.4-2.2)	17.47 (13.4-21.0)

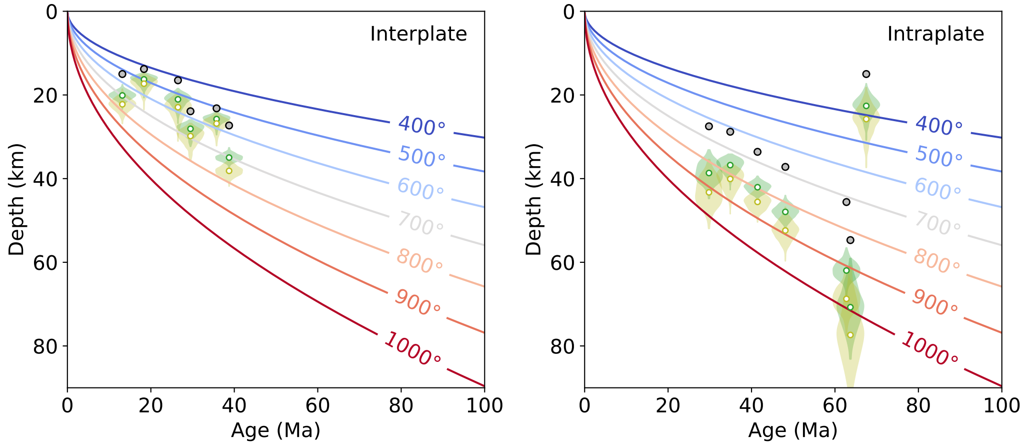

Figure 7.5: Depth extent of earthquakes plotted against lithospheric age. Isotherms generated using a half-space cooling model with an ambient mantle temperature of 1350°. Gray points are the gCMT centroid depths. Green violin plots are distributions of depth extents estimated by $\boldsymbol{\xi}^c(z) + \frac{1}{2}Z$. Yellow violin plots are depth extents estimated by $\boldsymbol{\xi}^c(z) + \frac{\sqrt{2}}{2}Z$. Left and right figures includes all interplate and intraplate events included in this study for which oceanic lithosphere age was obtainable respectively. Lithospheric age is obtained from Seton et al. (2020).

fault plane for these earthquakes (if one exists) is an important problem, because the enigmatic rupture of these very large events may broaden our understanding of the strength of the oceanic lithosphere and the nature of these earthquakes. A frequent assumption is that these events rupture fossil fracture zones, crustal fabric imparted by ocean spreading. However, some detailed studies of several events suggest rupture plane strikes that disagree with those of nearby fracture zones or rupture several nearly-orthogonal fault planes (Nettles et al., 1999; Meng et al., 2012; Lay et al., 2018), making the fracture zone hypothesis an unlikely universal explanation for weakening of the oceanic lithosphere. Fault slip distributions are often used to resolve nodal plane ambiguity by comparing the data fitting between different fault plane parameterizations (Hayes, 2017), and this too has been used to suggest that oceanic intraplate ruptures are often unaligned with fossil fracture zones in Wharton Basin, for example (Aderhold and Abercrombie, 2016). However, resolving fault plane ambiguity this way requires initial assumptions about the fault geometry and rupture process and ultimately a subjective, albeit data-informed, decision about the true fault plane. Backprojection of the energy radiated from the source has been used to successfully image the rupture surfaces of earthquakes (e.g., Ishii et al., 2005; Meng et al., 2012; Ruppert et al., 2018), but estimation of uncertainty with this method is difficult, and the quality of backprojection recovery is heavily dependent on the array used for backprojection's density of coverage and distribution of azimuths and distances (Kiser and Ishii, 2017). The second moment formulation can be used to supplement these prior studies by providing an objective and probabilistic assessment of the orientation of the rupture.

The second moment formulation can be used to resolve the nodal plane ambiguity of a point source moment tensor solution. Since we expect the slip variance to be maximized along the rupture plane, the principal eigenvector of the spatial second moment should be approximately aligned with the strike of the true nodal plane. We can verify this by comparing the strike of the principal eigenvectors of the ensembles of second spatial moments with true nodal plane of earthquakes for which this can be easily inferred. For all continental strike-slip earthquakes and interplate oceanic events, we can be reasonably confident of the true nodal plane in the presence of an observed surface rupture or nearby plate boundary information. For each of these events, we plot (Fig. 7.6) the difference in angle between the strike of the inferred nodal plane and the strike of the principal eigenvectors for the corresponding ensemble of spatial second moments. The median and vast majority of the angular differences of each ensemble are less than 45°, suggesting that this methodology is an effective tool for approximating the strike of the true rupture plane. We avoid interpreting the strike of the principal eigenvectors at a more granular level, because, as is apparent in Figure 6, some misalignment of the principal eigenvector and the true nodal plane is common. The threshold of 45° used to determine alignment is large enough to exceed potential errors in the principal eigenvector strike.

Intraplate oceanic ruptures have been observed to rupture multiple, near-orthogonal faults throughout the course of the rupture (Meng et al., 2012; Lay et al., 2018; Yamashita et al., 2021). As stated earlier, for these ruptures, the source mechanism remains approximately constant because the rupturing faults are nearly orthogonal, and thus the geometric assumption of this methodology remains valid. The stress glut covariance will track the distribution of moment release throughout the course of the rupture, and so for multi-fault ruptures the principal eigenvector may be unaligned with the rupture planes. For an intraplate oceanic earthquake, if this results in the principal eigenvector being unaligned with fossil fracture zones, we consider this a valid example of weakening resulting in a rupture that cannot be explained solely by fossil fracture zones, because such a rupture necessarily propagates on multiple faults, some of which will be oriented at high angle to local fossil fractures.

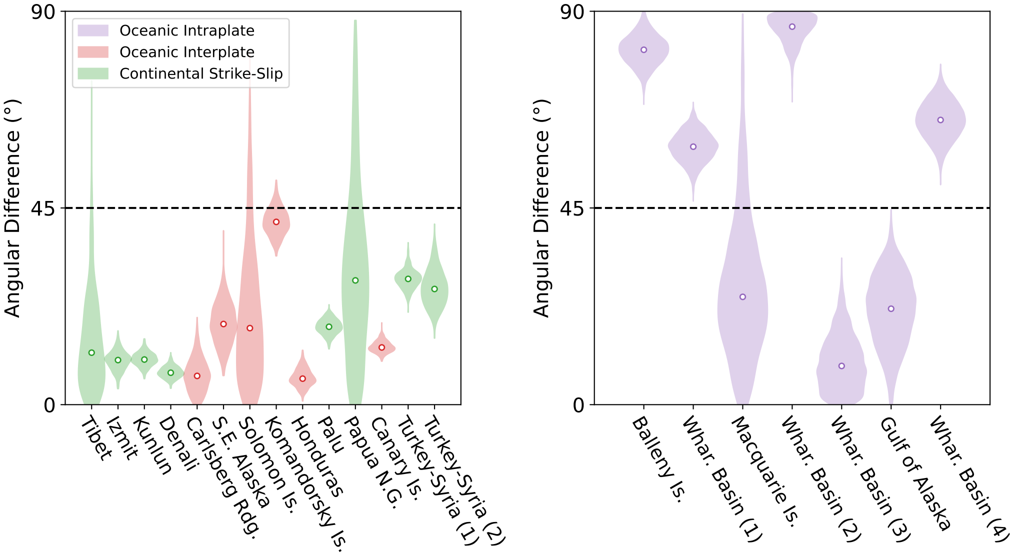

Figure 7.6: Evaluating source orientation against faults and crustal fabric. Left: Comparison of principal eigenvector strike ensembles with true nodal plane strikes for all continental strike-slip and interplate oceanic earthquakes. Right: Comparison of principal eigenvector strike ensembles with fracture zone strike estimation described in the main text for intraplate oceanic earthquakes near mapped fossil fracture zones. For both plots, black dotted lines correspond to differences of 45°. Green, red, and purple correspond to continental strike-slip, oceanic interplate, and oceanic intraplate, respectively.

We apply this technique to the intraplate oceanic earthquakes that are situated near mapped fracture zones. We estimate the fracture zone strike in the area by considering the strikes of the fracture zones within 2° the event centroid. We compute fracture strikes using the shapefiles provided by Seton et al. (2014) and Wessel et al. (2015). For each event, we take the angular difference between the entire ensemble of principal eigenvectors and every potential fracture strike to create a distribution of potential angular differences. We plot these distributions in Figure 7.6. We find that only 3 of the 7 distributions have any members within 45° of the fracture zone strike, suggesting that, more often than not, these ruptures are unaligned with the surrounding ocean fabric. Indeed, this methodology cannot decisively say whether or not the ruptures with principal eigenvectors that fall within 45° of the fracture zone strike actually ruptured the fracture zone, but the large disagreement between principal eigenvector strike and fracture zone strike for the other ruptures suggest that it is very unlikely that fossil fracture zones dictated the primary rupture plane. This motivates new explanations for weakening in the interior of the oceanic lithosphere that could host these large events, such as the explanation that diffuse deformation away from the plate boundary may induce faulting independent of preexisting ocean fabric.

Comparisons with previous studies

Many of the events included here are well-studied, and we thus devote considerable space to evaluating our solutions in the context of prior literature. In Figure 7.7 we show projections of the ensembles of spatial deviation ellipsoids for a subset of the events used in this study. These deviation ellipsoids are defined such that the axes are the principal components of the second spatial moments scaled by the standard deviation along that component. This is equivalent to finding an ellipsoid that captures a single standard deviation of the source distribution in all directions. We selected these events for display here because there exist readily available fault slip distributions that were constrained using high-quality geodetic observations and thus have a data constraint that is independent from seismic observations (Mai and Thingbaijam, 2014; Socquet et al., 2019). We plot the ellipsoid representation and expected vertical extent for a larger subset of events against all the events with available peer-reviewed fault slip distributions in the SRCMOD database in Figures 7.S9 and 7.S10. We compute the expected spatial deviation ellipsoids for these fault slip distributions and compare them to our solutions to assess the strengths and shortcomings of our inversion. In general, there is good agreement between our solutions and that of the fault slip distributions in terms of the rupture azimuths, the ruptures' vertical deviations, and, factoring in the subsequently discussed uncertainties, the overall spatial deviations of these ruptures. Notably, this agreement holds for the 2012 Wharton Basin earthquake for which, despite high variability between slip distributions, a large component of approximately east-west moment release is resolved in each study. All of these comparisons are made more difficult by the intrinsic variability between slip models due to the use of different datasets, inversion techniques, fault parameterization, and assumptions about the rupture process. For example, in the case of the 1999 Izmit Earthquake, the difference between the largest and smallest characteristic spatial deviations of the models included in this study is over 70%. Given these factors, the solutions presented in this study provide a valuable contribution, as this methodology avoids the a priori parameterizations and assumptions present in slip distributions, and is applied uniformly to all of these earthquakes.

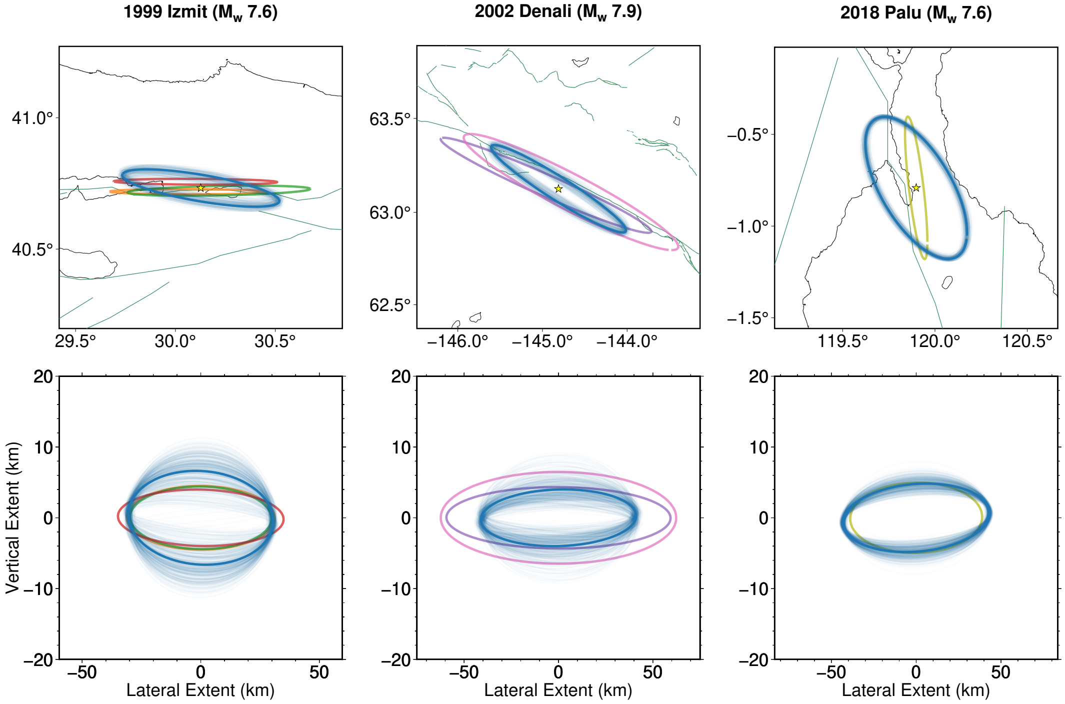

Figure 7.7: Map view (top row) and vertical plane (bottom row) projections of median (dark blue) and individual ensemble members (light blue) of spatial second moment ellipsoids for several events considered in this study. Other colored ellipsoid projections come from geodetically-constrained fault slip distributions reduced to the second moment form. Orange, green, red, purple, pink, and olive colored ellipsoids correspond to solutions from Çakir et al. (2003), Delouis (2002), Reilinger et al. (2000), Asano (2005), and Socquet et al. (2019), respectively.

One key difference between our results and those of the fault slip distributions is that our ellipsoids are much wider in the fault normal direction than those computed from the slip distributions; this is in fact expected behavior. This difference is a consequence of the fact that the fault slip distributions parameterize slip on planar/curved surfaces rather than 3D volumes, resulting in spatial deviation ellipsoids that are artificially much narrower than they would be if the inversions were solved without this constraint. We also note that for the 1998 Ceram Sea Earthquake, the strike of our characteristic ellipsoid is at high angle to the solution from Hayes (2017). Selection of the true nodal plane for this event which, as reported in Hayes (2017), was an intraplate earthquake in a poorly instrumented area with localized slip near a single asperity, is difficult. Our methodology does not require us to define a rupture plane a priori, and instead characterizes a moment distribution directly from the waveforms. We expect this moment distribution to be aligned with the true nodal plane. As we discussed previously, this methodology is particularly useful for resolving nodal plane ambiguity for such challenging cases.

Another important difference is that for the events that are expected to have the greatest spatial length, our inversion resolves characteristic spatial deviations that are sometimes lower than those of the fault slip distributions. There are several potential reasons for these discrepancies, including spatial smoothing due to regularization of the fault slip distributions and imaged slip artifacts due to inaccuracies in the a priori assumptions of the inverse model (Graves and Wald, 2001; Gombert et al., 2018; Ragon, Sladen, and Simons, 2019; Ortega-Culaciati et al., 2021). Both of these factors would contribute to increases in the dimensions of spatial second moments computed from slip distributions because they can artificially increase the spread of inferred slipping regions. These factors are likely compounded for large ruptures because the a priori fault surface dimensions of the slip model are set to be conservatively large to ensure the incorporation of the entire rupture process, and thus extend inversion artifacts farther from the centroid. This is acceptable for a qualitative description of the rupture process; however, this slip can significantly bias the spatial second moments of these slip distributions. For example, in the case of the 1998 Balleny Islands Earthquake, the authors note that deep slip in this model is poorly-resolved and potentially overestimated (Antolik et al., 2000). We thus excise a segment of deep slip to the west of the centroid of their slip model, which greatly reduces the size of the spatial ellipsoid to be much closer to our second moment solution. We can systematically alleviate this issue by removing slip patches with less than 10% of the peak slip, a very conservative estimate of the amplitude of poorly constrained slip in these models, from each of these slip distributions prior to computing their second moments. We plot these corrected second moment ellipsoids and vertical deviations in Figures 7.S11 and 7.S12. This accounts for a large amount of the characteristic spatial deviation discrepancy for some of these events, particularly the Denali and Balleny Islands Earthquakes.

Another potential issue with some of these slip distributions is that, if they are performed using only geodetic data with sparse temporal resolution, such as Interferometric Synthetic Aperture Radar (InSAR), they will include postseismic slip into their solutions and resolve coseismic slip with high uncertainty (Weston et al., 2012; Twardzik et al., 2019; Ragon, Sladen, Bletery, et al., 2019). This is potentially the explanation for a large discrepancy between our solution for the 2001 Kunlun Earthquake and that of Lasserre et al. (2005), who perform their inversion using coseismic InSAR data that incorporate between 1 and 6 months of postseismic slip. For example, there is a large amount of slip along the Taiyang Lake Fault that is resolved using data far from the fault with a large temporal window between frames (3.7 years before the earthquake and 6 months after the earthquake). Excising the slip from this fault segment almost completely removes the difference in second moments between their solution and our solution. We are not suggesting that there was no slip on the Taiyang Lake Fault during this earthquake, as other slip distributions suggest a low-amplitude subevent to the west (e.g., Antolik et al., 2004), but this comparison illustrates the high degree of sensitivity these second moments computed from slip distributions have to poorly constrained and potentially overestimated slip far from the centroid.

There are also many slip models not included in this direct comparison. While we cannot discuss all of them here, we note several key differences between these stress glut variances and finite fault slip distributions that are important in contextualizing these results. The stress glut covariance only yields an estimate of a parameter that summarizes the distribution of slip, and does not estimate the full slip on the fault. For example, although several hundred kilometers of the Bering Fracture Zone are expected to have ruptured during the Komandorsky Islands earthquake (Lay et al., 2017), the slip distribution suggests highly concentrated moment release along a much shorter segment of the fault. This type of distribution would yield a source spatial variance that is much smaller than the full length of slip on the rupturing fault. The temporal deviations should be interpreted similarly. Additionally, the average centroid velocity describes the integrated velocity behavior of the entire rupture, and thus should not be confused with instantaneous rupture speed. For example, a rupture that experienced supershear propagation could have a much lower average centroid velocity if the rupture had a bilateral component or if the rupture was slower before or after the supershear period.

Finally, solutions for the Tibet, Balleny Islands, Ceram Sea, and Izmit earthquakes were computed with stress glut second moment inversion frameworks in prior studies (McGuire et al., 2000; McGuire et al., 2002; Clévédé et al., 2004). The characteristic quantities from these studies are shown in Table 7.S2. In general, while these solutions agree for many parameters, there are several differences between these sets of solutions. The Izmit Earthquake is the most useful earthquake for comparison, because second moments were computed for this event in three different frameworks, and this event is the best documented of the overlapping events. In short, the spatial deviations are largely consistent between studies, McGuire et al. (2002) reports a much narrower temporal deviation than Clévédé et al. (2004) and this study, and this study reports a much lower average centroid velocity than McGuire et al. (2002) and Clévédé et al. (2004). For this event, the longer temporal deviation estimates and the expectation of near-bilateral directivity reported in this study are consistent with studies that investigated the time-dependent slip of this earthquake (Yagi and Kikuchi, 2000; Delouis, 2002; Bouchon, 2002; X. Li, 2002), so we believe our framework yields the preferred solution for this event. Again, for the other events, there are many commonalities but several differences between solutions. These differences may arise from the differences in priors and parameterizations between studies. For instance, McGuire et al. (2000) and McGuire et al. (2002) allow the lower order moments to vary, constrain the radial component of the spatial covariance, use a fixed frequency band for all events, and use a different Earth model and distinct phases. We choose to fix the lower moments and allow the second moments to vary freely, because we consider the centroid moment tensor solutions for these large events to be very well-constrained relative to our knowledge of the finite properties of these events. Our selection of the frequency band and Earth model are meant to improve the isolation of the contribution of the second moments of these ruptures.

7.5 Conclusions

By computing ensembles of stress glut second moments for all large strike-slip earthquakes of the past few decades, we illuminated several patterns in these ruptures that suggest predominant behaviors and variability with tectonic environment. Our results show that large strike-slip ruptures usually have a large component of unilateral behavior, with many ruptures exhibiting evidence for complicated rupture propagation sequences. We also observed that intraplate oceanic events have wider ruptures than other large strike-slip earthquakes, potentially illustrating a systematic behavior of rupturing below the expected brittle-ductile transition zone depth. Finally, we show that by resolving the approximate rupture plane strike of major oceanic intraplate earthquakes, most of the earthquakes show no alignment with the fossil fracture zones in the area. This suggests that the assumption that large oceanic intraplate earthquakes reactivate fossil fracture zones is usually incorrect.

Supplementary Materials

Table 7.S1: Frequency bands used for the second moment inversion for each event.

Name	Date	M_w	Frequency Band (mHz)
Tibet	1997-11-11	7.53	8.1-13.4
Balleny Is.	1998-03-25	8.14	4.0-6.6
Ceram Sea	1998-11-29	7.75	6.3-10.4
Izmit	1999-10-17	7.61	7.5-12.3
Sulawesi	2000-05-04	7.57	7.8-12.8
Whar. Basin (1)	2000-06-18	7.92	5.2-8.6
Kunlun	2001-11-14	7.81	5.9-9.7
Irian Jaya	2002-10-10	7.58	7.7-12.7
Denali	2002-11-03	7.88	5.4-9.0
Carlsberg Rdg.	2003-07-15	7.57	7.8-12.8
Macquarie Is.	2004-12-23	8.11	4.2-6.9
Whar. Basin (2)	2012-04-11	8.6	2.4-3.9
Whar. Basin (3)	2012-04-11	8.28	3.5-5.7
S.E. of Alaska	2013-01-05	7.56	7.9-13.0
Solomon Is.	2014-04-12	7.66	7.0-11.6
Whar. Basin (4)	2016-03-02	7.82	5.9-9.7
Komandorski Is.	2017-07-17	7.79	6.1-10.0
Honduras	2018-01-10	7.55	8.0-13.1
Gulf of Alaska	2018-01-23	7.96	5.0-8.2
Palu	2018-09-28	7.60	7.5-12.4
Papua N.G.	2019-05-14	7.60	7.5-12.4
Canary Is.	2020-01-28	7.72	6.5-10.8
S. of Alaska	2020-10-19	7.62	7.4-12.2
Turkey-Syria (1)	2023-02-06	7.83	5.8-9.5
Turkey-Syria (2)	2023-02-06	7.78	6.2-10.1

Table 7.S2: Summary of second moment parameter results from prior studies.

Name	L_c (km)	$\|\|\boldsymbol{v_0}\|\|$ (km/s)	t_c (s)	Study
Tibet	44 ± 5	4.3 ± 0.2	10 ± 1	McGuire et al. (2002)
Balleny Is.	178 ± 14	3.6 ± 0.1	48 ± 1	McGuire et al. (2002)
Ceram Sea	76.5 ± 5	3.7 ± 0.6	6 ± 1	McGuire et al. (2002)
Izmit	64.0	3.9 ± 0.3	15.0	Clévédé et al. (2004)
Izmit	52 ± 7	6.3 ± 1.4	7 ± 1	McGuire et al. (2002)

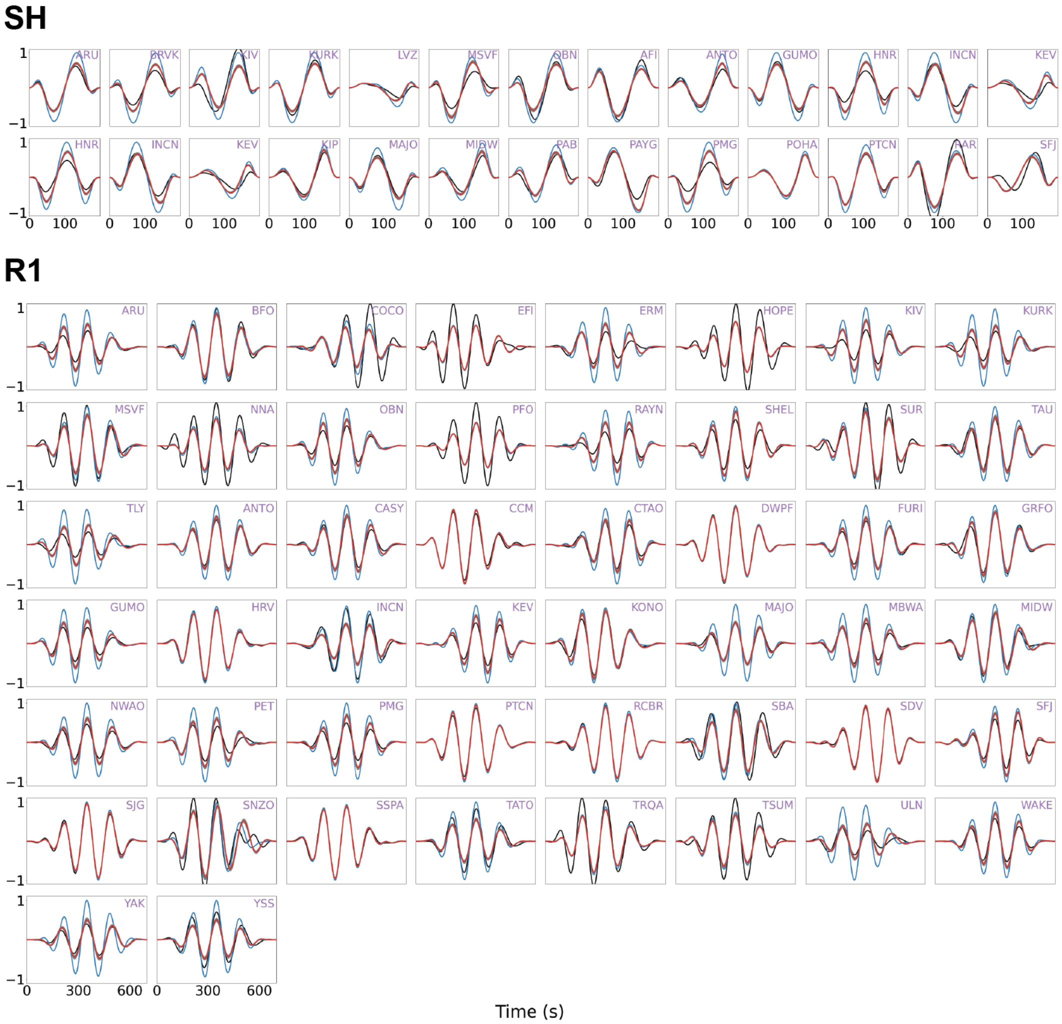

Figure 7.S1: Examples of waveform fits for the 2002 M_w7.88 Denali earthquake. The waveforms in the top grouping are fits to the SH phase. The waveforms in the bottom grouping are fits to the R1 phase. The black and blue lines correspond to the observed waveforms and the point source theoretical Green's functions at each respective station. The red and gray lines correspond to the waveform fit of the mean solution and the distribution of fits for the ensemble of solutions respectively.

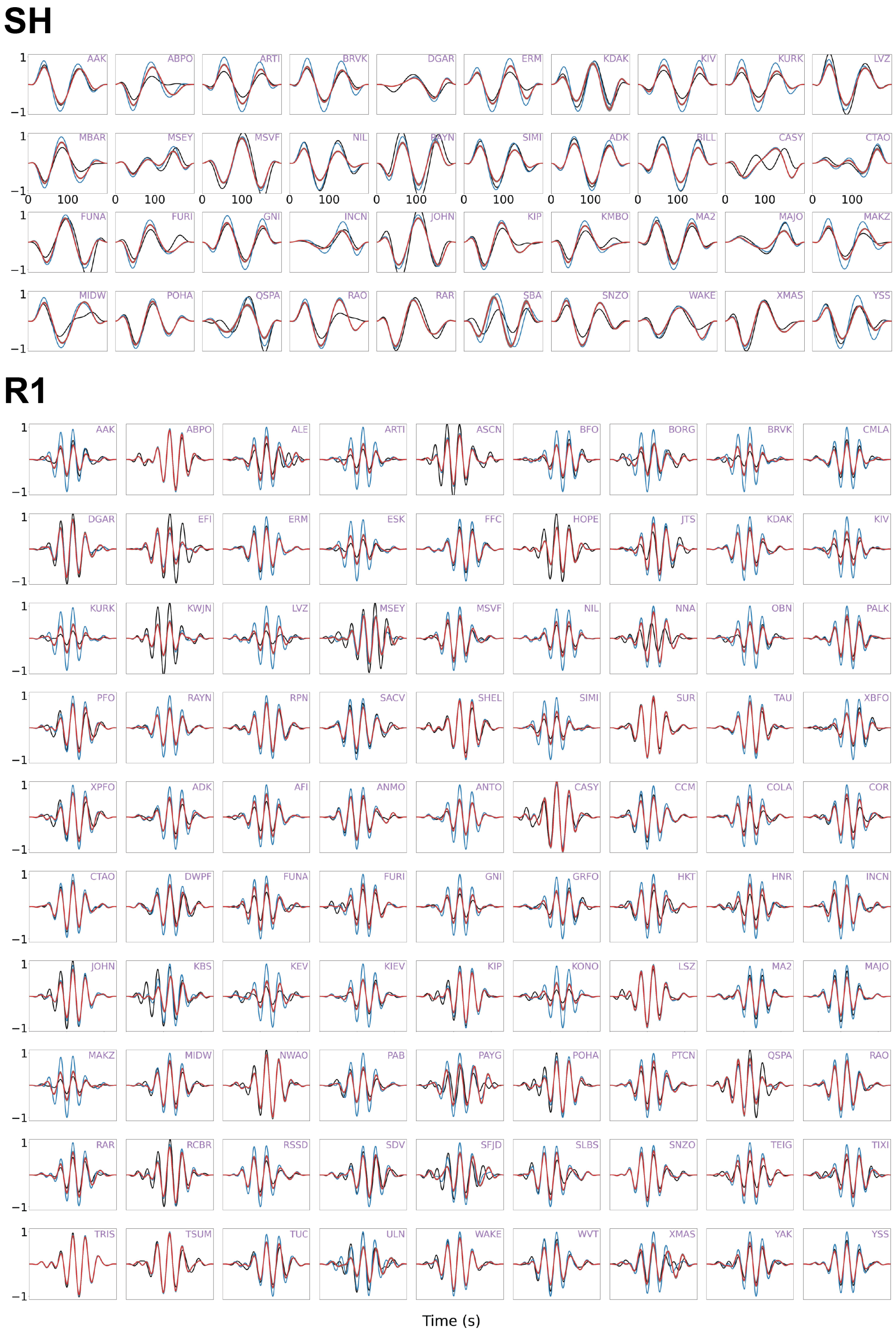

Figure 7.S2: Examples of waveform fits for the 2018 M_w7.60 Palu earthquake. The waveforms in the top grouping are fits to the SH phase. The waveforms in the bottom grouping are fits to the R1 phase. The black and blue lines correspond to the observed waveforms and the point source theoretical Green's functions at each respective station. The red and gray lines correspond to the waveform fit of the mean solution and the distribution of fits for the ensemble of solutions, respectively.

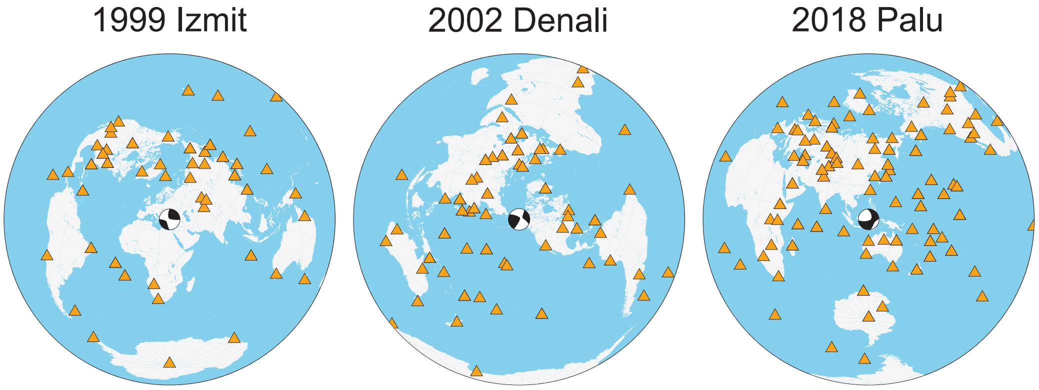

Figure 7.S3: Station distribution for the three events plotted in Figure 3 of the main text in an azimuthal equidistant projection. Orange triangles represent Global Seismographic Network Stations and focal mechanisms are produced using the gCMT solution (Ekström et al., 2012).

Figure 7.S4: Ensembles of parameters defined in equations 4 and 5 of the main text for the oceanic interplate earthquakes considered in this study.

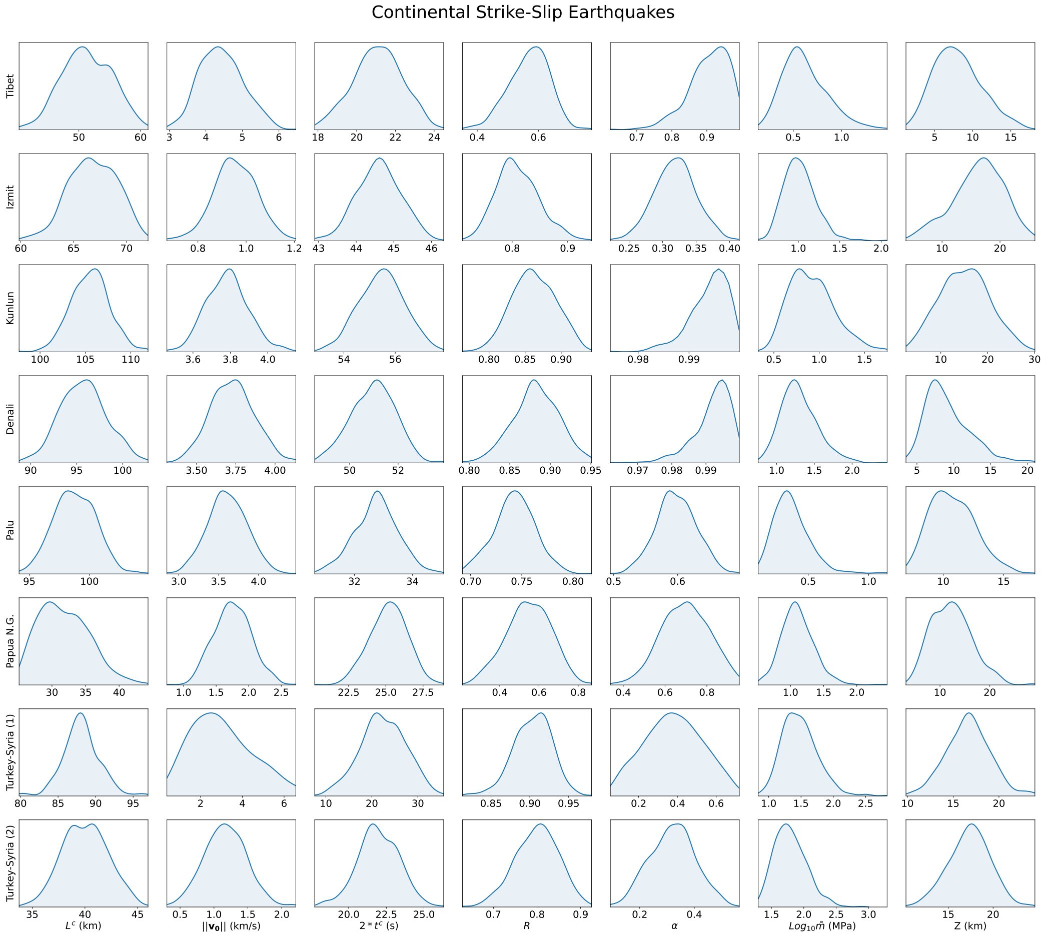

Figure 7.S5: Ensembles of parameters defined in equations 4 and 5 of the main text for the continental strike-slip earthquakes considered in this study.

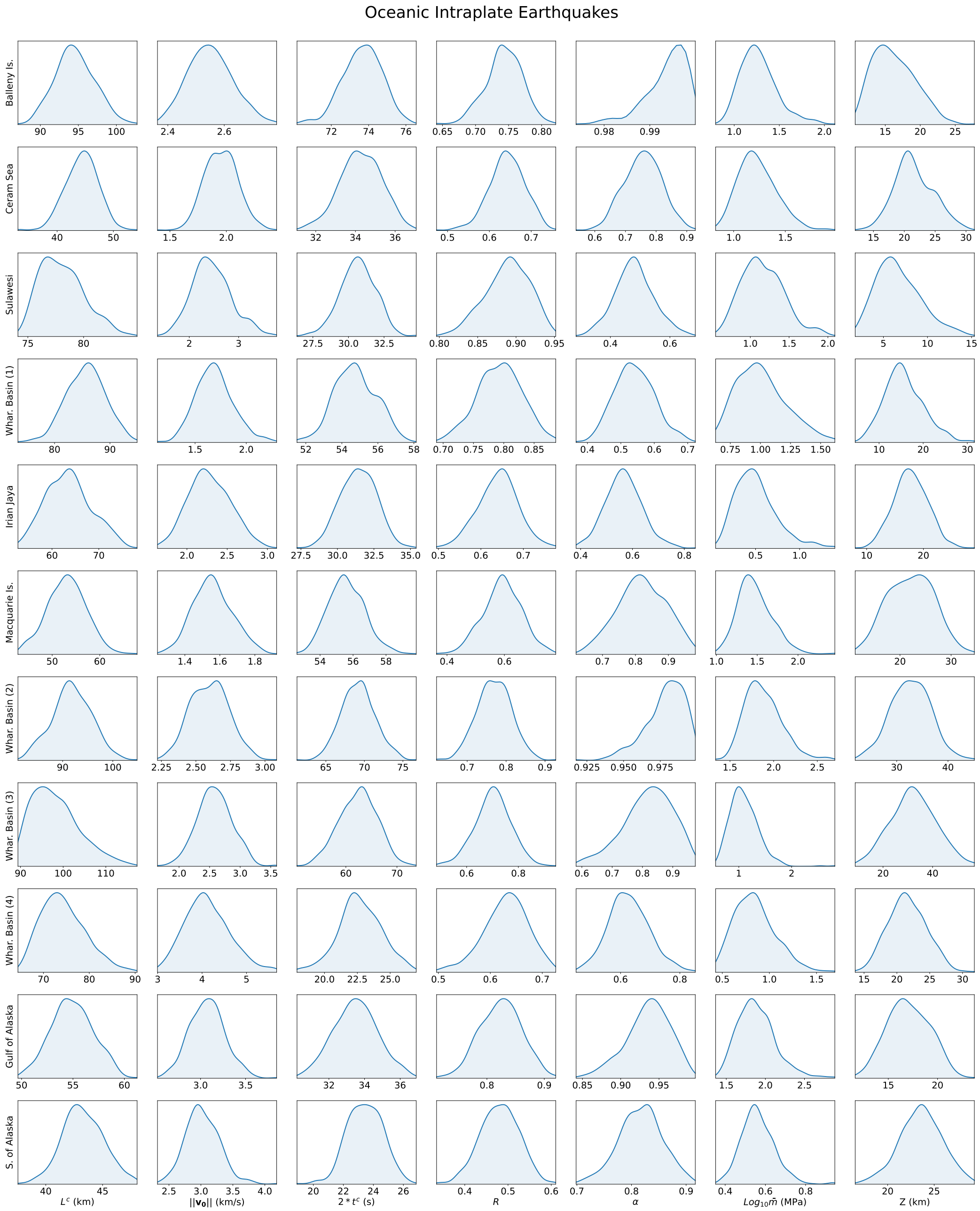

Figure 7.S6: Ensembles of parameters defined in equations 4 and 5 of the main text for the oceanic intraplate earthquakes considered in this study.

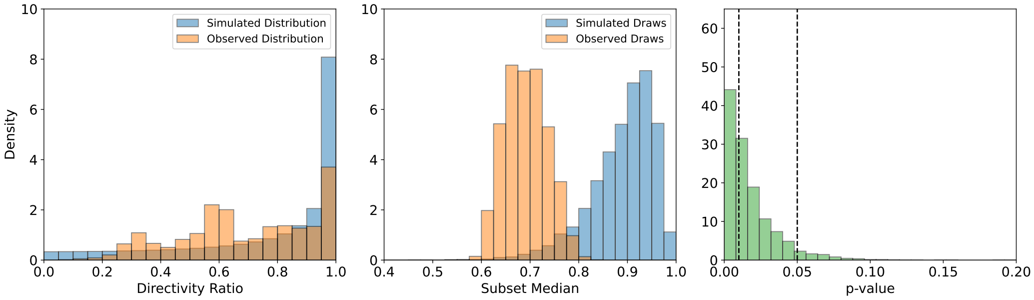

Figure 7.S7: Evaluation of the significance of directivity ratio results. Left: Histogram comparing the combined ensembles of directivity ratios computed in this study (observed distribution) plotted against the expected distribution of directivity ratios given 1D rupture scenarios with random hypocenter locations on predefined faults with uniform slip (simulated distribution). Middle: Median values for many random draws of 25 directivity ratios from simulated distribution plotted against median values from random ensemble draws from the observed distribution. Right: Distribution of p-values for median for the observed distribution draws compared to the distribution of median computed from the simulated distribution.

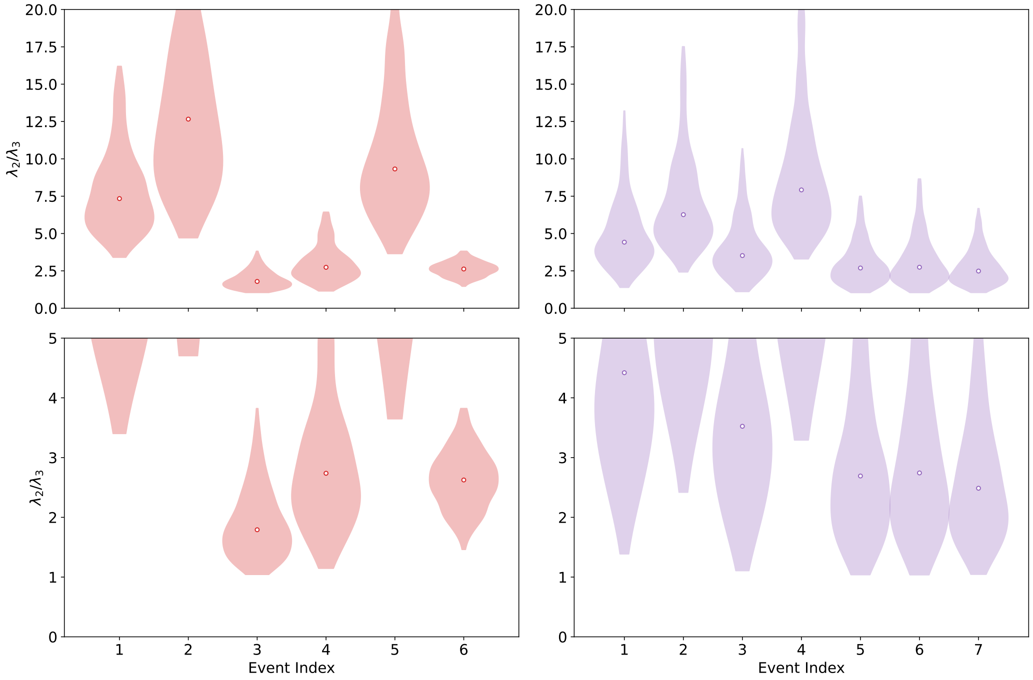

Figure 7.S8: λ_2/λ_3 for the events shown in Figure 5. Left and right columns correspond to oceanic interplate and oceanic intraplate events, respectively. Top and bottom show the same plots but with different y-axis bounds. The event index corresponds to the relative lithospheric age (youngest to oldest) plotted in Figure 5.

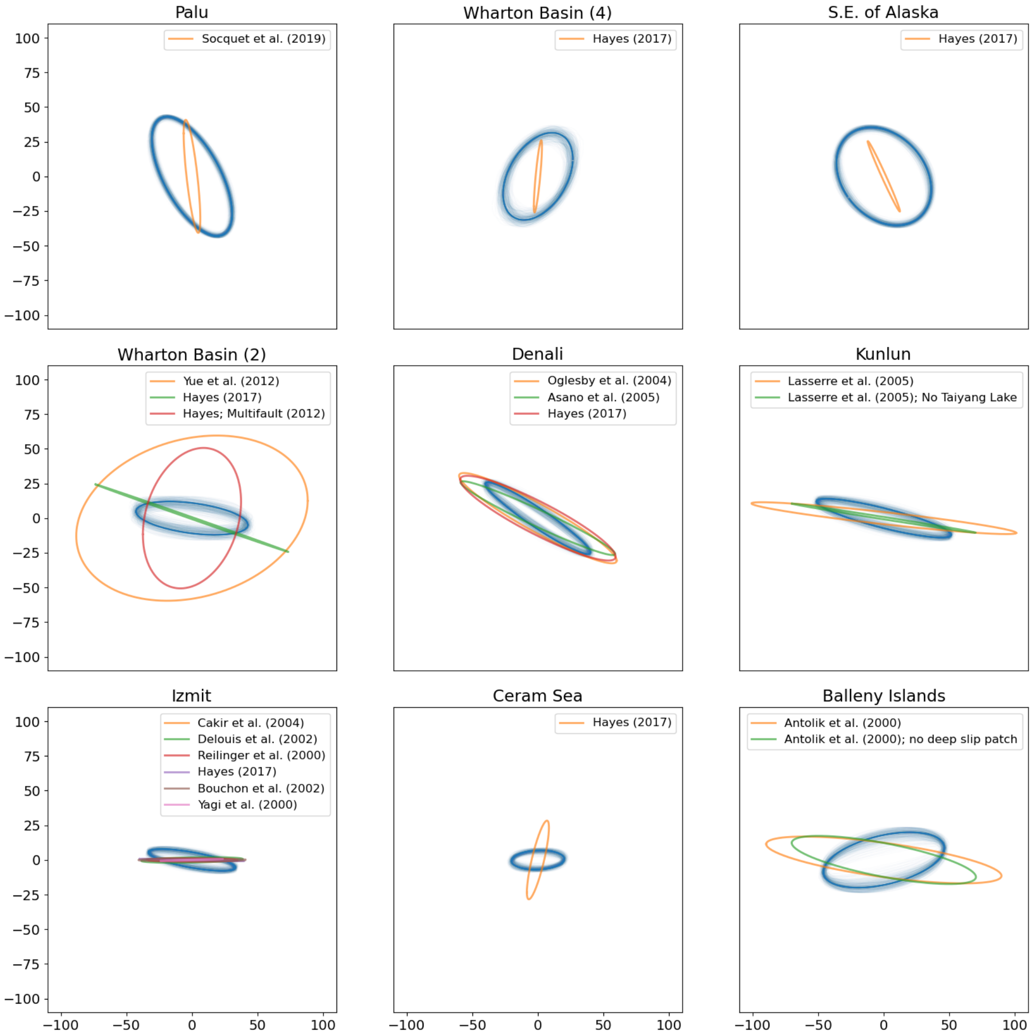

Figure 7.S9: Map-view comparison of deviation ellipsoids between the second moment solutions produced in this study and those computed from peer-reviewed fault slip distributions in the SRCMOD database (Mai and Thingbaijam, 2014). Additional solutions for Palu earthquake from Socquet et al. (2019) and Hayes (2012), which is not peer reviewed but includes multiple faults, are included as well.

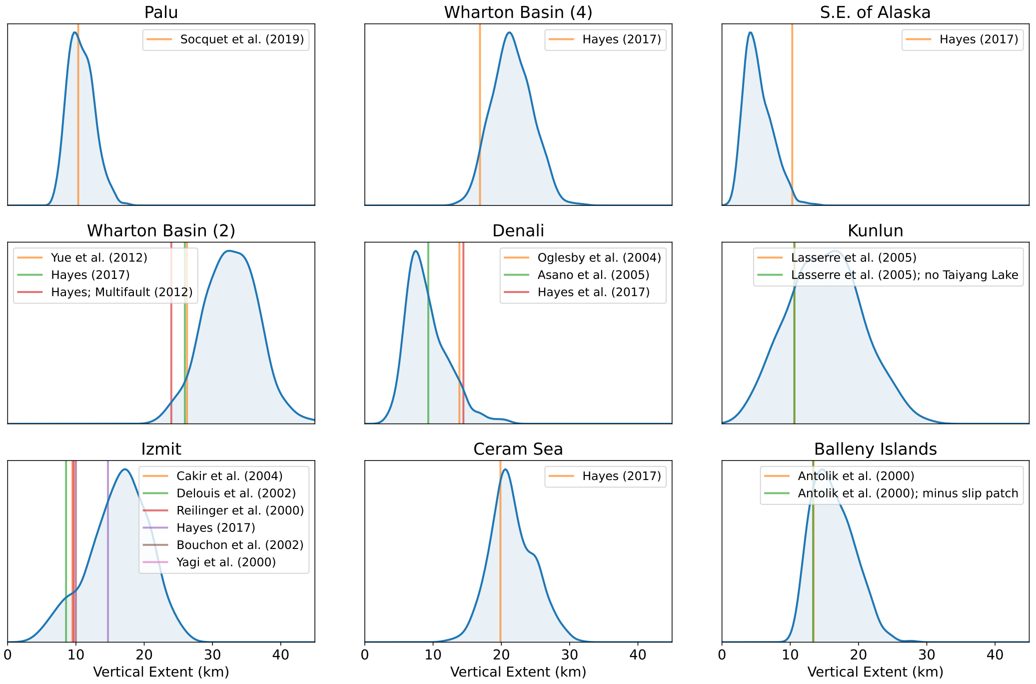

Figure 7.S10: Comparisons of vertical deviations between the second moment solutions produced in this study and those computed from peer-reviewed fault slip distributions in the SRCMOD database (Mai and Thingbaijam, 2014). Additional solutions for Palu earthquake from Socquet et al. (2019) and Hayes (2012), which is not peer reviewed but includes multiple faults, are included as well.

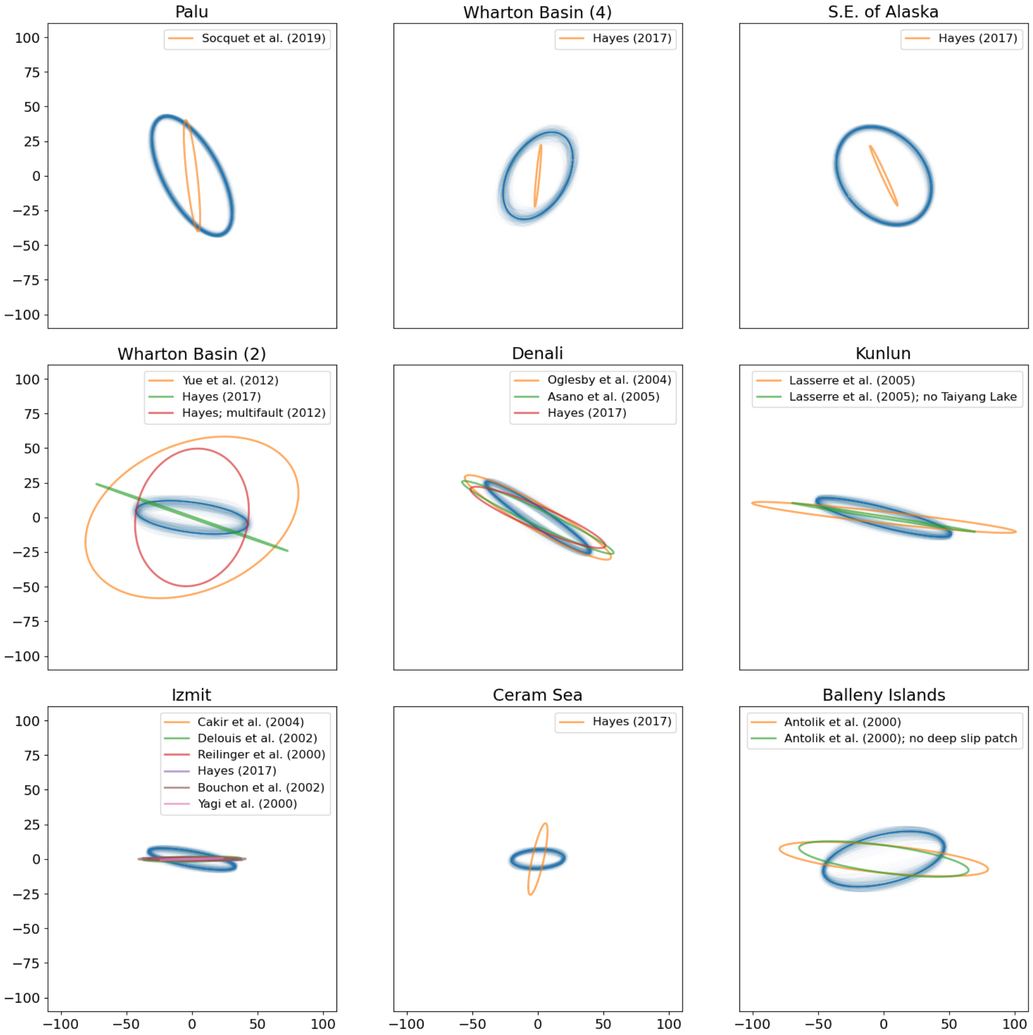

Figure 7.S11: The same plots as shown in Figure 7.S7, but produced with all slip patches with slip $< 10\%$ of the peak slip removed.

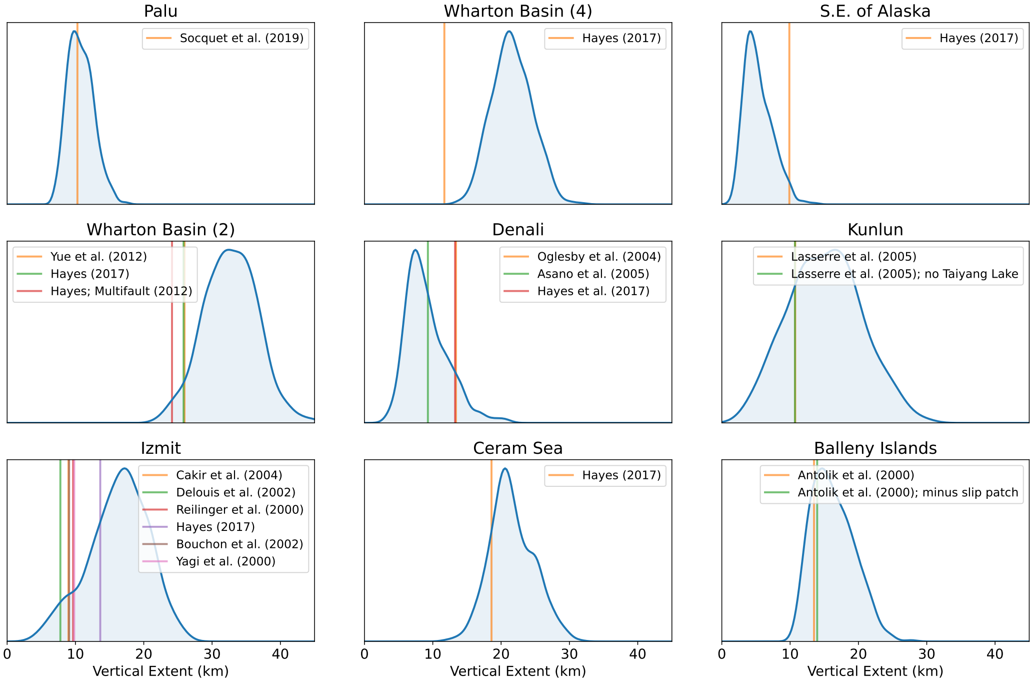

Figure 7.S12: The same plots as shown in Figure 7.S8, but produced with all slip patches with slip < 10% of the peak slip removed.

Chapter 8

MEASURING FAULT ORIENTATION EVOLUTION USING SEISMICITY

Atterholt, J. and Ross, Z. E. (In Prep). The evolution of fault orientation in the 2019 Ridgecrest Earthquake Sequence with a new long-term catalog of seismicity and moment tensors.

Abstract

Throughout an earthquake sequence, perturbations to the stress field may lead to changes in the distribution of active fault orientations. Resolving such changes for narrow spatiotemporal windows requires high-quality seismicity catalogs and objective techniques to measure fault orientations. We investigate the evolution of fault orientations throughout the 2019 Ridgecrest earthquake sequence using a new seismicity catalog that captures the sequence over several years. We generate this catalog using a state-of-the-art workflow for event detection, absolute and relative relocation, and moment tensor inversion. With this catalog, we measure high resolution, time-dependent changes in the orientations of active faults using a technique from spatial statistics that quantifies anisotropic features in point processes. We evaluate the results alongside those of more standard techniques based on focal mechanisms. Near the centroid of the mainshock, we observe a substantial shift in the distribution of fault orientations, whereas to the south of the mainshock centroid, we observe only a moderate transient change in the distribution of fault orientations. Compared with results derived from focal mechanisms alone, our findings suggest a smaller background differential stress and a distinct response of the stress state to postseismic deformation.

8.1 Introduction

Earthquakes are expressions of inelastic strain driven by stress. Stress is relieved and redistributed by earthquakes. If a rupture is large and the stress drop is a substantial proportion of the differential stress, the orientation of the stress field in the volume surrounding the fault before and after the earthquake may differ measurably (Hardebeck and Hauksson, 2001; Michael, 1987; Yin and Rogers, 1995; Zoback and Beroza, 1993). These so-called stress rotations have been observed for many earthquakes and are typically resolved by measuring changes in focal mechanisms (see Hardebeck and Okada (2018) for review). Earthquakes exhibit nonuniform slip and postseismic behavior (e.g., Ozawa et al., 2012; Perfettini and Avouac, 2007; Yue et al., 2021). By extension, the corresponding perturbation to the stress field in the volume around the rupture is expectedly varied. Thus, imaging perturbations to the stress field around rupture zones with increasing granularity is valuable, because this provides an observational constraint on how heterogeneous slip redistributes stress and influences what faults become active in the volume around the rupture zone (Yoshida et al., 2015) and how postseismic processes variably reload faults (Hardebeck, 2012; Zhao et al., 1997).

In July of 2019, the Ridgecrest earthquake sequence initiated in the Eastern California Shear Zone. This sequence included a large, left-lateral Mw 6.4 foreshock and an orthogonal, right-lateral Mw 7.1 mainshock (Ross et al., 2019). Both earthquakes exhibited heterogeneous slip and postseismic deformation (e.g., Jin and Fialko, 2020; Pollitz et al., 2022) and so may have variably affected the stress state. These earthquakes occurred in a well-instrumented area and were accompanied by numerous smaller foreshocks and aftershocks. The aftershock sequence lasted for over 3 years. The abundance of seismicity in this sequence provides an opportunity to measure the evolution of active fault orientations with high spatial and temporal resolution. A noteworthy feature of this earthquake is the abundant conjugate faulting that is clearly visible in the surface ruptures and patterns of seismicity (Shelly, 2020). This conjugate faulting allows for the estimation of the average dihedral angle and coefficient of friction of the rock (Fialko, 2021) and demonstrates the potential difficulty of describing faulting using focal mechanisms alone.

The Ridgecrest sequence is exceptionally well-studied, and it is an ideal place to evaluate emergent methodologies because there are many baseline studies with which to contextualize new types of observations. Some studies have estimated the change in active fault orientations due to the Ridgecrest earthquake using focal mechanism-based techniques. Sheng and Meng (2020) performed a spatially compartmentalized stress inversion before and after the mainshock using a focal mechanism catalog and found a small clockwise rotation in a region surrounding the Mw 6.4 foreshock centroid. These authors also report a heterogeneous postseismic stress field in the centroid zone and infer a near complete stress release in that area. Using summations of focal mechanisms, Cheng et al. (2023) resolve a counterclockwise rotation of focal mechanisms immediately after the mainshock in the vicinity of the centroid, suggesting a localized change in the stress state. One way we build on these studies is by applying these standard techniques to a new, long-term and dense relocated seismicity and moment tensor catalog. This increases the temporal resolution, the precision, and the duration over which we can evaluate the evolution of the stress state.

Focal mechanisms are often used to invert for rotations of the stress field (Gephart and Forsyth, 1984; Michael, 1984). The physical basis for this approach is that focal mechanisms define rupture planes that are partially a function of the stress orientation. However, using these inversions to infer stress at finer scales presents several challenges. These inversions require high focal mechanism diversity to infer the true stress orientation (Hardebeck and Hauksson, 2001). This is increasingly difficult to achieve over narrower spatiotemporal windows, especially when the true nodal planes are not known, or the focal mechanism uncertainty is high. Additionally, these inversions assume homogeneous stress in the volume encompassing the included focal mechanisms, an assumption that may break down near large earthquakes (Townend, 2004). This means that the zonation of the rupture volume, which is usually arbitrary, may have a substantial influence on the resolved stress state (Smith and Heaton, 2011; Townend and Zoback, 2001). Relatedly, other factors such as crustal anisotropy affect the orientations of active faults (Nevitt et al., 2023; Segall and Pollard, 1983). This means certain populations of faults may not necessarily be representative of the stress orientation. This may serve to bias resultant stress orientation estimates if such populations are included in the volume.

In some circumstances, earthquake hypocenters can be used to measure geometrical attributes of faults (e.g., Fialko, 2021; Plesch et al., 2007). Techniques from statistical point process theory have recently been demonstrated capable of measuring various geometrical properties of seismicity catalogs, such as the distribution of fault orientations in a volume (Ross et al., 2022; Ross, 2024). Seismicity derived measurements may provide complementary constraints on active fault orientations at fine spatiotemporal scales, with possible additional benefits such as the ability to uniquely define fault planes and measure distinct modes of fault orientations. Methods based on seismicity may avoid issues pertaining to nodal plane ambiguity and biases arising from reducing all observations in a volume to a single quantity. We further build on previous studies by applying a new technique for estimating fault evolution throughout a seismic sequence using hypocenter locations. The results from this hypocenter technique provide new and exciting insights into the progression of the state of stress throughout the sequence.

The contributions of this study are as follows. 1. We present a long-term, high-precision seismicity catalog of the Ridgecrest earthquake sequence that spans several years and captures the full aftershock sequence. We also compute thousands of moment tensor solutions in a Bayesian framework using first-break amplitudes and polarities. 2. We objectively evaluate the progression of fault orientation throughout the sequence in narrow spatial and temporal windows using a measure from point process theory. We additionally compute estimates of fault orientations using the focal mechanism catalog for comparison. Each of these techniques suggest a localized change in the dominant faulting regime around the centroid of the mainshock and the largest foreshock. We show, however, that the hypocenter-based measurement resolves a larger change in orientation than the focal mechanism results and a distinct postseismic response. We thus present new constraints on the background differential stress and new insights into how postseismic deformation relates to the recovery of stress following a large earthquake.

8.2 Constructing a Seismicity and Moment Tensor Catalog

We generate a seismicity catalog for the Ridgecrest earthquake sequence using a comprehensive workflow. The process of building a catalog from scratch begins by scanning the continuous seismic data for probable P and S wave arrivals. We do this using Phase Neural Operator (PhaseNO) (Sun et al., 2023), a new algorithm that incorporates Fourier and graph neural operators to consider both temporal and spatial patterns in continuous data to more effectively mine seismic data for phase arrivals. We apply this to continuous waveform data from a multi-network array of 66 3-component broadband seismometers (SCEDC, 2013; University of Nevada, 1971; USGS, 1980) that spans the period from April 2019 to May of 2023. These stations were selected by searching for all available broadband stations within a conservatively wide spatial window (200x200 km) centered on the approximate mainshock hypocenter. Both vertical and horizontal (N) components were used during the earthquake detection step. The station distribution used for this catalog is shown in Figure 8.S1. Seismograms were high-pass filtered above 1 Hz. The neural network graphs, which encoded spatial relationships between stations when making picks, included 18 stations. We associate resultant picks to seismic events using Gaussian Mixture Model Association (GaMMA) (Zhu et al., 2022), which casts association as an unsupervised clustering problem that clusters arrivals according to relative arrival time and amplitude decay. For this catalog, we enforce that there need be at least 15 picks for an earthquake to be associated and we set the maximum phase time error to be 2 s. The GaMMA algorithm requires dividing the dataset into temporal sub-windows; we set this window length to 10 s. This association step yields 326,345 events.

We subsequently compute absolute event locations using hypocenter inversion with Stein variational inference (HypoSVI) (Smith, Ross, et al., 2021). This combines a physics informed neural network used to solve the Eikonal equation (EikoNet) (Smith, Azizzadenesheli, et al., 2021) with Stein variational inference, a technique that instantiates a set of particles that march towards an approximation of the distribution of potential hypocenter locations. We use a smoothed version of the Hadley-Kanamori model (Hadley and Kanamori, 1977) for Southern California as the velocity model and use source-specific station term corrections to improve relative locations and partially account for 3D structure (Richards-Dinger and Shearer, 2000). We perform these corrections using 8 iterations to approach stable site terms and earthquake locations. To quantify the uncertainty of these locations, we estimate the 90th percentile of the maximum horizontal and vertical uncertainty for the nonrelocated events that are ultimately preserved in the final catalog. Using the posterior distributions computed with HypoSVI, we find that 90% of these events have horizontal uncertainties less than 700 m and vertical uncertainties less than 1 km. We perform relative relocation using differential arrival times computed by cross-correlating nearby event waveforms and subsequently performing relocation using GrowClust (Trugman and Shearer, 2017). GrowClust uses a flexible cluster criterion and minimizes differential travel-time differences using the L1 norm. We enforce a minimum cross-correlation coefficient of 0.65 and that each event pair has at least 6 differential time observations. Only events that were relocated are preserved, leaving 214,467 events. The resultant seismicity catalog is shown in Figure 8.1a.

We calculate moment tensors for the catalog using P-wave amplitudes following the methodology of Wilding and Ross (2024). In this technique, automated measurements of signed P-wave amplitudes are extracted from vertical-component displacement waveforms by integrating the area underneath the first swing of the P arrival. We solve for moment tensors in a Bayesian framework to determine the full range of uncertainty of our solutions. Applying this measurement algorithm, we retrieve 226,615 P amplitude measurements for 45,684 events. We set a mini-

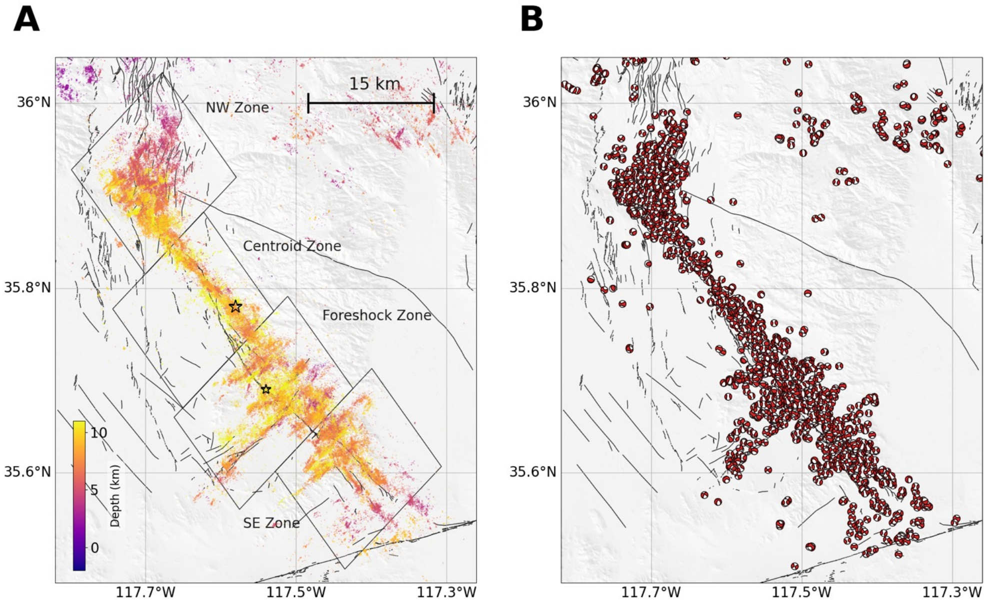

Figure 8.1: Plot of the seismicity (A) and focal mechanisms (B) resolved during the catalog creation step in this study. The regionalization used to measure faulting evolution over narrower spatial windows is shown in A. Also shown are the locations of the Mw 6.4 foreshock and Mw 7.1 mainshock centroid locations as the smaller and larger black star, respectively.

mum threshold of 15 measured amplitudes to invert for a moment tensor and obtain 7,645 events that meet this criterion. We correct for unmodeled 3D structure by iteratively calculating source-specific station correction terms for each event using the amplitude residuals of neighboring events within 10 km. For each solution, we estimate uncertainties in strike, dip, and rake by measuring the standard deviations of the posterior distributions (Fig. S2). We impose a strict criterion of having strike, dip, and rake uncertainties below 7.5 degrees and discard events with uncertainties above this threshold, preserving 4,892 moment tensor solutions. We find that these well-constrained solutions are predominantly double couple (e.g., Fig. S2), justifying our subsequent assumption of double-couple faulting. These remaining focal mechanism solutions are plotted in Figure 8.1b.

A map-view representation of the catalog produced in this study is shown in Figure 8.1. As resolved in previous studies (Shelly, 2020), there is abundant horsetail faulting in the northwest and pervasive conjugate faulting in the region around the Mw6.4 foreshock. An important advantage of the catalog produced in this study over other high-resolution seismicity catalogs for this sequence (Ross, Idini, et al., 2019; Shelly, 2020) is its temporal extent (Figure 8.S3). In this region, the seismicity rate is elevated above the rate for the months preceding the mainshock for over 3 years. Over the course of the catalog, we record over 150,000 events in the immediate vicinity of the mainshock. For the period during which the catalogs overlap, we record nearly 3 times the number of relocated events as reported in the Hauksson et al. (2012) catalog. But the catalogs we generate in this study still only provide a snapshot of the seismicity during the earthquake sequence and the months immediately preceding and following it. To obtain a reference for the state of stress from seismicity over the decades prior to the earthquake sequence, we use the updated relocated seismicity catalog from Hauksson et al. (2012) and the updated focal mechanism catalog produced with the methods of Yang et al. (2012). These catalogs have solutions for the region dating back to 1981 and are shown in Figure 8.S4. For the focal mechanism catalog, we only use the highest quality solutions (quality A).

We use these catalogs and three complementary methods (described subsequently) to evaluate the evolution of active fault orientations throughout the sequence. We apply these methods within several spatial windows presumed to capture distinct behavioral regimes. These windows are intentionally narrow to minimize the possible effect of spatial variability in seismicity within a window mapping into temporal variability, but large enough to include sufficient seismicity and focal mechanism diversity to infer the fault orientation evolution. This zonation is shown in Figure 8.1. The NW zone captures the abundant horsetail faulting in the sequence. The centroid zone is, by contrast, structurally simpler and encompasses the region of maximum mainshock slip. The foreshock zone encompasses almost the entire foreshock sequence, allowing us to test for transient stress behavior between the large foreshock and mainshock. The SE zone captures the subparallel faulting near the Garlock Fault.

8.3 Computing Fault Orientations with Focal Mechanisms

To establish a baseline with which to evaluate the results of the hypocenter derived measurements, we evaluate the evolution of fault orientation using two standard techniques that employ focal mechanisms. The large number and high quality of the moment tensors produced in our catalog allow for us to apply these methods at high temporal resolution within our defined regions. The first of these metrics is normalized potency tensor summation (NPTS) (Bailey et al., 2009; Kostrov, 1976). For this method, we assume a double couple mechanism for each moment tensor solution, normalize the components by a value proportional to the seismic moment, and sum the corresponding tensor components for all source mechanisms within a spatiotemporal window,

$$S_{ij} = \sum_{k}^{N} \hat{P}_{ij}^{(k)}. \tag{8.1}$$

where $\hat{\mathbf{P}}^{(k)}$ is the kth normalized potency tensor. Normalizing the tensors removes magnitude-dependent weighting and thus allows for a summed tensor that is more representative of the diversity of faulting in the window. We consider the orientation of the vector defining the middle of the dilatational quadrant of the focal mechanism (P-axis) of the summed tensor as a measure of the relative orientation of active faults.

For a double-couple potency tensor, the intermediate eigenvalue, λ_2, is zero. For a sum of double-couple potency tensors with dissimilar rupture orientations, λ_2 may be nonzero and corresponds to a nonzero compensated linear vector dipole (CLVD) component. This quantity can be a useful measure of the heterogeneity of slip in a window, and can be represented as,

$$r_{CLVD} = \frac{\sqrt{6}}{2} \frac{\lambda_2}{\sqrt{S_{ij} S_{ij}}}. \tag{8.2}$$

This value is by design bounded between -0.5 and 0.5 and quantifies potency tensor scatter.

We apply this methodology to the updated Yang et al. (2012) catalog to define a long term reference, and separately within narrow spatiotemporal windows for our moment tensor catalog. For the events in our catalog, we select the temporal sampling such that each time window includes 150 focal mechanisms. We include some important time windows before the mainshock, during the foreshock sequence, and towards the end of the aftershock sequence that may have fewer than 150 focal mechanisms but have what we deem a sufficiently large set to recover a representative average (more than 50 focal mechanisms). We estimate error by bootstrapping the potency tensors included in the summation. The evolution of the P-axis and r_{CLVD} resolved from these summations for each zone are shown in Figures 8.2 and 8.3, respectively, and we additionally report these values in Table 8.S1.

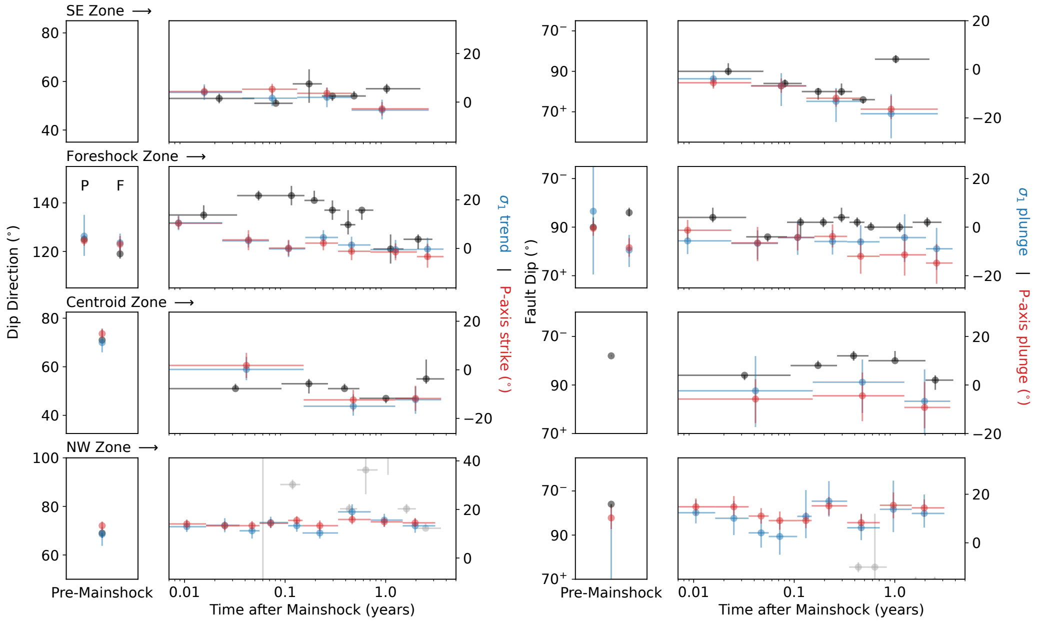

Figure 8.2: Direct comparison plot showing time evolution of faulting between methods applied in this study. The progression of the dip direction (black) measured using the peaks of the K_{cyl} plots is compared to the horizontal trend of σ_1 (blue) and the P-axis (red) by transforming the y-axis bounds using the measured dihedral angle. The direction of deviation in the dip from 90 degrees is chosen according to whether the dip is towards the corresponding dip direction (+) or away from the corresponding dip direction (-). In the foreshock zone, the pre-mainshock bin has two windows, one prior to the Mw6.4 foreshock (labelled P) and one between the Mw6.4 foreshock and the Mw7.1 mainshock (labelled F). K_{cyl} values of the aftershock sequence in the NW zone are plotted as light gray to highlight that these values do not show a stable progression of the primary fault orientation mode with time.

We next summarize the results of these figures for each spatial window. (i) SE Zone. In this region, closest to the Garlock fault, the P-axis orientation remains effectively unchanged with time and is scattered around 0-degree azimuth. This region unfortunately has too few focal mechanisms available to compute a reference NPTS estimate prior to the mainshock, so we cannot establish whether a stress rotation occurred here. (ii) Foreshock Zone. Here, there is no significant change in P-axis strike following the Mw 6.4 foreshock; however, following the mainshock, there is a transient 10-degree clockwise rotation in the P-axis strike that lasts one week. In the following time window, the P-axis strike recovers to the initial 0-degree azimuth and does not change significantly for the rest of the sequence. This behavior could suggest a rotation of the stress state due to the mainshock, and a recovery of the initial stress state due to very early postseismic deformation. (iii) Mainshock Zone. The P-axis strike prior to the mainshock is approximately 10 degrees and rotates counterclockwise to 0-degree azimuth. In the postseismic period, for a window that begins approximately one month after the mainshock, the P-axis strike is rotated another 10 degrees counterclockwise. This behavior would suggest a rotation of the stress state due to the mainshock and a further rotation due to postseismic deformation. (iv) NW Zone. does not show a significant change in P-axis strike, which is approximately 15 degrees, throughout the earthquake sequence.

In nearly all spatiotemporal windows, the P-axis plunge has a much larger uncertainty than the P-axis strike but is close to zero. The only exception is the centroid zone in the pre-mainshock period, which has a steeper plunge (31-51 degrees). Although zonation varies, when comparable, our results are largely consistent with focal mechanism results from previous studies. The large change in active fault orientation across the mainshock in the centroid zone is consistent with a rotation for a similar region in Cheng et al. (2023) and an inferred complete stress release from Sheng and Meng (2020) in a similar region from heterogeneous faulting behavior. The change in orientation immediately after the mainshock in the foreshock zone agrees with a clockwise rotation resolved in a similar region in Sheng and Meng (2020). Because the catalog in Sheng and Meng (2020) is abbreviated in time, this study does not resolve the subsequent recovery.

As shown in Figure 8.3, r_{CLVD} values for all spatiotemporal windows are negative. Negative r_{CLVD}, combined with a P-axis orientation with a low plunge, suggest a strike-slip dominated regime with a mix of normal faulting. This is in agreement with studies that evaluate the distribution of focal mechanisms for this sequence by faulting type (e.g., Hardebeck, 2020; Wang and Zhan, 2020). However, making more detailed observations of the evolution of r_{CLVD} with time is difficult. In the SE and Foreshock zones, r_{CLVD} is relatively stable over time, showing that the composition is not changing. However, in the centroid and NW zones, there is an increase in r_{CLVD} following the mainshock. This would suggest a reduction in the amount of normal faulting or an increase in the amount of reverse faulting in these zones following the mainshock. The latter explanation would support the suggestion made by (Sheng and Meng, 2020) of increased heterogeneity of faulting in this region and a nearly complete stress release. However, this observation could also be an artifact of computing pre- and post-mainshock r_{CLVD} values with different

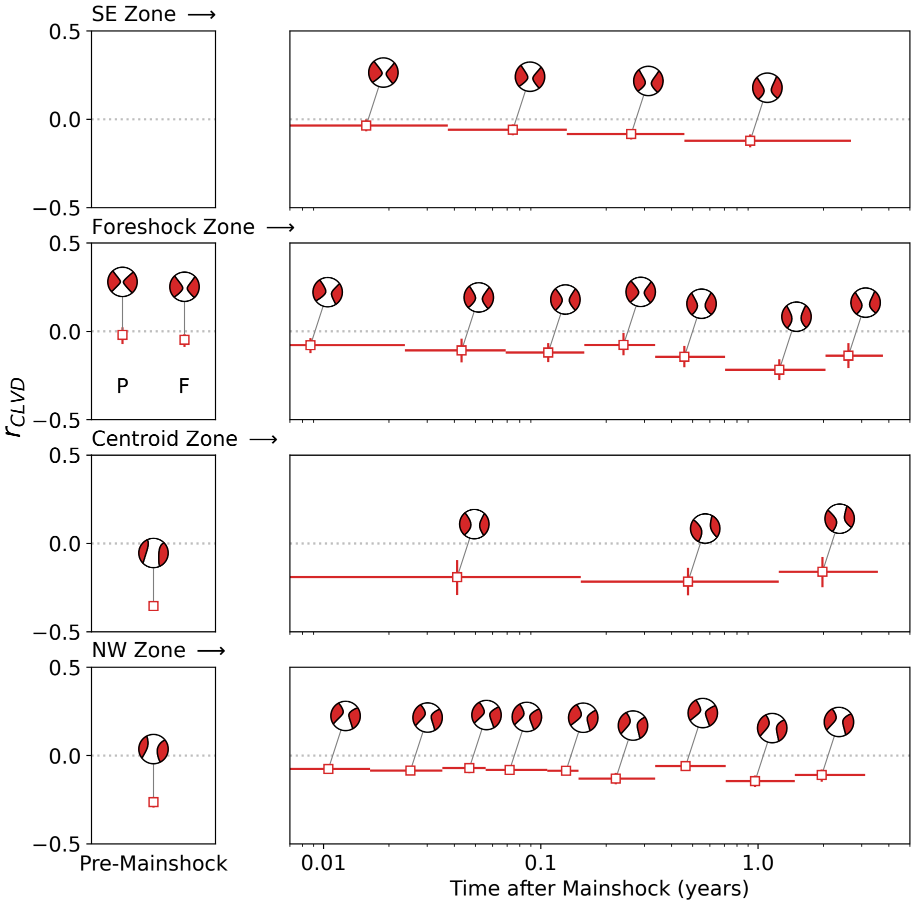

Figure 8.3: r_{CLVD} values and corresponding focal mechanism diagrams for the normalized summed potency tensor solutions for the spatial and temporal windows used in this study. The dotted line marks where r_{CLVD} is equal to zero. In the foreshock zone, the pre-mainshock bin has two windows, one prior to the M6.4 foreshock (labelled P) and one between the M6.4 foreshock and the M7.1 mainshock (labelled F).

catalogs. This could map into an apparent change in faulting heterogeneity across the mainshock due to different uncertainties between catalogs. As shown in Figure 8.S7, when computing r_{CLVD} using the Yang et al. (2012) catalog prior to and following the mainshock, these changes in r_{CLVD} largely disappear.

The second technique we employ is the Spatial and Temporal Stress Inversion (SATSI) algorithm to invert for the stress orientation and stress ratio (R) within spatiotemporal windows using focal mechanism solutions (Hardebeck and Michael, 2006; Martinez-Garzon et al., 2014). The stress ratio is defined as,

$$R = \frac{\sigma_2 - \sigma_1}{\sigma_3 - \sigma_1}, \tag{8.3}$$

where σ_1, σ_2, and σ_3 are the three principal stresses. This technique is routinely applied when quantifying stress evolution and we include it to contextualize the results of this study in the broader literature. This algorithm allows for the use of a damping term; to ensure comparability between methods used in this study, we set this term to zero. Nodal plane ambiguity is addressed by randomly picking one of the two nodal planes for each focal mechanism solution. The resultant error on each tensor is estimated via bootstrapping, with alternative fault selection for each bootstrapped sample. We choose the same sets of focal mechanisms for this inversion as used in the NPTS for comparability.

Hardebeck and Hauksson (2001) show that substantial focal mechanism diversity is necessary to recover the stress orientation using a stress inversion. They show that for a set of focal mechanisms with nodal plane ambiguity and 10-degree errors, if the mean RMS angular difference of the set of focal mechanism is at least 40 degrees, then an unbiased recovery of the stress orientation is possible. In our case, this focal mechanism diversity varies by region. These values are given in Table 8.S2. The RMS angular difference is at or above 40 degrees for the centroid zone, but in other regions lower values are common (generally, 25-40 degrees). Slightly lower values are acceptable in our case because the expected nodal plane uncertainty in our moment tensor catalog is usually much lower than 10 degrees. But even in the absence of error, low angular diversity will still generate biasing away from the true stress orientation and must be accounted for when interpreting these results. This is emblematic of the challenge involved when attempting to measure changes in the stress state at relatively granular scales near ruptures. Stress inversions also assume that each cell has a homogeneous stress field. The validity of this assumption can be evaluated by computing the average misfit between the predicted tangential traction and the observed slip direction ($\bar{\beta}$) (Michael, 1991). For a moderately varying stress field, the stress inversion will generally recover the average stress if $\bar{\beta} \leq 45°$. Values larger than this show too much variability to reliably recover the average stress. The $\bar{\beta}$ values for each inversion performed in this study fall below 45° and are shown in Table 8.S2.

We apply the SATSI inversion to the same sets of focal mechanisms to which we applied NPTS. We plot the evolution of the σ_1 trend and plunge on the same plot as the P-axis strike and plunge determined with NPTS in Figure 8.4. These values are also given in Table 8.S2. There are no significant differences between the σ_1 and P-axes orientations, as for each spatiotemporal window, the bootstrapped error bounds of these axes always overlap. Generally, the P-axis and σ_1 orientation should not be coincident, because aligning these two axes would suggest a dihedral angle of 90 degrees. However, the observed close alignment of these two quantities in our results is perhaps not surprising; it has been observed that near faults, in the absence of sufficient diversity, as is commonly found near recent ruptures, the resolved σ_1 axis converges to be coincident with the P-axis (Townend, 2004). We additionally report the stress ratio values in Table 8.S2, which generally fall between 0.1 and 0.5, but there is too much uncertainty to identify clear trends across the sequence.

8.4 Measuring Seismicity Anisotropy with Cylindrical K-Functions

We have evaluated fault orientations using some standard focal mechanism-based techniques to establish a baseline for what may be learned with only a focal mechanism catalog. We now apply an emergent technique that uses only hypocenter locations to learn new things about the evolution of fault orientation throughout the sequence. Hypocenter distributions are well known to exhibit linear and planar features in space (Rubin et al., 1999; Waldhauser and Ellsworth, 2000). Such geometrical features can be described quantitatively with a statistical framework called anisotropic point processes (e.g., Møller and Toftaker, 2014; Nasirzadeh et al., 2021). That is, we can characterize seismicity as a collection of points that are driven by a stochastic process and have directional inhomogeneity. We can then apply a tool developed to characterize anisotropic point processes to seismicity catalogs to understand their fundamental characteristics. The high density of events in the seismicity catalog produced in this study allows for the estimation of this anisotropy at high temporal resolution.

We evaluate the predominant modes of anisotropy in the seismicity catalogs using a measure of spatial correlation called the Cylindrical K-function. The K-function is a cumulative function that measures the average number of points around each point within a sphere of variable radius (Ripley, 1976). That is, for each point in a volume, a K-function counts the number of neighboring points. To detect anisotropic spatial patterns, a variant of the K-function, called the Cylindrical K-function, was proposed that instead uses neighborhoods of cylindrical shape (Møller et al., 2016). The motivation for using a cylinder is that the function may be evaluated at many orientations of the cylinder to measure anisotropy of seismicity. We care about the anisotropy of seismicity because the direction of anisotropy is expectedly coincident with the orientation of active faults.

For a unit vector $n = [cos\varphi sin\theta, sin\varphi cos\theta, cos\theta]$, defining the orientation of a cylinder centered at the position of a point x_i, $C_n(x_i)$, with radius r and height 2t, the cylindrical K-function is defined as,

$$K_{cyl}(r, t, \theta, \varphi) = \frac{1}{\gamma} \sum_{i}^{m} \sum_{j \neq i}^{m} \mathbf{1}\{x_j \in C_n(x_i)\} e_{ij}, \tag{8.4}$$

where m is the number of points in the volume, γ is a normalization factor, and e_{ij} is a translation-based edge correction factor. In words, we parameterize a cylinder with a size and orientation and center it around each point in a volume. We then count the number of points that fall within the cylinder.

Ross (2024) showed that K_{cyl} could detect the orientations (strike and dip) of planar fabrics in fault zones in southern California, even if the fault zone was distributed over kilometers. Here we also use this method to quantify the distribution of fault orientations present in the Ridgecrest region. We compute K_{cyl} for many orientations defined by θ and φ. For a scale defined by r and t (1.0 and 0.1 in this study), the predominant fault strike and dip modes may be inferred from the θ and φ values that maximize K_{cyl}.

The error is estimated by bootstrapping over the contributing events and computing the fault normal vector with the largest value of K_{cyl} for each bootstrapped sample. We compute K_{cyl} for a full sweep of strikes and dips over several time intervals within each spatial window defined over our seismicity catalogs. The seismicity rate is not the same within each zone, and we set the temporal resolution to be dependent on the seismicity rate. So, different zones have different numbers of temporal samples. We find that 5,000 hypocenters allow for reliable recovery of clear modes in K_{cyl}. We thus compute K_{cyl} over disjoint time intervals that include 5,000 events, again with some exceptions made for constrained time intervals such as before the mainshock, during the foreshock sequence, and near the end of the aftershock sequence.

We compute cylindrical K-functions using the seismicity catalog produced in this study for the four spatial windows, alongside that of the entire region (Figure 8.4). These diagrams show clear modes in the distribution of fault orientations for these regions. For example, in the full catalog, there are two modes that correspond to

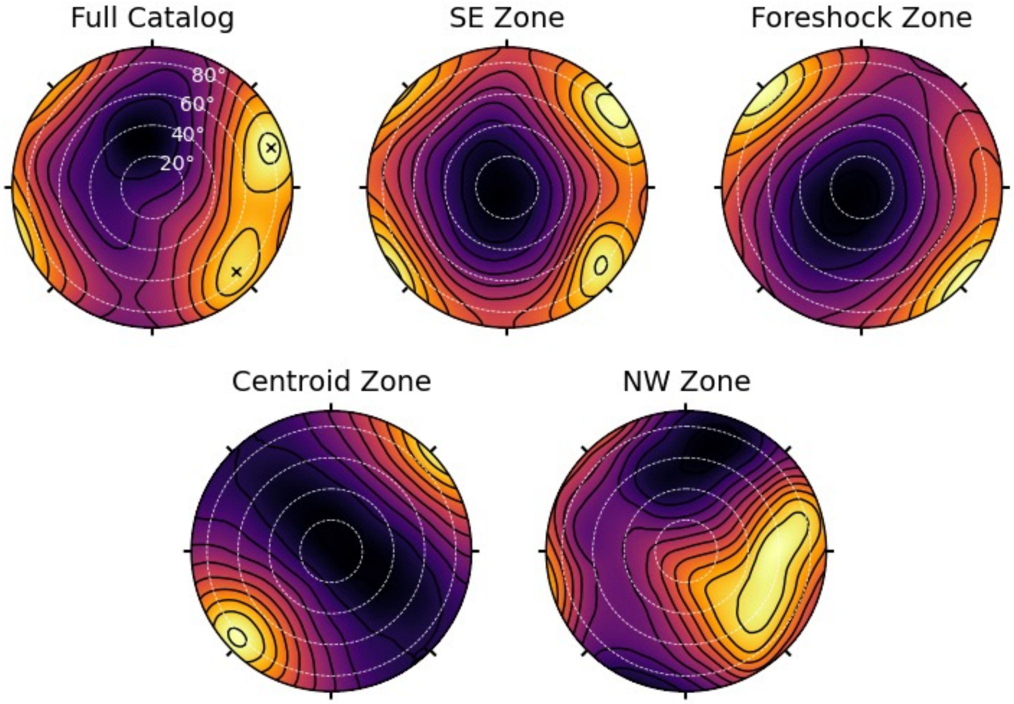

Figure 8.4: K_{cyl} values for sweeps of dip direction (φ) and dip (θ) for the time-integrated seismicity for the regions defined in and the catalog produced in this study. The azimuth and the distance from the center define the dip direction and dip, respectively. Locations of the crosses in the full catalog plot correspond to the picked modes of anisotropy used to define the dihedral angle used for comparison in this study.

planar fabric in the seismicity that dip 80 degrees to the northeast and southeast. This fabric corresponds to the alignment of seismicity on faults in the dataset and captures the strikes and dips of the active faults. The K_{cyl} plots quantify what is qualitatively observable from visual inspection of the seismicity in Figure 8.1; there are clear and distinct lineations in the seismicity corresponding to conjugate faults striking to the northwest and northeast. Once quantified, we can objectively evaluate how the distributions of active fault orientations as defined by seismicity relate to each other and vary with space and time.

The K_{cyl} plot for the SE zone also shows conjugate fault orientations with one orientation dipping approximately 85 degrees to the northeast and another dipping 80 degrees to the southeast. The foreshock zone is dominated by a single mode of fault orientations dipping nearly 90 degrees to either the northwest or southeast, as the dip direction is nonunique for a vertically dipping fault. The centroid zone shows a clear mode dipping 80 degrees to the southwest. Finally, the NW zone shows a smeared mode that suggests a dip of 60 degrees in directions ranging from due east to the southeast. This smearing of the mode suggests the overprinting of planar fabrics in the seismicity with a diversity of strikes and no predominant azimuth.

The conjugate faulting observed in the K_{cyl} plots for the full catalog and the catalog in the SE region allow for the computation of a dihedral angle between fault modes. The dihedral angle between conjugate faults is an important control on the coefficient of friction of the faulting rock. Measurements of the full catalog suggest a dihedral angle of 62.5 degrees, whereas the conjugate faulting in the SE zone suggests a larger dihedral angle of 77 degrees. These angles are consistent with the results of Fialko (2021), and assuming these active faults are young fractures, suggest average coefficients of friction either slightly or well below 0.6.

The distributions of fault orientations measured over narrow temporal windows are shown in Figure 8.5. These plots show a detailed view of how the modes of fault orientations evolve with time. Note that the pre-mainshock K_{cyl} values are computed using the Hauksson et al. (2012) catalog events prior to the initiation of the Ridgecrest sequence. In the SE zone, we see that the conjugate modes are not contemporaneous; at first the northwest dipping mode is predominant, followed by the southeast dipping mode, and ultimately the northwest dipping mode again becomes predominant. However, as illustrated in Movie 8.S1, this behavior notably results from spatial inhomogeneity in the active sections of the SE zone. As shown in seismicity plot in Figure 8.1, the SE zone has a region with northeast striking seismicity and another region with southwest striking seismicity. Active sequences in these portions of the zone will produce time intervals with distinct predominant modes. This spatial inhomogeneity is difficult to distinguish with only focal mechanisms and demonstrates some of the value added from K_{cyl}.

The progression of K_{cyl} in the foreshock zone in Figure 8.5 shows that a single mode of seismicity is predominant throughout the aftershock sequence. However, the foreshock sequence shows two modes of similar amplitude that are subparallel. These modes are too close to be conjugate modes, and their contemporaneous activation may be the result from a diversity of fault orientations being favorable in the stress regime, but with another controlling factor, such as crustal anisotropy, dictating that these two narrow, subparallel modes are dominant. The centroid zone in Figure 8.5 shows the southwest dipping mode is dominant throughout the entire

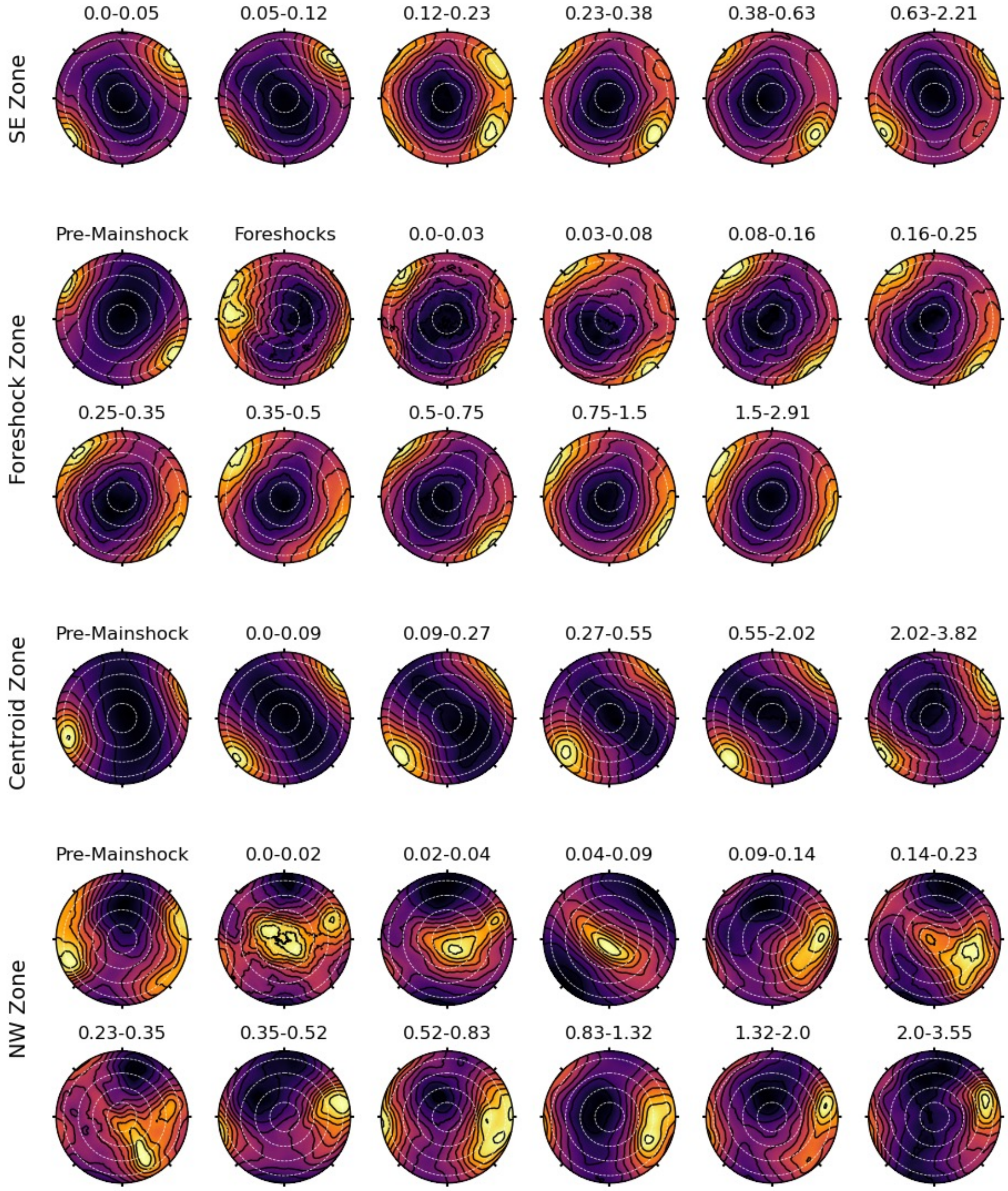

Figure 8.5: K_{cyl} plots, like those defined in Figure 8.2, for narrower temporal windows within each region. Pre-mainshock plots were made using hypocenter locations from the Hauksson et al. (2012) catalog. The time ranges correspond to the time of the first and last earthquake used for each K_{cyl} in years after the mainshock. The azimuth and the distance from the center define the dip direction and dip, respectively. White dotted lines denote dip values defined in Figure 8.4.

sequence in this region. The progression of the NW zone in Figure 8.5 shows that the smeared mode in Figure 8.4 is the result of a highly complicated superposition of modes that strongly vary temporally.

We can furthermore track the evolution of the mode with the highest amplitude with time (Figure 8.2). In the SE zone, which lacked sufficient seismicity to establish a pre-mainshock value, the dip direction of the predominant mode persists around 55 degrees and does not show significant changes in the postseismic period. The foreshock zone shows substantial changes; there is no discernible change immediately following the Mw 6.4 foreshock, but there is a large clockwise movement (10 degrees) of the dominant mode following the mainshock that recovers over the following year. This would suggest a sharp perturbation of the stress state due to the mainshock slip, but a reloading of the stress on the fault due to postseismic deformation. The centroid zone exhibits a sharp counterclockwise movement (20 degrees) of the predominant mode following the mainshock, and there is little change in the distribution of fault orientations in this zone in the postseismic period. This would suggest a large rotation of the stress orientation due to the rupture and a low contribution of postseismic deformation to the stress state in the years following the event. The northwest zone exhibits highly heterogeneous faulting behavior, with abundant high angle and low angle faults and diverse strikes. This heterogeneity highlights a limitation of this methodology for tracking the evolution of fault orientation distributions. The cylindrical K-function produces a result with higher dimensionality than those of the focal mechanism techniques. This is powerful because modes of active fault fabric may be uniquely identified and tracked, but it also means that there need to be persistent predominant modes of faulting in the data. Techniques that sum or invert for a single representative orientation, such as focal mechanism techniques described in this study, are better suited for regions where these modes do not exist.

8.5 Comparison of Results and Discussion

Here we attempt to more systematically compare the results between the various methods used in this study. Direct comparisons of these quantities are complicated by the fact that the methods are not measuring identical information. The cylindrical K-function provides orientations of small-scale planar fabric in seismicity. For a strike-slip stress regime, reactivation is favored for faults at a particular angle to the principal stress axis that is controlled by the coefficient of friction (Fialko, 2021; Sibson, 1985). For the case where the fault orientations are indeed a direct reflection of the stress state, the principal stress axis can be obtained from the sum of the fault strike angle and half the dihedral angle. As shown previously, the pervasive conjugate faulting in the Ridgecrest sequence allows us to measure the average dihedral angle of the conjugate faults by computing the angle between the two dominant faulting modes in the cylindrical K-function. Note that this comparison of fault orientations with stress orientations through time requires the assumption of a constant dihedral angle. This is a reasonable assumption for this case, as we are mostly concerned with seismicity clusters of small events on a diversity of faults, rather than faults that may be subject to weakening from continued displacement (Collettini et al., 2019) or faults that are transiently weakened during a large slip event (e.g., Thomas et al., 2014). We thus use the measured dihedral angle to directly compare the dip direction estimates to those of the stress axis orientation made using focal mechanisms. We use the measured dihedral angle between conjugate modes for the full catalog to make this comparison in the foreshock zone, centroid zone, and NW zone, and we use the dihedral angle measured between conjugate modes from only the SE zone to make the comparison in the SE zone.

Based on the aforementioned assumptions we can compare the results from the cylindrical K-functions to those from the focal mechanism-based techniques. Here we focus on the different axes in Figure 8.2, which are directly comparable. The bounds for the dip direction axes are the same as the bounds used for the focal mechanism results, however they are translated according to the dihedral angle. There is some agreement in trends between the K_{cyl} results and the focal mechanism results. In the SE zone, the absolute values from all methods are in close agreement and no methods resolve a significant change in stress orientation during the postseismic period. In the foreshock zone, all methods agree on the stress orientation during the period before the Ridgecrest sequence and during the foreshock sequence. All methods also resolve a clockwise rotation in the stress orientation immediately following the mainshock and there is some recovery postseismically. In the centroid zone, all methods again agree on the pre-mainshock stress orientation and resolve a rotation, albeit with different amplitudes, following the mainshock. The pre-mainshock stress orientation values also agree for all methods in the NW zone. For all regions, for values included in Figure 8.2, fault dips from the K_{cyl} results are very high angle, which agrees with the near 0-degree P-axis and σ_1 plunges from the focal mechanism methods. In general, the uncertainties in the P-axis and σ_1 plunges are much higher than those of the trends.

While there are many similarities between the results of these methods, there are key differences that speak to the potential strengths of using K_{cyl} to augment standard techniques. In the foreshock zone, the orientations of active faults following the initial change due to the mainshock are markedly different between methods. In particular, the K_{cyl} distributions suggest a larger change (in degrees) following the mainshock, which gradually recovers to pre-mainshock values over the course of approximately one year. This behavior contrasts sharply with the results from the focal mechanism methods, which suggest that the initial change in the average fault orientation was immediately erased little over a week following the mainshock. In the centroid zone, the amplitude of the initial change in measured fault orientation is much larger when measured using K_{cyl} than when measured using the focal mechanism methods. The K_{cyl} orientation does not change significantly in the postseismic period, and the orientations measured using the focal mechanisms eventually match the amplitude of the change immediately following the mainshock measured by K_{cyl}, postseismically.

We first address the question: what do these different results mean? In the foreshock zone, the cylindrical K-function estimates suggest changes in the fault orientations recover within a year and the focal mechanism estimates suggest changes in orientation that recover in approximately one week. Some studies suggest recovery of the stress orientation is related to reloading due to postseismic deformation (e.g., Hardebeck, 2012; Wilding and Ross, 2022). For this earthquake, afterslip is expectedly the dominant contributor to postseismic deformation immediately following the mainshock, but later becomes negligible relative to viscoelastic relaxation (Pollitz et al., 2022). The dominant mechanism of reloading may then depend on which measure of fault orientation evolution we expect more reliably captures the state of stress. The duration of the recovery observed from the K_{cyl} result would suggest that both afterslip and viscoelastic relaxation could contribute to reloading, while the duration of recovery observed from the focal mechanism results would suggest that the primary mechanism is afterslip. Further, estimates of postseismic deformation for this earthquake are generally largest within the centroid zone (He et al., 2022; Pollitz et al., 2022; Wang et al., 2020; Yue et al., 2021). However, the cylindrical K-functions show little to no recovery in the centroid zone, and instead the recovery is confined to the south. The focal mechanism results show an accentuation of the change in orientation in the centroid zone during the postseismic period. Thus the K_{cyl} results only show a postseismic response that is remote from the zone with the most postseismic deformation, whereas the focal mechanism results show a postseismic response that is collocated with the zone of maximum postseismic deformation.

The amplitude of the change in strike of the fault orientation for the K_{cyl} results is also larger than estimates from the focal mechanism results in both the foreshock zone and the centroid zone. Assuming these changes are reliable measures of the rotation in the stress orientation, the differences in the change in orientation across the mainshock map into different estimates of the ratio between the stress drop and the absolute differential stress. As shown in Figure 8.6, relating the pre-mainshock stress to the stress rotation after Hardebeck and Hauksson (2001) and assuming fault orientations (Milliner and Donnellan, 2020), we find that from the measurements in the foreshock zone and the centroid zone made using the hypocenter measurements, which yield a much tighter constraint on this value, suggest the ratio between stress drop and maximum shear stress is likely between 0.6 and 0.9 in the foreshock zone and between 0.8 and 0.9 in centroid zone. The expected errors for the focal mechanism methods are much larger, ranging between 0.2 and 1.0 for the foreshock zone and 0.6 and 1.0 for the centroid zone. The uncertainties for the focal mechanisms are too large to say these values are significantly different from those of the K_{cyl} results. However, the distribution of bootstrapped samples from the focal mechanism solutions are shifted towards smaller values that those of the K_{cyl} solutions. This is particularly true when considering the σ_1 orientations from the stress inversion, which expectedly approximate the stress orientation prior to the mainshock better than the P-axis from NPTS. In this sense, it is probabilistically favored that these ratios are larger for the K_{cyl} results. This is important, because larger ratios for the same zone and slip would suggest lower values of background pre-mainshock shear stress. Thus, the K_{cyl} results may suggest that absolute differential stress could be overestimated by focal mechanism measurements.

We next address the question: which of these measurements is correct? The short answer is that these methods are likely all correct but measure different things. However, the K_{cyl} measurement technique offers several advantages over the focal mechanism methods. One major objective of this study is to introduce and demonstrate a method for investigating the temporal change in seismicity that avoids several of the biases that are inherent to focal mechanism-based techniques. The K_{cyl} results are most sensitive to the dominant mode of fault orientation, while the focal mechanism techniques are most sensitive to the average. If fault orientations in the volume are not randomly distributed around the primary mode, but rather biased in one direction or another, the focal mechanisms may yield fault behavior that is distinct. For example, consider the toy case of a regime with two modes of faulting, one that is approximately aligned with the foreshock mode resolved in this study,

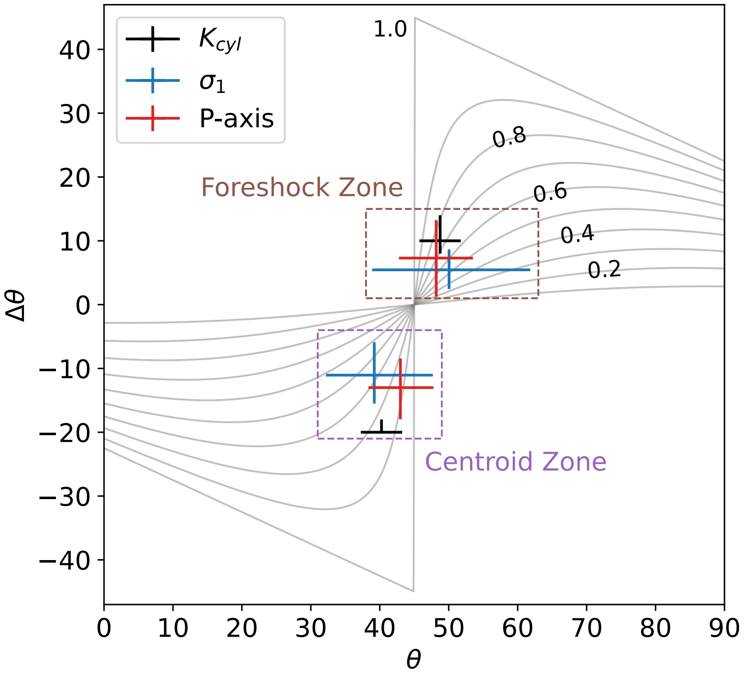

Figure 8.6: Comparison of difference between pre-mainshock stress axis and mainshock fault strike (θ) and the stress rotation ($\Delta\theta$) computed using the methods and assumptions necessary for transformation to stress used in this study. Gray contours correspond to different ratios between the stress drop and the deviatoric stress from the relationship defined by Hardebeck and Hauksson (2001). Purple and brown dashed boxes correspond to values drawn from the centroid and foreshock regions, respectively.

and the other rotated 30 degrees counterclockwise. As illustrated by the measured subparallel faulting during the foreshock sequence, this scenario is plausible for the foreshock zone. If we generate focal mechanisms that sample both modes of faulting, the NPTS of these focal mechanisms produces an average focal mechanism that is somewhere between the primary mode of faulting and the secondary mode, depending on the proportion of focal mechanisms that sample each fault orientation mode. This example is illustrated in Figure 8.7. This example uses NPTS for simplicity; however, the correlation between NPTS and the stress inversion results shown in this study suggest that the stress inversion results may be sensitive to the same effect. It is plausible that some of the differences between the K_{cyl} results and focal mechanism-based results is the product of this biasing.

Also note that even when the proportion of perfectly aligned focal mechanisms is 100%, there is still an offset between the true σ_1 direction and the P-axis; this is

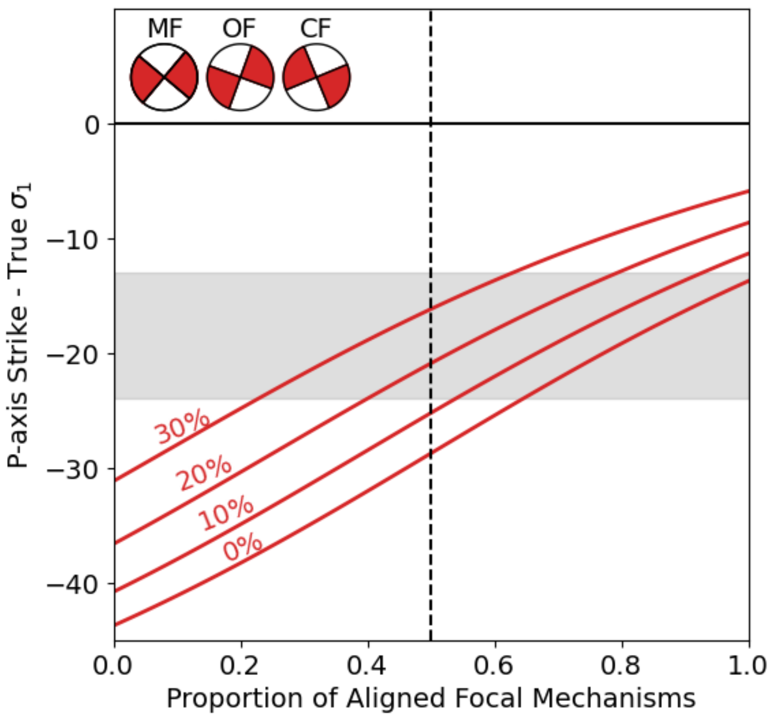

Figure 8.7: Synthetic test for possible biases in P-axis strike due to assumptions of fault alignment. Figure shows deviation of P-axis strike from the true maximum horizontal stress direction for variable proportion of misaligned faults (from the σ_1 axis). Focal mechanisms correspond to the source mechanism aligned with the stress field (labelled MF), misaligned from the stress field by a 30 degree counterclockwise rotation (labelled OF), and source mechanism aligned with the stress field but rupturing a conjugate fault (labelled CF). The x-axis refers to the relative proportion of MF and OF (with 1.0 being entirely MF sources). Different lines correspond to different proportions of the summed mechanisms that are of the CF class. The vertical black dotted line indicates the point at which there is an equal mix between OF and MF sources. The horizontal black line marks the point at which there is no difference between the P-axis strike and the true principal stress axis. The gray rectangle indicates the range possible differences between the P-axis strike and the dip direction in the foreshock zone at a point where the two values diverge substantially (0.05 years after the mainshock).

because the P-axis is only coincident with the maximum stress when the dihedral angle is 90 degrees. Relatedly, in this test, a higher proportion of rupturing conjugate faults that are aligned with the stress field brings the P-axis in closer alignment with the true stress regime. As shown in Figure 8.2, immediately after the mainshock, the K_{cyl} and NPTS results are nearly in agreement, both in terms of absolute value and change relative to the preceding time interval. The time window following the mainshock in this region also corresponds to the time at which the conjugate mode is most prominent in the K_{cyl} plot in Figure 8.4. This temporary increase in faulting along the conjugate mode during this time interval may in part explain the transient agreement between these two methods. In Figure 8.7, we also plot a range of possible differences, given uncertainty, between the dip direction and the P-axis strike that are observed when these two values diverge during the postseismic period in the foreshock zone. As shown in Figure 8.7, these differences can be reasonably explained by these described biases of the NPTS P-axis.

As evidenced by this comparison, the methods described in this study are complementary. Indeed, the K_{cyl} results in the northwest zone make clear that cylindrical K-functions will not always be able to stably resolve a clear progression of fault orientations through time, particularly in regimes without clearly dominant fault orientation modes. In contrast, the focal mechanism methods resolve a clear and stable orientation for the northwest zone. However, the cylindrical K-functions provide measurements of fault orientations that are easily interpretable and have higher dimensionality. This allows for uniquely identifying and tracking specific modes of fault orientations, which is impossible when only using the focal mechanism techniques described and applied in this study. That we can identify these modes means that arbitrary regionalization of the catalog will not hide phenomena that may otherwise be negated or obscured in an average. That these modes are identifiable also means that the effect of nodal plane ambiguity, and the associated biases from increasing or decreasing the relative proportion of conjugate fault ruptures, is vastly reduced. The minimization of these biases allows us to obtain a more accurate representation of how the distribution of active faults is changing.

In this paper we primarily discuss differences in the trend of the stress orientation among the different methodologies, because the plunge values usually have high uncertainties and are scattered near zero. However, there is one exception; the P-axis and σ_1 plunges for the pre-mainshock focal mechanism results in the centroid zone are steep. This would suggest some amount of non-strike-slip faulting is biasing the focal mechanism results. Interestingly, no lower-angle dipping modes are observable in the cylindrical K-functions; suggesting the seismicity does not support the existence of abundant normal faulting. One explanation for this could be that these high plunges are artifacts of inaccurate focal mechanisms in the pre-mainshock catalog in this region. This explanation is supported by the fact that in the centroid zone, for the aftershock sequence, the r_{CLVD} values from our focal mechanism catalog (Figure 8.3) are much less negative than those of the Yang et al. (2013) catalog for the overlapping time period (Figure 8.S6). Recalling that negative r_{CLVD} in this case suggests added non-strike-slip faulting, this would suggest that the Yang et al. (2013) catalog produces apparent source mechanism diversity, at least in the centroid zone, that is not supported by our high precision moment tensor catalog.

Relatedly, some assumptions are made regarding the catalogs that need to be discussed. The first is that the differences observed across the mainshock are due to physical effects rather than a change of catalogs. The Hauksson et al. (2012) and Yang et al. (2012) catalogs extend beyond the mainshock, and we can perform these same analyses using only these catalogs to see if these results, which are lower precision and duration, are consistent with the results found using multiple catalogs. We plot these results in Figure 8.S5 and find that the results are indeed consistent. These also illustrate the value added by building a new seismicity and moment tensor catalog. The added event density and moment tensor precision allow us to investigate the stress with vastly improved precision and confidence. Additionally, the pre-mainshock date range used in this catalog is very long (1981-2019). We use an extensive time window to ensure there is enough measured seismicity to stably measure K_{cyl}. Of particular concern is the centroid zone, which exhibited elevated seismicity during a 1995 earthquake sequence (Hauksson et al., 1995). If this sequence is not representative of the pre-mainshock stress, then our results will be biased. To address this problem, we also compute the pre-mainshock values using only seismicity from 2000 onwards. We find that the results, though noisier than the results obtained using all the data, produce similar pre-mainshock stress orientation estimates using both the hypocenter location and focal mechanism estimates (Figure 8.S7). This still requires the assumption that the stress is approximately constant between the year 2000 and the mainshock but suggests a reasonably stable stress regime in the decades before the mainshock.

8.6 Conclusions

We present a new, state-of-the-art seismicity and moment tensor catalog that captures the entire 2019 Ridgecrest earthquake sequence. We use these catalogs to infer faulting evolution over narrow spatiotemporal windows using complementary techniques that measure faulting with hypocenter locations and focal mechanisms. We find that measuring faulting using hypocenter locations can yield unique insights into transient phenomena caused by earthquakes. All techniques in this study resolve a change of fault orientations near the maximum slip of the mainshock, but the hypocenter technique resolves a much larger rotation near the centroid and uniquely resolves a large and persistent rotation to the south of the centroid that recovered over the following year. These hypocenter-based observations provide key constraints on the absolute differential stress in the crust and insights into how postseismic deformation is related to reloading. The results in this study highlight several advantages for using seismicity distributions to measure fault orientations in addition to focal mechanisms. This study has important implications both for how we measure changes in fault activation and by extension the evolution of stress during an earthquake sequence.

Supplementary Materials

Table 8.S1: Certain parameters and results from the normalized potency tensor summation for the spatiotemporal windows for the spatiotemporal windows of focal mechanisms described in this study.

Zone	Time Index	# of focal mech.	Median P-axis Strike (°) [5th-95th pct.]	Median P-axis Plunge (°) [5th-95th pct.]	Median r_{CLVD} [5th-95th pct.]
SE	1	150	4.4 [2.2 - 6.5]	-5.5 [-8.2 - -3.1]	-0.04 [-0.07 - -0.0]
	2	150	5.3 [2.8 - 7.5]	-6.9 [-10.0 - -4.1]	-0.06 [-0.09 - -0.03]
	3	150	3.6 [0.9 - 6.0]	-11.9 [-15.6 - -8.4]	-0.09 [-0.11 - -0.06]
	4	150	-2.8 [-5.6 - 0.1]	-16.4 [-22.0 - -12.3]	-0.12 [-0.16 - -0.09]
Foreshock	Pre-Sequence	96	3.2 [1.0 - 5.4]	-0.5 [-3.5 - 2.7]	-0.02 [-0.08 - 0.03]
	Foreshocks	120	1.8 [-1.2 - 5.1]	-8.4 [-12.3 - -4.7]	-0.05 [-0.08 - -0.01]
	1	150	10.3 [7.9 - 13.2]	-1.3 [-5.5 - 2.5]	-0.08 [-0.12 - -0.03]
	2	150	3.5 [-0.7 - 7.5]	-6.5 [-13.1 - 1.1]	-0.11 [-0.18 - -0.04]
	3	150	0.1 [-3.1 - 3.5]	-4.2 [-9.9 - 1.2]	-0.12 [-0.17 - -0.06]
	4	150	2.2 [-0.8 - 5.4]	-3.8 [-8.8 - 0.7]	-0.07 [-0.14 - -0.01]
	5	150	-1.2 [-4.9 - 2.7]	-12.0 [-19.3 - -4.8]	-0.14 [-0.19 - -0.08]
	6	150	-1.5 [-4.9 - 2.1]	-11.4 [-19.9 - -2.8]	-0.22 [-0.28 - -0.16]
	7	94	-3.4 [-8.0 - 1.9]	-14.8 [-22.6 - -6.2]	-0.14 [-0.2 - -0.07]
Centroid	Pre-Sequence	733	14.9 [13.1 - 17.0]	43.6 [37.3 - 51.6]	-0.35 [-0.38 - -0.33]
	1	150	1.8 [-3.4 - 7.0]	-5.8 [-14.0 - 4.1]	-0.19 [-0.29 - -0.1]
	2	150	-12.4 [-17.1 - -8.3]	-4.5 [-14.0 - 6.0]	-0.22 [-0.3 - -0.14]
	3	68	-11.8 [-17.0 - -6.6]	-9.3 [-19.8 - -0.7]	-0.16 [-0.25 - -0.06]
NW	Pre-Sequence	446	13.3 [11.5 - 15.0]	10.3 [5.7 - 14.9]	-0.26 [-0.29 - -0.23]
	1	150	13.2 [11.4 - 15.1]	17.4 [14.6 - 20.1]	-0.04 [-0.06 - -0.02]
	2	150	14.0 [11.9 - 15.9]	14.8 [11.4 - 18.3]	-0.08 [-0.1 - -0.05]
	3	150	13.2 [11.4 - 15.1]	14.8 [10.4 - 18.5]	-0.08 [-0.11 - -0.06]
	4	150	13.3 [11.4 - 15.2]	11.0 [7.8 - 14.1]	-0.07 [-0.1 - -0.05]
	5	150	14.3 [12.3 - 16.0]	9.2 [5.4 - 13.0]	-0.08 [-0.11 - -0.06]
	6	150	15.5 [13.7 - 17.2]	9.2 [5.8 - 12.3]	-0.09 [-0.11 - -0.06]
	7	150	13.3 [11.1 - 15.5]	15.2 [11.5 - 19.1]	-0.13 [-0.17 - -0.1]
	8	150	15.9 [13.9 - 17.9]	8.3 [4.6 - 11.7]	-0.06 [-0.09 - -0.03]
	9	150	14.9 [12.8 - 16.6]	15.5 [10.2 - 20.8]	-0.14 [-0.17 - -0.11]
	10	150	14.5 [12.8 - 16.5]	14.4 [10.9 - 18.0]	-0.11 [-0.15 - -0.08]

Table 8.S2: Certain parameters and results for the SATSI inversion for the spatiotemporal windows of focal mechanisms described in this study.

Zone	Time Index	# of focal mech.	Median σ_1 Strike (°) [5th - 95th pct.]	Median σ_1 Plunge (°) [5th - 95th pct.]	RMS Angular Difference	Average Misfit $\bar{\beta}$ (°)	Stress Ratio R [5th-95th pct.]
SE	1	150	4.0 [0.9 - 7.3]	-3.9 [-7.4 - -0.6]	26.5	15.6	[0.29-0.57]
	2	150	1.6 [-1.6 - 5.0]	-6.8 [-15.1 - -1.6]	27.3	15.3	[0.14-0.42]
	3	150	2.0 [-2.1 - 5.9]	-13.2 [-21.7 - -7.7]	28.8	16.5	[0.16-0.33]
	4	150	-3.3 [-7.1 - 1.0]	-18.3 [-28.4 - -10.2]	32.5	18.2	[0.14-0.32]
Foreshock	Pre-Sequence	96	5.0 [-3.1 - 13.8]	6.6 [-19.5 - 55.4]	26.0	18.7	[0.1-0.59]
	Foreshocks	120	2.3 [-1.4 - 6.1]	-9.4 [-16.4 - -3.2]	29.6	19.5	[0.2-0.43]
	1	150	10.5 [7.5 - 13.7]	-5.6 [-11.1 - -0.7]	32.5	21.9	[0.27-0.45]
	2	150	3.1 [0.4 - 5.8]	-6.7 [-13.3 - -1.3]	36.7	27.1	[0.28-0.48]
	3	150	-0.2 [-3.6 - 3.2]	-4.3 [-11.4 - 2.2]	34.4	24.3	[0.23-0.43]
	4	150	4.5 [1.1 - 7.5]	-5.9 [-11.3 - -1.3]	36.3	24.9	[0.3-0.51]
	5	150	1.4 [-2.0 - 4.8]	-6.0 [-12.7 - 0.8]	37.8	30.3	[0.26-0.46]
	6	150	-0.5 [-4.0 - 3.5]	-4.3 [-14.4 - 5.3]	39.6	29.6	[0.18-0.36]
	7	94	-0.3 [-4.6 - 4.4]	-8.9 [-17.6 - -0.3]	36.7	28.6	[0.21-0.48]
Centroid	Pre-Sequence	733	11.2 [7.2 - 16.7]	52.0 [33.1 - 71.4]	45.8	17.1	[0.05-0.2]
	1	150	0.1 [-4.3 - 5.3]	-2.4 [-17.3 - 11.9]	44.0	39.2	[0.13-0.41]
	2	150	-15.0 [-18.9 - -10.1]	1.2 [-11.5 - 10.5]	44.9	34.5	[0.14-0.35]
	3	68	-12.3 [-18.1 - -6.9]	-6.7 [-21.1 - 6.4]	39.6	25.7	[0.12-0.42]
NW	Pre-Sequence	446	9.8 [5.0 - 12.8]	-17.4 [-49.2 - 14.1]	41.6	13.6	[0.03-0.16]
	1	150	11.9 [9.7 - 14.5]	16.8 [12.9 - 20.8]	22.6	11.3	[0.26-0.4]
	2	150	12.9 [10.7 - 15.3]	12.4 [8.0 - 17.7]	26.1	12.0	[0.23-0.39]
	3	150	13.5 [10.6 - 16.4]	10.1 [3.2 - 17.2]	28.3	17.1	[0.2-0.34]
	4	150	11.2 [8.0 - 14.4]	4.1 [-2.0 - 9.6]	26.6	14.5	[0.2-0.35]
	5	150	14.6 [12.4 - 17.0]	2.6 [-4.9 - 8.8]	27.5	14.9	[0.18-0.35]
	6	150	13.3 [10.8 - 15.7]	10.9 [1.9 - 21.7]	26.6	11.9	[0.1-0.25]
	7	150	10.3 [8.0 - 12.8]	17.2 [10.8 - 25.4]	31.3	13.3	[0.14-0.28]
	8	150	19.0 [15.5 - 22.1]	6.2 [1.1 - 11.7]	28.6	17.4	[0.23-0.4]
	9	150	15.6 [12.9 - 18.2]	13.8 [4.4 - 25.6]	32.8	15.2	[0.13-0.28]
	10	150	13.2 [10.4 - 16.2]	12.1 [6.3 - 19.9]	31.1	14.0	[0.15-0.3]

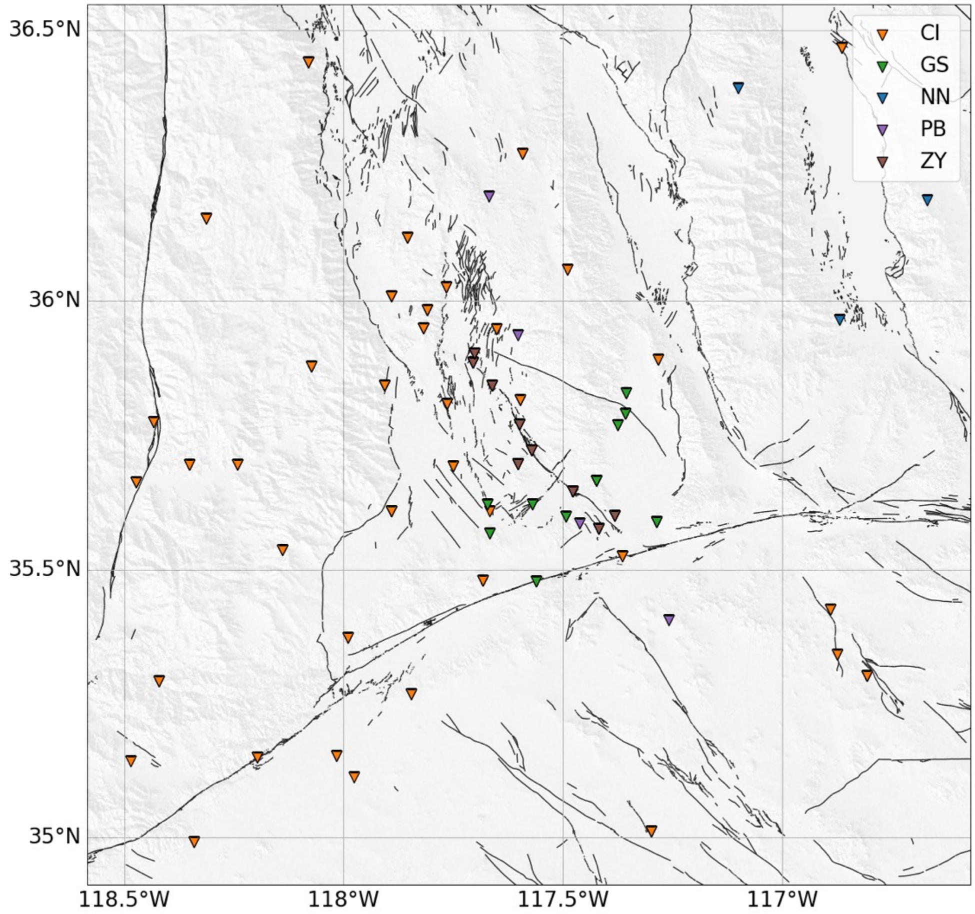

Figure 8.S1: The station distribution used for catalog creation in this study. Colors indicate the network code of the corresponding station.

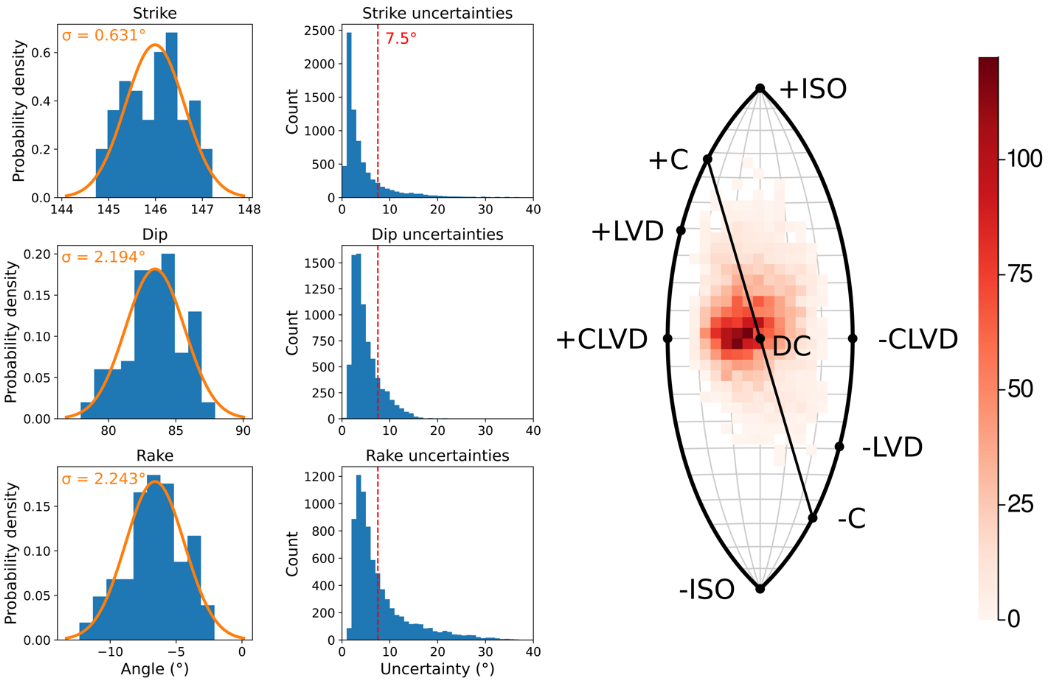

Figure 8.S2: Evaluation of moment tensor uncertainties and non-double-couple components. Left column: an example extraction of strike, dip, and rake uncertainties from the posterior distribution of a single moment tensor. The posterior is shown in blue and the fitted Gaussian distribution is shown in orange. Middle column: distribution of strike, dip, and rake uncertainties for all 7,645 moment tensor solutions. We use a maximum threshold of 7.5° to identify well-constrained solutions. Right column: 2D histogram on the lune plot showing the results of moment tensor decompositions for all 4,892 well-constrained solutions.

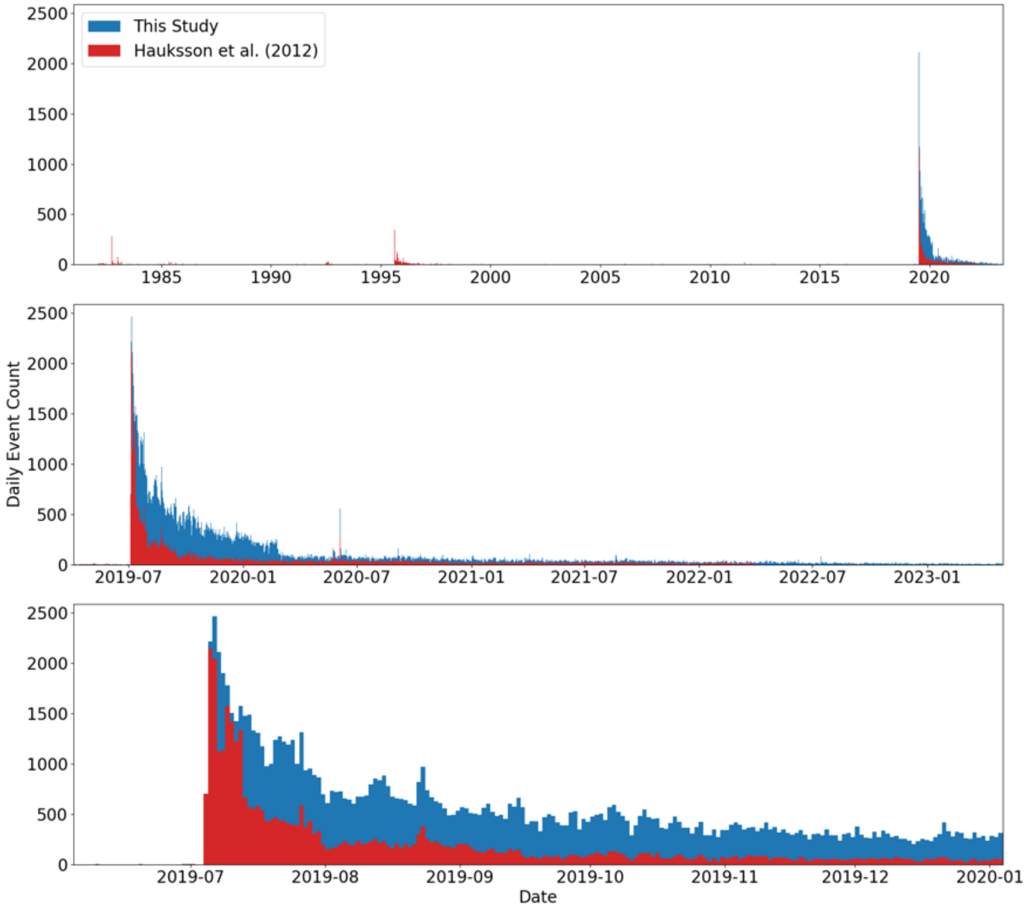

Figure 8.S3: Number of earthquakes per day for the duration of the catalog produced in this study (blue) and that of Hauksson et al. (2012) (red).

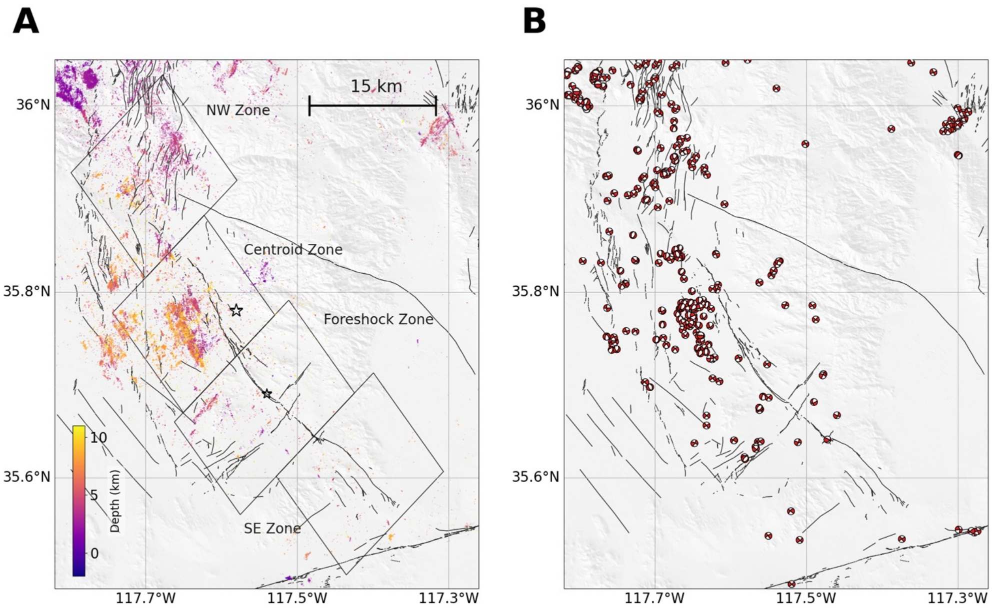

Figure 8.S4: Plot of all the seismicity (A) and focal mechanisms (B) from Hauksson et al. (2012) and Yang et al. (2012) used for the pre-mainshock computations in this study.

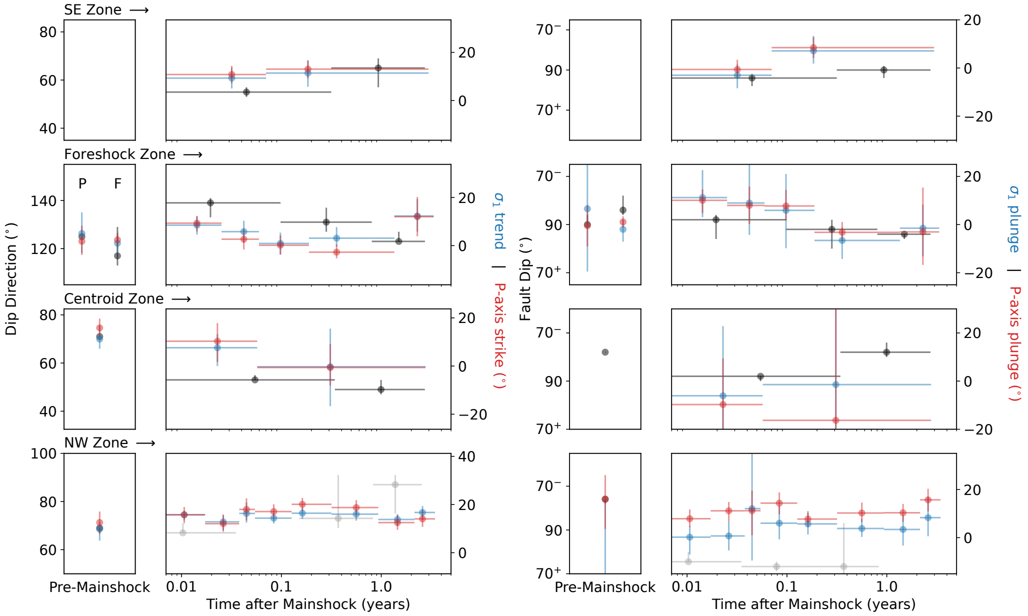

Figure 8.S5: Equivalent of the plot shown in Figure 8.2 but produced using only the catalogs from Hauksson et al. (2012) and Yang et al. (2012) for both the pre-mainshock and the post-mainshock windows.

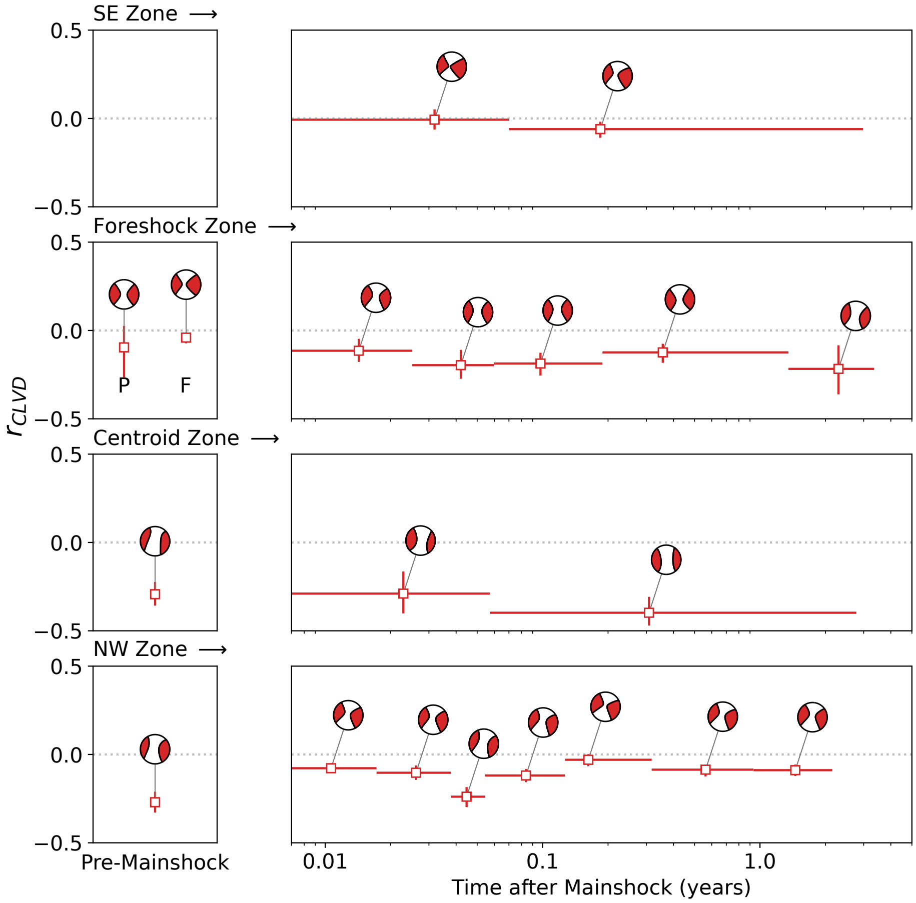

Figure 8.S6: Equivalent of the plot shown in Figure 8.3 but produced using only the catalogs from Yang et al. (2013) for both the pre-mainshock and the post-mainshock windows.

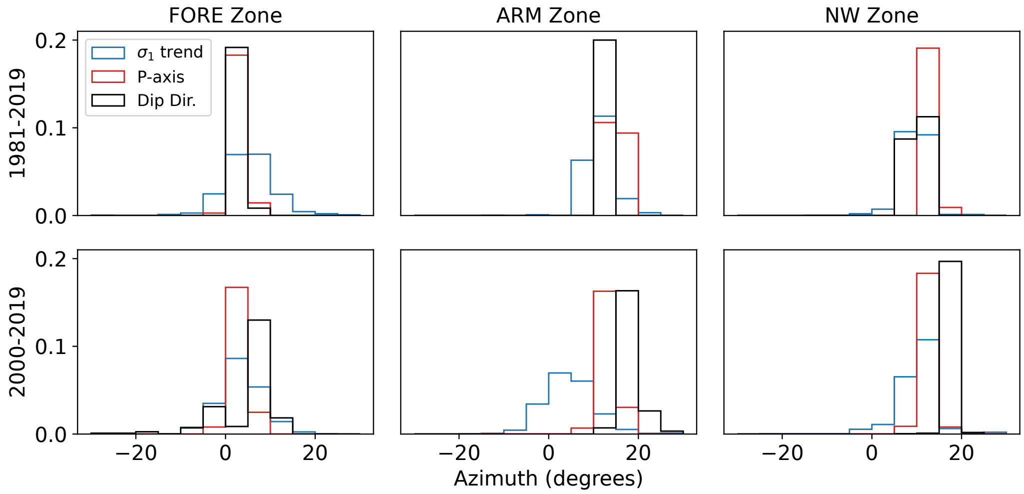

Figure 8.S7: Comparison of the pre-mainshock stress orientation analogs from the methods described in this study using both the entirety of the pre-mainshock seismicity from the Hauksson et al. (2012) seismicity catalog and the Yang et al. (2012) focal mechanism catalog. Dip direction values have been transformed to stress orientation using the dihedral angle measured in this study.

Chapter 9

CONCLUSIONS

In this thesis I have shown several examples of how fiber-optic seismology may be used to develop our understanding of fault zone structure. Chapter 2 showed that the seismic wavefield in DAS data has a diversity of phases that encode information on sources and structure and may be isolated from other signals and noise. Chapter 3 showed that DAS arrays are valuable tools for discovering unmapped faults and describing small faults. Chapter 4 showed that the combination of spatial density and long deployment times afforded by DAS allows for detailed descriptions of major faults like the Garlock Fault. Chapter 5 showed that a particular secondary phase can be used to investigate crustal thickness; combined with the high spatial sampling of DAS, this allows us to learn about Moho topography at low wavelengths.

I also show that second moments are valuable tools for finding patterns both in the distribution of earthquake slip and the spatial distribution of earthquake hypocenters. Chapter 6 showed that earthquake second moments, which form a low order representation of the source distribution, can be computed in a Bayesian framework. Chapter 7 applied this framework to many large earthquakes and showed that this low order representation can be used to establish certain properties of strike-slip earthquakes with measures of confidence. Chapter 8 showed that systematic changes in the distribution of hypocenter with time, observed using a second moment measure, can inform changes in the stress state.

Some challenges for using DAS for fault zone studies are that DAS channels are single component and the amplitude information for dark fibers is poorly understood because the fiber-ground coupling is unknown (Lindsey et al., 2020). The former problem means that techniques that require polarization information for either phase identification or processing are more challenging with DAS. This is a challenge for identifying fault zone head waves and fault zone trapped waves, because the polarity of these phases often distinguishes them from other phases (e.g., McGuire and Ben-Zion, 2005; Fohrmann et al., 2004). This also presents a challenge for receiver function deconvolution (Zhu and Kanamori, 2000); which is important for resolving the velocity structure and lateral discontinuities across fault zones at depth (Jiang et al., 2021; Allam et al., 2017). This issue can be ameliorated with collocated 3-component seismometers (Yu et al., 2019; Muir and Zhan, 2021b), but jointly processing 3-component seismometer data with DAS channels requires assumptions that increasingly break down the further the DAS channel is from the seismometer. Creative solutions towards identifying fault zone waves and recovering useful information from teleseismic observations with DAS arrays is thus an important avenue for future research. The latter problem, that the trustworthiness of amplitude information for DAS channels is unknown for dark fibers, presents challenges for tying the amplitude variability along DAS arrays to structural variability in fault zones and associated site response heterogeneity (e.g., Song and Yang, 2022). Work towards understanding whether or how much we may tie variability in the amplitude information recorded by dark fiber arrays to ground motion variability may prove highly valuable.

The results presented here suggest a suite of opportunities for using DAS for fault zone research. That DAS arrays may be used to identify unmapped fault zones and characterize their dimensions means that the dense fiber infrastructure may be used to systematically identify and map faults both to better understand their locations in urban areas and near critical infrastructure and to better characterize and understand fault connectivity. The results shown at the Garlock Fault suggest that fibers crossing major faults can be useful tools towards understanding major fault structure in detail. Major faults are often crossed by one or more fibers, and new fibers are continuously being deployed. This means that the techniques used here to investigate the Garlock Fault are readily transferable to other major faults. This offers an opportunity to systematically evaluate how parameters of major faults correspond to lithology and slip history. As shown through the use of PmP to image the Moho, DAS-measured earthquake wavefields contain secondary phases in the body wave coda that provide valuable constraints on material interfaces. PmP is not the only identifiable secondary phase, and there are likely phases that can be used to constrain sharp boundaries in the crust such as basin interfaces, crustal layering, and faults. These secondary phases thus present exciting opportunities for crustal imaging.

Our understanding of sources benefits from using a variety of descriptors with complementary sensitivities. The second moment framework for source inversion offers a solution that requires minimal a priori assumptions about the fault geometry and rupture velocity and provides a physically motivated low dimensional description of the source that is easy to directly compare between events. In this thesis, I only computed these solutions for strike-slip earthquakes, but there is no impediment for computing these solutions for other large events, such as thrust earthquakes, that are more numerous. A more complete catalog of second moments for global events may yield additional fascinating insights into the relationship between structure, tectonics, and earthquake sources. In general, developing a more complete perspective for more events is ideal, as this has the effect of moderating the biases due to assumptions of individual methods. The second moment solution is a useful complement to other source characterization methods such as slip distribution inversion (Ji, 2002), subevent inversion (Jia, Shen, et al., 2020), and backprojection (Ishii et al., 2005) in developing a fuller picture of earthquake sources. To this end, future work could also entail developing an automated framework for computing these second moments regularly for large earthquakes. Accomplishing this presents some challenges. Firstly, the accuracy of these solutions is heavily dependent on the quality of the Green's functions. For synthetic Green's functions, this is dependent on the accuracy of the Earth model and dictates the magnitude threshold above which computing reasonably accurate second moments is feasible. Additionally, as discussed in Chapter 6, quality control of the waveforms is a substantial challenge, and developments towards automating quality control for this problem are necessary before computations become routine.

In general, finding patterns within and between high-dimensional processes or datasets often requires a reduction in dimensionality using the right measures to isolate essential features. This requires decisions about what is essential given the problem at hand. The source second moment solutions presented in this thesis reduce the source to its spatiotemporal covariance. The cylindrical K-functions reduce a distribution of seismicity to the strike and dip of its anisotropy. As stated previously, DAS arrays make more low wavelength imaging studies of major fault zones possible. For comparability, these images will need to be reduced to their essential components. In this way, the first and second half of this thesis are related. Future work on the subject of the first half may draw inspiration from the second half. New patterns determined from the essential components drawn from the moments described in this thesis are made more meaningful when a more complete understanding of the structural, geologic, and tectonic settings for these earthquake sources are available. And so future work on the second half of the thesis may draw inspiration from the first half.

BIBLIOGRAPHY

Abdelmeguid, M. and Elbanna, A. (2022). Sequences of seismic and aseismic slip on bimaterial faults show dominant rupture asymmetry and potential for elevated seismic hazard. *Earth and Planetary Science Letters* 593. DOI: `10.1016/j.epsl.2022.117648`. P. 117648.

Aben, F. M., Doan, M.-L., Gratier, J.-P., and Renard, F. (2017). Experimental postseismic recovery of fractured rocks assisted by calcite sealing: Experimental recovery of fractured rocks. *Geophysical Research Letters* 44.14. DOI: `10.1002/2017GL073965`. Pp. 7228–7238.

Abercrombie, R. E., Antolik, M., and Ekström, G. (2003). The June 2000 M7.9 earthquakes south of Sumatra: Deformation in the India-Australia Plate. *Journal of Geophysical Research: Solid Earth* 108.B1. DOI: `10.1029/2001JB000674`. ESE 6–1–ESE 6–16.

Abercrombie, R. E. and Ekström, G. (2001). Earthquake slip on oceanic transform faults. *Nature* 410.6824. DOI: `10.1038/35065064`. Pp. 74–77.

– (2003). A reassessment of the rupture characteristics of oceanic transform earthquakes. *Journal of Geophysical Research: Solid Earth* 108.B5. DOI: `10.1029/2001JB000814`.

Aderhold, K. and Abercrombie, R. E. (2016). Seismotectonics of a diffuse plate boundary: Observations off the Sumatra-Andaman trench. *Journal of Geophysical Research: Solid Earth* 121.5. DOI: `10.1002/2015JB012721`. Pp. 3462–3478.

Afanasiev, M., Boehm, C., Driel, M. van, Krischer, L., Rietmann, M., May, D. A., Knepley, M. G., and Fichtner, A. (2019). Modular and flexible spectral-element waveform modelling in two and three dimensions. *Geophysical Journal International* 216.3. DOI: `10.1093/gji/ggy469`. Pp. 1675–1692.

Ajo-Franklin, J., Tribaldos, V. R., Nayak, A., Cheng, F., Mellors, R., Chi, B., Wood, T., Robertson, M., Rotermund, C., Matzel, E., Templeton, D. C., Morency, C., Wu, K., Dong, B., and Dobson, P. (2022). The Imperial Valley Dark Fiber Project: Toward Seismic Studies Using DAS and Telecom Infrastructure for Geothermal Applications. P. 14.

Ajo-Franklin, J. B., Dou, S., Lindsey, N. J., Monga, I., Tracy, C., Robertson, M., Rodriguez Tribaldos, V., Ulrich, C., Freifeld, B., Daley, T., and Li, X. (2019). Distributed Acoustic Sensing Using Dark Fiber for Near-Surface Characterization and Broadband Seismic Event Detection. *Scientific Reports* 9.1. DOI: `10.1038/s41598-018-36675-8`. P. 1328.

Aki, K. (1993). Local site effects on weak and strong ground motion. *Tectonophysics* 218. Pp. 93–111.

Aki, K. and Richards, P. G. (2002). *Quantitative seismology*. en. 2nd ed. Sausalito, Calif: University Science Books.

Allam, A. A., Ben-Zion, Y., and Peng, Z. (2014). Seismic Imaging of a Bimaterial Interface Along the Hayward Fault, CA, with Fault Zone Head Waves and Direct P Arrivals. *Pure and Applied Geophysics* 171.11. DOI: `10.1007/s00024-014-0784-0`. Pp. 2993–3011.

Allam, A., Schulte-Pelkum, V., Ben-Zion, Y., Tape, C., Ruppert, N., and Ross, Z. (2017). Ten kilometer vertical Moho offset and shallow velocity contrast along the Denali fault zone from double-difference tomography, receiver functions, and fault zone head waves. *Tectonophysics* 721. DOI: `10.1016/j.tecto.2017.09.003`. Pp. 56–69.

Almuhaidib, A. M. and Toksöz, M. N. (2014). Numerical modeling of elastic-wave scattering by near-surface heterogeneities. *GEOPHYSICS* 79.4. DOI: `10.1190/geo2013-0208.1`. T199–T217.

Ammon, C. J. (2005). Rupture process of the 2004 Sumatra-Andaman Earthquake. *Science* 308.5725. DOI: `10.1126/science.1112260`. Pp. 1133–1139.

Amos, C. B., Brownlee, S. J., Rood, D. H., Fisher, G. B., Burgmann, R., Renne, P. R., and Jayko, A. S. (2013). Chronology of tectonic, geomorphic, and volcanic interactions and the tempo of fault slip near Little Lake, California. *Geological Society of America Bulletin* 125.7-8. DOI: `10.1130/B30803.1`. Pp. 1187–1202.

Ampuero, J., Vilotte, J., and Sánchez-Sesma, F. J. (2002). Nucleation of rupture under slip dependent friction law: Simple models of fault zone. *Journal of Geophysical Research: Solid Earth* 107.B12. DOI: `10.1029/2001JB000452`. ESE 2–1–ESE 2–19.

Andrews, D. J. and Ben-Zion, Y. (1997). Wrinkle-like slip pulse on a fault between different materials. *Journal of Geophysical Research: Solid Earth* 102.B1. DOI: `10.1029/96JB02856`. Pp. 553–571.

Anooshehpoor, A. and Brune, J. N. (1999). Wrinkle-like Weertman pulse at the interface between two blocks of foam rubber with different velocities. *Geophysical Research Letters* 26.13. DOI: `10.1029/1999GL900397`. Pp. 2025–2028.

Antolik, M., Rachel E. Abercrombie, and Göran Ekström (2004). The 14 November 2001 Kokoxili (Kunlunshan), Tibet, Earthquake: Rupture Transfer through a Large Extensional Step-Over. *Bulletin of the Seismological Society of America* 94.4. DOI: `10.1785/012003180`. Pp. 1173–1194.

Antolik, M., Abercrombie, R. E., Pan, J., and Ekström, G. (2006). Rupture characteristics of the 2003 M_w 7.6 mid-Indian Ocean earthquake: Implications for seismic properties of young oceanic lithosphere. *Journal of Geophysical Research* 111.B4. DOI: `10.1029/2005JB003785`. B04302.

Antolik, M., Kaverina, A., and Dreger, D. S. (2000). Compound rupture of the great 1998 Antarctic plate earthquake. *Journal of Geophysical Research: Solid Earth* 105.B10. DOI: `10.1029/2000JB900246`. Pp. 23825–23838.

Asano, K. (2005). Estimation of Source Rupture Process and Strong Ground Motion Simulation of the 2002 Denali, Alaska, Earthquake. *Bulletin of the Seismological Society of America* 95.5. DOI: `10.1785/0120040154`. Pp. 1701–1715.

Atterholt, J. and Ross, Z. E. (In Prep). The evolution of fault orientation in the 2019 Ridgecrest Earthquake Sequence with a new long-term catalog of seismicity and moment tensors.

Atterholt, J. and Zhan, Z. (In Review). Fine scale Southern California Moho structure uncovered with distributed acoustic sensing.

Atterholt, J., Zhan, Z., Yang, Y., and Zhu, W. (2024). Imaging the Garlock Fault Zone with a fiber: a limited damage zone and hidden bimaterial contrast. *Journal of Geophysical Research: Solid Earth* 129. DOI: `10.1029/2024JB028900`. e2024JB028900.

Atterholt, J. and Ross, Z. E. (2023). Finite source properties of large strike-slip earthquakes. *Geophysical Journal International*. DOI: `10.1093/gji/ggad459`. ggad459.

– (2022). Bayesian Framework for Inversion of Second-Order Stress Glut Moments: Application to the 2019 Ridgecrest Sequence Mainshock. *Journal of Geophysical Research: Solid Earth* 127.4. DOI: `10.1029/2021JB023780`.

Atterholt, J., Zhan, Z., Shen, Z., and Li, Z. (2021). A unified wavefield-partitioning approach for distributed acoustic sensing. *Geophysical Journal International* 228.2. DOI: `10.1093/gji/ggab407`. Pp. 1410–1418.

Atterholt, J., Zhan, Z., and Yang, Y. (2022). Fault Zone Imaging With Distributed Acoustic Sensing: Body-To-Surface Wave Scattering. *Journal of Geophysical Research: Solid Earth* 127.11. DOI: `10.1029/2022JB025052`.

Backus, G. and Mulcahy, M. (1976a). Moment tensors and other phenomenological descriptions of seismic sources–I. Continuous displacements. *Geophysical Journal International* 46.2. DOI: `10.1111/j.1365-246X.1976.tb04162.x`. Pp. 341–361.

– (1976b). Moment tensors and other phenomenological descriptions of seismic sources–II. Discontinuous displacements. *Geophysical Journal International* 47.2. DOI: `10.1111/j.1365-246X.1976.tb01275.x`. Pp. 301–329.

Backus, G. E. (1977). Interpreting the seismic glut moments of total degree two or less. *Geophysical Journal International* 51.1. DOI: `10.1111/j.1365-246X.1977.tb04187.x`. Pp. 1–25.

Bailey, I. W., Becker, T. W., and Ben-Zion, Y. (2009). Patterns of co-seismic strain computed from southern California focal mechanisms. *Geophysical Journal International* 177.3. DOI: `10.1111/j.1365-246X.2009.04090.x`. Pp. 1015–1036.

Bailey, I. W., Ben-Zion, Y., Becker, T. W., and Holschneider, M. (2010). Quantifying focal mechanism heterogeneity for fault zones in central and southern California: Focal mechanism heterogeneity. *Geophysical Journal International* 183.1. DOI: `10.1111/j.1365-246X.2010.04745.x`. Pp. 433–450.

Bakku, S. (2015). "Fracture characterization from seismic measurements in a borehole". PhD thesis. Massachusetts Institute of Technology.

Bao, H., Xu, L., Meng, L., Ampuero, J.-P., Gao, L., and Zhang, H. (2022). Global frequency of oceanic and continental supershear earthquakes. *Nature Geoscience* 15.11. DOI: `10.1038/s41561-022-01055-5`. Pp. 942–949.

Barajas, A., Margerin, L., and Campillo, M. (2022). Coupled body and surface wave sensitivity kernels for coda-wave interferometry in a three-dimensional scalar scattering medium. *Geophysical Journal International* 230.2. DOI: `10.1093/gji/ggac091`. Pp. 1013–1029.

Barnhart, W. D., Hayes, G. P., and Gold, R. D. (2019). The July 2019 Ridgecrest, California, Earthquake Sequence: Kinematics of Slip and Stressing in Cross-Fault Ruptures. *Geophysical Research Letters* 46.21. DOI: `10.1029/2019GL084741`. Pp. 11859–11867.

Ben-Zion, Y. and Andrews, D. J. (1998). Properties and implications of dynamic rupture along a material interface. *Bulletin of the Seismological Society of America* 88.4. DOI: `10.1785/BSSA0880041085`. Pp. 1085–1094.

Ben-Zion, Y., Peng, Z., Okaya, D., Seeber, L., Armbruster, J. G., Ozer, N., Michael, A. J., Baris, S., and Aktar, M. (2003). A shallow fault-zone structure illuminated by trapped waves in the Karadere-Duzce branch of the North Anatolian Fault, western Turkey. *Geophysical Journal International* 152.3. DOI: `10.1046/j.1365-246X.2003.01870.x`. Pp. 699–717.

Benioff, H. (1935). A linear strain seismograph. *Bulletin of the Seismological Society of America* 25.4. DOI: `10.1785/BSSA0250040283`. Pp. 283–309.

Bense, V., Gleeson, T., Loveless, S., Bour, O., and Scibek, J. (2013). Fault zone hydrogeology. *Earth-Science Reviews* 127. DOI: `10.1016/j.earscirev.2013.09.008`. Pp. 171–192.

Bernardino, M. V., Jones, C. H., Levandowski, W., Bastow, I., Owens, T. J., and Gilbert, H. (2019). A multicomponent Isabella anomaly: Resolving the physical state of the Sierra Nevada upper mantle from Vp/Vs anisotropy tomography. *Geosphere* 15.6. DOI: `10.1130/GES02093.1`. Pp. 2018–2042.

Biondi, E., Zhu, W., Li, J., Williams, E. F., and Zhan, Z. (2023). An upper-crust lid over the Long Valley magma chamber. *Science Advances* 9.42. DOI: `10.1126/sciadv.adi9878`. eadi9878.

Bird, P. (2003). An updated digital model of plate boundaries. *Geochemistry, Geophysics, Geosystems* 4.3. DOI: `10.1029/2001GC000252`. Pp. 297–356.

Bishop, B. T., Cho, S., Warren, L., Soto-Cordero, L., Pedraza, P., Prieto, G. A., and Dionicio, V. (2023). Oceanic intraplate faulting as a pathway for deep hydration of the lithosphere: Perspectives from the Caribbean. *Geosphere* 19.1. DOI: `10.1130/GES02534.1`. Pp. 206–234.

Blaser, L., Kruger, F., Ohrnberger, M., and Scherbaum, F. (2010). Scaling Relations of Earthquake Source Parameter Estimates with Special Focus on Subduction Environment. *Bulletin of the Seismological Society of America* 100.6. DOI: `10.1785/0120100111`. Pp. 2914–2926.

Boettcher, M. S., Hirth, G., and Evans, B. (2007). Olivine friction at the base of oceanic seismogenic zones. *Journal of Geophysical Research* 112.B1. DOI: `10.1029/2006JB004301`. B01205.

Booth, A., Christoffersen, P., Schoonman, C., Clarke, A., Hubbard, B., Law, R., Doyle, S., Chudley, T., and Chailari, A. (2020). Distributed Acoustic Sensing of seismic properties in a borehole drilled on a fast-flowing Greenlandic outlet glacier. *Geophysical Research Letters* 47. e2020GL088148.

Bouchon, M. (2002). Space and Time Evolution of Rupture and Faulting during the 1999 Izmit (Turkey) Earthquake. *Bulletin of the Seismological Society of America* 92.1. DOI: `10.1785/0120000845`. Pp. 256–266.

Bowden, D. C. and Tsai, V. C. (2017). Earthquake ground motion amplification for surface waves: Ground Motions for Surface Waves. *Geophysical Research Letters* 44.1. DOI: `10.1002/2016GL071885`. Pp. 121–127.

Bozdağ, E. and Trampert, J. (2008). On crustal corrections in surface wave tomography. *Geophysical Journal International* 172.3. DOI: `10.1111/j.1365-246X.2007.03690.x`. Pp. 1066–1082.

Brantley, S. L. (1992). The effect of fluid chemistry on quartz microcrack lifetimes. *Earth and Planetary Science Letters* 113.1-2. DOI: `10.1016/0012-821X(92)90216-I`. Pp. 145–156.

Brantley, S. L., Evans, B., Hickman, S. H., and Crerar, D. A. (1990). Healing of microcracks in quartz: Implications for fluid flow. *Geology* 18.2. DOI: `10.1130/0091-7613(1990)018<0136:HOMIQI>2.3.CO;2`. P. 136.

Brantut, N., Heap, M., Meredith, P., and Baud, P. (2013). Time-dependent cracking and brittle creep in crustal rocks: A review. *Journal of Structural Geology* 52. DOI: `10.1016/j.jsg.2013.03.007`. Pp. 17–43.

Brocher, T. M. (2008). Key elements of regional seismic velocity models for long period ground motion simulations. *Journal of Seismology* 12.2. DOI: `10.1007/s10950-007-9061-3`. Pp. 217–221.

Buehler, J. S. and Shearer, P. M. (2014). Anisotropy and *Vp / Vs* in the uppermost mantle beneath the western United States from joint analysis of *Pn* and *Sn* phases. *Journal of Geophysical Research: Solid Earth* 119.2. DOI: `10.1002/2013JB010559`. Pp. 1200–1219.

Buehler, J. S. and Shearer, P. M. (2010). Pn tomography of the western United States using USArray. *Journal of Geophysical Research: Solid Earth* 115.B9. DOI: `10.1029/2009JB006874`. 2009JB006874.

Bukchin, B. (1995). Determination of stress glut moments of total degree 2 from teleseismic surface wave amplitude spectra. *Tectonophysics* 248.3-4. DOI: `10.1016/0040-1951(94)00271-A`. Pp. 185–191.

Caine, J. S., Evans, J. P., and Forster, C. B. (1996). Fault zone architecture and permeability structure. *Geology* 24.11. DOI: `10.1130/0091-7613(1996)024<1025:FZAAPS>2.3.CO;2`. P. 1025.

Çakir, Z., Chabalier, J.-B. d., Armijo, R., Meyer, B., Barka, A., and Peltzer, G. (2003). Coseismic and early post-seismic slip associated with the 1999 Izmit earthquake (Turkey), from SAR interferometry and tectonic field observations. *Geophysical Journal International* 155.1. DOI: `10.1046/j.1365-246X.2003.02001.x`. Pp. 93–110.

Candés, E. and Donoho, D. (2004). New tight frames of curvelets and optimal representations of objects with piecewise C2 singularities. *Communications on Pure and Applied Mathematics* 28. Pp. 219–266.

Candès, E., Demanet, L., Donoho, D., and Ying, L. (2006). Fast Discrete Curvelet Transforms. *Multiscale Modeling & Simulation* 5.3. DOI: `10.1137/05064182X`. Pp. 861–899.

Catchings, R. D., Goldman, M. R., Li, Y.-G., and Chan, J. H. (2016). Continuity of the West Napa–Franklin Fault Zone Inferred from Guided Waves Generated by Earthquakes Following the 24 August 2014 M_{w} 6.0 South Napa Earthquake. *Bulletin of the Seismological Society of America* 106.6. DOI: `10.1785/0120160154`. Pp. 2721–2746.

Cheadle, M. J., Czuchra, B. L., Byrne, T., Ando, C. J., Oliver, J. E., Brown, L. D., Kaufman, S., Malin, P. E., and Phinney, R. A. (1986). The deep crustal structure of the Mojave Desert, California, from Cocorp seismic reflection data. *Tectonics* 5.2. DOI: `10.1029/TC005i002p00293`. Pp. 293–320.

Chen, P. (2005). Finite-moment tensor of the 3 September 2002 Yorba Linda Earthquake. *Bulletin of the Seismological Society of America* 95.3. DOI: `10.1785/0120040094`. Pp. 1170–1180.

Cheng, F., Chi, B., Lindsey, N. J., Dawe, T. C., and Ajo-Franklin, J. B. (2021). Utilizing distributed acoustic sensing and ocean bottom fiber optic cables for submarine structural characterization. *Scientific Reports* 11.1. DOI: `10.1038/s41598-021-84845-y`. P. 5613.

Cheng, Y., Hauksson, E., and Ben-Zion, Y. (2023). Refined Earthquake Focal Mechanism Catalog for Southern California Derived With Deep Learning Algorithms. *Journal of Geophysical Research: Solid Earth* 128.2. DOI: `10.1029/2022JB025975`. e2022JB025975.

Chuang, R. Y. and Johnson, K. M. (2011). Reconciling geologic and geodetic model fault slip-rate discrepancies in Southern California: Consideration of nonsteady mantle flow and lower crustal fault creep. *Geology* 39.7. DOI: `10.1130/G32120.1`. Pp. 627–630.

Clévédé, E., Bouin, M.-P., Bukchin, B., Mostinskiy, A., and Patau, G. (2004). New constraints on the rupture process of the 1999 August 17 Izmit earthquake deduced from estimates of stress glut rate moments. *Geophysical Journal International* 159.3. DOI: `10.1111/j.1365-246X.2004.02304.x`. Pp. 931–942.

Cochard, A. and Rice, J. R. (2000). Fault rupture between dissimilar materials: Ill-posedness, regularization, and slip-pulse response. *Journal of Geophysical Research: Solid Earth* 105.B11. DOI: `10.1029/2000JB900230`. Pp. 25891–25907.

Cochran, E. S., Li, Y.-G., Shearer, P. M., Barbot, S., Fialko, Y., and Vidale, J. E. (2009). Seismic and geodetic evidence for extensive, long-lived fault damage zones. *Geology* 37.4. DOI: `10.1130/G25306A.1`. Pp. 315–318.

Collettini, C., Tesei, T., Scuderi, M., Carpenter, B., and Viti, C. (2019). Beyond Byerlee friction, weak faults and implications for slip behavior. *Earth and Planetary Science Letters* 519. DOI: `10.1016/j.epsl.2019.05.011`. Pp. 245–263.

Costa, L., Martins, H., Martín-López, S., Fernández-Ruiz, M., and González-Herráez, M. (2019). Fully Distributed Optical Fiber Strain Sensor With $10^{-12}\epsilon/\sqrt{}$ Hz Sensitivity. *Journal of Lightwave Technology* 37. Pp. 4487–4495.

Crotwell, H. P., Owens, T. J., and Ritsema, J. (1999). The TauP Toolkit: Flexible Seismic Travel-time and Ray-path Utilities. *Seismological Research Letters* 70.2. DOI: `10.1785/gssrl.70.2.154`. Pp. 154–160.

Dahlen, F. and Tromp, J. (1998). *Theoretical Global Seismology*. en. Princeton, N.J.: Princeton University Press.

Davis, G. A. and Burchfiel, B. C. (1973). Garlock Fault: An Intracontinental Transform Structure, Southern California. *Geological Society of America Bulletin* 84.4. DOI: `10.1130/0016-7606(1973)84<1407:GFAITS>2.0.CO;2`. P. 1407.

Dawson, T. E., McGill, S. F., and Rockwell, T. K. (2003). Irregular recurrence of paleoearthquakes along the central Garlock fault near El Paso Peaks, California. *Journal of Geophysical Research: Solid Earth* 108.B7. DOI: `10.1029/2001JB001744`.

Delouis, B. (2002). Joint Inversion of InSAR, GPS, Teleseismic, and Strong-Motion Data for the Spatial and Temporal Distribution of Earthquake Slip: Application to the 1999 Izmit Mainshock. *Bulletin of the Seismological Society of America* 92.1. DOI: `10.1785/0120000806`. Pp. 278–299.

Delph, J. R., Levander, A., and Niu, F. (2019). Constraining Crustal Properties Using Receiver Functions and the Autocorrelation of Earthquake-Generated Body Waves. *Journal of Geophysical Research: Solid Earth* 124.8. DOI: `10.1029/2019JB017929`. Pp. 8981–8997.

Ding, W., Li, T., Yang, X., Ren, K., and Tong, P. (2022). Deep Neural Networks for Creating Reliable PmP Database With a Case Study in Southern California. *Journal of Geophysical Research: Solid Earth* 127.4. DOI: `10.1029/2021JB023830`. e2021JB023830.

Dou, S., Lindsey, N., Wagner, A., Daley, T., Freifeld, B., Robertson, M., Peterson, J., Ulrich, C., Martin, E., and Ajo-Franklin, J. (2017). Distributed acoustic sensing for seismic monitoring of the near surface: A traffic-noise interferometry case study. *Scientific Reports* 7. Pp. 1–12.

Dougherty, S. L., Jiang, C., Clayton, R. W., Schmandt, B., and Hansen, S. M. (2020). Seismic evidence for a fossil slab origin for the Isabella anomaly. *Geophysical Journal International* 224.2. DOI: `10.1093/gji/ggaa472`. Pp. 1188–1196.

Du, Y., Aydin, A., and Segall, P. (1992). Comparison of various inversion techniques as applied to the determination of a geophysical deformation model for the 1983 Borah Peak Earthquake. *Bulletin of the Seismological Society of America* 82.4. Pp. 1840–1866.

Dunham, E. M., Belanger, D., Cong, L., and Kozdon, J. E. (2011). Earthquake Ruptures with Strongly Rate-Weakening Friction and Off-Fault Plasticity, Part 1: Planar Faults. *Bulletin of the Seismological Society of America* 101.5. DOI: `10.1785/0120100075`. Pp. 2296–2307.

Duputel, Z., Agram, P. S., Simons, M., Minson, S. E., and Beck, J. L. (2014). Accounting for prediction uncertainty when inferring subsurface fault slip. *Geophysical Journal International* 197.1. DOI: `10.1093/gji/ggt517`. Pp. 464–482.

DuRoss, C. B., Gold, R. D., Dawson, T. E., Scharer, K. M., Kendrick, K. J., Akciz, S. O., Angster, S. J., Bachhuber, J., Bacon, S., Bennett, S. E. K., Blair, L., Brooks, B. A., Bullard, T., Burgess, W. P., Chupik, C., DeFrisco, M., Delano, J., Dolan, J. F., Frost, E., Graehl, N., Haddon, E. K., Hatem, A. E., Hernandez, J. L., Hitchcock, C., Hudnut, K., Thompson Jobe, J., Koehler, R., Kozaci, O., Ladinsky, T., Madugo, C., McPhillips, D. S., Milliner, C., Morelan, A., Olson, B., Patton, J., Philibosian, B., Pickering, A. J., Pierce, I., Ponti, D. J., Seitz, G., Spangler, E., Swanson, B., Thomas, K., Treiman, J., Valencia, F., Williams, A., and Zinke, R. (2020). Surface Displacement Distributions for the July 2019 Ridgecrest, California, Earthquake Ruptures. *Bulletin of the Seismological Society of America* 110.4. DOI: `10.1785/0120200058`. Pp. 1400–1418.

Dziewonski, A. M. and Anderson, D. (1981). Preliminary Reference Earth Model. *Physics of the Earth and Planetary Interiors* 25. Pp. 297–356.

Eberhart-Phillips, D., Thurber, C., and Fletcher, J. B. (2014). Imaging P and S Attenuation in the Sacramento-San Joaquin Delta Region, Northern California. *Bulletin of the Seismological Society of America* 104.5. DOI: `10.1785/0120130336`. Pp. 2322–2336.

Ekström, G., Nettles, M., and Dziewoński, A. (2012). The global CMT project 2004–2010: Centroid-moment tensors for 13,017 earthquakes. *Physics of the Earth and Planetary Interiors* 200-201. DOI: `10.1016/j.pepi.2012.04.002`. Pp. 1–9.

Ellsworth, W. L. (2013). Injection-Induced Earthquakes. *Science* 341.6142. DOI: `10.1126/science.1225942`. P. 1225942.

Embree, P., Berg, J., and Backus, M. (1963). Wide-band velocity filtering - the pie slice process. *Geophysics* 28. Pp. 948–974.

Ende, M. van den, Lior, I., Ampuero, J., Sladen, A., Ferrari, A., and Richard, C. (2021). A self-supervised deep learning approach for blind denoising and waveform coherence enhancement in distributed acoustic sensing data. *EarthArXiv*.

Erickson, B. A. and Day, S. M. (2016). Bimaterial effects in an earthquake cycle model using rate-and-state friction. *Journal of Geophysical Research: Solid Earth* 121.4. DOI: `10.1002/2015JB012470`. Pp. 2480–2506.

Eshelby, J. (1957). The determination of the elastic field of an ellipsoidal inclusion, and related problems.

Fang, G., Li, Y., Zhao, Y., and Martin, E. (2020). Urban near-surface seismic monitoring using distributed acoustic sensing. *Geophysical Research Letters* 47. e2019GL086115.

Faulkner, D., Jackson, C., Lunn, R., Schlische, R., Shipton, Z., Wibberley, C., and Withjack, M. (2010). A review of recent developments concerning the structure, mechanics and fluid flow properties of fault zones. *Journal of Structural Geology* 32.11. DOI: `10.1016/j.jsg.2010.06.009`. Pp. 1557–1575.

Fialko, Y. (2021). Estimation of Absolute Stress in the Hypocentral Region of the 2019 Ridgecrest, California, Earthquakes. *Journal of Geophysical Research: Solid Earth* 126.7. DOI: `10.1029/2021JB022000`. e2021JB022000.

Field, E. H., Arrowsmith, R. J., Biasi, G. P., Bird, P., Dawson, T. E., Felzer, K. R., Jackson, D. D., Johnson, K. M., Jordan, T. H., Madden, C., Michael, A. J., Milner, K. R., Page, M. T., Parsons, T., Powers, P. M., Shaw, B. E., Thatcher, W. R., Weldon, R. J., and Zeng, Y. (2014). Uniform California Earthquake Rupture Forecast, Version 3 (UCERF3)–The Time-Independent Model. *Bulletin of the Seismological Society of America* 104.3. DOI: `10.1785/0120130164`. Pp. 1122–1180.

Fliedner, M. M., Klemperer, S. L., and Christensen, N. I. (2000). Three-dimensional seismic model of the Sierra Nevada arc, California, and its implications for crustal and upper mantle composition. *Journal of Geophysical Research: Solid Earth* 105.B5. DOI: `10.1029/2000JB900029`. Pp. 10899–10921.

Fohrmann, M., Igel, H., Jahnke, G., and Ben-Zion, Y. (2004). Guided Waves from Sources Outside Faults: An Indication for Shallow Fault Zone Structure? *Pure and Applied Geophysics* 161.11-12. DOI: `10.1007/s00024-004-2553-y`.

Freed, A. M. and Lin, J. (2001). Delayed triggering of the 1999 Hector Mine earthquake by viscoelastic stress transfer. *Nature* 411.6834. DOI: `10.1038/35075548`. Pp. 180–183.

Garbuno-Inigo, A., Hoffmann, F., Li, W., and Stuart, A. M. (2020). Interacting Langevin Diffusions: Gradient Structure and Ensemble Kalman Sampler. *SIAM Journal on Applied Dynamical Systems* 19.1. DOI: `10.1137/19M1251655`. Pp. 412–441.

GCMT (2019). *Mw 7.0 Central California*. URL: `https://www.globalcmt.org/cgi-bin/globalcmt-cgi-bin/CMT5/form?itype=ymd&yr=2019&mo=07&day=1&otype=ymd&oyr=2019&omo=07&oday=10&jyr=1976&jday=1&ojyr=1976&ojday=1&nday=1&lmw=7&umw=10&lms=0&ums=10&lmb=0&umb=10&llat=-90&ulat=90&llon=-180&ulon=180&lhd=0&uhd=1000&lts=-9999&uts=9999&lpe1=0&upe1=90&lpe2=0&upe2=90&list=0`.

Gelman, A., Carlin, J., Stern, H., Dunson, D., Vehtari, A., and Rubin, D. (2010). *Bayesian Data Analysis*. en. Boca Raton, F.L.: Chapman and Hall-CRC Press.

Gelman, A. and Rubin, D. (1992). Inference from iterative simulation using multiple sequences. *Statistical Science* 7.4. Pp. 457–511.

Gephart, J. W. and Forsyth, D. W. (1984). An improved method for determining the regional stress tensor using earthquake focal mechanism data: Application to the San Fernando Earthquake Sequence. *Journal of Geophysical Research: Solid Earth* 89.B11. DOI: `10.1029/JB089iB11p09305`. Pp. 9305–9320.

Gibbons, S. and Ringdal, F. (2006). The detection of low magnitude seismic events using array-based waveform correlation. *Geophysical Journal International* 165. Pp. 149–166.

Goldberg, D. E., Melgar, D., Sahakian, V. J., Thomas, A. M., Xu, X., Crowell, B. W., and Geng, J. (2020). Complex Rupture of an Immature Fault Zone: A Simultaneous Kinematic Model of the 2019 Ridgecrest, CA Earthquakes. *Geophysical Research Letters* 47.3. DOI: `10.1029/2019GL086382`.

Gombert, B., Duputel, Z., Jolivet, R., Doubre, C., Rivera, L., and Simons, M. (2018). Revisiting the 1992 Landers earthquake: a Bayesian exploration of coseismic slip and off-fault damage. *Geophysical Journal International* 212.2. DOI: `10.1093/gji/ggx455`. Pp. 839–852.

Grad, M., Tiira, T., and ESC Working Group (2009). The Moho depth map of the European Plate. *Geophysical Journal International* 176.1. DOI: `10.1111/j.1365-246X.2008.03919.x`. Pp. 279–292.

Graves, R. W. and Pitarka, A. (2010). Broadband Ground-Motion Simulation Using a Hybrid Approach. *Bulletin of the Seismological Society of America* 100.5A. DOI: `10.1785/0120100057`. Pp. 2095–2123.

Graves, R. W. and Wald, D. J. (2001). Resolution analysis of finite fault source inversion using one- and three-dimensional Green's functions: 1. Strong motions. *Journal of Geophysical Research: Solid Earth* 106.B5. DOI: `10.1029/2000JB900436`. Pp. 8745–8766.

Hadley, D. and Kanamori, H. (1977). Seismic structure of the Transverse Ranges, California. *Geological Society of America Bulletin* 88.10. DOI: `10.1130/0016-7606(1977)88<1469:SSOTTR>2.0.CO;2`. P. 1469.

Hardebeck, J. L. (2012). Coseismic and postseismic stress rotations due to great subduction zone earthquakes. *Geophysical Research Letters* 39.21. DOI: `10.1029/2012GL053438`. 2012GL053438.

– (2020). A Stress-Similarity Triggering Model for Aftershocks of the Mw 6.4 and 7.1 Ridgecrest Earthquakes. *Bulletin of the Seismological Society of America*. DOI: `10.1785/0120200015`.

Hardebeck, J. L. and Hauksson, E. (2001). Crustal stress field in southern California and its implications for fault mechanics. *Journal of Geophysical Research: Solid Earth* 106.B10. DOI: `10.1029/2001JB000292`. Pp. 21859–21882.

Hardebeck, J. L. and Michael, A. J. (2006). Damped regional-scale stress inversions: Methodology and examples for southern California and the Coalinga aftershock sequence. *Journal of Geophysical Research: Solid Earth* 111.B11. DOI: `10.1029/2005JB004144`. 2005JB004144.

Hardebeck, J. L. and Okada, T. (2018). Temporal Stress Changes Caused by Earthquakes: A Review. *Journal of Geophysical Research: Solid Earth* 123.2. DOI: `10.1002/2017JB014617`. Pp. 1350–1365.

Harris, R. A. and Day, S. M. (1993). Dynamics of fault interaction: parallel strike-slip faults. *Journal of Geophysical Research: Solid Earth* 98.B3. DOI: `10.1029/92JB02272`. Pp. 4461–4472.

Harris, R. A. and Day, S. M. (1999). Dynamic 3D simulations of earthquakes on En Echelon Faults. *Geophysical Research Letters* 26.14. DOI: `10.1029/1999GL900377`. Pp. 2089–2092.

– (2005). Material contrast does not predict earthquake rupture propagation direction. *Geophysical Research Letters* 32.23. DOI: `10.1029/2005GL023941`. P. L23301.

Hartog, H. (2017). *An Introduction to Distributed Optical Fibre Sensors*. Florida: CRC Press.

Hartzell, S. H. and Heaton, T. H. (1983). Inversion of strong ground motion and teleseismic waveform data for the fault rupture history of the 1979 Imperial Valley, California Earthquake. *Bulletin of the Seismological Society of America* 73.6. Pp. 1553–1583.

Hauksson, E., Hutton, K., Kanamori, H., Jones, L., Mori, J., Hough, S., and Roquemore, G. (1995). Preliminary Report on the 1995 Ridgecrest Earthquake Sequence in Eastern California. *Seismological Research Letters* 66.6. DOI: `10.1785/gssrl.66.6.54`. Pp. 54–60.

Hauksson, E., Yang, W., and Shearer, P. M. (2012). Waveform Relocated Earthquake Catalog for Southern California (1981 to June 2011). *Bulletin of the Seismological Society of America* 102.5. DOI: `10.1785/0120120010`. Pp. 2239–2244.

Hayes, G. P. (2017). The finite, kinematic rupture properties of great-sized earthquakes since 1990. *Earth and Planetary Science Letters* 468. DOI: `10.1016/j.epsl.2017.04.003`. Pp. 94–100.

He, H., Li, H., Pan, W., Luo, B., Zou, X., and Yan, L. (2017). SNR enhancement in phase-sensitive OTDR with adaptive 2-D bilateral filtering algorithm. *IEEE Photonics Journal* 9. Pp. 655–666.

He, K., Xu, C., and Wen, Y. (2022). Coseismic and early post-seismic deformations due to the 2019 earthquake sequence in Ridgecrest, California. *Geophysical Journal International* 230.2. DOI: `10.1093/gji/ggac103`. Pp. 957–975.

Hennenfent, G. and Herrmann, F. (2006). Seismic denoising with nonuniformly sampled curvelets. *Computing in Science & Engineering* 8.3. DOI: `10.1109/MCSE.2006.49`. Pp. 16–25.

Herrmann, R. B. (2013). Computer Programs in Seismology: An Evolving Tool for Instruction and Research. *Seismological Research Letters* 84.6. DOI: `10.1785/0220110096`. Pp. 1081–1088.

Hickman, S., Zoback, M., Ellsworth, W., Boness, N., Malin, P., Roecker, S., and Thurber, C. (2007). Structure and Properties of the San Andreas Fault in Central California: Recent Results from the SAFOD Experiment. *Scientific Drilling* SpecialIssue. DOI: `10.5194/sd-SpecialIssue-29-2007`. Pp. 29–32.

Hill, D. and Prejean, S. (2015). "Dynamic Triggering". en. In: *Treatise on Geophysics*. Elsevier, pp. 273–304. DOI: `10.1016/B978-0-444-53802-4.00078-6`.

Hiramatsu, Y., Honma, H., Saiga, A., Furumoto, M., and Ooida, T. (2005). Seismological evidence on characteristic time of crack healing in the shallow crust. *Geophysical Research Letters* 32.9. DOI: `10.1029/2005GL022657`. 2005GL022657.

Huang, X., Yang, D., Tong, P., Badal, J., and Liu, Q. (2016). Wave equation-based reflection tomography of the 1992 Landers earthquake area. *Geophysical Research Letters* 43.5. DOI: `10.1002/2016GL067717`. Pp. 1884–1892.

Huang, Y. (2018). Earthquake Rupture in Fault Zones With Along-Strike Material Heterogeneity. *Journal of Geophysical Research: Solid Earth* 123.11. DOI: `10.1029/2018JB016354`. Pp. 9884–9898.

Ibrahim, A., Lin, S., Xiong, J., Jiang, J., Fu, Y., and Wang, Z. (2020). Integrated principal component analysis denoising technique for phase-sensitive optical time domain reflectometry vibration detection. *Applied Optics* 59. Pp. 669–675.

Ide, S., Baltay, A., and Beroza, G. C. (2011). Shallow Dynamic Overshoot and Energetic Deep Rupture in the 2011 Mw 9.0 Tohoku-Oki Earthquake. *Science* 332.6036. DOI: `10.1126/science.1207020`. Pp. 1426–1429.

Illian, J., Penttinen, A., Stoyan, H., and Stoyan, D. (2007). *Statistical Analysis and Modelling of Spatial Point Patterns: Illian/Statistical Analysis and Modelling of Spatial Point Patterns*. en. Chichester, UK: John Wiley & Sons, Ltd. DOI: `10.1002/9780470725160`.

Innes, M. (2019). Don't Unroll Adjoint: Differentiating SSA-Form Programs. *arXiv:1810.07951 [cs]*. arXiv: 1810.07951.

Ishii, M., Shearer, P. M., Houston, H., and Vidale, J. E. (2005). Extent, duration and speed of the 2004 Sumatra–Andaman earthquake imaged by the Hi-Net array. *Nature* 435.7044. DOI: `10.1038/nature03675`. Pp. 933–936.

Jean-Luc Starck, Candes, E., and Donoho, D. (2002). The curvelet transform for image denoising. *IEEE Transactions on Image Processing* 11.6. DOI: `10.1109/TIP.2002.1014998`. Pp. 670–684.

Ji, C. (2002). Source Description of the 1999 Hector Mine, California, Earthquake, Part I: Wavelet Domain Inversion Theory and Resolution Analysis. *Bulletin of the Seismological Society of America* 92.4. DOI: `10.1785/0120000916`. Pp. 1192–1207.

Jia, Z., Jin, Z., Marchandon, M., Ulrich, T., Gabriel, A.-A., Fan, W., Shearer, P., Zou, X., Rekoske, J., Bulut, F., Garagon, A., and Fialko, Y. (2023). The complex dynamics of the 2023 Kahramanmaraş, Turkey, M_w 7.8-7.7 earthquake doublet. *Science* 381.6661. DOI: `10.1126/science.adi0685`. Pp. 985–990.

Jia, Z., Shen, Z., Zhan, Z., Li, C., Peng, Z., and Gurnis, M. (2020). The 2018 Fiji M 8.2 and 7.9 deep earthquakes: One doublet in two slabs. *Earth and Planetary Science Letters* 531. DOI: `10.1016/j.epsl.2019.115997`. P. 115997.

Jia, Z., Wang, X., and Zhan, Z. (2020). Multifault Models of the 2019 Ridgecrest Sequence Highlight Complementary Slip and Fault Junction Instability. *Geophysical Research Letters* 47.17. DOI: `10.1029/2020GL089802`.

Jiang, C., Schmandt, B., Hansen, S. M., Dougherty, S. L., Clayton, R. W., Farrell, J., and Lin, F.-C. (2018). Rayleigh and S wave tomography constraints on subduction termination and lithospheric foundering in central California. *Earth and Planetary Science Letters* 488. DOI: `10.1016/j.epsl.2018.02.009`. Pp. 14–26.

Jiang, X., Hu, S., and Yang, H. (2021). Depth Extent and V_p / V_s Ratio of the Chenghai Fault Zone, Yunnan, China Constrained From Dense-Array-Based Teleseismic Receiver Functions. *Journal of Geophysical Research: Solid Earth* 126.8. DOI: `10.1029/2021JB022190`. e2021JB022190.

Jin, Z. and Fialko, Y. (2020). Finite Slip Models of the 2019 Ridgecrest Earthquake Sequence Constrained by Space Geodetic Data and Aftershock Locations. *Bulletin of the Seismological Society of America* 110.4. DOI: `10.1785/0120200060`. Pp. 1660–1679.

Jousset, P. (2019). Illuminating Earth's faults. *Science* 366.6469. DOI: `10.1126/science.aaz7750`. Pp. 1076–1077.

Jousset, P., Reinsch, T., Ryberg, T., Blanck, H., Clarke, A., Aghayev, R., Hersir, G. P., Henninges, J., Weber, M., and Krawczyk, C. M. (2018). Dynamic strain determination using fibre-optic cables allows imaging of seismological and structural features. *Nature Communications* 9.1. DOI: `10.1038/s41467-018-04860-y`. P. 2509.

Joyce, K. E., Belliss, S. E., Samsonov, S. V., McNeill, S. J., and Glassey, P. J. (2009). A review of the status of satellite remote sensing and image processing techniques for mapping natural hazards and disasters. *Progress in Physical Geography: Earth and Environment* 33.2. DOI: `10.1177/0309133309339563`. Pp. 183–207.

Jurkevics, A. (1988). Polarization analysis of three-component array data. *Bulletin of the Seismological Society of America* 78.5. Pp. 1725–1743.

Kane, D. L., Shearer, P. M., Goertz-Allmann, B. P., and Vernon, F. L. (2013). Rupture directivity of small earthquakes at Parkfield. *Journal of Geophysical Research: Solid Earth* 118.1. DOI: `10.1029/2012JB009675`. Pp. 212–221.

Kay, I., Musacchio, G., White, D., Asudeh, I., Roberts, B., Forsyth, D., Hajnal, Z., Koperwhats, B., and Farrell, D. (1999). Imaging the moho and V_p/V_s ratio in the Western Superior Archean Craton with wide angle reflections. *Geophysical Research Letters* 26.16. DOI: `10.1029/1999GL010422`. Pp. 2585–2588.

Kelemen, P. B. and Hirth, G. (2007). A periodic shear-heating mechanism for intermediate-depth earthquakes in the mantle. *Nature* 446.7137. DOI: `10.1038/nature05717`. Pp. 787–790.

Kiser, E. and Ishii, M. (2017). Back-Projection Imaging of Earthquakes. *Annual Review of Earth and Planetary Sciences* 45.1. DOI: `10.1146/annurev-earth-063016-015801`. Pp. 271–299.

Kostrov, V. (1976). Seismic moment and energy of earthquakes, and seismic flow of rock. *International Journal of Rock Mechanics and Mining Sciences & Geomechanics Abstracts* 13.1. DOI: `10.1016/0148-9062(76)90256-4`. A4.

Kurzon, I., Vernon, F. L., Ben-Zion, Y., and Atkinson, G. (2014). Ground Motion Prediction Equations in the San Jacinto Fault Zone: Significant Effects of Rupture Directivity and Fault Zone Amplification. *Pure and Applied Geophysics* 171.11. DOI: `10.1007/s00024-014-0855-2`. Pp. 3045–3081.

Lai, V. H., Graves, R. W., Yu, C., Zhan, Z., and Helmberger, D. V. (2020). Shallow Basin Structure and Attenuation Are Key to Predicting Long Shaking Duration in Los Angeles Basin. *Journal of Geophysical Research: Solid Earth* 125.10. DOI: `10.1029/2020JB019663`.

Lasserre, C., Peltzer, G., Crampé, F., Klinger, Y., Van Der Woerd, J., and Tapponnier, P. (2005). Coseismic deformation of the 2001 $M_w = 7.8$ Kokoxili earthquake in Tibet, measured by synthetic aperture radar interferometry. *Journal of Geophysical Research* 110.B12. DOI: `10.1029/2004JB003500`. B12408.

Lay, T. (2018). A review of the rupture characteristics of the 2011 Tohoku-oki Mw 9.1 earthquake. *Tectonophysics* 733. DOI: `10.1016/j.tecto.2017.09.022`. Pp. 4–36.

– (2019). “Reactivation of Oceanic Fracture Zones in Large Intraplate Earthquakes?” en. In: *Transform Plate Boundaries and Fracture Zones*. Elsevier, pp. 89–104. DOI: `10.1016/B978-0-12-812064-4.00004-9`.

Lay, T., Ye, L., Bai, Y., Cheung, K. F., and Kanamori, H. (2018). The 2018 M7.9 Gulf of Alaska Earthquake: Multiple Fault Rupture in the Pacific Plate. *Geophysical Research Letters* 45.18. DOI: `10.1029/2018GL079813`. Pp. 9542–9551.

Lay, T., Ye, L., Bai, Y., Cheung, K. F., Kanamori, H., Freymueller, J., Steblov, G. M., and Kogan, M. G. (2017). Rupture Along 400 km of the Bering Fracture Zone in the Komandorsky Islands Earthquake (M_W 7.8) of 17 July 2017. *Geophysical Research Letters* 44.24. DOI: `10.1002/2017GL076148`.

Lay, V., Buske, S., Townend, J., Kellett, R., Savage, M., Schmitt, D. R., Constantinou, A., Eccles, J. D., Gorman, A. R., Bertram, M., Hall, K., Lawton, D., and Kofman, R. (2021). 3D Active Source Seismic Imaging of the Alpine Fault Zone and the Whataroa Glacial Valley in New Zealand. *Journal of Geophysical Research: Solid Earth* 126.12. DOI: `10.1029/2021JB023013`.

Lee, E.-J., Chen, P., Jordan, T. H., Maechling, P. B., Denolle, M. A. M., and Beroza, G. C. (2014). Full-3-D tomography for crustal structure in Southern California based on the scattering-integral and the adjoint-wavefield methods. *Journal of Geophysical Research: Solid Earth* 119.8. DOI: `10.1002/2014JB011346`. Pp. 6421–6451.

Lee, E.-J., Chen, P., Jordan, T. H., and Wang, L. (2011). Rapid full-wave centroid moment tensor (CMT) inversion in a three-dimensional earth structure model for earthquakes in Southern California: Rapid full-wave CMT inversion. *Geophysical Journal International* 186.1. DOI: `10.1111/j.1365-246X.2011.05031.x`. Pp. 311–330.

Lee, Y.-J. and Morse, J. W. (1999). Calcite precipitation in synthetic veins: implications for the time and fluid volume necessary for vein filling. *Chemical Geology* 156.1-4. DOI: `10.1016/S0009-2541(98)00183-1`. Pp. 151–170.

Lellouch, A., Yuan, S., Spica, Z., Biondi, B., and Ellsworth, W. L. (2019). Seismic Velocity Estimation Using Passive Downhole Distributed Acoustic Sensing Records: Examples From the San Andreas Fault Observatory at Depth. *Journal of Geophysical Research: Solid Earth* 124.7. DOI: `10.1029/2019JB017533`. Pp. 6931–6948.

Levin, V., VanTongeren, J. A., and Servali, A. (2016). How sharp is the sharp Archean Moho? Example from eastern Superior Province. *Geophysical Research Letters* 43.5. DOI: `10.1002/2016GL067729`. Pp. 1928–1933.

Lewis, M. A. and Ben-Zion, Y. (2010). Diversity of fault zone damage and trapping structures in the Parkfield section of the San Andreas Fault from comprehensive analysis of near fault seismograms: Diversity of fault zone damage at Parkfield. *Geophysical Journal International* 183.3. DOI: `10.1111/j.1365-246X.2010.04816.x`. Pp. 1579–1595.

Li, H., Zhu, L., and Yang, H. (2007). High-resolution structures of the Landers fault zone inferred from aftershock waveform data: High-resolution Landers fault zone structures. *Geophysical Journal International* 171.3. DOI: `10.1111/j.1365-246X.2007.03608.x`. Pp. 1295–1307.

Li, T., Wu, S., and Tong, P. (2024). Multilevel transcrustal magmatic system beneath the Geysers-Clear Lake area. *Proceedings of the National Academy of Sciences* 121.12. DOI: `10.1073/pnas.2317809121`. e2317809121.

Li, T., Yao, J., Wu, S., Xu, M., and Tong, P. (2022). Moho Complexity in Southern California Revealed by Local PmP and Teleseismic Ps Waves. *Journal of Geophysical Research: Solid Earth* 127.2. DOI: `10.1029/2021JB023033`. e2021JB023033.

Li, X. (2002). Complex Source Process of the 17 August 1999 Izmit, Turkey, Earthquake. *Bulletin of the Seismological Society of America* 92.1. DOI: `10.1785/0120000839`. Pp. 267–277.

Li, Y.-G. (2002). Study of the 1999 M 7.1 Hector Mine, California, Earthquake Fault Plane by Trapped Waves. *Bulletin of the Seismological Society of America* 92.4. DOI: `10.1785/0120000909`. Pp. 1318–1332.

Li, Y.-G. and Vidale, J. E. (2001). Healing of the shallow fault zone from 1994-1998 After the 1992 *M* 7.5 Landers, California, Earthquake. *Geophysical Research Letters* 28.15. DOI: `10.1029/2001GL012922`. Pp. 2999–3002.

Li, Y.-G., Henyey, T. L., and Leary, P. C. (1992). Seismic reflection constraints on the structure of the crust beneath the San Bernardino Mountains, Transverse Ranges, southern California. *Journal of Geophysical Research: Solid Earth* 97.B6. DOI: `10.1029/92JB00386`. Pp. 8817–8830.

Li, Y.-G., Vidale, J. E., Aki, K., and Xu, F. (2000). Depth-dependent structure of the Landers fault zone from trapped waves generated by aftershocks. *Journal of Geophysical Research: Solid Earth* 105.B3. DOI: `10.1029/1999JB900449`. Pp. 6237–6254.

Li, Y.-G., Vidale, J. E., and Cochran, E. S. (2004). Low-velocity damaged structure of the San Andreas Fault at Parkfield from fault zone trapped waves. *Geophysical Research Letters* 31.12. DOI: `10.1029/2003GL019044`. 2003GL019044.

Li, Z. and Zhan, Z. (2018). Pushing the limit of earthquake detection with distributed acoustic sensing and template matching: a case study at the Brady geothermal field. *Geophysical Journal International* 215. Pp. 1583–1593.

Li, Z., Shen, Z., Yang, Y., Williams, E., Wang, X., and Zhan, Z. (2021). Rapid Response to the 2019 Ridgecrest Earthquake With Distributed Acoustic Sensing. *AGU Advances* 2.2. DOI: `10.1029/2021AV000395`.

Liberty, L. M., St. Clair, J., and McKean, A. P. (2021). A Broad, Distributed Active Fault Zone Lies beneath Salt Lake City, Utah. *The Seismic Record* 1.1. DOI: `10.1785/0320210009`. Pp. 35–45.

Lin, A. and Yamashita, K. (2013). Spatial variations in damage zone width along strike-slip faults: An example from active faults in southwest Japan. *Journal of Structural Geology* 57. DOI: `10.1016/j.jsg.2013.10.006`. Pp. 1–15.

Lin, Y.-P. and Jordan, T. H. (2018). Frequency-Dependent Attenuation of *P* and *S* Waves in Southern California. *Journal of Geophysical Research: Solid Earth* 123.7. DOI: `10.1029/2018JB015448`. Pp. 5814–5830.

Lindsey, N. J., Dawe, T. C., and Ajo-Franklin, J. B. (2019). Illuminating seafloor faults and ocean dynamics with dark fiber distributed acoustic sensing. *Science* 366.6469. DOI: `10.1126/science.aay5881`. Pp. 1103–1107.

Lindsey, N. J., Rademacher, H., and Ajo-Franklin, J. B. (2020). On the Broadband Instrument Response of Fiber-Optic DAS Arrays. *Journal of Geophysical Research: Solid Earth* 125.2. DOI: `10.1029/2019JB018145`. e2019JB018145.

Lior, I., Sladen, A., Mercerat, D., Ampuero, J.-P., Rivet, D., and Sambolian, S. (2021). Strain to ground motion conversion of distributed acoustic sensing data for earthquake magnitude and stress drop determination. *Solid Earth* 12.6. DOI: `10.5194/se-12-1421-2021`. Pp. 1421–1442.

Liu, C., Lay, T., Brodsky, E. E., Dascher-Cousineau, K., and Xiong, X. (2019). Coseismic Rupture Process of the Large 2019 Ridgecrest Earthquakes From Joint Inversion of Geodetic and Seismological Observations. *Geophysical Research Letters* 46.21. DOI: `10.1029/2019GL084949`. Pp. 11820–11829.

Liu, K.-S. and Tsai, Y.-B. (2009). Large Effects of Moho Reflections (SmS) on Peak Ground Motion in Northwestern Taiwan. *Bulletin of the Seismological Society of America* 99.1. DOI: `10.1785/0120080258`. Pp. 255–267.

Liu, Z., AlTheyab, A., Hanafy, S. M., and Schuster, G. (2017). Imaging near-surface heterogeneities by natural migration of backscattered surface waves: Field data test. *Geophysics* 82.3. DOI: `10.1190/geo2016-0253.1`. S197–S205.

Louie, J. N. and Qin, J. (1991). Subsurface imaging of the Garlock Fault, Cantil Valley, California. *Journal of Geophysical Research: Solid Earth* 96.B9. DOI: `10.1029/91JB01273`. Pp. 14461–14479.

Luo, Y., Long, M. D., Karabinos, P., Kuiper, Y. D., Rondenay, S., Aragon, J. C., Sawade, L., and Makus, P. (2021). High-Resolution Ps Receiver Function Imaging of the Crust and Mantle Lithosphere Beneath Southern New England and Tectonic Implications. *Journal of Geophysical Research: Solid Earth* 126.7. DOI: `10.1029/2021JB022170`. e2021JB022170.

Ma, J. and Plonka, G. (2010). The Curvelet Transform. *IEEE Signal Processing Magazine* 27.2. DOI: `10.1109/MSP.2009.935453`. Pp. 118–133.

Madden Madugo, C., Dolan, J. F., and Hartleb, R. D. (2012). New Paleoearthquake Ages from the Western Garlock Fault: Implications for Regional Earthquake Occurrence in Southern California. *Bulletin of the Seismological Society of America* 102.6. DOI: `10.1785/0120110310`. Pp. 2282–2299.

Mai, P. M. and Beroza, G. C. (2000). Source Scaling Properties from Finite-Fault-Rupture Models. *Bulletin of the Seismological Society of America* 90.3. DOI: `10.1785/0119990126`. Pp. 604–615.

Mai, P. M., Spudich, P., and Boatwright, J. (2005). Hypocenter Locations in Finite-Source Rupture Models. *Bulletin of the Seismological Society of America* 95.3. DOI: `10.1785/0120040111`. Pp. 965–980.

Mai, P. M. and Thingbaijam, K. K. S. (2014). SRCMOD: An Online Database of Finite-Fault Rupture Models. *Seismological Research Letters* 85.6. DOI: `10.1785/0220140077`. Pp. 1348–1357.

Manighetti, I., Campillo, M., Sammis, C., Mai, P. M., and King, G. (2005). Evidence for self-similar, triangular slip distributions on earthquakes: Implications for earthquake and fault mechanics. *Journal of Geophysical Research* 110.B5. DOI: `10.1029/2004JB003174`. B05302.

Marone, C., Vidale, J. E., and Ellsworth, W. L. (1995). Fault healing inferred from time dependent variations in source properties of repeating earthquakes. *Geophysical Research Letters* 22.22. DOI: `10.1029/95GL03076`. Pp. 3095–3098.

Martin, E. R., Huot, F., Ma, Y., Cieplicki, R., Cole, S., Karrenbach, M., and Biondi, B. L. (2018). A Seismic Shift in Scalable Acquisition Demands New Processing: Fiber-Optic Seismic Signal Retrieval in Urban Areas with Unsupervised Learning for Coherent Noise Removal. *IEEE Signal Processing Magazine* 35.2. DOI: `10.1109/MSP.2017.2783381`. Pp. 31–40.

Martinez-Garzon, P., Kwiatek, G., Ickrath, M., and Bohnhoff, M. (2014). MSATSI: A MATLAB Package for Stress Inversion Combining Solid Classic Methodology, a New Simplified User-Handling, and a Visualization Tool. *Seismological Research Letters* 85.4. DOI: `10.1785/0220130189`. Pp. 896–904.

McGill, S. and Rockwell, T. (1998). Ages of Late Holocene earthquakes on the central Garlock fault near El Paso Peaks, California. *Journal of Geophysical Research: Solid Earth* 103.B4. DOI: `10.1029/97JB02129`. Pp. 7265–7279.

McGuire, J. J. (2004). Estimating Finite Source Properties of Small Earthquake Ruptures. *Bulletin of the Seismological Society of America* 94.2. DOI: `10.1785/0120030091`. Pp. 377–393.

McGuire, J. and Ben-Zion, Y. (2005). High-resolution imaging of the Bear Valley section of the San Andreas fault at seismogenic depths with fault-zone head waves and relocated seismicity. *Geophysical Journal International* 163.1. DOI: `10.1111/j.1365-246X.2005.02703.x`. Pp. 152–164.

McGuire, J. J. and Beroza, G. C. (2012). A Rogue Earthquake Off Sumatra. *Science* 336.6085. DOI: `10.1126/science.1223983`. Pp. 1118–1119.

McGuire, J. J., Zhao, L., and Jordan, T. H. (2002). Predominance of Unilateral Rupture for a Global Catalog of Large Earthquakes. *Bulletin of the Seismological Society of America* 92.8. DOI: `10.1785/0120010293`. Pp. 3309–3317.

McGuire, J. J., Zhao, L., and Jordan, T. H. (2000). Rupture dimensions of the 1998 Antarctic Earthquake from low-frequency waves. *Geophysical Research Letters* 27.15. DOI: `10.1029/1999GL011186`. Pp. 2305–2308.

– (2001). Teleseismic inversion for the second-degree moments of earthquake space-time distributions. *Geophysical Journal International* 145.3. DOI: `10.1046/j.1365-246x.2001.01414.x`. Pp. 661–678.

McKenzie, D., Nimmo, F., Jackson, J. A., Gans, P. B., and Miller, E. L. (2000). Characteristics and consequences of flow in the lower crust. *Journal of Geophysical Research: Solid Earth* 105.B5. DOI: `10.1029/1999JB900446`. Pp. 11029–11046.

Melgar, D. and Hayes, G. P. (2019). The Correlation Lengths and Hypocentral Positions of Great Earthquakes. *Bulletin of the Seismological Society of America* 109.6. DOI: `10.1785/0120190164`. Pp. 2582–2593.

Meng, H., McGuire, J. J., and Ben-Zion, Y. (2020). Semiautomated estimates of directivity and related source properties of small to moderate Southern California earthquakes using second seismic moments. *Journal of Geophysical Research: Solid Earth* 125.4. DOI: `10.1029/2019JB018566`. e2019JB018566.

Meng, L., Ampuero, J.-P., Stock, J., Duputel, Z., Luo, Y., and Tsai, V. C. (2012). Earthquake in a Maze: Compressional Rupture Branching During the 2012 M_{w} 8.6 Sumatra Earthquake. *Science* 337.6095. DOI: `10.1126/science.1224030`. Pp. 724–726.

Michael, A. J. (1984). Determination of stress from slip data: Faults and folds. *Journal of Geophysical Research: Solid Earth* 89.B13. DOI: `10.1029/JB089iB13p11517`. Pp. 11517–11526.

Michael, A. J. (1987). Stress rotation during the Coalinga Aftershock Sequence. *Journal of Geophysical Research: Solid Earth* 92.B8. DOI: `10.1029/JB092iB08p07963`. Pp. 7963–7979.

Milliner, C. and Donnellan, A. (2020). Using Daily Observations from Planet Labs Satellite Imagery to Separate the Surface Deformation between the 4 July Mw 6.4 Foreshock and 5 July Mw 7.1 Mainshock during the 2019 Ridgecrest Earthquake Sequence. *Seismological Research Letters* 91.4. DOI: `10.1785/0220190271`. Pp. 1986–1997.

Minson, S. E., Simons, M., and Beck, J. L. (2013). Bayesian inversion for finite fault earthquake source models I—theory and algorithm. *Geophysical Journal International* 194.3. DOI: `10.1093/gji/ggt180`. Pp. 1701–1726.

Møller, J., Safavimanesh, F., and Rasmussen, J. G. (2016). The cylindrical K-function and Poisson line cluster point processes. *Biometrika* 103.4. DOI: `10.1093/biomet/asw044`. Pp. 937–954.

Møller, J. and Toftaker, H. (2014). Geometric Anisotropic Spatial Point Pattern Analysis and Cox Processes. *Scandinavian Journal of Statistics* 41.2. DOI: `10.1111/sjos.12041`. Pp. 414–435.

Molnar, P., Anderson, H. J., Audoine, E., Eberhart-Phillips, D., Gledhill, K. R., Klosko, E. R., McEvilly, T. V., Okaya, D., Savage, M. K., Stern, T., and Wu, F. T. (1999). Continuous Deformation Versus Faulting Through the Continental Lithosphere of New Zealand. *Science* 286.5439. DOI: `10.1126/science.286.5439.516`. Pp. 516–519.

Monastero, F. C., Sabin, A. E., and Walker, J. D. (1997). Evidence for post-early Miocene initiation of movement on the Garlock fault from offset of the Cudahy Camp Formation, east-central California. *Geology* 25.3. DOI: `10.1130/0091-7613(1997)025<0247:EFPEMI>2.3.CO;2`. P. 247.

Monelli, D., Mai, P. M., Jónsson, S., and Giardini, D. (2009). Bayesian imaging of the 2000 Western Tottori (Japan) earthquake through fitting of strong motion and GPS data. *Geophysical Journal International* 176.1. DOI: `10.1111/j.1365-246X.2008.03943.x`. Pp. 135–150.

Moreno, M., Rosenau, M., and Oncken, O. (2010). 2010 Maule earthquake slip correlates with pre-seismic locking of Andean subduction zone. *Nature* 467.7312. DOI: `10.1038/nature09349`. Pp. 198–202.

Mori, J. and Helmberger, D. (1996). Large-amplitude Moho reflections (*SmS*) from Landers aftershocks, southern California. *Bulletin of the Seismological Society of America* 86.6. DOI: `10.1785/BSSA0860061845`. Pp. 1845–1852.

Moulik, P. and Ekström, G. (2014). An anisotropic shear velocity model of the Earth's mantle using normal modes, body waves, surface waves and long-period waveforms. *Geophysical Journal International* 199.3. DOI: `10.1093/gji/ggu356`. Pp. 1713–1738.

Mu, X., Song, J., Yang, H., Huang, J., Yao, H., and Tian, B. (2024). High-Resolution Shallow Structure along the Anninghe Fault Zone, Sichuan, China, Constrained by Active Source Tomography. *Seismological Research Letters* 95.1. DOI: `10.1785/0220230137`. Pp. 408–420.

Muir, J. B. and Tsai, V. C. (2020). Geometric and level set tomography using ensemble Kalman inversion. *Geophysical Journal International* 220.2. DOI: `10.1093/gji/ggz472`. Pp. 967–980.

Muir, J. B. and Zhan, Z. (2021a). Seismic wavefield reconstruction using a preconditioned wavelet–curvelet compressive sensing approach. *Geophysical Journal International* 227.1. DOI: `10.1093/gji/ggab222`. Pp. 303–315.

– (2021b). Wavefield-based evaluation of DAS instrument response and array design. *Geophysical Journal International* 229.1. DOI: `10.1093/gji/ggab439`. Pp. 21–34.

Muir, J. B., Clayton, R. W., Tsai, V. C., and Brissaud, Q. (2022). Parsimonious Velocity Inversion Applied to the Los Angeles Basin, CA. *Journal of Geophysical Research: Solid Earth* 127.2. DOI: `10.1029/2021JB023103`.

Nakajima, J., Matsuzawa, T., and Hasegawa, A. (2002). Moho depth variation in the central part of northeastern Japan estimated from reflected and converted waves. *Physics of the Earth and Planetary Interiors* 130.1-2. DOI: `10.1016/S0031-9201(01)00307-7`. Pp. 31–47.

Nasirzadeh, F., Shishebor, Z., and Mateu, J. (2021). On new families of anisotropic spatial log-Gaussian Cox processes. *Stochastic Environmental Research and Risk Assessment* 35.2. doi: `10.1007/s00477-020-01906-w`. Pp. 183–213.

Neal, R. (2010). *MCMC using Hamiltonian Dynamics*. en. Boca Raton, F.L.: Chapman and Hall-CRC Press.

Nettles, M., Wallace, T. C., and Beck, S. L. (1999). The March 25, 1998 Antarctic Plate Earthquake. *Geophysical Research Letters* 26.14. doi: `10.1029/1999GL900387`. Pp. 2097–2100.

Nevitt, J. M., Brooks, B. A., Hardebeck, J. L., and Aagaard, B. T. (2023). 2019 M7.1 Ridgecrest earthquake slip distribution controlled by fault geometry inherited from Independence dike swarm. *Nature Communications* 14.1. doi: `10.1038/s41467-023-36840-2`. P. 1546.

Ortega-Culaciati, F., Simons, M., Ruiz, J., Rivera, L., and Díaz-Salazar, N. (2021). An EPIC Tikhonov Regularization: Application to Quasi-Static Fault Slip Inversion. *Journal of Geophysical Research: Solid Earth* 126.7. doi: `10.1029/2020JB021141`.

Ozakin, Y., Ben-Zion, Y., Aktar, M., Karabulut, H., and Peng, Z. (2012). Velocity contrast across the 1944 rupture zone of the North Anatolian fault east of Ismetpasa from analysis of teleseismic arrivals. *Geophysical Research Letters* 39.8. doi: `10.1029/2012GL051426`. n/a–n/a.

Ozawa, S., Nishimura, T., Munekane, H., Suito, H., Kobayashi, T., Tobita, M., and Imakiire, T. (2012). Preceding, coseismic, and postseismic slips of the 2011 Tohoku earthquake, Japan. *Journal of Geophysical Research: Solid Earth* 117.B7. doi: `10.1029/2011JB009120`. 2011JB009120.

Perfettini, H. and Avouac, J.-P. (2007). Modeling afterslip and aftershocks following the 1992 Landers earthquake. *Journal of Geophysical Research: Solid Earth* 112.B7. doi: `10.1029/2006JB004399`. 2006JB004399.

Plesch, A., Shaw, J. H., Benson, C., Bryant, W. A., Carena, S., Cooke, M., Dolan, J., Fuis, G., Gath, E., Grant, L., Hauksson, E., Jordan, T., Kamerling, M., Legg, M., Lindvall, S., Magistrale, H., Nicholson, C., Niemi, N., Oskin, M., Perry, S., Planansky, G., Rockwell, T., Shearer, P., Sorlien, C., Suss, M. P., Suppe, J., Treiman, J., and Yeats, R. (2007). Community Fault Model (CFM) for Southern California. *Bulletin of the Seismological Society of America* 97.6. doi: `10.1785/0120050211`. Pp. 1793–1802.

Pollitz, F. F., Wicks, C. W., Svarc, J. L., Phillips, E., Brooks, B. A., Murray, M. H., and Turner, R. C. (2022). Postseismic Relaxation Following the 2019 Ridgecrest, California, Earthquake Sequence. *Bulletin of the Seismological Society of America* 112.2. doi: `10.1785/0120210170`. Pp. 734–749.

Ponti, D. J., Blair, J. L., Rosa, C. M., Thomas, K., Pickering, A. J., Akciz, S., Angster, S., Avouac, J.-P., Bachhuber, J., Bacon, S., Barth, N., Bennett, S., Blake, K., Bork, S., Brooks, B., Bullard, T., Burgess, P., Chupik, C., Dawson, T., DeFrisco, M., Delano, J., DeLong, S., Dolan, J., Donnellan, A., DuRoss, C., Ericksen, T., Frost, E., Funning, G., Gold, R., Graehl, N., Gutierrez, C., Haddon, E., Hatem, A., Helms, J., Hernandez, J., Hitchcock, C., Holland, P., Hudnut, K., Kendrick, K., Koehler, R., Kozaci, O., Ladinsky, T., Leeper, R., Madugo, C., Mareschal, M., McDonald, J., McPhillips, D., Milliner, C., Mongovin, D., Morelan, A., Nale, S., Nevitt, J., O'Neal, M., Olson, B., Oskin, M., Padilla, S., Patton, J., Philibosian, B., Pierce, I., Pridmore, C., Roth, N., Sandwell, D., Scharer, K., Seitz, G., Singleton, D., Smith-Konter, B., Spangler, E., Swanson, B., Jobe, J. T., Treiman, J., Valencia, F., Vanderwal, J., Williams, A., Xu, X., Zachariasen, J., Zimmerman, J., and Zinke, R. (2020). Documentation of Surface Fault Rupture and Ground-Deformation Features Produced by the 4 and 5 July 2019 Mw 6.4 and Mw 7.1 Ridgecrest Earthquake Sequence. *Seismological Research Letters* 91.5. DOI: `10.1785/0220190322`. Pp. 2942–2959.

Qin, L., Share, P.-E., Qiu, H., Allam, A. A., Vernon, F. L., and Ben-Zion, Y. (2020). Internal structure of the San Jacinto fault zone at the Ramona Reservation, north of Anza, California, from dense array seismic data. *Geophysical Journal International* 224.2. DOI: `10.1093/gji/ggaa482`. Pp. 1225–1241.

Qin, Z., Chen, H., and Chang, J. (2017a). Detection performance improvement of distributed vibration sensor based on curvelet denoising method. *Sensors* 17. Pp. 1380–1388.

– (2017b). Signal-to-noise ratio enhancement based on empirical mode decomposition in phase-sensitive optical time domain reflectometry systems. *Sensors* 17. Pp. 1870–1880.

Qin, Z., Chen, L., and Bao, X. (2012). Wavelet denoising method for improving detection performance of distributed vibration sensor. *IEEE Photonics Technology Letters* 24. Pp. 542–544.

Qiu, H., Ben-Zion, Y., Catchings, R., Goldman, M. R., Allam, A. A., and Steidl, J. (2021). Seismic Imaging of the Mw 7.1 Ridgecrest Earthquake Rupture Zone From Data Recorded by Dense Linear Arrays. *Journal of Geophysical Research: Solid Earth* 126.7. DOI: `10.1029/2021JB022043`.

Qiu, H., Chi, B., and Ben-Zion, Y. (2023). Internal Structure of the Central Garlock Fault Zone From Ridgecrest Aftershocks Recorded by Dense Linear Seismic Arrays. *Geophysical Research Letters* 50.2. DOI: `10.1029/2022GL101761`. e2022GL101761.

Qiu, H., Niu, F., and Qin, L. (2021). Denoising Surface Waves Extracted From Ambient Noise Recorded by 1-D Linear Array Using Three-Station Interferometry of Direct Waves. *Journal of Geophysical Research: Solid Earth* 126.8. DOI: `10.1029/2021JB021712`.

Qiu, Q., Barbot, S., Wang, T., and Wei, S. (2020). Slip Complementarity and Triggering between the Foreshock, Mainshock, and Afterslip of the 2019 Ridgecrest Rupture Sequence. *Bulletin of the Seismological Society of America* 110.4. DOI: `10.1785/0120200037`. Pp. 1701–1715.

R. Fernández-Ruiz, M., Costa, L., and F. Martins, H. (2019). Distributed Acoustic Sensing Using Chirped-Pulse Phase-Sensitive OTDR Technology. *Sensors* 19.20. DOI: `10.3390/s19204368`. P. 4368.

Ragon, T., Sladen, A., Bletery, Q., Vergnolle, M., Cavalié, O., Avallone, A., Balestra, J., and Delouis, B. (2019). Joint Inversion of Coseismic and Early Postseismic Slip to Optimize the Information Content in Geodetic Data: Application to the 2009 M_w 6.3 L'Aquila Earthquake, Central Italy. *Journal of Geophysical Research: Solid Earth* 124.10. DOI: `10.1029/2018JB017053`. Pp. 10522–10543.

Ragon, T., Sladen, A., and Simons, M. (2019). Accounting for uncertain fault geometry in earthquake source inversions – II: application to the Mw 6.2 Amatrice earthquake, central Italy. *Geophysical Journal International* 218.1. DOI: `10.1093/gji/ggz180`. Pp. 689–707.

Raikes, S. A. (1980). Regional variations in upper mantle structure beneath Southern California. *Geophysical Journal International* 63.1. DOI: `10.1111/j.1365-246X.1980.tb02616.x`. Pp. 187–216.

Ranjith, K. and Rice, J. (2001). Slip dynamics at an interface between dissimilar materials. *Journal of the Mechanics and Physics of Solids* 49.2. DOI: `10.1016/S0022-5096(00)00029-6`. Pp. 341–361.

Reilinger, R. E., Ergintav, S., Bürgmann, R., McClusky, S., Lenk, O., Barka, A., Gurkan, O., Hearn, L., Feigl, K. L., Cakmak, R., Aktug, B., Ozener, H., and Töksoz, M. N. (2000). Coseismic and Postseismic Fault Slip for the 17 August 1999, M = 7.5, Izmit, Turkey Earthquake. *Science* 289.5484. DOI: `10.1126/science.289.5484.1519`. Pp. 1519–1524.

Rempe, M., Mitchell, T. M., Renner, J., Smith, S. A. F., Bistacchi, A., and Di Toro, G. (2018). The Relationship Between Microfracture Damage and the Physical Properties of Fault-Related Rocks: The Gole Larghe Fault Zone, Italian Southern Alps. *Journal of Geophysical Research: Solid Earth* 123.9. DOI: `10.1029/2018JB015900`. Pp. 7661–7687.

Renard, F., Gratier, J.-P., and Jamtveit, B. (2000). Kinetics of crack-sealing, intergranular pressure solution, and compaction around active faults. *Journal of Structural Geology* 22.10. DOI: `10.1016/S0191-8141(00)00064-X`. Pp. 1395–1407.

Richards-Dinger, K. B. and Shearer, P. M. (1997). Estimating crustal thickness in southern California by stacking *PmP* arrivals. *Journal of Geophysical Research: Solid Earth* 102.B7. DOI: `10.1029/97JB00883`. Pp. 15211–15224.

Richards-Dinger, K. B. and Shearer, P. M. (2000). Earthquake locations in southern California obtained using source-specific station terms. *Journal of Geophysical Research: Solid Earth* 105.B5. DOI: `10.1029/2000JB900014`. Pp. 10939–10960.

Ripley, B. D. (1976). The second-order analysis of stationary point processes. *Journal of Applied Probability* 13.2. DOI: `10.2307/3212829`. Pp. 255–266.

Robinson, D. P. (2011). A rare great earthquake on an oceanic fossil fracture zone: The 2004 Tasman Sea earthquake. *Geophysical Journal International* 186.3. DOI: `10.1111/j.1365-246X.2011.05092.x`. Pp. 1121–1134.

Romanowicz, B. (1992). Strike-slip earthquakes on quasi-vertical transcurrent faults: Inferences for general scaling relations. *Geophysical Research Letters* 19.5. DOI: `10.1029/92GL00265`. Pp. 481–484.

Ross, Z. (2024). Insights on the dip of fault zones in Southern California from modeling of seismicity with anisotropic point processes. *Seismica* 3.1. DOI: `10.26443/seismica.v3i1.1092`.

Ross, Z. E., Ben-Zion, Y., and Zaliapin, I. (2022). Geometrical properties of seismicity in California. *Geophysical Journal International* 231.1. DOI: `10.1093/gji/ggac189`. Pp. 493–504.

Ross, Z. E., Idini, B., Jia, Z., Stephenson, O. L., Zhong, M., Wang, X., Zhan, Z., Simons, M., Fielding, E. J., Yun, S.-H., Hauksson, E., Moore, A. W., Liu, Z., and Jung, J. (2019). Hierarchical interlocked orthogonal faulting in the 2019 Ridgecrest earthquake sequence. *Science* 366.6463. DOI: `10.1126/science.aaz0109`. Pp. 346–351.

Ross, Z. E., Trugman, D. T., Azizzadenesheli, K., and Anandkumar, A. (2020). Directivity Modes of Earthquake Populations with Unsupervised Learning. *Journal of Geophysical Research: Solid Earth* 125.2. DOI: `10.1029/2019JB018299`.

Ross, Z. E., Trugman, D. T., Hauksson, E., and Shearer, P. M. (2019). Searching for hidden earthquakes in Southern California. *Science* 364.6442. DOI: `10.1126/science.aaw6888`. Pp. 767–771.

Ross, Z. E., Yue, Y., Meier, M.-A., Hauksson, E., and Heaton, T. H. (2019). PhaseLink: A Deep Learning Approach to Seismic Phase Association. *Journal of Geophysical Research: Solid Earth* 124.1. DOI: `10.1029/2018JB016674`. Pp. 856–869.

Rubin, A. M. and Gillard, D. (2000). Aftershock asymmetry/rupture directivity among central San Andreas fault microearthquakes. *Journal of Geophysical Research: Solid Earth* 105.B8. DOI: `10.1029/2000JB900129`. Pp. 19095–19109.

Rubin, A. M., Gillard, D., and Got, J.-L. (1999). Streaks of microearthquakes along creeping faults. *Nature* 400.6745. DOI: `10.1038/23196`. Pp. 635–641.

Ruppert, N. A., Rollins, C., Zhang, A., Meng, L., Holtkamp, S. G., West, M. E., and Freymueller, J. T. (2018). Complex Faulting and Triggered Rupture During the 2018 M $_W$ 7.9 Offshore Kodiak, Alaska, Earthquake. *Geophysical Research Letters* 45.15. DOI: `10.1029/2018GL078931`. Pp. 7533–7541.

Saito, T., Ito, Y., Inazu, D., and Hino, R. (2011). Tsunami source of the 2011 Tohoku-Oki earthquake, Japan: Inversion analysis based on dispersive tsunami simulations. *Geophysical Research Letters* 38.7. DOI: `10.1029/2011GL049089`. L00G19.

Salah, M. K. and Zhao, D. (2004). Mapping the crustal thickness in southwest Japan using Moho-reflected waves. *Physics of the Earth and Planetary Interiors* 141.2. DOI: `10.1016/j.pepi.2003.10.002`. Pp. 79–94.

Saleeby, J., Ducea, M., and Clemens-Knott, D. (2003). Production and loss of high-density batholithic root, southern Sierra Nevada, California. *Tectonics* 22.6. DOI: `10.1029/2002TC001374`. 2002TC001374.

Sass, J., Galanis, S., Marshall, B., Lachenbruch, A., Munroe, R., and Moses, T. (1978). *Conductive heat flow in the Randsburg area, California*. Tech. rep. University of North Texas Libraries.

Savage, H. M. and Brodsky, E. E. (2011). Collateral damage: Evolution with displacement of fracture distribution and secondary fault strands in fault damage zones. *Journal of Geophysical Research* 116.B3. DOI: `10.1029/2010JB007665`. B03405.

SCEDC (2013). *Southern California Earthquake Center*. DOI: `10.7909/C3WD3xH1`.

Scholtz, C. (2019). *The Mechanics of Earthquakes and Faulting*. en. Cambridge, U.K.: Cambridge University Press.

Scholz, C. (1982). Scaling Laws for Large Earthquakes: Consequences for Physical Models. *Bulletin of the Seismological Society of America* 72.1. Pp. 1–14.

Scholz, C. H. and Choi, E. (2022). What comes first: The fault or the ductile shear zone? *Earth and Planetary Science Letters* 577. DOI: `10.1016/j.epsl.2021.117273`. P. 117273.

Segall, P. and Pollard, D. D. (1983). Nucleation and growth of strike slip faults in granite. *Journal of Geophysical Research: Solid Earth* 88.B1. DOI: `10.1029/JB088iB01p00555`. Pp. 555–568.

Sethian, J. A. (1996). A fast marching level set method for monotonically advancing fronts. *Proceedings of the National Academy of Sciences* 93.4. DOI: `10.1073/pnas.93.4.1591`. Pp. 1591–1595.

Seton, M., Müller, R. D., Zahirovic, S., Williams, S., Wright, N. M., Cannon, J., Whittaker, J. M., Matthews, K. J., and McGirr, R. (2020). A Global Data Set of Present-Day Oceanic Crustal Age and Seafloor Spreading Parameters. *Geochemistry, Geophysics, Geosystems* 21.10. DOI: `10.1029/2020GC009214`.

Seton, M., Whittaker, J. M., Wessel, P., Müller, R. D., DeMets, C., Merkouriev, S., Cande, S., Gaina, C., Eagles, G., Granot, R., Stock, J., Wright, N., and Williams, S. E. (2014). Community infrastructure and repository for marine magnetic identifications. *Geochemistry, Geophysics, Geosystems* 15.4. DOI: `10.1002/2013GC005176`. Pp. 1629–1641.

Share, P. E. and Ben-Zion, Y. (2018). A Bimaterial Interface Along the Northern San Jacinto Fault Through Cajon Pass. *Geophysical Research Letters* 45.21. DOI: `10.1029/2018GL079834`.

Share, P. E., Qiu, H., Vernon, F. L., Allam, A. A., Fialko, Y., and Ben-Zion, Y. (2022). General Seismic Architecture of the Southern San Andreas Fault Zone around the Thousand Palms Oasis from a Large-N Nodal Array. *The Seismic Record* 2.1. DOI: `10.1785/0320210040`. Pp. 50–58.

Share, P.-E., Tábořík, P., Štěpančíková, P., Stemberk, J., Rockwell, T. K., Wade, A., Arrowsmith, J. R., Donnellan, A., Vernon, F. L., and Ben-Zion, Y. (2020). Characterizing the uppermost 100 m structure of the San Jacinto fault zone southeast of Anza, California, through joint analysis of geological, topographic, seismic and resistivity data. *Geophysical Journal International* 222.2. DOI: `10.1093/gji/ggaa204`. Pp. 781–794.

Shelly, D. R. (2020). A High-Resolution Seismic Catalog for the Initial 2019 Ridgecrest Earthquake Sequence: Foreshocks, Aftershocks, and Faulting Complexity. *Seismological Research Letters* 91.4. DOI: `10.1785/0220190309`. Pp. 1971–1978.

Sheng, S. and Meng, L. (2020). Stress Field Variation During the 2019 Ridgecrest Earthquake Sequence. *Geophysical Research Letters* 47.15. DOI: `10.1029/2020GL087722`. e2020GL087722.

Shimizu, K., Yagi, Y., Okuwaki, R., and Fukahata, Y. (2020). Development of an inversion method to extract information on fault geometry from teleseismic data. *Geophysical Journal International* 220.2. DOI: `10.1093/gji/ggz496`. Pp. 1055–1065.

Shlomai, H. and Fineberg, J. (2016). The structure of slip-pulses and supershear ruptures driving slip in bimaterial friction. *Nature Communications* 7.1. DOI: `10.1038/ncomms11787`. P. 11787.

Sibson, R. H. (1985). A note on fault reactivation. *Journal of Structural Geology* 7.6. DOI: `10.1016/0191-8141(85)90150-6`. Pp. 751–754.

Silver, P. G. and Jordan, T. H. (1983). Total-moment spectra of fourteen large earthquakes. *Journal of Geophysical Research* 88.B4. DOI: `10.1029/JB088iB04p03273`. P. 3273.

Sladen, A., Rivet, D., Ampuero, J. P., De Barros, L., Hello, Y., Calbris, G., and Lamare, P. (2019). Distributed sensing of earthquakes and ocean-solid Earth interactions on seafloor telecom cables. *Nature Communications* 10.1. DOI: `10.1038/s41467-019-13793-z`. P. 5777.

Small, P., Gill, D., Maechling, P. J., Taborda, R., Callaghan, S., Jordan, T. H., Olsen, K. B., Ely, G. P., and Goulet, C. (2017). The SCEC Unified Community Velocity Model Software Framework. *Seismological Research Letters* 88.6. DOI: `10.1785/0220170082`. Pp. 1539–1552.

Smith, D. E. and Heaton, T. H. (2011). Models of Stochastic, Spatially Varying Stress in the Crust Compatible with Focal-Mechanism Data, and How Stress Inversions Can Be Biased toward the Stress Rate. *Bulletin of the Seismological Society of America* 101.3. DOI: `10.1785/0120100058`. Pp. 1396–1421.

Smith, G. (1962). Large Lateral Displacement on Garlock Fault, Califonia, as Measured from Offset Dike Swarm. *AAPG Bulletin* 46. DOI: `10.1306/BC74375F-16BE-11D7-8645000102C1865D`.

Smith, J. D., Azizzadenesheli, K., and Ross, Z. E. (2021). EikoNet: Solving the Eikonal Equation With Deep Neural Networks. *IEEE Transactions on Geoscience and Remote Sensing* 59.12. DOI: `10.1109/TGRS.2020.3039165`. Pp. 10685–10696.

Smith, J. D., Ross, Z. E., Azizzadenesheli, K., and Muir, J. B. (2021). HypoSVI: Hypocentre inversion with Stein variational inference and physics informed neural networks. *Geophysical Journal International* 228.1. DOI: `10.1093/gji/ggab309`. Pp. 698–710.

Socquet, A., Hollingsworth, J., Pathier, E., and Bouchon, M. (2019). Evidence of supershear during the 2018 magnitude 7.5 Palu earthquake from space geodesy. *Nature Geoscience* 12.3. DOI: `10.1038/s41561-018-0296-0`. Pp. 192–199.

Somerville, P. and Yoshimura, J. (1990). The influence of critical Moho Reflections on strong ground motions recorded in San Francisco and Oakland during the 1989 Loma Prieta Earthquake. *Geophysical Research Letters* 17.8. DOI: `10.1029/GL017i008p01203`. Pp. 1203–1206.

Song, J. and Yang, H. (2022). Seismic Site Response Inferred From Records at a Dense Linear Array Across the Chenghai Fault Zone, Binchuan, Yunnan. *Journal of Geophysical Research: Solid Earth* 127.1. DOI: `10.1029/2021JB022710`. e2021JB022710.

Spica, Z., Nishida, K., Akuhara, T., Pétrélis, F., Shinohara, M., and Yamaha, T. (2020). Marine sediment characterized by ocean bottom fiber-optic seismology. *Geophysical Research Letters* 47. e2020GL088360.

Spica, Z. J., Castellanos, J. C., Viens, L., Nishida, K., Akuhara, T., Shinohara, M., and Yamada, T. (2022). Subsurface Imaging With Ocean-Bottom Distributed Acoustic Sensing and Water Phases Reverberations. *Geophysical Research Letters* 49.2. DOI: `10.1029/2021GL095287`.

Spica, Z. J., Nishida, K., Akuhara, T., Pétrélis, F., Shinohara, M., and Yamada, T. (2020). Marine Sediment Characterized by Ocean-Bottom Fiber-Optic Seismology. *Geophysical Research Letters* 47.16. DOI: `10.1029/2020GL088360`.

Spica, Z. J., Perton, M., Martin, E. R., Beroza, G. C., and Biondi, B. (2020). Urban Seismic Site Characterization by Fiber-Optic Seismology. *Journal of Geophysical Research: Solid Earth* 125.3. DOI: `10.1029/2019JB018656`. e2019JB018656.

Sui, S., Shen, W., Holt, W., and Kim, J. (2023). Crustal Architecture Across Southern California and Its Implications on San Andreas Fault Development. *Geophysical Research Letters* 50.8. DOI: `10.1029/2022GL101976`. e2022GL101976.

Sun, H., Ross, Z. E., Zhu, W., and Azizzadenesheli, K. (2023). Phase Neural Operator for Multi-Station Picking of Seismic Arrivals. *Geophysical Research Letters* 50.24. DOI: `10.1029/2023GL106434`. e2023GL106434.

Tape, C., Plesch, A., Shaw, J. H., and Gilbert, H. (2012). Estimating a Continuous Moho Surface for the California Unified Velocity Model. *Seismological Research Letters* 83.4. DOI: `10.1785/0220110118`. Pp. 728–735.

Tarantola, A. (2005). *Inverse Problem Theory and Methods for Model Parameter Estimation*. en. Society for Industrial and Applied Mathematics. DOI: `10.1137/1.9780898717921`.

Thakur, P., Huang, Y., and Kaneko, Y. (2020). Effects of Low-Velocity Fault Damage Zones on Long-Term Earthquake Behaviors on Mature Strike-Slip Faults. *Journal of Geophysical Research: Solid Earth* 125.8. DOI: `10.1029/2020JB019587`.

Thatcher, W. and Hill, D. P. (1991). Fault orientations in extensional and conjugate strike-slip environments and their implications. *Geology* 19.11. DOI: `10.1130/0091-7613(1991)019<1116:FOIEAC>2.3.CO;2`. P. 1116.

Thingbaijam, K. K. S., Martin Mai, P., and Goda, K. (2017). New Empirical Earthquake Source-Scaling Laws. *Bulletin of the Seismological Society of America* 107.5. DOI: `10.1785/0120170017`. Pp. 2225–2246.

Thomas, M. Y., Lapusta, N., Noda, H., and Avouac, J.-P. (2014). Quasi-dynamic versus fully dynamic simulations of earthquakes and aseismic slip with and without enhanced coseismic weakening. *Journal of Geophysical Research: Solid Earth* 119.3. DOI: `10.1002/2013JB010615`. Pp. 1986–2004.

Toda, S. and Stein, R. S. (2020). Long- and Short-Term Stress Interaction of the 2019 Ridgecrest Sequence and Coulomb-Based Earthquake Forecasts. *Bulletin of the Seismological Society of America* 110.4. DOI: `10.1785/0120200169`. Pp. 1765–1780.

Tong, P., Yao, J., Liu, Q., Li, T., Wang, K., Liu, S., Cheng, Y.-W., and Wu, S. (2021). Crustal Rotation and Fluids: Factors for the 2019 Ridgecrest Earthquake Sequence? *Geophysical Research Letters* 48.3. DOI: `10.1029/2020GL090853`. e2020GL090853.

Touma, R., Aubry, A., Ben-Zion, Y., and Campillo, M. (2022). Distribution of seismic scatterers in the San Jacinto Fault Zone, southeast of Anza, California, based on passive matrix imaging. *Earth and Planetary Science Letters* 578. DOI: `10.1016/j.epsl.2021.117304`. P. 117304.

Townend, J. (2004). Regional tectonic stress near the San Andreas fault in central and southern California. *Geophysical Research Letters* 31.15. DOI: `10.1029/2003GL018918`. L15S11.

Townend, J. and Zoback, M. D. (2001). Implications of earthquake focal mechanisms for the frictional strength of the San Andreas fault system. *Geological Society, London, Special Publications* 186.1. DOI: `10.1144/GSL.SP.2001.186.01.02`. Pp. 13–21.

Trugman, D. T. and Shearer, P. M. (2017). GrowClust: A Hierarchical Clustering Algorithm for Relative Earthquake Relocation, with Application to the Spanish Springs and Sheldon, Nevada, Earthquake Sequences. *Seismological Research Letters* 88.2A. DOI: `10.1785/0220160188`. Pp. 379–391.

Twardzik, C., Vergnolle, M., Sladen, A., and Avallone, A. (2019). Unravelling the contribution of early postseismic deformation using sub-daily GNSS positioning. *Scientific Reports* 9.1. DOI: `10.1038/s41598-019-39038-z`. P. 1775.

University of Nevada, R. (1971). *Nevada Seismic Network*. DOI: `https://doi.org/10.7914/SN/NN`.

USGS (1980). *US Geological Survey Networks*. DOI: `https://doi.org/10.7914/SN/GS`.

– (2019). *M 7.1 - 2019 Ridgecrest Earthquake Sequence*. URL: `https://earthquake.usgs.gov/earthquakes/eventpage/ci38457511/moment-tensor?source=us&code=us_70004bn0_mww`.

USGS and CGS (2022). *Quaternary fault and fold database for the United States*. URL: `https://www.usgs.gov/natural-hazards/earthquake-hazards/faults`.

Vallée, M. and Douet, V. (2016). A new database of source time functions (STFs) extracted from the SCARDEC method. *Physics of the Earth and Planetary Interiors* 257. DOI: `10.1016/j.pepi.2016.05.012`. Pp. 149–157.

Vidale, J. E. (1986). Complex polarization analysis of particle motion. *Bulletin of the Seismological Society of America* 76.5. Pp. 1393–1405.

Viens, L., Perton, M., Spica, Z. J., Nishida, K., Yamada, T., and Shinohara, M. (2022). Understanding surface wave modal content for high-resolution imaging of submarine sediments with distributed acoustic sensing. *Geophysical Journal International* 232.3. DOI: `10.1093/gji/ggac420`. Pp. 1668–1683.

Wald, D. J. and Heaton, T. H. (1992). Spatial and temporal distribution of slip for the 1992 Landers, California, Earthquake. *Bulletin of the Seismological Society of America*. June 1994 84.3. Pp. 668–691.

Waldhauser, F. and Ellsworth, W. (2000). A Double-Difference Earthquake Location Algorithm: Method and Application to the Northern Hayward Fault, California. *Bulletin of the Seismological Society of America* 90.6. DOI: `10.1785/0120000006`. Pp. 1353–1368.

Walsh, D., Arnold, R., and Townend, J. (2009). A Bayesian approach to determining and parametrizing earthquake focal mechanisms. *Geophysical Journal International* 176.1. DOI: `10.1111/j.1365-246X.2008.03979.x`. Pp. 235–255.

Wang, D., Wu, S., Li, T., Tong, P., and Gao, Y. (2022). Elongated Magma Plumbing System Beneath the Coso Volcanic Field, California, Constrained by Seismic Reflection Tomography. *Journal of Geophysical Research: Solid Earth* 127.6. DOI: `10.1029/2021JB023582`. e2021JB023582.

Wang, E. and Rubin, A. M. (2011). Rupture directivity of microearthquakes on the San Andreas Fault from spectral ratio inversion: Bimaterial microearthquake directivity. *Geophysical Journal International* 186.2. DOI: `10.1111/j.1365-246X.2011.05087.x`. Pp. 852–866.

Wang, H. F., Zeng, X., Miller, D. E., Fratta, D., Feigl, K. L., Thurber, C. H., and Mellors, R. J. (2018). Ground motion response to an ML 4.3 earthquake using co-located distributed acoustic sensing and seismometer arrays. *Geophysical Journal International* 213.3. DOI: `10.1093/gji/ggy102`. Pp. 2020–2036.

Wang, H., Liu, M., Duan, B., and Cao, J. (2020). Rupture Propagation along Stepovers of Strike-Slip Faults: Effects of Initial Stress and Fault Geometry. *Bulletin of the Seismological Society of America* 110.3. DOI: `10.1785/0120190233`. Pp. 1011–1024.

Wang, X. and Zhan, Z. (2020). Seismotectonics and Fault Geometries of the 2019 Ridgecrest Sequence: Insight From Aftershock Moment Tensor Catalog Using 3-D Green's Functions. *Journal of Geophysical Research: Solid Earth* 125.5. DOI: `10.1029/2020JB019577`. e2020JB019577.

Wang, Y., Allam, A., and Lin, F.-C. (2019). Imaging the Fault Damage Zone of the San Jacinto Fault Near Anza With Ambient Noise Tomography Using a Dense Nodal Array. *Geophysical Research Letters* 46.22. DOI: `10.1029/2019GL084835`. Pp. 12938–12948.

Wang, Y., Forsyth, D. W., Rau, C. J., Carriero, N., Schmandt, B., Gaherty, J. B., and Savage, B. (2013). Fossil slabs attached to unsubducted fragments of the Farallon plate. *Proceedings of the National Academy of Sciences* 110.14. DOI: `10.1073/pnas.1214880110`. Pp. 5342–5346.

Wéber, Z. (2006). Probabilistic local waveform inversion for moment tensor and hypocentral location. *Geophysical Journal International* 165.2. DOI: `10.1111/j.1365-246X.2006.02934.x`. Pp. 607–621.

Wells, D. L. and Coppersmith, K. J. (1994). New Empirical Relationships among Magnitude, Rupture Length, Rupture Width, Rupture Area, and Surface Displacement. *Bulletin of the Seismological Society of America* 84.4. Pp. 974–1002.

Weng, H., Yang, H., Zhang, Z., and Chen, X. (2016). Earthquake rupture extents and coseismic slips promoted by damaged fault zones: Ruptures Promoted by Fault Zones. *Journal of Geophysical Research: Solid Earth* 121.6. DOI: `10.1002/2015JB012713`. Pp. 4446–4457.

Wernicke, B., Spencer, J. E., Burchfiel, B. C., and Guth, P. L. (1982). Magnitude of crustal extension in the southern Great Basin. *Geology* 10. Pp. 499–502.

Wesnousky, S. G. (2008). Displacement and Geometrical Characteristics of Earthquake Surface Ruptures: Issues and Implications for Seismic-Hazard Analysis and the Process of Earthquake Rupture. *Bulletin of the Seismological Society of America* 98.4. DOI: `10.1785/0120070111`. Pp. 1609–1632.

Wessel, P., Matthews, K. J., Müller, R. D., Mazzoni, A., Whittaker, J. M., Myhill, R., and Chandler, M. T. (2015). Semiautomatic fracture zone tracking. *Geochemistry, Geophysics, Geosystems* 16.7. DOI: `10.1002/2015GC005853`. Pp. 2462–2472.

Weston, J., Ferreira, A. M., and Funning, G. J. (2012). Systematic comparisons of earthquake source models determined using InSAR and seismic data. *Tectonophysics* 532-535. DOI: `10.1016/j.tecto.2012.02.001`. Pp. 61–81.

White, M. C. A., Fang, H., Catchings, R. D., Goldman, M. R., Steidl, J. H., and Ben-Zion, Y. (2021). Detailed traveltime tomography and seismic catalogue around the 2019 *M* w7.1 Ridgecrest, California, earthquake using dense rapid-response seismic data. *Geophysical Journal International* 227.1. DOI: `10.1093/gji/ggab224`. Pp. 204–227.

White, M. C. A., Fang, H., Nakata, N., and Ben-Zion, Y. (2020). PyKonal: A Python Package for Solving the Eikonal Equation in Spherical and Cartesian Coordinates Using the Fast Marching Method. *Seismological Research Letters* 91.4. DOI: `10.1785/0220190318`. Pp. 2378–2389.

Wiens, D. A. and Stein, S. (1983). Age dependence of oceanic intraplate seismicity and implications for lithospheric evolution. *Journal of Geophysical Research* 88.B8. DOI: `10.1029/JB088iB08p06455`. P. 6455.

Wilding, J. D. and Ross, Z. E. (2022). Aftershock Moment Tensor Scattering. *Geophysical Research Letters* 49.9. DOI: `10.1029/2022GL098473`. e2022GL098473.

– (2024). Insights on the state of stress in the mantle beneath Pahala, Hawai‘i. *Volcanica* 7.1. DOI: `10.30909/vol.07.01.0119`. Pp. 1–19.

Williams, E. F., Fernández-Ruiz, M. R., Magalhaes, R., Vanthillo, R., Zhan, Z., González-Herráez, M., and Martins, H. F. (2019). Distributed sensing of microseisms and teleseisms with submarine dark fibers. *Nature Communications* 10.1. DOI: `10.1038/s41467-019-13262-7`. P. 5778.

Williams, J. N., Toy, V. G., Massiot, C., McNamara, D. D., and Wang, T. (2016). Damaged beyond repair? Characterising the damage zone of a fault late in its interseismic cycle, the Alpine Fault, New Zealand. *Journal of Structural Geology* 90. DOI: `10.1016/j.jsg.2016.07.006`. Pp. 76–94.

Xia, K., Rosakis, A. J., Kanamori, H., and Rice, J. R. (2005). Laboratory Earthquakes Along Inhomogeneous Faults: Directionality and Supershear. *Science* 308.5722. DOI: `10.1126/science.1108193`. Pp. 681–684.

Xia, S., Zhao, D., Qiu, X., Nakajima, J., Matsuzawa, T., and Hasegawa, A. (2007). Mapping the crustal structure under active volcanoes in central Tohoku, Japan using P and PmP data. *Geophysical Research Letters* 34.10. DOI: `10.1029/2007GL030026`. 2007GL030026.

Xie, Y., Bao, H., and Meng, L. (2021). Source Imaging With a Multi-Array Local Back-Projection and Its Application to the 2019 M_w 6.4 and M_w 7.1 Ridgecrest Earthquakes. *Journal of Geophysical Research: Solid Earth* 126.10. DOI: `10.1029/2020JB021396`.

Xu, X., Sandwell, D. T., and Smith-Konter, B. (2020). Coseismic Displacements and Surface Fractures from Sentinel-1 InSAR: 2019 Ridgecrest Earthquakes. *Seismological Research Letters* 91.4. DOI: `10.1785/0220190275`. Pp. 1979–1985.

Xue, L., Li, H.-B., Brodsky, E. E., Xu, Z.-Q., Kano, Y., Wang, H., Mori, J. J., Si, J.-L., Pei, J.-L., Zhang, W., Yang, G., Sun, Z.-M., and Huang, Y. (2013). Continuous Permeability Measurements Record Healing Inside the Wenchuan Earthquake Fault Zone. *Science* 340.6140. DOI: `10.1126/science.1237237`. Pp. 1555–1559.

Yagi, Y. and Kikuchi, M. (2000). Source rupture process of the Kocaeli, Turkey, earthquake of August 17, 1999, obtained by joint inversion of near-field data and teleseismic data. *Geophysical Research Letters* 27.13. DOI: `10.1029/1999GL011208`. Pp. 1969–1972.

Yamashita, S., Yagi, Y., Okuwaki, R., Shimizu, K., Agata, R., and Fukahata, Y. (2021). Consecutive ruptures on a complex conjugate fault system during the 2018 Gulf of Alaska earthquake. *Scientific Reports* 11.1. DOI: `10.1038/s41598-021-85522-w`. P. 5979.

Yan, Z. and Clayton, R. W. (2007). Regional mapping of the crustal structure in southern California from receiver functions. *Journal of Geophysical Research: Solid Earth* 112.B5. DOI: `10.1029/2006JB004622`. 2006JB004622.

Yang, H., Duan, Y., Song, J., Jiang, X., Tian, X., Yang, W., Wang, W., and Yang, J. (2020). Fine Structure of the Chenghai Fault Zone, Yunnan, China, Constrained From Teleseismic Travel Time and Ambient Noise Tomography. *Journal of Geophysical Research: Solid Earth* 125.7. DOI: `10.1029/2020JB019565`.

Yang, W., Hauksson, E., and Shearer, P. M. (2012). Computing a Large Refined Catalog of Focal Mechanisms for Southern California (1981-2010): Temporal Stability of the Style of Faulting. *Bulletin of the Seismological Society of America* 102.3. DOI: `10.1785/0120110311`. Pp. 1179–1194.

Yang, Y., Atterholt, J. W., Shen, Z., Muir, J. B., Williams, E. F., and Zhan, Z. (2022). Sub-Kilometer Correlation Between Near-Surface Structure and Ground Motion Measured With Distributed Acoustic Sensing. *Geophysical Research Letters* 49.1. DOI: `10.1029/2021GL096503`.

Yang, Y., Zhan, Z., Shen, Z., and Atterholt, J. (2022a). Fault Zone Imaging with Distributed Acoustic Sensing: Surface-Wave Scattering.

– (2022b). Fault Zone Imaging With Distributed Acoustic Sensing: Surface-To-Surface Wave Scattering. *Journal of Geophysical Research: Solid Earth* 127.6. DOI: `10.1029/2022JB024329`.

Yin, J., Li, Z., and Denolle, M. A. (2021). Source Time Function Clustering Reveals Patterns in Earthquake Dynamics 92.4.

Yin, Z.-M. and Rogers, G. C. (1995). Rotation of the principal stress directions due to earthquake faulting and its seismological implications. *Bulletin of the Seismological Society of America* 85.5. DOI: `10.1785/BSSA0850051513`. Pp. 1513–1517.

Yoshida, K., Hasegawa, A., and Okada, T. (2015). Spatially heterogeneous stress field in the source area of the 2011 Mw 6.6 Fukushima-Hamadori earthquake, NE Japan, probably caused by static stress change. *Geophysical Journal International* 201.2. DOI: `10.1093/gji/ggv068`. Pp. 1062–1071.

Yu, C., Day, E., Van de Hoop, M., Campillo, M., and Van der Hilst, R. (2017). Mapping mantle transition zone discontinuities beneath the Central Pacific with array processing of SS precursors. *Journal of Geophysical Research: Solid Earth* 122. Pp. 364–378.

Yu, C., Castellanos, J. C., and Zhan, Z. (2021). Imaging Strong Lateral Heterogeneities Across the Contiguous US Using Body-To-Surface Wave Scattering. *Journal of Geophysical Research: Solid Earth* 126.1. DOI: `10.1029/2020JB020798`. e2020JB020798.

Yu, C., Zhan, Z., Lindsey, N. J., Ajo-Franklin, J. B., and Robertson, M. (2019). The Potential of DAS in Teleseismic Studies: Insights From the Goldstone Experiment. *Geophysical Research Letters* 46.3. DOI: `10.1029/2018GL081195`. Pp. 1320–1328.

Yue, H., Sun, J., Wang, M., Shen, Z., Li, M., Xue, L., Lu, W., Zhou, Y., Ren, C., and Lay, T. (2021). The 2019 Ridgecrest, California earthquake sequence: Evolution of seismic and aseismic slip on an orthogonal fault system. *Earth and Planetary Science Letters* 570. DOI: `10.1016/j.epsl.2021.117066`. P. 117066.

Zandt, G., Gilbert, H., Owens, T. J., Ducea, M., Saleeby, J., and Jones, C. H. (2004). Active foundering of a continental arc root beneath the southern Sierra Nevada in California. *Nature* 431.7004. DOI: `10.1038/nature02847`. Pp. 41–46.

Zhan, Z. (2020). Distributed Acoustic Sensing Turns Fiber-Optic Cables into Sensitive Seismic Antennas. *Seismological Research Letters* 91.1. DOI: `10.1785/0220190112`. Pp. 1–15.

Zhan, Z., Ni, S., Helmberger, D. V., and Clayton, R. W. (2010). Retrieval of Moho-reflected shear wave arrivals from ambient seismic noise: SmS reflections from seismic noise. *Geophysical Journal International*. DOI: `10.1111/j.1365-246X.2010.04625.x`. no–no.

Zhang, J. and Langston, C. A. (2020). Separating the scattered wavefield from teleseismic P using curvelets on the long beach array data set. *Geophysical Journal International* 220.2. DOI: `10.1093/gji/ggz487`. Pp. 1112–1127.

Zhang, Q. and Lin, G. (2014). Three-dimensional Vp and Vp/Vs models in the Coso geothermal area, California: Seismic characterization of the magmatic system. *Journal of Geophysical Research: Solid Earth* 119.6. DOI: `10.1002/2014JB010992`. Pp. 4907–4922.

Zhang, Z., Deng, Y., Qiu, H., Peng, Z., and Liu-Zeng, J. (2022). High-Resolution Imaging of Fault Zone Structure Along the Creeping Section of the Haiyuan Fault, NE Tibet, From Data Recorded by Dense Seismic Arrays. *Journal of Geophysical Research: Solid Earth* 127.9. DOI: `10.1029/2022JB024468`. e2022JB024468.

Zhao, D., Kanamori, H., and Wiens, D. (1997). State of stress before and after the 1994 Northridge Earthquake. *Geophysical Research Letters* 24.5. DOI: `10.1029/97GL00258`. Pp. 519–522.

Zhou, J., Pan, Z., Ye, Q., Cai, H., Qu, R., and Fang, Z. (2013). Characteristics and explanations of interference Fading of a -OTDR with a multi-frequency source. *Journal of Lightwave Technology* 31. Pp. 2947–2954.

Zhu, L. (2000). Crustal structure across the San Andreas Fault, southern California from teleseismic converted waves. *Earth and Planetary Science Letters* 179.1. DOI: `10.1016/S0012-821X(00)00101-1`. Pp. 183–190.

Zhu, L. and Kanamori, H. (2000). Moho depth variation in southern California from teleseismic receiver functions. *Journal of Geophysical Research: Solid Earth* 105.B2. DOI: `10.1029/1999JB900322`. Pp. 2969–2980.

Zhu, L., Mitchell, B. J., Akyol, N., Cemen, I., and Kekovali, K. (2006). Crustal thickness variations in the Aegean region and implications for the extension of continental crust. *Journal of Geophysical Research: Solid Earth* 111.B1. DOI: `10.1029/2005JB003770`. 2005JB003770.

Zhu, T., Xiao, X., He, Q., and Diao, D. (2013). Enhancement of SNR and spatial resolution in -OTDR system by using two-dimensional edge detection method. *Journal of Lightwave Technology* 31. Pp. 2851–2856.

Zhu, W. and Beroza, G. C. (2018). PhaseNet: A Deep-Neural-Network-Based Seismic Arrival Time Picking Method. *Geophysical Journal International*. DOI: `10.1093/gji/ggy423`.

Zhu, W., Biondi, E., Li, J., Yin, J., Ross, Z. E., and Zhan, Z. (2023). Seismic arrival-time picking on distributed acoustic sensing data using semi-supervised learning. *Nature Communications* 14.1. DOI: `10.1038/s41467-023-43355-3`. P. 8192.

Zhu, W., McBrearty, I. W., Mousavi, S. M., Ellsworth, W. L., and Beroza, G. C. (2022). Earthquake Phase Association Using a Bayesian Gaussian Mixture Model. *Journal of Geophysical Research: Solid Earth* 127.5. DOI: `10.1029/2021JB023249`. e2021JB023249.

Zigone, D., Ben-Zion, Y., Campillo, M., and Roux, P. (2015). Seismic Tomography of the Southern California Plate Boundary Region from Noise-Based Rayleigh and Love Waves. *Pure and Applied Geophysics* 172.5. DOI: `10.1007/s00024-014-0872-1`. Pp. 1007–1032.

Zigone, D., Ben-Zion, Y., Lehujeur, M., Campillo, M., Hillers, G., and Vernon, F. L. (2019). Imaging subsurface structures in the San Jacinto fault zone with high-frequency noise recorded by dense linear arrays. *Geophysical Journal International* 217.2. DOI: `10.1093/gji/ggz069`. Pp. 879–893.

Zoback, M. D. and Beroza, G. C. (1993). Evidence for near-frictionless faulting in the 1989 (M 6.9) Loma Prieta, California, earthquake and its aftershocks. *Geology* 21.2. DOI: `10.1130/0091-7613(1993)021<0181:EFNFFI>2.3.CO;2`. P. 181.